NOTE TO USERS

DALHOUSIE UNIVERSITY

To comply with the Canadian Privacy Act the National Library of Canada has requested that the following pages be removed from this copy of the thesis:

Preliminary Pages
- Examiners Signature Page
- Dalhousie Library Copyright Agreement

Appendices
- Copyright Releases (if applicable)

STEEL-FREE BRIDGE DECKS UNDER CYCLIC LOADING: A STUDY OF CRACK PROPAGATION AND STRENGTH DEGRADATION

by

Vidyadhar Narayan Limaye

Submitted

in partial fulfillment of the requirements

for the degree of

DOCTOR OF PHILOSOPHY

Major Subject: Civil Engineering

at

DALHOUSIE UNIVERSITY

Halifax, Nova Scotia April, 2004

Your file Votre référence
ISBN: 0-494-02126-8
Our file Notre référence
ISBN: 0-494-02126-8

TABLE OF CONTENTS

LIST OF TABLES

LIST OF FIGURES

Page

LIST OF SYMBOLS AND ABBREVIATIONS

AASHTO	American Association of State Highway and Transportation Officials
CHBDC	Canadian Highway Bridge Design Code
CSA	Canadian Standards Association
DT	Displacement Transducer
FRC	Fiber Reinforced Concrete
GFRP	Glass Fiber Reinforced Polymers
GI	Galvanized Iron
GSF-1	Grace Structural Fiber
Hz	Frequency in Cycles per Second
kN	kiloNewtons
KPa	kilo Pascal, a unit of pressure
LED	Light Emitting Diode
MPa	Mega Pascal, a unit of pressure
OHBDC	Ontario Highway Bridge Design Code
PC	Personal Computer
PVC	Polyvinyl Chloride
SCXI	Signal Conditioning System
SHS	Structural Hollow Section
SLS II	Serviceability Limit State-II
ULS	Ultimate Limit State

A	A coefficient used in fatigue life calculation, area of steel strap
ADT	Average Daily Traffic on one highway lane
ADTT	Average Daily Truck Traffic on one highway
$ADTT_{SL}$	Average daily Truck Traffic on a single highway lane
$Atten_{rel}$	Relative attenuation of waveform
B	Exponential power used in fatigue calculation
CB	Bottom embedment gauge at centre of panel
CD2	Group of 2 crack detection gauges

CD4	Group of 4 crack detection gauges
CM	Middle embedment gauge at centre of panel
CPG	Cluster of crack propagation gauges
CPL1	Lower crack propagation gauge number 1
CPL2	Lower crack propagation gauge number 2
CPU2	Upper crack propagation gauge number 2
CT	Top embedment gauge at centre of panel
e	Exponential
ELC	Equivalent Load Cycles
EN	Equivalent Fatigue Life
E_o	Modulus of elasticity at beginning of cyclic loading
f_c'	Compressive strength of concrete
F_S	Factor related to inner and outer girders in Steel-free bridge decks
$IAmp_a$	Integrated amplitude of waveform recorded by active sensor
$Iamp_r$	Integrated amplitude of waveform recorded by reference sensor
Ln( )	Natural logarithm of a number
Log( )	Logarithm of a number to base
M	Normalized magnitude of acoustic waveform
M_n	Normalized magnitude of acoustic waveform at sector n
M_{n+1}	Normalized magnitude of acoustic waveform at sector n+1
MR	Modulus of rupture
N	Log of number of load cycles to failure (Batchelor and Hewitt, 1974)
N	Number of load cycles required to failure
n_1, n_2, n_n	Number of load cycles applied at cyclic peak loads P_1, P_2, P_n
N_1, N_n, N_1	Number of load cycles to failure at cyclic peak loads P_1, P_2, P_n
NB	Bottom embedment gauge at north
NM	Middle embedment gauge at north
NT	Top embedment gauge at north
P	Applied load, applied peak load on deck slab
P'_S	Estimated static failure load
P_1, P_2, P_n	Cyclic peak loads
P_f	Applied cyclic load

PFRC1	Steel-free deck model-1 (Matsui et al.)
PFRC2	Steel-free deck model-2 (Matsui et al.)
PFRC3	Steel-free deck model-3 (Matsui et al.)
P_s	Static punching failure load of deck slab
R	Stress ratio
R_1	Ratio of peak load P_1 to static failure load P
R_2	Ratio of peak load P_2 to static failure load P
Ri	Residual strength index
S	Stress level, spacing of girders, maximum stress
S_{+ve}	maximum positive stress
SB	Bottom embedment gauge at south
S_l	Spacing of Straps in a steel free bridge deck
SM	Middle embedment gauge at south
S_{max}	Maximum stress
S_{min}	Minimum stress of the same nature as S_{max}
SN-1	First strain gauge from southern end of instrumented bar
SN-2	Second strain gauge from southern end of instrumented bar
SN-3	Third strain gauge from southern end of instrument bar
SN-4	Fourth strain gauge from southern end of instrument bar
SN-5	Fifth strain gauge from southern end of instrument bar
SR	Stress range
ST	Top embedment gauge at south
S_{-ve}	Maximum negative Stress
t	Thickness of deck slab
Ω	Ohms, a unit for electrical resistance of strain gauge
$\delta_{elastic}$	Elastic shortening of slab
ε	Strain
$\varepsilon_{elastic}$	Elastic strain
$\mu\varepsilon$	Micro strain
σ_{max}	Maximum stress
σ_{min}	Minimum stress
σ_2, σ_3	Principal stresses

ACKNOWLEDGEMENTS

My foremost thanks are due to my supervisor Dr. Aftab Mufti who made this research possible by providing financial support through NSERC's Network of Centres of Excellence for Intelligent Sensing for Innovative Structures, ISIS Canada. His continued guidance in every other form was vital to the completion of my research. Equally important was the financial, technical and moral support provided by my co-supervisor, Dr. Baidar Bakht. His easy accessibility for consultation, coupled with his periodic visits to Halifax ensured that important decisions could be taken without delay. Guidance committee member, Dr. Stephen Butt, provided partial funding for research assistance and installed the Acoustic Attenuation System. His team provided excellent technical support throughout the test period. The successful application of Acoustic Attenuation Technique added a new dimension to my research. Dr. J. F. Trottier, also a member of my guidance committee, maintained an active interest in my work and made valuable suggestions during our regular briefing sessions. He, along with Ms. Leigh Beauchamp-Day, helped raise the profile of my research work by providing suitable media exposure. Thanks are due to Dr. Gamil Tadros for his valuable advice concerning embedded instrumentation and crack control reinforcement. Advice from Dr. Javad Jalali during the planning stage of the research is appreciated.

Special thanks are due to the man on the spot, and my on-campus co-supervisor, Dr. John Newhook, who, with a unique insight in this area of research, provided a strong support throughout, and helped me see clearly through a maze of apparently conflicting data.

Thanks to Peter Jones whose advice was invaluable in eliminating numerous bugs in LabVIEW that cropped up from time to time. David Connors from Mining Program assisted with acoustic imaging of the deck model. Help from fellow graduate students, Dean Forgeron, Vaibhav Banthia, Amjad Memon, Greg Peters, and undergraduate student, Christian Deveau, is greatly appreciated. Chris Barnes and Mike Mahoney, both of ISIM Group helped greatly by their flexibility in sharing the testing apparatus. Technician Blair Nickerson helped in many different ways throughout the test.

Technician Albert Murphy's suggestion to modify the hydraulic pump was the most valuable advice that speeded up the test process, without which, the testing would have extended over a much longer period.

The two persons who made the largest contribution to the testing process are, lab technician Mark MacDonald, and former undergraduate student Randy Cormier. Mark provided a strong technical support in various forms, such as maintaining the testing apparatus in working order, operating the pump whenever he could, and carrying out numerous modifications to the hydraulic system to speed up the test process. Randy made the testing process very smooth with his excellent control of the pump remote, and by being available over a countless number of weekends and holidays.

I would like to thank Dr. Farid Taheri, Dr. Thorburn and the staff of Civil Engineering department, the Graduate Studies Office at Sexton Campus, and the Faculty of Graduate Studies, Dalhousie University, for their continued support.

No project, however small, can be completed without a strong administrative support. Ms. Kathleen Dempsey of Nova Scotia CAD/CAM Centre did everything from ensuring timely processing of requisitions, to keeping track of funding and supplies. Subsequent support from Jeanne Mutch is also greatly appreciated.

My research extended over a period of almost four years. A large portion of this period was spent in actual testing of the model. It is therefore no surprise, that a large number of people have been acknowledged for contributing to the success of my research. I have endeavoured to acknowledge every one who helped in my work. However, if someone has been overlooked inadvertently, I take full responsibility for the omission and offer my sincere apologies for the omission.

Last but not least, I wish to thank my wife Anita, and my daughters Navika, Deepti, and Warda, who encouraged and motivated me throughout my graduate studies.

ABSTRACT

Steel-free bridge decks, based on the concept of the arching action in confined concrete slabs, fail in punching shear at loads that are significantly higher than those for the unconfined reinforced concrete slabs, which typically fail in flexure.

The arching action produces a longitudinal crack at the centre of the slab at an early stage in the service life of the structure. This crack, however, does not affect the performance of the slab and is more of an aesthetic issue. The current research was undertaken to find a method to reduce or 'train' these cracks and to study the fatigue resistance of various configurations of steel-free bridge decks.

A full-scale model comprising four panels, each with a different internal configuration, was designed, constructed, and tested at Dalhousie University. The model was extensively instrumented to monitor its response under cyclic loading. An acoustic attenuation technique was also used to independently assess the extent of damage in the deck slab. In the first phase of testing, each panel was subjected to 1700 cycles of pulsating load with a peak value of 400 kN. The growth of cracks in each panel was charted and compared. An important part of this research was to assess the fatigue resistance of one of the deck slab panels with a pre-induced longitudinal crack, under asymmetrical loading conditions. Results from the first phase of the testing have shown that the crack width can be reduced significantly with the use of a bottom layer of nominal crack control reinforcement.

In the second phase of testing, the control panel was subjected to a pulsating load of progressively increasing magnitude until failure. Two other panels with nominal crack control reinforcement were also subjected to pulsating load with peak magnitudes corresponding to 90% of their ultimate static failure load, while the panel with the pre-induced longitudinal crack was tested under monotonically increasing load to failure.

A unique feature of this research was the rate of load application. Most of the fatigue tests conducted in the past have been carried out at high frequency cyclic loading in excess of 0.5 Hz. In this research, the load was applied at speeds between 4 and 10 load cycles per minute (0.07 to 0.16 Hz). The slow loading rate afforded the opportunity to closely monitor the development and propagation of cracks throughout the test. The slab surface was inspected after each 100 load cycles during the first and the second phase of the testing.

This research has shown that the bottom longitudinal cracks do not affect the performance of the steel-free deck slabs under cyclic loading. Furthermore, it has been shown that the fatigue life of steel-free deck slabs exceeds the commonly accepted minimum fatigue life requirements by a wide margin. The aesthetic issue of the crack width has also been addressed adequately. It has been shown that, the width of the longitudinal crack can be controlled by provision of a bottom layer of nominal reinforcement. It has also been established that acoustic attenuation can be used successfully in conjunction with the conventional instrumentation to detect the structural degradation of concrete structures.

1.0 INTRODUCTION

1.1 Conventional Bridge Deck Slabs

Slab-on-girder bridges are one of the most common forms of bridges used in short and medium span construction all over the world. A slab-on-girder bridge usually comprises a series of steel or prestressed concrete girders spanning between abutments and/or piers. The girders support a reinforced concrete slab spanning across the girders with or without overhangs beyond the outer girders. Such bridges are more common due to simplicity of their design and ease of construction. Research has shown that the deck slabs were able to sustain loads that were much higher than the design wheel loads and that their ultimate capacities were significantly higher than those calculated by various code specified equations. It could be said that the bridge deck slabs were over-designed. The enhanced capacities were attributed to the internal arching action that develops in well-confined deck slabs (Hewitt and Batchelor 1975). Taking into account the beneficial effects of internal arching in deck slabs, an empirical method was first introduced in Ontario Highway Bridge Design Code (OHBDC-1979). The empirical method permitted the use of isotropic reinforcement in the design of bridge deck slabs, resulting in substantial savings in the quantity of reinforcing steel used (Bakht and Markovic 1986). However, the deterioration of the reinforced concrete decks slabs due to the corrosion of reinforcement continues to be a major problem for bridge engineers. The use of de-icing salts, coupled with the cracking of concrete leads to the corrosion of reinforcing steel and subsequent delamination of concrete.

1.2 Steel-Free Decks

In early 1990s, a team of Canadian researchers developed the concept of steel-free bridge decks which harnessed the internal arching action effectively by eliminating internal steel reinforcement and replacing it with external steel straps placed below the deck slab (Mufti et al.1993). Several bridges and one fishing wharf have been constructed in Canada using this technology (Bakht and Mufti 1998; Newhook et al. 2000).

1.3 Motivation for Current Research and its Scope

It was observed in the field that steel-free deck slabs develop a longitudinal crack on the soffit mid-way between adjacent girders early in their life. In some cases, this crack exceeded 1 mm in width (Mufti et al. 1999). Although such cracks have not affected the performance of bridges; aesthetically, large cracks in concrete structures are unacceptable. Laboratory investigations under static loads did not develop these cracks, (Wegner 1993; Newhook 1997; Thorburn 1998). Bakht and Selvadurai (1996), and Selvadurai and Bakht (1995) conducted simulated rolling wheel tests on steel-free deck slabs and also observed longitudinal cracks similar to those observed in the field. It is noted that the load levels in these fatigue tests were too low for the results to be conclusive.

The research in this thesis was initiated to study this cracking and to investigate the effects of longitudinal cracks on the performance of steel-free deck slabs under fatigue loading. Crack widths and lengths are important visual indicators of the extent of damage in concrete. The integrity of the structure can be compromised by extensive cracking. An extensively cracked structure loses its stiffness and may not be able to withstand cyclic loading without undergoing large displacements. It was felt that the width of longitudinal cracks could be controlled or reduced without changing the basic concepts or the mechanics behind the steel-free bridge deck system. The alternatives considered in this thesis for controlling or reducing the crack widths were:

a) a crack trainer,
b) a glass fiber reinforced (GFRP) crack control grid,
c) a steel crack control mesh.

A full-scale two-girder bridge deck model with four different internal configurations was constructed and tested under cyclic loading to failure. The model was instrumented extensively to monitor changes in its response under fatigue loading. An acoustic transmission technique was also used as an independent means of detecting the internal changes occurring in concrete.

The testing was conducted under low-cycle, high-load conditions. A detailed comparison of visual cracking and the test data was performed. Fatigue life prediction models are examined compared in Chapter 7. Reinforcement details to control and reduce the longitudinal crack and the Y-shaped cracks near the edge beam are proposed. As well, a fatigue life prediction curve has been proposed.

1.4 General Approach and Methodology

1.4.1 Design of Model

To avoid the scale effects that are associated with the fatigue tests on small-scale models, a full-scale model was constructed. The design and construction of the model was carried out in accordance with Section 16 of the Canadian Highway Bridge Design Code (CAN/CSA-S6-00). The first of the four panels served as the control panel and was designated as Panel-A. The second panel, designated as Panel-B, had a crack trainer on the soffit to simulate the field conditions. The crack trainer, fabricated by folding a thin galvanized iron strip into a 75 mm high inverted T shape, was installed mid-way between the girders. The remaining two panels, Panel-C and Panel-D, were provided with nominal GFRP and steel crack control reinforcement, respectively, near the bottom surface of the slab. The model was extensively instrumented. Acoustic transmission technique was used as a parallel system for detecting damage within the concrete deck slab.

1.4.2 Testing

The testing was carried in two phases. In Phase-I, all the panels were subjected to an equal number of load cycles. Loading was alternated between two load pads creating a kneading effect in order to induce the propagation of longitudinal crack along its length.
In Phase-II, Panels A, C, and D were tested to failure under fatigue loading, while Panel-B was tested under static loading conditions. The deck slab surfaces were inspected at regular intervals, and crack patterns were mapped whenever some changes in the crack patterns were observed. The entire testing program was conducted under a slow rate of loading. The test program is discussed in detail in Chapter 4.

1.4.3 Test Results

The test results indicated that the strains in the straps, deck deflection, acoustic attenuation and the crack patterns were the four most important parameters that reflected the changes in the structural behaviour of the decks. The changes in these parameters were closely monitored throughout the test and compared.

The change in the response of key sensors at failure was followed to establish the sequence of failure for each panel. The maximum values of strains in the straps at failure were compared. After failure of all the four panels, an acoustic survey of the model was carried out and a tomographic image of the deck slab highlighting the extent of the damage was created and compared with the visual (photographic) image of the deck surface.

It was observed that, during Phase-I, most of the cracking occurred on the bottom surface of the test panels. The crack widths in Panel-A were the largest while those in Panel-D were the smallest. The crack widths in Panel-C were moderate. The acoustic tests conducted on Panel-B showed that the longitudinal crack closed partially under full-load conditions.

During Phase-II, most of the cracking was observed to have occurred on the top surface of the panels. The changes in the strap strains and deflection showed that initially the increase in damage was rapid followed by a period of stable behaviour. In each panel, each increase in the peak load was accompanied by an immediate and sharp increase in strains and deflection, followed by a stable behaviour. At higher loads, the strains and deflection increased rapidly before failure. Representative test results are presented in Chapter 5. The results are analyzed and discussed in Chapter 6.

1.5 Significance and Contribution of This Study

This investigation provided an opportunity to study the initiation and subsequent growth of cracks until failure. This is the first known fatigue test on steel-free deck slab that was carried out to failure at a very slow rate of loading. The majority of fatigue tests in the past, were conducted at faster loading rates and were concluded when the number of load cycles applied exceeded the code requirements. This was the first study to use nominal crack-control reinforcement in steel-free bridge decks. As well, this research initiated the use of acoustic attenuation to detect internal damage in concrete deck slabs under fatigue loading. This study examines for the first time the fatigue life prediction models developed for the conventionally reinforced and steel-free deck slabs tested under a low-amplitude and high loading rate, and examines its applicability to deck slabs tested under a high-amplitude and low loading rate.

This study demonstrated that:

- Longitudinal cracks on the soffit of steel-free deck slabs does not affect their fatigue performance.
- The width of longitudinal cracks can be controlled effectively by means of nominal crack-control reinforcement.
- The fatigue life of steel-free deck slabs exceeds the commonly accepted fatigue life requirements.
- Acoustic transmission technique can be used to detect the damage in the concrete.

This work is of significance as:

- The resilience of the steel-free deck slabs has been established under slow speed fatigue loading.
- This study has also demonstrated a means to eliminate the problem of excessive width of longitudinal crack, while enhancing the stiffness of the confining system and reducing internal strain levels in concrete.

2.0 REVIEW OF CONCRETE BRIDGE DECK SLABS

2.1 General

The majority of short and medium span highway bridges built in North America and other countries since the 1940s are of composite construction, commonly known as the slab-on-girder bridge. A typical slab-on-girder bridge comprises a reinforced concrete deck slab supported on a series of longitudinal girders. The girders are either rolled-steel joists, steel plate girders, prestressed or reinforced concrete girders. The girders are connected by a series of steel or concrete diaphragms at regular interval. Shear connectors ensure a composite action between the deck slab and the girders. The shear connectors are either welded to the top flanges of steel girders, or embedded in the top surface of concrete girders. The deck slab transfers the vehicular traffic loads to the girders. The girders, in turn, transfer the load to the substructure. The cross-section of a typical bridge is shown in Figure 2.1.

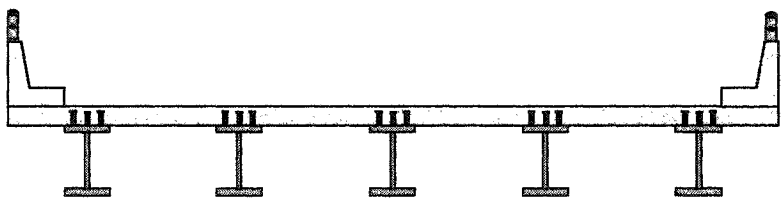

Figure 2-1 Cross-Section of a Typical Slab-on-Girder Bridge

2.2 Conventional Deck Slab Design

Reinforced concrete deck slabs are usually designed by the flexural design methods, e. g. "Standard Specifications for Highway Bridges" (1987), by the American Association of State Highway and Transportation Officials, (AASHTO). Other design codes, such as the Canadian and the British Design codes specify a similar approach. In flexural design, a deck slab is treated as a flexural component that is continuous over a series of girders.

This design necessitates the provision of top tensile reinforcement above the girders, and bottom tensile reinforcement in the positive moment region between the girders. Figure 2.2 shows the case of a deck slab in which the bars are bent to conform to the calculated pattern of transverse moments.

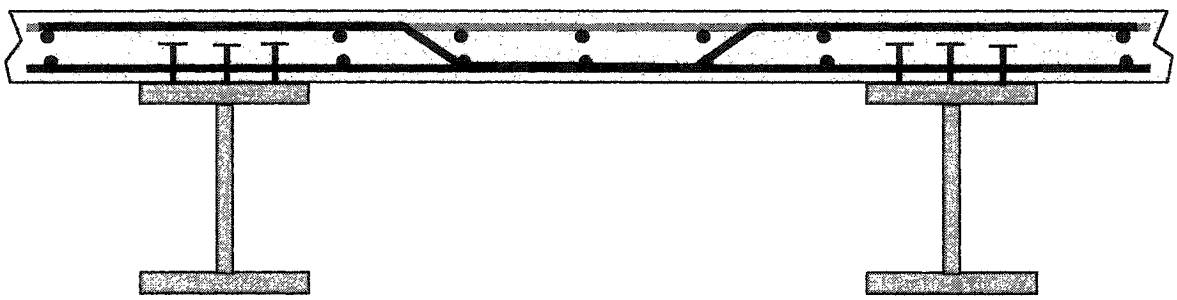

Figure 2-2 Cross-Section of a Deck Slab with Flexural Reinforcement Conforming to Calculated Transverse Moments

2.3 Punching Shear Failure

The failure of a reinforced concrete slab can occur either in flexure or in punching shear. A slab will fail in flexure if it is not well-confined and the bending moment due to the applied load exceeds the ultimate moment carrying capacity of the slab. A punching failure results when the slab is confined to harness its internal arching action (Figure 2.3).

Researchers studying the behaviour of reinforced concrete bridge deck slabs observed that the slabs failed in punching shear and that the failure loads found experimentally were significantly higher than the theoretically computed failure loads based on flexure. Kinnunen and Nylander (1960) proposed a theoretical model for calculating the punching strength of reinforced concrete slabs.

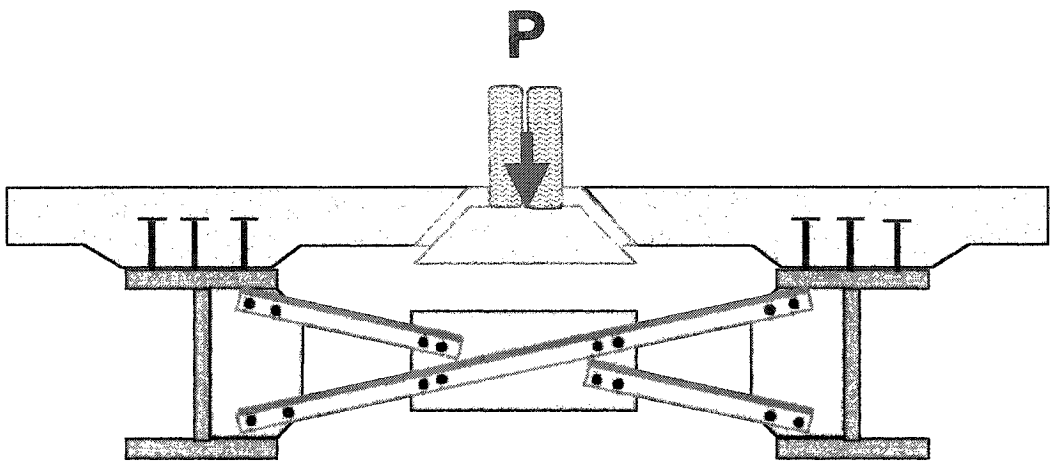

Figure 2-3 Punching Failure of a Well-Confined Deck Slab

2.4 Confinement and Restraint Factor

Hewitt and Batchelor (1975) extended the Kinnunen and Nylander model to restrained slabs. They reported that the reinforced concrete slabs that have their edges restrained against movement, develop forces that lead to enhancement in the failure loads. They described the progressive stages leading to failure as: (1) fixed boundary action; (2) cracking; (3) compressive membrane action if the slab is unreinforced, or compressive membrane action superimposed on fixed boundary action, if the slab is reinforced; and (4) punching. Hewitt and Batchelor (1975) observed that the increase in the failure load above the flexural failure load depends upon the magnitude of restraint provided by the system. Based on their experimental work, they suggested the use of restraint factor in transversely confined slabs. A higher restraint factor leads to higher punching strength while a slab with a low restraint factor will fail at a considerably lower punching load. Hewitt (1973) and Hewitt and Batchelor (1975) suggested the use of the restraint factor, ranging from 0 to 1.0, to account for the in-plane or transverse confinement provided by the system. A slab, with a restraint factor of zero, provides no transverse confinement and hence no enhancement to the failure load, while a slab with a restraint factor of 1.0 provides full confinement and therefore the maximum possible enhancement to the

punching load. The curve presented by Hewitt (1975) is represented in Figure 2.4. This figure has been reproduced from Hewitt and Batchelor (1975) showing only the SI units. The restraint factor is an empirical quantity, which is based on experimental results, and cannot be determined analytically.

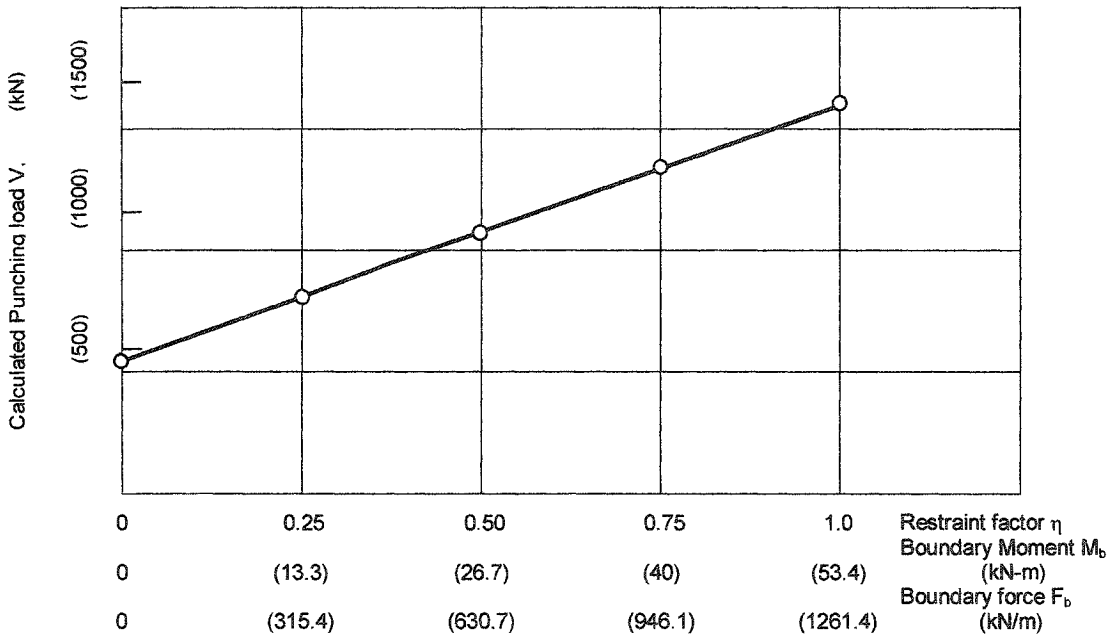

Figure 2-4 Variation of Calculated Punching Load with Restraint Factor (Reproduced from Hewitt and Batchelor, 1975)

The top flanges of the girders and the bottom transverse reinforcement of the deck slab provide significant lateral restraint. The relative effectiveness of the confining system depends on several factors such as the presence of diaphragms; the size and spacing of shear connectors, profile of the girders, and the area of the bottom transverse reinforcement. The shear connectors ensure a composite action at the slab-girder interface and confine the slab in the longitudinal direction. The bottom transverse reinforcement in the deck slab, in conjunction with the in-plane stiffness of the top flange of the girder can provide adequate lateral restraint to produce arching action in the deck slab. This is also known as the development of compressive membrane action.

2.5 Confinement and Restraint

The transverse confinement can broadly be divided into two categories: (a) active confinement, and (b) passive confinement.

In an actively confined deck slab, the in-plane confining forces are induced before the slab is subjected to any external load. The confinement is provided by the in-plane prestressing system. Guyon, (1960), reported significant enhancement in the punching failure load of transversely prestressed runway slabs. Similarly, Mellinger (1957) reported that the performance of a 4-in thick transversely prestressed concrete runway pavement slab was equivalent to that of an 8.6-in thick plain concrete slab. Braimah et al. (1998), and Hassan et al. (2002) have reported the results of tests on transversely prestressed steel-free deck slabs with carbon fiber reinforced polymer (CFRP) and steel, respectively. Other researchers have experimented with prestressed concrete straps (Banthia et al. 2002).

A passive confinement, as the term suggests, begins to function when the load is applied to the deck slab. The initial contribution of the passive confining system to the deck slab is zero under the no-load condition. After the load is applied, the girders tend to move away from each other laterally. The lateral outward displacement of the girders is restricted by the passive confining system. The extent to which the movement can be reduced will depend on the axial stiffness of the confining system. One or more of the following can contribute to the passive confinement:

- lateral stiffness of mainly the top flanges of girders,
- lateral stiffness of the end/edge beam at the extremities of the slab,
- in-plane stiffness of the slabs in adjacent panels,
- bottom transverse reinforcement in the deck slab,
- external axial restraints provided by as cross-frames and straps.

The code-specified procedures do not account for the restraint provided by the structural system and therefore underestimate the theoretical punching loads of deck slabs.

Active restraint has a clear advantage over passive restraint. Bridges that have in-plane prestressing in both the transverse and the longitudinal directions are usually built as prestressed concrete bridges. In such bridges, the role of prestressing is to control the flexural cracking of deck slab by inducing compressive stresses in the tensile zones. It is known that concrete under compressive fatigue loads has a significantly longer fatigue life than that under tensile fatigue loads. However, the effect of prestressing to enhance the punching shear capacity has not been fully exploited. As well, the provision of an active transverse confinement system is not economically viable.

2.6 Role of Transverse Confinement

Guyon (1960) described the load tests conducted on runway slabs at Orly Airport in Paris in 1948. The 165 mm-thick slab, measuring 14 x 12.5 m, was transversely prestressed. The tests, conducted at varying levels of prestress, showed that the punching strength of the slab increased with an increase in the magnitude of prestress. There were concentric circular cracks developed around the load pad. At lower load levels, the cracks closed completely when the load was removed. At higher loads the cracks opened and remained visible. Also, the crack width increased as the prestress level was reduced.

Mellinger (1957) also reported the formation of circular cracks at the top, and the radial cracks at the bottom, in transversely prestressed runway slabs subjected to cyclic loading.

Tests have showed that the failure load for the deck slabs exceeds the flexural failure loads. This increase has been attributed to the development of internal arching action (Hewitt and Batchelor 1975; Csagoly et al. 1978). The in-plane stiffness of the top flanges of the girders and the axial stiffness of the bottom transverse reinforcement help the deck slabs develop an internal arching action. The failure load and the failure mode are affected by the extent of restraint provided by the structural system of the bridge deck slab. An adequately restrained deck slab fails in punching shear at significantly higher loads as compared to a poorly restrained deck slabs that typically fails in flexure

at lower loads. Utilizing the beneficial effect of the internal arching action, the proportion of internal transverse reinforcement could be reduced considerably without compromising safety. In 1979, the Ministry of Transportation of Ontario incorporated the isotropic reinforcement for bridge deck slabs for the first time in Clause 8.16-Empirical Design Method of the Ontario Highway Design Code (OHBDC 1979). Clause 8-16-4.2 permitted the provision of steel reinforcement equal to 0.3% of the gross cross-sectional area of concrete, in each direction, for the top and the bottom layers of reinforcing mesh for slab-on-girder bridges with skew angles of up to 20^0 (Figure 2.5). A substantial reduction in the quantity of the reinforcing steel and saving in the bridge cost was achieved. However, an important drawback of reinforced concrete deck slabs is their vulnerability to reinforcement corrosion caused mainly by the use of deicing salts.

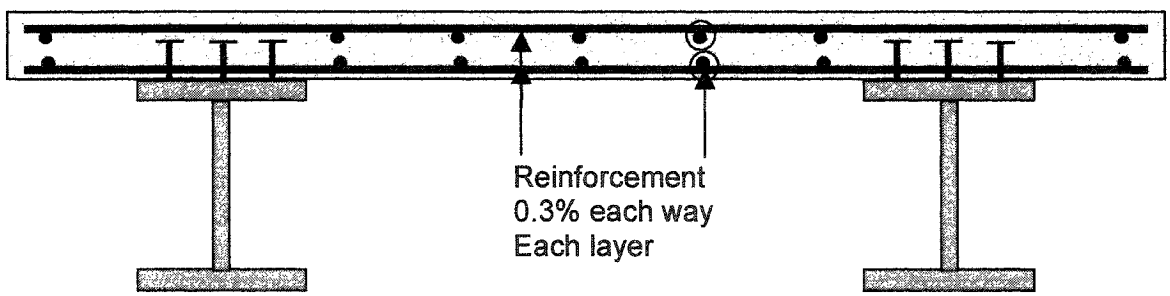

Figure 2-5 Cross-Section of an Isotropically Reinforced Bridge Deck Slab (OHBDC)

2.7 Arching Action

2.7.1 Historical Context

The concept of arching action has been successfully employed throughout history. Masonry arches, both, curved and flat, transfer loads through compressive action, as the mortar binder cannot sustain tensile or shearing forces. The Roman Aqueducts are a fine example of such arches. Until the prevalence of concrete slabs, masonry roof construction, known as the jack arch roof, was commonly used as a roof covering in

many countries. The jack arch roof comprised a series of steel beams, laterally restrained by steel tie rods at regular intervals, supporting masonry arches. The arches were built with bricks. There are numerous masonry bridges that employ the superior performance of stone and brick arches.

The first attempt to take the compressive membrane action into account has been attributed to the researchers in the former Soviet Union (Braestrup 1980).

Fritsche (1948) has described a concrete arch-on-girder railway bridge built in the pre-World War-II era, in Germany. The cross-section of the bridge is shown in Figure 2.6. The details show circular concrete arches rising above the bottom flanges of the steel girders, which form an integral part of the deck slab. The girders are connected by tie rods at each end. The arching action can be easily appreciated. As well, the concrete arches provide lateral stability by restraining the bottom flanges.

All of the arch forms described above conform in geometry to the arching action, therefore it is easy to visualize the arching action. However, the topic of the research presented herein pertains to the implicit form of arching that does not relate immediately to engineering judgment, and has therefore remained relatively unexplored until recently.

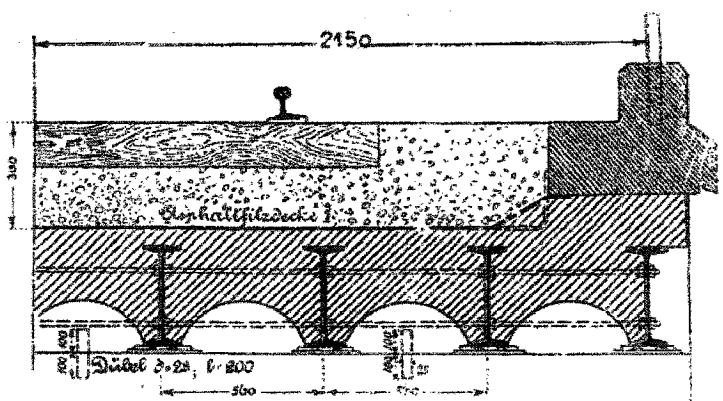

Figure 2-6 Concrete Arch Bridge in Germany from the pre-WW-II Era

2.7.2 Development of Steel-Free Bridge Decks

Realizing the significance of compressive membrane action, a team of Canadian researchers developed a new structural system for concrete bridge decks that effectively utilized the arching action in concrete deck slabs. The internal reinforcement was completely eliminated and replaced by a series of uniformly spaced steel straps connecting the top flanges of the girders. A schematic cross-section of a steel-free deck slab is shown in Figure 2.7. The straps provide the transverse confinement that is necessary for producing the arching action in the slab. The confinement in the longitudinal direction is provided by shear connectors and transverse edge beams. The new system of the deck slabs is referred to as steel-free deck slabs (Mufti et al. 1993). Wegner (1993) conducted laboratory tests on half-scale and full-scale models of steel-free deck slabs. Thorburn (1996) conducted tests on full-scale models. Her experimental work helped optimize the strap size. Newhook (1997) carried out parametric studies and examined design details leading to the first field application. Mufti and Newhook (1998) proposed a rational model to predict the punching strength of steel-free deck slabs.

Provisions for the design of steel-free bridge deck slabs are included in Clause 16- FRC Decks, of the Canadian Highway Bridge Design Code (CAN/CSA-S6-00).

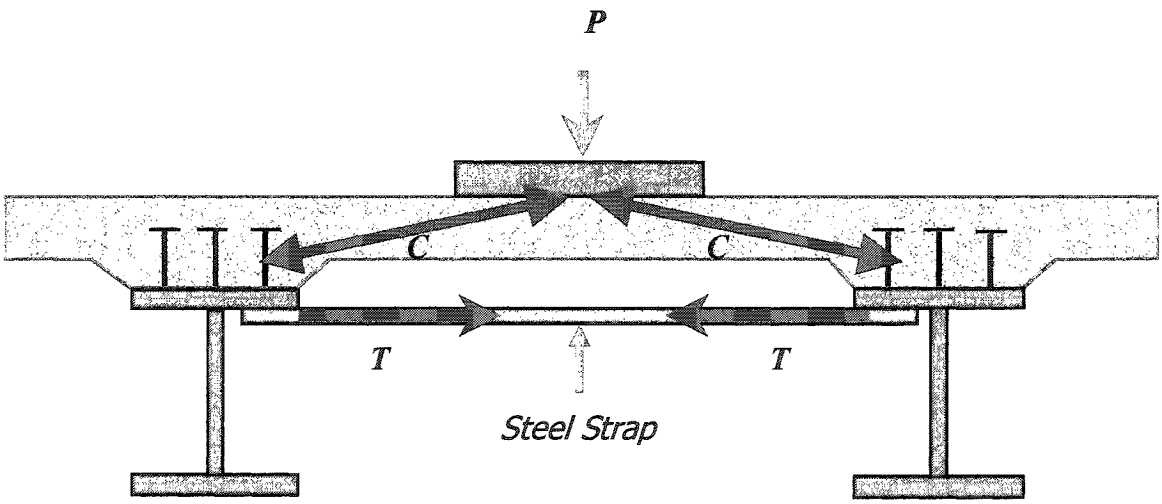

Figure 2-7 Schematic View of Steel-Free Bridge Deck

This research initiated by Mufti et al. (1993) is significant in many ways. Exclusion of steel reinforcement from the deck slab eliminates the major cause of deck deterioration. Concrete structures develop cracks during their service life due to various reasons. During winter, deicing salts are used to keep the bridges free from ice accumulation. Water, laden with dissolved salts, penetrates the concrete partly through cracks on the surface of the deck slab and causes the corrosion of steel reinforcement. The resulting compounds of iron occupy a larger volume than the original steel bar, causing the reinforcement to expand and induce tensile stresses in the surrounding concrete. When the stresses exceed the tensile strength of concrete, the concrete cracks and delaminates. Also carbon dioxide dissolved in rainwater produces carbolic acid, causing carbonation of the concrete (Neville1996). Other gases such as sulfur dioxide and nitrogen dioxide also reduce the pH levels of pore water in concrete, thus breaking down the passive layer around the reinforcement. By removing the internal reinforcement from the deck slab, a major cause of deck concrete degradation was eliminated. The elimination of internal steel reinforcement also results in lower construction costs and reduced construction time.

2.7.3 Field Application of Steel-Free Decks

After successful testing of steel-free deck slabs in the laboratory (Mufti et al. 1993), the technology was applied in the field. The Salmon River Bridge, in Nova Scotia, Canada, thus became the first bridge in the world to incorporate the steel-free technology (Newhook and Mufti 1996). There are two simply supported spans each on the East and the West bound carriageway of the Trans Canada Highway No. 4 over the Salmon River. The deck slab of one of the spans on the eastbound lane has a steel-free deck slab. The deck slabs of the other three spans have steel reinforcement designed in accordance with CSA-S6. The two-lane bridge has a span of 32 m, each supported by six plate girders. (Figure 2.8). Four other bridges constructed in Canada using this btechnology are: Crowchild Trail Bridge (1997) (Alberta, Canada), Chatham Bridge, (1996) (Ontario, Canada), Waterloo Creek Bridge (1996) (British Columbia, Canada), and Lindquist Bridge (1996) (British Columbia).

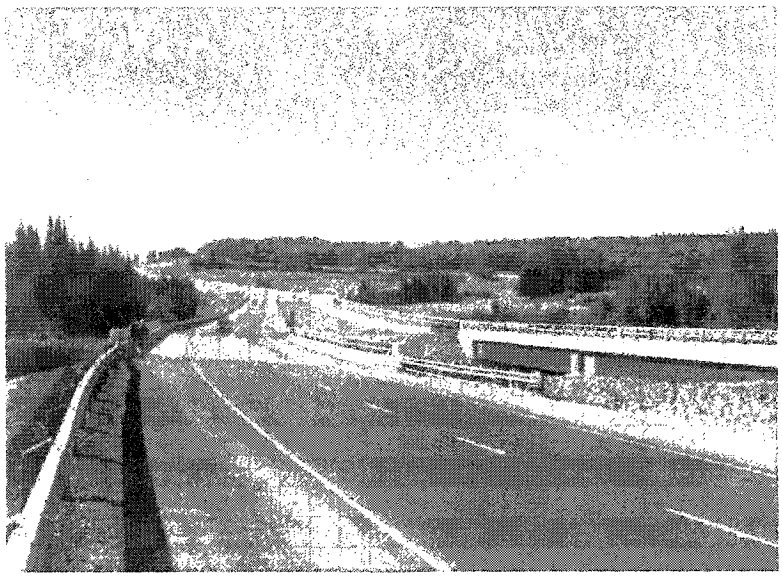

Figure 2-8 Salmon River Bridge (Nova Scotia, Canada)

2.7.4 Phenomenon of Cracking in Steel-Free Decks

The Salmon River Bridge, built using steel-free deck technology, was opened to traffic in 1996. Since then, it has been inspected regularly. At the early stages, it was observed that a series of longitudinal cracks had developed on the soffit of the deck slab (Mufti et al. 1999). The cracks were located between the girders and extended along the entire length of the bridge. Some transverse cracks were also observed in the side panels of the deck slab. The discussed crack pattern is shown in Figure 2.9. The appearance of the longitudinal cracks in the steel-free bridge decks is explained in Section 2.7.5.

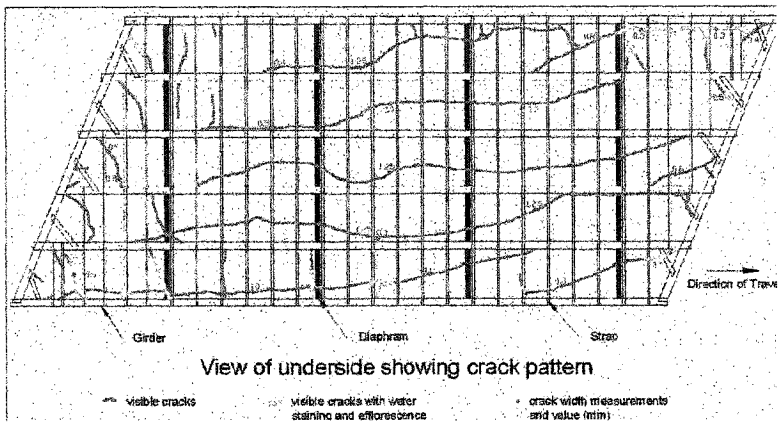

Figure 2-9 Salmon River Bridge, Soffit Crack Pattern (Mufti et al. 1999)

2.7.5 Likely Cause of Longitudinal Cracks

The steel-free deck slab design is based on the development of arching action due to both longitudinal and transverse confinement. However, the confinement is mobilized only after the slab develops a stable system of cracks by first acting in bending. It can be seen that the formation of longitudinal cracks, due to transverse bending moments, is essential for the arching action. After cracking, the deck slab, acting as an arch, exerts horizontal thrust on the supporting girders. The straps connecting the top flanges of the girders function as ties and resist the lateral displacement of the supports (the girders). The straps undergo tensile strain and elongate, thus propagating the flexural cracks further. The deck system now functions as a dome. The cracking is schematically shown in Figure 2.10. Under single pulsating loads, the compressive stress regime near the top of the deck slab prevents the crack from propagating to the top. When there are more than one pulsating loads, or rolling wheels, the cracks eventually become full-depth cracks.

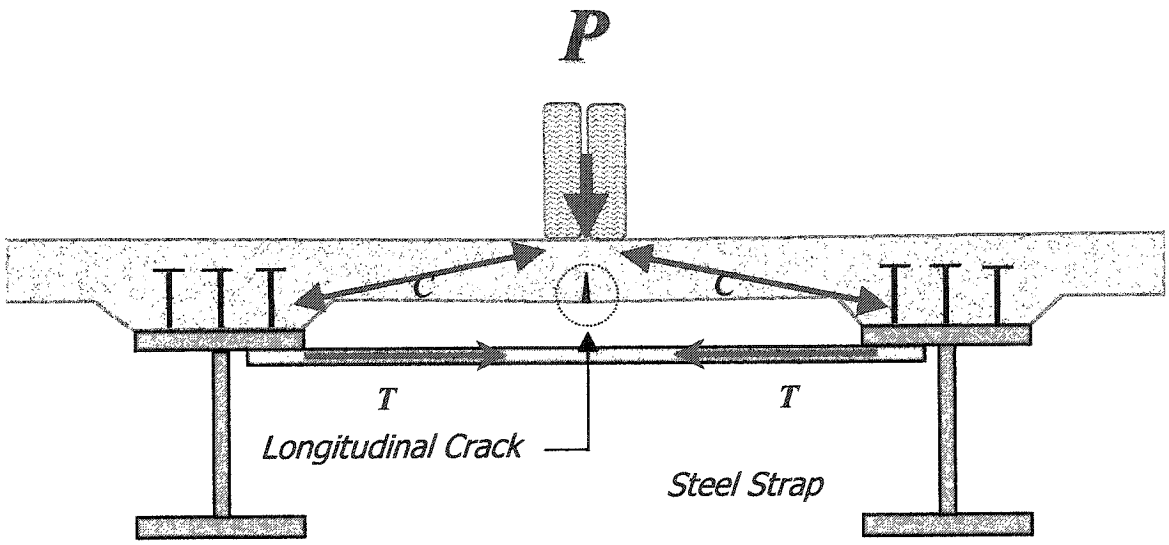

Figure 2-10 Development of the Longitudinal Crack in the Steel-Free Deck Slab

2.7.6 Monitoring of Cracks

All the bridges built with steel-free technology have been monitored since their construction. Salmon River Bridge, the first ever steel-free bridge, has been inspected periodically and cracks have been monitored closely since they were first detected. Crack width grew for a short period and has now stabilized at a maximum width of approximately 1.5-mm. The other four bridges mentioned in 2.7.3 also developed longitudinal cracks at an early stage. In all the cases, crack width stabilized after an initial period of growth. All the experimental models that were built prior to this study developed longitudinal cracks.

A field assessment of Salmon River Bridge was carried out (Mufti et al.1999). The assessment focussed on the following:

1. mapping of crack patterns,
2. load sharing among the bridge girders,
3. fatigue performance of the welded straps,
4. participation of the kerbs in carrying live loads.

The study concluded that the cracks developed soon after the opening of the bridge to the traffic had stabilized and did not affect the performance of the bridge. The load sharing among the girders was not affected by the crack pattern. The stress range recorded for the steel straps was well within the acceptable stress limits for fatigue damage. The adjacent conventionally reinforced deck slabs tend to develop a series of cracks of smaller widths as compared to a single, wide crack in the steel-free deck slabs. Tests have shown that the combined width of all the small cracks in the reinforced concrete deck slabs is nearly equal to the width of the single crack in steel-free bridge decks (Matsui et al. 2001).

During previous inspections, no visible cracks were noticed in the other three spans designed by Empirical Design Method of the CSA S-6. However, a recent inspection carried out by the inventors and this author in June 2003, has shown that longitudinal cracks have appeared in at least two spans. The width of those cracks is significantly smaller as compared to the cracks in the steel-free deck slab.

3.0 THEORETICAL BACKGROUND ON FATIGUE

3.1 Phenomenon of Fatigue

Fatigue results from the repeated application of load on a structure. Repeated or cyclic loading gradually reduces the strength of the parent material. The reduction continues until the strength of the material equals load effects due to the applied load. If the loading continues further, it results in the failure of the structure. Fatigue failure can be defined as the phenomenon of strength-degradation under cyclic loading and consequent failure. The fatigue failure starts by initiation of cracks in the material, which continue to grow until the material fractures. Poorman (1945) described the fracture due to fatigue as follows.

"*Such fractures apparently begin with small cracks which spread progressively on account of greater stress at the base of the crack, and after failure, the fracture even of ductile material has the appearance of a brittle material. Such failures are called fatigue failures, but the term progressive fracture would be more descriptive.*"

3.2 Relevance of Fatigue Studies

The study of fatigue is essential for structures that are primarily designed to resist cyclic loads. Bridges, marine structures, skyscrapers and chimneystacks are some of the examples of structures that are constantly subjected to cyclic loading due to traffic, wave action, wind, or a combination of two or more loads. A well-designed structure subjected to fatigue loading is expected to function without any signs of distress throughout its service life.

For satisfactory performance of a structure subjected to cyclic loading, the fatigue behaviour must be studied at a) the level of the material, and b) at the level of the structure. The fatigue behaviour of the material, such as concrete, steel, or fiber reinforced polymer (FRP), must be known to make the most efficient use. The response

of the structure to the fatigue loading must also be studied. In the following sub-sections the fatigue of concrete and the concrete deck slab has been discussed. A detailed discussion on fatigue is presented in Appendix-A.

3.3 Fatigue Resistance and Limits

To determine the fatigue life of a specimen, it must be tested to failure under cyclic loading. In order to be able to apply cyclic loading, the magnitude of the load effects due to the peak load must be smaller than the static strength of that specimen (Neville, 1996). The number of load cycles, *N*, that can be applied before failure, is influenced by the magnitude of the applied peak load. Higher magnitudes cause rapid failure while lower magnitudes will prolong the fatigue life. If the magnitude of the applied load is below a certain level, the loading can be cycled indefinitely. However, in practice, it is impossible to test a specimen over an infinite number of load cycles. Therefore, to be deemed as having the required fatigue resistance, a structure may be required to withstand a minimum number of repetitions of a load of a specified magnitude without failure. The specified number of cycles must exceed, by a substantially large margin, the total number of load cycles that the structure will most likely to be subjected to, during its entire service life. The endurance limit is defined, as the threshold load level, below which the material will not fail in fatigue.

3.4 Phenomenon of Fatigue in Concrete

In metals, the appearance of the first crack is taken as the first sign of impending fatigue failure. In metallic components subjected to high frequency cyclic loading, the time required for total failure after the appearance of the first crack can vary considerably. However, total failure of such components may have fatal consequences. For example, the failure of a rotating component, or a crack in the frame of an aircraft wing could lead to disastrous consequences. However, in concrete, cracks are generally present in various forms such as shrinkage cracks, and do not necessarily represent a failure. As well, even the most compacted concrete contains air voids. Concrete, as a

heterogeneous material, has a distinctly different behaviour when compared to metals. It exhibits totally different properties under tensile and compressive loads. While the conclusions in Section A-1 (Appendix-A) are generally applicable to concrete, the number of cycles required to fail a concrete component after the first crack is significantly larger than the corresponding number of cycles in a metallic component.

3.5 Cumulative Damage

In the early 20th century, Swedish researcher, A. Palmgren (1945) used the concept of cumulative damage for predicting the fatigue life of ball bearings. If a material were subjected to a series of cyclic loads of different magnitudes, each load would cause a certain amount of permanent damage. As the material continues to be subjected to such loads, damage accumulates. At a certain stage in the loading life, the accumulated damage would be sufficient to cause a failure. If the total damage is represented mathematically by unity, then the partial damage caused by each load can be represented by a fraction. When the sum of all the partial damages, represented by various fractions, approaches unity, failure occurs. Miner (1945) further developed the concept of cumulative damage under fatigue loading. His research related to the fatigue of aluminum components in aircraft. He stated that *"the number of loading cycles applied at a given stress level would be the useful life expended"*. When the total damage, as defined by this concept reaches 100 percent, the fatigue specimen should fail. Furthermore, the damage may be expressed as the number of cycles applied divided by the number of cycles required to produce failure at a given stress level. When the summation of these increments of damage at several stress levels approaches unity, failure occurs. The rule is commonly referred to as the Palmgren-Miner hypothesis.

The rule can be expressed mathematically by the following expressions,

$$n_1/N_1 + n_2/N_2 + n_3/N_3 + \cdots\cdots\cdots + n_n/N_n = 1 \qquad (3.4a)$$

or

$$\Sigma(n_i/N_i) = 1 \qquad (3.4b)$$

where,

n_i = number of cycles applied at a particular stress level

N_i = total number of load cycles required to produce failure at the same stress level

If the number of cycles required to cause fatigue failure at each stress level are known, the effect of cumulative damage and consequently the remaining fatigue life can be easily assessed at any stage.

3.6 Prediction of Fatigue Life of Concrete

The fatigue life of a material depends on several factors that were discussed in the previous sections and in Appendix A. Statistically, the fatigue life of several identical objects tested under identical circumstances will be distributed over a certain range. Even in the case of metals, in which the physical properties and the chemical compositions are more uniform due to homogeneity of the matter and better quality control in manufacture, fatigue life has been found to exhibit a certain range of variation. In the case of concrete, due to its heterogeneous nature, fatigue life tests show a larger range of variation. Therefore, the prediction of the fatigue life is, at best, an approximation.

Oh (1991) reported that the fatigue life variation changes with the magnitude of the maximum stress. The variation of data is smaller at a higher magnitude of maximum stress level, and greater at a lower magnitude. Several methods have been proposed to predict the fatigue life of concrete under different loading conditions.

3.6.1 S-N curves

The relationship between the maximum stress, *S*, and the number of cycles to failure, *N*, can be represented by Wöhler or S-N curves. On a typical S-N curve, the x-axis represents the number of load cycles, N, to failure and the y-axis represents the corresponding maximum stress level, S. The S-N relationship for a particular stress range is represented by a curve. A series of such curves can be drawn for various stress ranges.

3.7 Previous Studies of Fatigue in Concrete

3.7.1 General

Concrete strength is influenced by numerous factors such as material properties and proportions, mixing, transporting, placing, quality control, and testing procedures (Mirza et al. 1979). Testing for fatigue involves additional variables such as the type of the test, magnitude and the rate of loading. Therefore, it is important to understand the fatigue behaviour of concrete as a material, and as a structural element. It is understood that as cyclic loading is applied to concrete, a certain amount of damage is caused in the concrete mass from the reduction in the bond strength, initiation and propagation of cracks. The fatigue studies, on concrete as a material, are discussed in this section, while some of the important studies on reinforced concrete and steel-free deck slabs are discussed in Section 3.8.

The majority of research on the fatigue strength of plain and fiber reinforced concrete focuses on the flexural behaviour. However, in steel-free bridge decks, the concrete deck slab sustains load by developing compressive membrane action. Therefore a discussion on the fatigue performance of concrete under compressive loading has a greater relevance. The phenomenon of fatigue under compressive loading, and under flexural loading are discussed respectively, in Section 3.7.2, and Section 3.7.3.

3.7.2 Fatigue under Compressive Loads

Before discussing the fatigue in concrete under compressive loads, it is necessary to discuss the behaviour of concrete under compression. When a concrete specimen is subjected to uniaxial compressive loads, shear stresses develop in the specimen as a whole, and in particular at the aggregate-paste interface, also known as the Transition Zone (TZ). Tensile stresses develop in the direction perpendicular to the plane of shear stress. As the load is increased, the magnitude of the tensile stress also increases. When the induced tensile stresses in concrete exceed its tensile strength, failure occurs. The compressive strength of concrete is enhanced by lateral confinement (Mander et al. 1988). In a reinforced concrete column, the lateral confinement is provided by transverse shear reinforcement. In steel-free deck slabs, a state of 3-D compressive stress exists in concrete under the load pad due to the lateral confinement provided by the straps and the shear studs, in the transverse and the longitudinal direction, respectively (Newhook 1997). The enhanced compressive strength of confined concrete is significant in that it raises the endurance limit. Thus the transverse confinement has a positive effect on the fatigue life of the deck.

Under repeated loads, the stress-strain response of concrete varies with the number of load cycles. The changes, from the initial loading up to the failure, occur in three phases (Do et al. 1993). In the first phase, there is a rapid growth of strain, however, at a reducing rate. In the second phase, the strain increases at an almost steady rate. In the third phase, the strain increases at an increasing rate until the concrete fails in fatigue. The three stages of fatigue are shown in Figure 3.1. An important observation of the researchers was that fatigue failure occurs only if the stress level exceeds the endurance limit. Fatigue loading below endurance limit is reported to increase the fatigue life of concrete (Neville 1996).

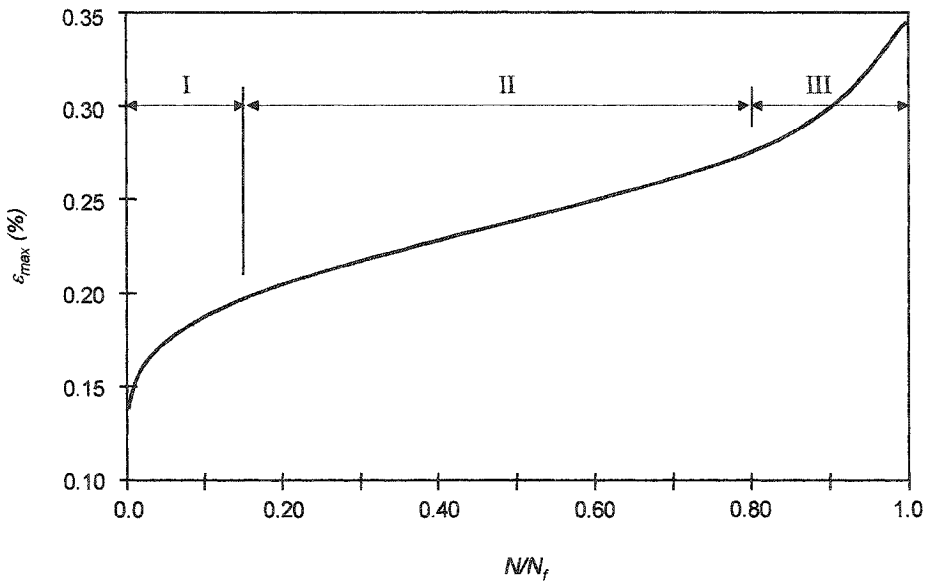

Figure 3-1 Typical Strain Development Curve Showing Three Stages in Fatigue Life of Concrete Under Compressive Load (Reproduced from Do et al. 1993)

Several studies have been conducted on concrete under uniaxial, biaxial, and triaxial compressive fatigue loading. Some of the significant studies are discussed below.

Bennett and Raju (1969) reported that, under repeated loads, there was a reduction in the secant modulus of concrete with the increase in the fatigue life that was used up, and that the relationship was independent of the stress level in the fatigue test.

Nelson et al. (1988) conducted fatigue tests on 127 x 127 x 12.7 mm thick high-strength concrete plates under biaxial compressive loads and reported an endurance limit of 45-55 percent. Nelson et. al (1988) also observed a beneficial effect of cyclic loading below fatigue limit on the static strength of concrete.

Su and Hsu (1988) conducted fatigue tests on 152 x 152 x 38 mm thick concrete specimens under biaxial compressive loads with the ratios of stresses σ_2/σ_3 of 1, 0.5 and 0.2, 0, where σ_2 and σ_3 are the applied principal compressive stresses applied in the

plane of loading. Su and Hsu (1988) reported a maximum strength increase of approximately 52 percent at ratios of σ_2/σ_3 of 0.2 and 0.5. They also observed the three distinctive stages in the development of maximum strains similar to those shown in Figure 3.1.

Holman (1982) conducted fatigue tests on 462 100 x 250 mm concrete cylinder specimen under constant and variable amplitude compressive loads. He concluded the following:

a) In S-N relationships, the scatter in number of cycles to failure at a given stress level can be explained from the scatter in the static compressive strength.

b) The maximum longitudinal strain variation by cyclic loading consists of two components:

$$\varepsilon_{max} = \varepsilon_e + \varepsilon_t$$

where ε_e is a function of consumed endurance life and ε_t is a function of the loading time.

c) The secant modulus of elasticity decreases during the fatigue life in both constant and variable amplitude loading

d) Variable amplitude loading seems to be more damaging than predicted by the Palmgren-Miner hypothesis. This is due to the sequence effect of variable loading.

e) Loading histograms with lower minimum stress levels seem to cause stronger sequence effects and will, therefore, be more damaging, i. e. lower cycle ratios at failure.

f) The presence of small amplitudes in a loading histograms seems to reduce the sequence effect. Therefore, small load amplitudes are favourable.

Takhar et al. (1974) conducted fatigue tests on concrete cylinders under triaxial compressive loading. They reported that the lateral confining pressure appeared to prolong the fatigue life of concrete considerably.

Ople and Hulsbos (1966) conducted fatigue tests on 101 x 152 x 305 mm plain concrete prisms under uniaxial compressive loads at varying eccentricities, and concluded the following:

1. The stress gradient has a significant effect on the fatigue strength of plain concrete in compression. The fatigue strength of nonuniformly stressed concrete specimens is higher than the uniformly stressed specimens by approximately 17 percent of the static ultimate strength.
2. Concrete fatigue life is highly sensitive to small changes in maximum stress levels. A change in stress of only 7.5 and 5 percent causes the fatigue life to change from 40,000 to 1,000,000 cycles.
3. Statistical analysis of test data is necessary due to the large degree of variability associated with plain concrete fatigue life.
4. An approximate empirical relationship between the variables (stress-level, fatigue life, probability of failure and stress gradient) can be established from the fatigue data and may be generalized to apply to specimens of different sizes by using a statistical explanation of size effect.
5. The results of plain concrete specimen tests can be used to develop a method for estimating beam fatigue life as limited by concrete fatigue in compression. The solution takes into particular consideration the effect of the compressive stress gradient on the fatigue life of concrete.
6. An approximate design check against the possibility of concrete fatigue failure in a beam subjected to repeated flexural loading can be formulated for specified values of fatigue life and probability "design limit".
7. The current AASHO allowable concrete compressive stress of 0.4 f_c' is a conservative estimate of the fatigue strength of concrete in compression. The results of this investigation indicate that for a fatigue life of N = 2,000,000 cycles, a probability of failure of P = 0.00001 and a minimum compressive top fiber stress of 0.10 f_c', a maximum compressive stress of 0.50 f_c' may be allowed at the top fibers of prestressed flexural members with a view towards preventing fatigue failure.

Mufti et al. (2002) conducted tests on standard concrete cylindrical specimens under concentric compressive fatigue loads and proposed relationships for the fatigue life of concrete deck slabs and for calculating equivalence between the load cycles applied at different magnitudes of cyclic loading. The relationship is further discussed in detail in Chapter 7.

3.7.3 Fatigue under Flexural Loads

Shi et al. (1993) reported the results of tests on plain concrete beams under flexural fatigue loading. They used stress level *S*, the ratio of the maximum loading stress, σ_{max}, to the modulus of rupture, *MR*, and stress ratio R, the ratio of the minimum stress, σ_{min}, to the maximum stress, σ_{max}. At a given stress level *S*, the stress ratio, *R*, may theoretically have any value between zero and one. They proposed the concept of equivalent fatigue life, *EN*, as represented by Equation 3.1 so that all fatigue life data at a certain stress level could be represented by a common measure.

$$EN = N^{1-R} \tag{3.1}$$

Using the equivalent fatigue life, EN, Shi et al. (1993) have developed the following fatigue life equation 3.2:

$$S = A\,(EN)^{-B} \tag{3.2}$$

On the basis of the test data, they proposed the following expression (3.3),

$$S = A\,(N)^{-0.0422\,(1-R)} \tag{3.3}$$

where coefficient A varies between 0.9611 and 1.0380 with the corresponding survival probability of 0.95 and 0.5, respectively.

Oh (1991) conducted variable-amplitude flexural fatigue tests on concrete beams with both increasing and decreasing amplitudes. He applied Miner's Rule of cumulative damage to the test results and proposed the nonlinear cumulative damage model. He concluded the following:

- *Fatigue failure of concrete is greatly influenced by the magnitude and sequence of applied variable amplitude fatigue loadings.*
- *The linear damage theory proposed by Palmgren and Miner is not directly applicable to concrete under such cases.*
- *The sum of cumulative damage is greater than 1 when the magnitude of fatigue loading is gradually increased, and less than 1 when the magnitude of fatigue loading is gradually decreased.*
- *The proposed nonlinear damage theory allows more realistic fatigue analysis of concrete structures.*

Lewis (2002) reporting the results of flexural fatigue tests on plain, and, fiber reinforced concrete containing 0.5% volume fraction of steel fibers and monofilament self fibrillating synthetic fibers, did not find any improvement in the flexural fatigue performance of concrete due to the addition of fibers.

3.8 Previous Fatigue Studies on Concrete Deck Slabs

3.8.1 General

There have been several studies on the performance of conventionally reinforced deck slabs under fatigue loading. However, only four studies have been conducted on steel-free deck slabs prior to the commencement of this research. Batchelor and Hewitt (1974) reported the results of tests conducted on 1/8-scale models of reinforced and unreinforced bridge deck models. They reported that one of the unreinforced panels did not fail after 2 million load cycles when the ratio (P/P_s) was less than 0.5. The load was progressively increased until failure occurred after application of more than 6 million load cycles. They recommended an endurance limit of 0.4 for the ratio (P/P_s) for the deck slab. Beim and Perdikaris (1988) conducted fatigue tests on small-scale models of reinforced concrete bridge deck slabs. However, the main focus of Batchelor and Hewitt (1974), and Beim and Perdikaris (1988) was the comparison of the performance of reinforced concrete decks slabs with orthotropic and isotropic reinforcement. It is

recalled that latter reinforcement is provided in deck slabs designed for their arching action.

Matsui et al. (2001) and Youn and Chang (1998) conducted fatigue tests on reinforced concrete and steel-free deck slabs, and reinforced concrete deck slabs, respectively. Selvadurai and Bakht (1996), and Mufti et al. (2001) conducted fatigue tests on the steel-free bridge deck slab model and the steel-free precast panel respectively. In both cases however, the cyclic loading was not taken to failure. In both the cases, the panels were subsequently tested to failure under static load. The three significant sets of tests, are discussed in Sections 3.8.2 through 3.8.5.

3.8.2 Perdikaris and Beim (1988) (Fatigue under Pulsating Load)

Perdikaris and Beim (1988) conducted tests on 1/6.6-scale models of bridge deck slabs. Three models were constructed, one with orthotropic reinforcement, one with isotropic reinforcement, and one model without any reinforcement at all. All the models were built on three longitudinal girders transversely connected by four diaphragms in each bay. The diaphragms were positioned at each end and at third points along the span. Each test panel was comprised of a rectangular segment of the deck slab bound by two adjacent girders and diaphragms. One model of each type was tested under static and pulsating load. The models with isotropic and orthotropic reinforcement, were tested under moving loads. Five panels from each type of model with reinforcement were tested under static loading condition while the remaining four panels were tested under pulsating load. Six panels from the unreinforced model were tested under static loading conditions while one panel was tested under pulsating load.

The static failure load for the central panel of the unreinforced deck slab was fairly high. This result was considered as unreliable by Perdikaris and Beim (1988). However, in the opinion of this author, the high failure load could be attributed mainly to the lateral restraint provided by the intermediate diaphragms. The magnitude of the pulsating and moving load was kept at 60% of the static ultimate capacity. The tests showed that under moving load, the deck with isotropic reinforcement had higher fatigue resistance

than the deck with orthotropic reinforcement under moving load. All the reinforced panels failed in punching shear. The unreinforced panel failed in flexure, after withstanding 577,800 load cycles at 60% of the ultimate static failure load. The average static failure load was about 12.1 kN.

3.8.3 Selvadurai and Bakht (1995/1996) (Fatigue under Simulated Rolling Wheel Load)

Two steel-free bridge deck slab models, each measuring 6.0x3.0 m on plan, were built at Carleton University. The 175-mm thick deck slab was supported on two girders spaced at 2.0-m centres. The transverse confinement was provided by 127x50 mm steel straps, welded to the top flange of the girders and spaced at 750 mm centres. The first model was constructed using fiber reinforced concrete containing 0.88% volume fraction of low-modulus fibrillated polypropylene fibers. The second model was constructed with plain concrete.

The loading was applied through four load pads spaced at 750-mm centres mid-way between five consecutive straps. Each load pad represented the footprint of a double tired rear wheel of a truck.

The load on each pad was applied through an actuator. The rolling movement of a single wheel was simulated by sequentially applying sinusoidal loading on each load pad, with a phase difference of $\pi/2$ between two consecutive load pads. The velocity of the simulated load was controlled by varying the frequency of the sine wave.

The first model was tested under cyclic load with peak load levels of 53, 71, 89, and 98 kN, respectively. The model was also tested under corresponding levels of static load before the commencement of cyclic loading. Two million load cycles were applied at each peak load level at a frequency of 2.5 Hz corresponding to a velocity of 30.38 km/h. The model was then further subjected to another two million load cycles at 3.0 Hz corresponding to a simulated velocity of 40.5 km/h.

The cross-sectional area of the straps was reduced by 50% by welding thinner straps adjacent to the existing straps and then flame cutting the existing straps at one location to render them ineffective. The slab was subjected to four million load cycles with a peak load of 98 kN.

The fatigue test was repeated with the top surface of the slab flooded with a 25-mm deep water layer.

At the end of the test, all the straps were removed while retaining the end diaphragms, each comprising C 310 x 32 mm channel section, and the slab was subjected to four million load cycles with a peak value of 98 kN. The slab did not show any sign of failure.

The slab was tested under static load to failure. The slab did not collapse but was declared to have failed due to excessive deflection at 390 kN.

The second model was also tested for two million passes at each of 53, 71, and 89 kN peak load and four million passes of 98 kN load without failure. The authors reported transverse cracking in addition to the single longitudinal crack that had developed in both models during early stages of testing. The testing program is summarized in Table 3.1.

Table 3-1 Testing Program Selvadurai and Bakht (1995-1996)

Model		1				2			
Peak Load (kN)		53	71	89	98	53	71	89	98
Number of load cycles (million)	With original straps	2	2	2	2	2	2	2	4
	With reduced strap size	-	-	-	4	-	-		
	With reduced strap size and flooded top surface	-	-	-	4	-	-		
	All Straps Removed	-	-	-	4	-	-		
Total Load cycles at each peak load		2	2	2	16	2	2	2	4

3.8.4 Matsui et al. (2001) (Fatigue Test under Running Wheel Load)

Three models of steel-free deck slabs (PFRC1, PFRC2 and PFRC3) were constructed at Osaka University in Japan. Each model measured 3.1x2.1 m on plan. The 150 mm thick slab was supported on girders spaced at 1.8 m centres. The transverse confinement was provided by four 50 x 9 mm steel straps spaced at 600 mm centres and edge beams, except for PFRC1, wherein the edge beams were kept detached. The straps were bolted to the girders and the bolts also acted as the shear connectors. The concrete for all the models contained fibers at a volume fraction of 0.55%.

The loading mechanism comprised a wheel assembly suspended from the crossbeam of an overhead loading frame. The wheel reacted against a rail that was supported by the deck slab. The load applied to the deck slab was controlled through a hydraulic jack mounted on the wheel assembly. The wheel assembly was attached to an electrically driven crank, which caused the wheel assembly to move horizontally over the rail between two edge beams (Figure 3.2). One complete revolution of the crank provided a reciprocating movement of 2 m in each direction.

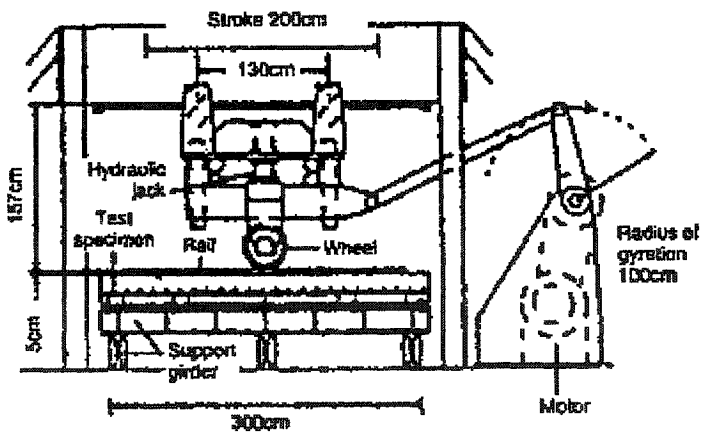

Figure 3-2 Schematic View of Matsui's Running Wheel (Matsui et al. 2001)

Under cyclic load, all the models developed Y-shaped cracks near the edge beams. Model PFRC1, which had its edge beams disconnected from the main girders, failed in flexure. The edge beams together with a triangular segment of the slab detached from the rest of the slab along the arms of the Y-shaped crack.

The model PFRC2 failed in punching shear after 514,000 cycles. Again the failure occurred at the junction of the three arms of the Y-shaped crack.

Model PFRC3 did not fail even after one million load cycles. The test results are summarized in Table 3.2.

Table 3-2. Loading Program (Matsui et al. 2001)

Designation	Wheel load (kN)	Load passes
PFRC1	118	20,000
	147	20,000
	176	218,000
		(Bending failure)
PFRC2	118	20,000
	147	20,000
	176	474,000
		(Punching shear failure)
PFRC3	118	20,000
	147	980,000
		(No failure)

3.8.5 Mufti et al. (2001) (Fatigue Testing of Precast Arch Panels)

Two precast arch panels were tested at the University of British Columbia, Canada. The panels were based on the concept of steel-free bridge deck slabs. The two panels, designated as Panel 1 and Panel 2, contained concrete mixed with 0.1% and 0.4% volume fraction respectively, of fibrillated polypropylene fibers. The 150 mm-thick precast panels were supported on two simply supported steel girders spaced at 3,500 mm centres. The girders were connected at their ends by cross frames. The panels were placed side-by-side along the girders with a 48 mm gap in between. The adjoining edges of the panels were unstiffened while the edges resting on the cross-frames were stiffened. The composite action between the panels, girders, and the cross-frames was achieved by grouted shear bulkheads.

Both the panels were tested under cyclic loading with a peak magnitude of 140 kN, after initial testing under static loads. In the case of Panel 1, the position of load patch was varied twice during the test, with the last position being very close to the unstiffened edge. The panel was subjected to a total of 370,000 load cycles. For Panel 2, only one load position was used to apply a total of 532,000 load cycles.

Both panels developed a longitudinal crack on the soffit, which bifurcated into a Y-shaped crack leading towards the stiffened edge. The longitudinal crack on the soffit propagated to the top surface of the panels near the unstiffened edged. The longitudinal crack on the soffit in Panel 1, which had the lower fiber volume fraction, progressed to the top surface after only 1,500 load cycles while the crack in Panel 2 developed after 272,000 cycles. The length of the crack at the top in Panel 1 was almost thrice the length of crack in Panel 2. Panel 1 had also developed a series of radial cracks. The details of the test are summarized in Table 3.3.

Table 3-3 Loading Program: Precast Arch Panels (Mufti et al. 2002)

Sequence No.	Load at Patch No.	No. of Cycles	Peak Load (kN)	Cumulative No. of cycles at end of sequence
1	1	50,000	140	50,000
2	1	50,000		100,000
3	1	50,000		150,000
4	2	50,000		200,000
5	2	50,000		250,000
6	2	50,000		300,000
7	2	50,000		350,000
8	3	20,000		370,000
9	1	1		1 (ultimate load test)

Both Panel 1 and 2, did not fail during the fatigue test and were tested to failure under static loading conditions. The failure load for Panel 1 was 454 kN and Panel 2 failed at a load slightly above 500 kN.

3.8.6 Discussion

Perdikaris and Beim (1988) focused mainly on the fatigue life comparison of bridge decks with orthotropic and isotropic reinforcements. They observed that the damage caused by a rolling load was more severe than the damage caused by a fixed pulsating load and that a single pass of a moving wheel load equals about 34 and 1,800 load cycles of pulsating load for the isotropically and orthotropically reinforced deck slab, respectively. They tested only one unreinforced concrete panel under pulsating load, which failed in flexure, possibly due a lack of adequate transverse confinement.

Selvadurai and Bakht's (1997) experiments helped establish the fatigue durability of steel-free deck slabs. The models were able to withstand up to 16 million load cycles at 98 kN simulated rolling wheel load without failure after being subjected to two million cycles each of 53, 71 and 89 kN peak load. The change in the cross-section of the straps and the saturation of the top surface of the slab with water did not produce failure.

Matsui et al. (2001) also showed that that the steel-free deck slabs have fatigue life well in excess of commonly accepted minimum fatigue life requirements. Their first model, PFRC1 with disconnected end diaphragms, failed in flexure due to inadequate transverse confinement, which reconfirmed the importance of adequately stiffened edge beams. Their second model failed in punching shear after being subjected to 20,000 cycles at 118 and 147 kN, and 474,000 cycles at 176 kN peak load. Their third model PFRC3, which was identical to their second model PFRC2, did not fail after 20,000 cycles at 118 kN and 980,000 cycles at 147 kN. An important conclusion can be drawn that the combined effect of 20,000 load cycles at 118 kN, 20,000 cycles at 147 kN, and 474,000 load cycles at 176 kN peak load has more damaging effect than the combined effect of 20,000 load cycles at 118 kN and 980,000 cycles at 147 kN peak load. As the model PFRC3 was not tested to failure, an equivalency of the number of cycles and the peak load level cannot be established. However, it can be said that a 20% increase in the peak load level reduces the total number of load cycles required to cause failure by a very large margin.

Mufti et al. (2001) showed that the fatigue resistance of the arch panels is in excess of the commonly accepted fatigue life requirements. The basic crack patterns of arch panels were similar to those of the cast-in-place steel free deck slabs. The upward propagation of the bottom longitudinal crack began at the unstiffened edge of the panel. However, they also reported that the fiber volume fraction of concrete did affect the initiation and the extent of the cracking and the ultimate load capacity of the panels. The panel with a higher volume fraction of fiber developed less cracking as compared to the panel having a low fiber dosage.

The experimental work of Selvadurai and Bakht (1995), Matsui et al. (2001), and Mufti et al. (2001) established that the fatigue life of steel free deck slabs exceeded the commonly accepted minimum requirements by a very large margin. However, only Matsui et al. were able to test their models to failure. Limitations such as the availability of the laboratory space and the availability of the research personnel for prolonged periods of time prevent the continuation of fatigue tests until failure. It must therefore be appreciated that once the test model exceeds the commonly accepted fatigue life

would be less incentive in continuing the experiment any further. This is especially true when several research projects vie for the same resources.

The aim of the present research was to study how the cracks develop, progress and culminate up to the punching failure. The other characteristics such as strap strains, concrete internal strains and the deflection patterns, acoustic attenuation were studied to observe the degradation in the slab. Application of cyclic load at a slower rate afforded the opportunity to follow the crack development and structural degradation closely, which would not be possible in high frequency fatigue tests.

3.9 Fatigue Life Estimation Models

Four different relationships proposed by the following researchers respectively were considered for estimating and comparing the fatigue life of various configurations of panels.

- Batchelor and Hewitt (1974)
- Youn and Chang (1998)
- Matsui et al. (2001)
- Mufti et al. (2002)

The first two relationships are based on tests conducted on reinforced concrete deck slabs, and the third relationship is based on the tests conducted on reinforced concrete and steel-free deck slabs. The fourth relationship is based on the tests conducted on steel-free deck slabs. The relationships for the reinforced concrete deck slabs are included to provide a basis for comparison between the two deck slab systems. These four fatigue life estimation relationships are discussed in detail in Chapter 7.

4.0 DESIGN OF EXPERIMENTAL PROGRAM

4.1 Design of Model

4.1.1 General

The design of the model focussed on addressing the issue of crack width in steel-free deck slabs. A full-scale bridge deck model was constructed to replicate a realistic, two-girder segment of a steel-free bridge in the laboratory. The decision to construct a full-scale model was taken to avoid the scale effects that are associated with fatigue testing of fractional-scale models. It would have been extremely difficult to correlate the width and the depth of the cracks observed in a fractional-scale model to a full-scale bridge deck. As well, the applicability of the results to actual service conditions could be questioned. However, the results obtained from the laboratory tests on a full-scale test model would be applicable in the field without any modification.

The selection of various components for the construction of the test model was done in accordance with the current design codes. However, an additional consideration was that the solution be an economical one and not affect the ease and simplicity of construction. Therefore, the materials used in the construction of the model were commercially available products. The construction of model was done with the available in-house skills except the placing and the finishing of the deck slab, which was done by a concreting sub-contractor. The design process of the test model is described in the following sections.

4.1.2 Test Model Parameters

The full-scale test model measured 12.2 x 3.0 m in plan. The 175 mm thick fiber reinforced concrete deck slab was supported on two steel girders, which were connected by steel straps, edge beams and an intermediate diaphragm. The girders were spaced at 2 m centres. The deck slab cantilevered 500 mm beyond the centerline of each girder.

The model was designed in accordance with the Canadian Highway Bridge Design Code, CAN/CSA S6-00 (2000).

4.1.3 Internal Configuration of Deck Panels

The model was conceptually divided into four sections or panels, designated A, B, C, and D, each measuring 3.05 x 3.0 m on plan. The details of each panel are described in 4.1.3.1 through 4.1.3.4. The layout of the panels is shown in Figure 4.1.

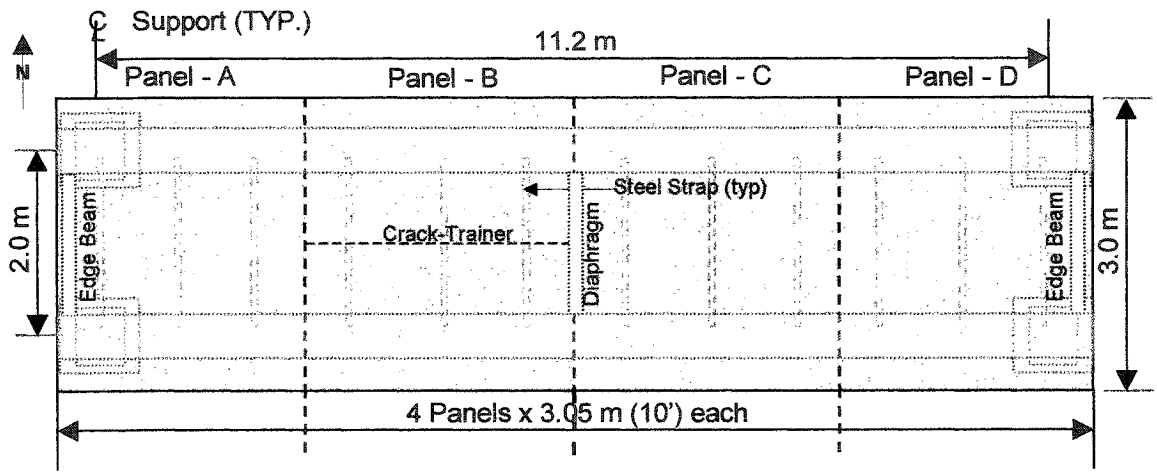

Figure 4-1 Layout of Panels

4.1.3.1 Panel-A (Control Panel)

Panel-A was a steel-free deck slab panel with no internal reinforcement. Three straps spaced at 1.02 m were placed symmetrically with respect to the transverse centreline of the panel (Figure 4.2).

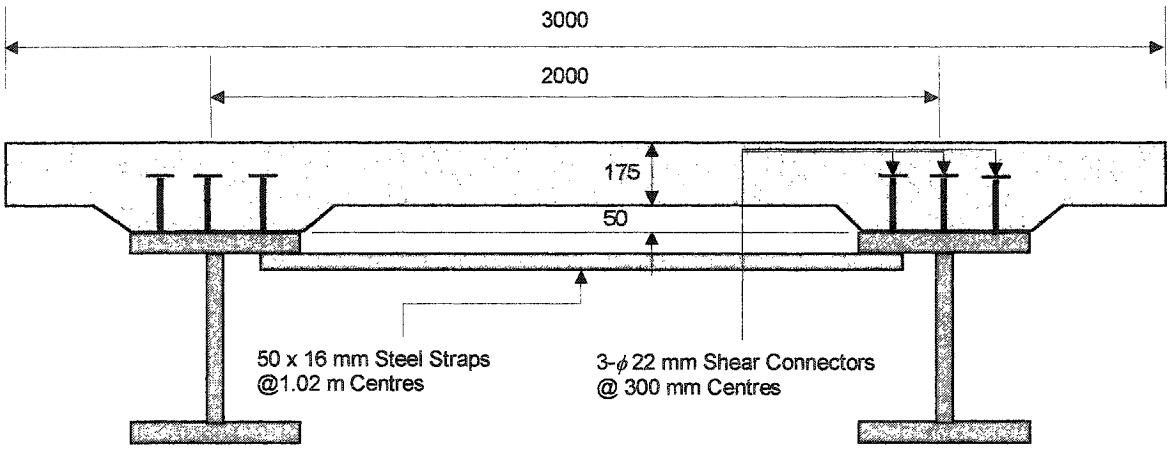

Figure 4-2 Cross-section of Panel-A

4.1.3.2 Panel-B

Panel-B was similar to Panel-A. As stated in Section 1, the steel free bridge decks develop longitudinal cracks mid-way between the girders shortly after the first application of load. Although the cracks have not affected the performance of the bridges that have been built so far, it was necessary to study the behavior of a deck slab with a wide full depth crack. It was decided to simulate this situation in the laboratory by pre-inducing a longitudinal crack in the soffit, extending up to almost 50% of its overall depth, by installing a 75 mm high crack trainer in the soffit of the slab along the length of the panel. The cross-section of the panel is shown in Figure 4.3.

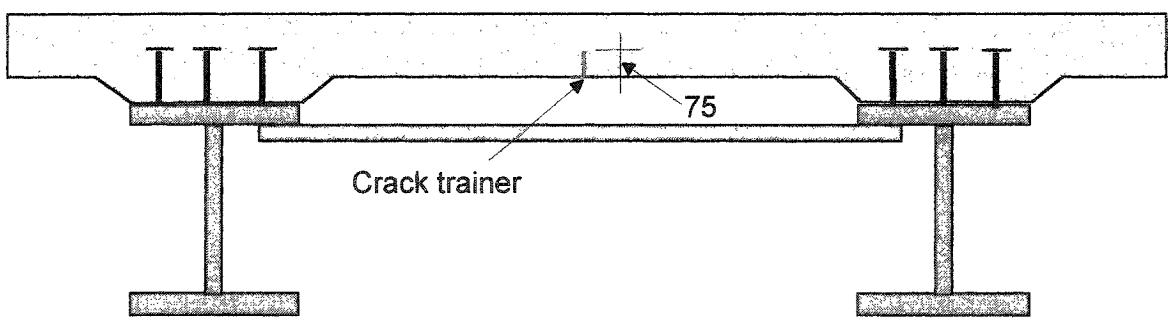

Figure 4-3 Cross-Section of Panel-B

4.1.3.3 Panel-C

While Panel-B was designed to study the performance of a deck panel with a pre-existing crack, the aim of the design of Panel-C was to control and reduce the crack width. It was known that the longitudinal crack always developed over time on the soffit and then propagated to the top surface of the slab. It was proposed that the longitudinal crack width may be controlled or reduced by providing some suitable form of transverse reinforcement near the bottom surface of the slab. One of the alternatives investigated in this thesis was to use GFRP reinforcing bars while another alternative was to provide steel reinforcing mesh. The cross-sectional area of steel reinforcement required to limit the crack width to 0.6 mm was calculated to be 300 mm^2. Providing GFRP reinforcement of equivalent axial stiffness would require 16 mm diameter GFRP bars at every 125 mm as bottom transverse reinforcement. This amount of GFRP would be uneconomical; therefore, only nominal amount of reinforcement was selected to control cracking. Sixteen-mm diameter GFRP bars were provided at 500 and 850 mm centres, in the transverse and the longitudinal directions, respectively. Two longitudinal bars were also provided along the outer edge of the girders as shown in Figure 4.4.

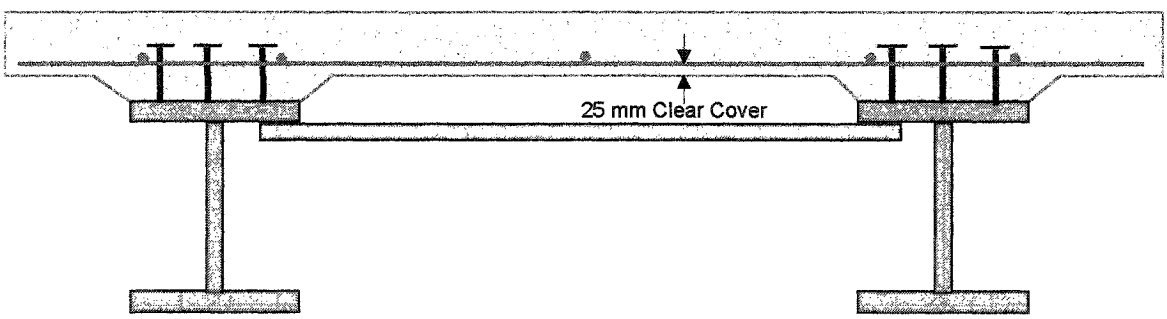

Figure 4-4 Cross-Section of Panel-C

4.1.3.4 Panel-D

A bottom layer of steel crack-control reinforcement mesh was provided in Panel-D consisting of 10M steel reinforcing bars spaced at 300 mm centres in each direction (Figure 4.5). As discussed in Section 4.1.3.3, this cross-sectional area of steel reinforcement was required to limit the longitudinal crack width to 0.6 mm.

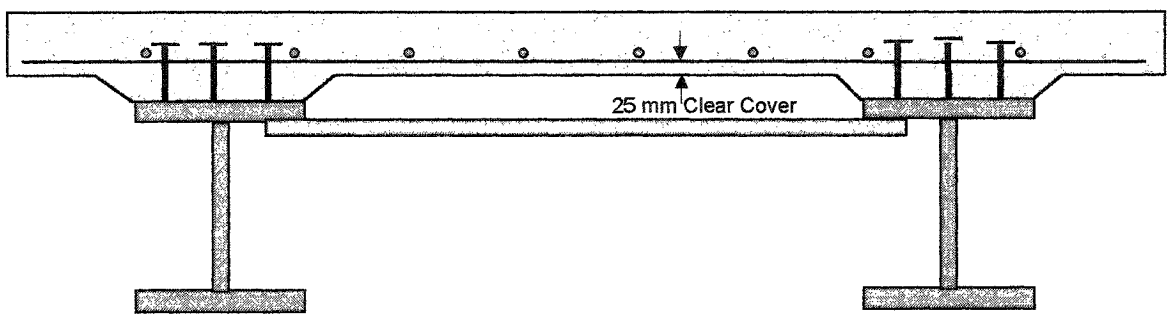

Figure 4-5 Cross-Section of Panel-D

4.1.4 Design of girders

Two steel girders, W 610 x 241, 12.4 m long, were provided to support the deck slab. The girders were spaced at 2.0 m centres. The size of the girders was adequate for resisting the maximum applied load without exceeding the permissible stresses and deflection.

4.1.5 Diaphragm

The code specifies that the adjacent longitudinal girders be connected by diaphragms spaced at a maximum length of 8.0 m centres. A diaphragm consisting of an X-shaped bracing with two 55 x 55 x 8 mm angles was provided at the mid-span. The diaphragm is shown in Fig. 4.6.

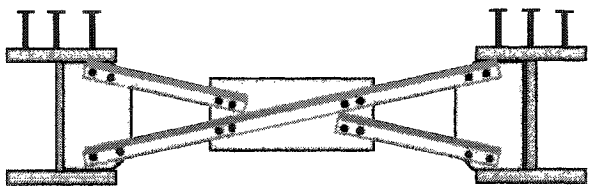

Figure 4-6 A View of Diaphragm at Mid-Span

4.1.6 Edge Beams

At the locations away from the supports, adequate confinement in the longitudinal direction is provided by in-plane stiffness of the slab affected by shear connectors. Due to the discontinuity of the deck slab at the supports, however, arching action cannot be affected by the slab. Edge beams are provided at the discontinuous transverse edges to provide adequate flexural stiffness in the horizontal direction. Each edge beam consisted of two 150 x 150 x 20 mm steel angles placed back-to-back 16 mm apart. One row of 22 mm ϕ x 150 mm long shear connectors were welded to the top face of each angle at 120-mm centres. The edge beam was made composite with the deck slab for effective transfer of force from the deck slab to the edge beam. An edge beam connected to the girders at one end is shown in Figure 4.7.

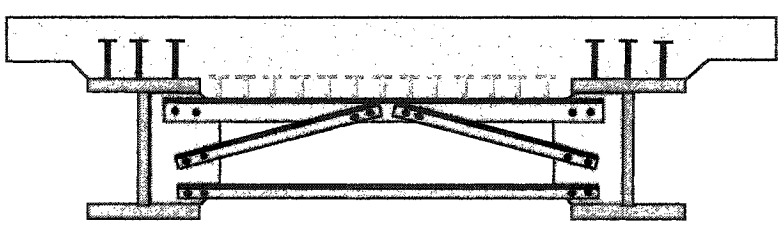

Figure 4-7 A View of Edge Beam

4.1.7 Design of Support Blocks

Four concrete support blocks measuring 610 x 550 x 500 mm (L x B x H), were cast in place to support the main girders. The blocks were adequately sized for the stability during testing. The concrete mix for the support blocks was the same as the one used for the deck slab. Thus the properties of concrete could be ascertained well in advance. Two 25 mm ϕ guide bars were embedded in concrete in each block to help position and guide the movement of the base plate.

4.1.8 Laminated Bearings

Each end of the girder was supported on 40 mm thick laminated rubber bearing pads measuring 350 X 450 mm in plan. The bearing pads were manufactured by Goodco Limited, Laval Quebec. The properties of the bearing pads are given in Table 4.1.

Table 4-1 Properties of Laminated-Rubber Bearing Pads

SLS II Dead load (kN)	SLS II Live load (kN)	ULS Dead Load (kN)	ULS Live Load (kN)	Maximum shear rate (kN/mm)	Maximum Comp. rate (kN/mm)	Maximum Rotation (radians)
709	1,103	1,103	1,575	4.91	608.7	0.010

4.1.9 Sliding Mechanism

Each girder was provided with a sliding mechanism at one end to prevent the girders from exerting lateral thrust on the supporting blocks during loading. This mechanism permitted the girders to move freely at one end in the longitudinal direction when loaded. A base plate was welded to the bottom flange of the girder at each end. At the free end, the base plate rested on a second greased steel plate, which in turn, was set on the bearing pad as shown in Fig 4.8. At the other end, the base plate rested directly on the bearing pad.

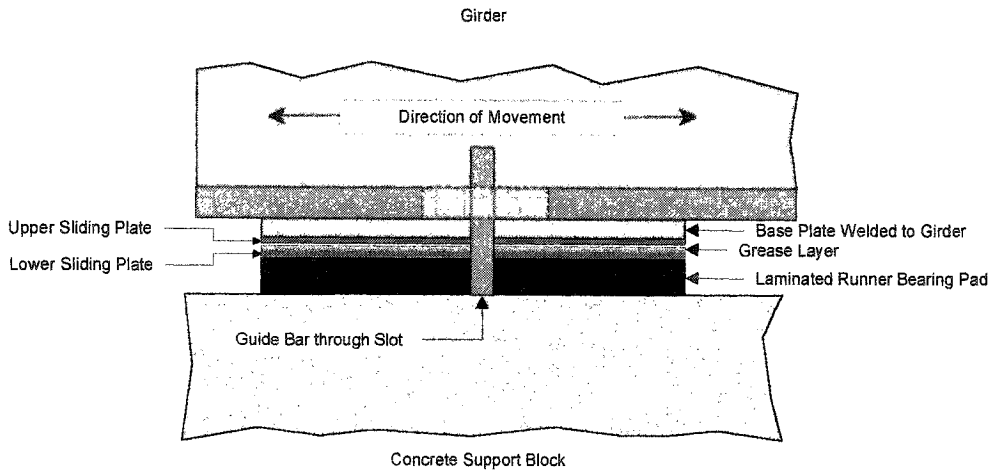

Figure 4-8 A View of Sliding Mechanism

4.1.10 Design of Deck-Slab

As per Clause 16.7 (c) of CAN/CSA-S6-00, the minimum thickness, t, of an FRC deck slab should be at least $S/15$, where S is the spacing of the supporting beams, and not less than 175 mm. As the steel girders were spaced at 2.0 m, the specified minimum thickness of 175 mm controlled the selection of the slab thickness. Therefore a slab thickness of 175 mm was adopted for the test model.

4.1.10.1 Haunch Height

Clause 16.7(e) of CAN/CSA-S6-00 permits the height of haunch between the deck slab and the supporting girder to vary between 25 and 125 mm. A height of 50 mm was selected.

4.1.11 Steel Straps

Clauses 16.7(f) and (g) of the code require that the spacing of the straps, S_l, should not exceed 1.25 m and the minimum cross-sectional area of the strap, A in mm^2, should be determined by Equation 4.1,

$$A = \frac{F_s S^2 S_l}{Et} 10^9, \tag{4.1}$$

where, the factor F_s is 6.0 MPa for outer girders, and 5.0 MPa for inner girders. E is the modulus of elasticity of the steel strap in MPa, t is the thickness of the deck slab in milimeters, and S is the girder spacing in meters.

Due to the considerations of symmetry, a straps spacing of 1.016 m was adopted. This spacing ensured that the position of load pads and the straps was symmetrical and identical in all panels. The computed cross-sectional area of the strap was 696.7 mm^2. It was decided to use 50 x 16 mm steel straps, providing a cross-sectional area of 800 mm^2. A typical strap is shown in Figure 4.9.

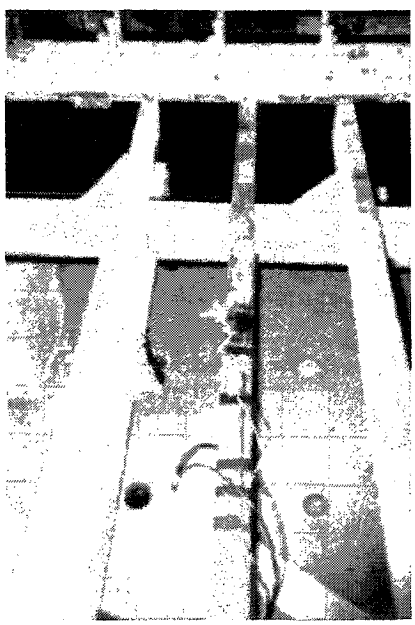

Figure 4-9 A View of Instrumented Steel Strap

4.1.12 Design of Crack Trainer

In order to pre-induce a longitudinal crack in Panel-B, a crack trainer was fabricated in the laboratory by folding a thin galvanized iron strip into a 75mm high inverted T shape. The crack trainer was installed along the longitudinal centerline of the panel. To prevent the crack from extending into the adjacent Panels A and C, a transition piece was added to each end of the crack trainer, as shown in Figure 4.10.

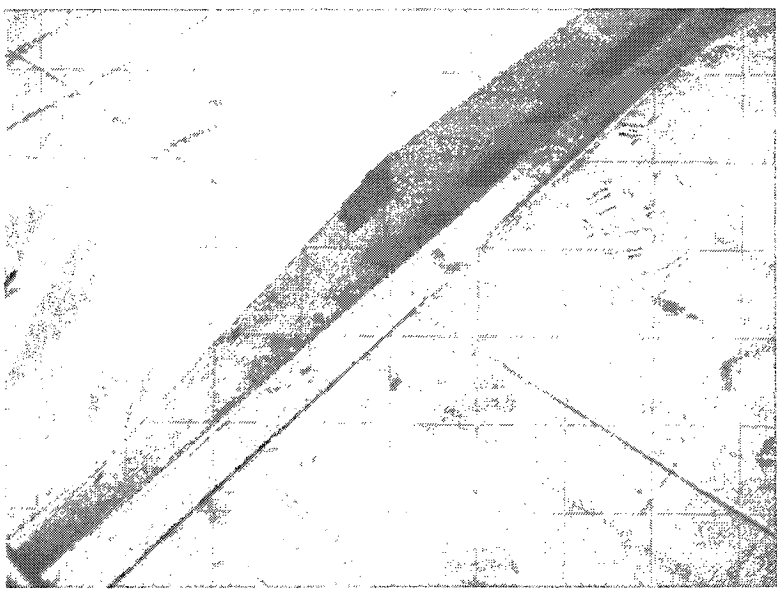

Figure 4-10 A Close-up View of Crack Trainer and the Transition Piece

4.1.13 Layout of Crack-Control Reinforcement

The layout of crack control reinforcement in Panel-C and Panel-D, and the crack-trainer in Panel-B, is shown in Figure 4.11. A clear cover of 25 mm was provided by means of PVC spacers placed on the formwork.

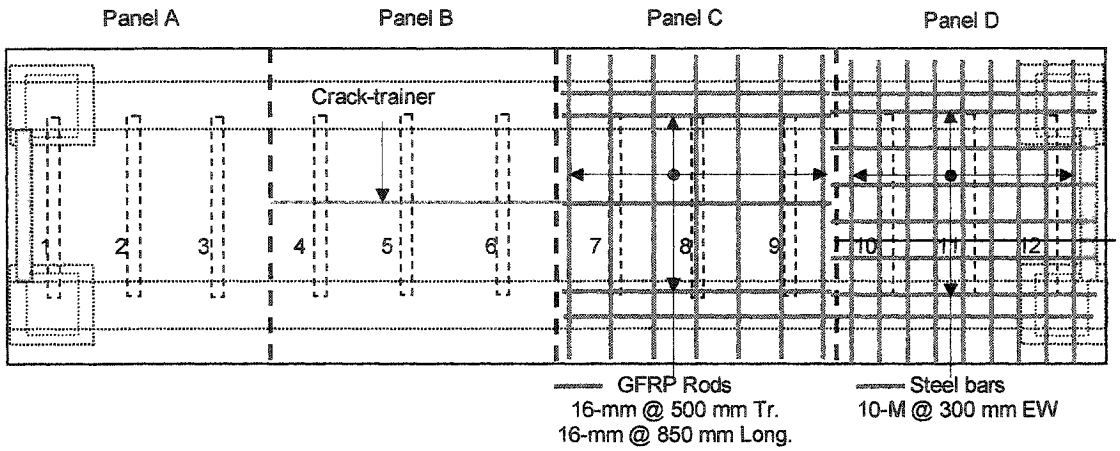

Figure 4-11 Layout of Crack-Control Reinforcement and Crack-Trainer

4.1.14 Design of Instrumentation

4.1.14.1 General

The instrumentation required for testing under fatigue load is quite unlike that required for a one-time, short duration test that is conducted under static loading conditions. It is essential to ensure that the various sensors used during the test continue to function reliably and provide meaningful data during the entire duration of the test. The installation of sensors, particularly those embedded within the concrete slab, must be carried out with utmost care to avoid their premature failure. Redundancy is essential to take into account any possible sensor failure.

4.1.14.2 Instrumentation of Straps

As described in 4.1.3, the deck model was internally divided into four panels. Each panel had three steel straps located symmetrically about its transverse centre line. As the straps were to be subjected to cyclic loading, any separation of the strain gauge from the strap would have resulted in a loss of data. Therefore, each strap was instrumented with one 350-Ω weldable electrical strain gauge. Two rows of closely-spaced, minute spot

welds all around the gauge ensured a positive and reliable bond between the strain gauge and the steel strap.

In addition to the weldable strain gauge, the central strap in each panel was also instrumented with one Fabri-Perot fiber optic sensor. The central strap in each panel was equidistant from the two load pads and was therefore used to monitor the structural degradation in that panel while the load was alternated between the two load pads.

4.1.14.3 Concrete Internal Strain Measurement

As the load is applied to a panel, it initially exhibits a bending behaviour. When the magnitude of the load exceeds a certain level, compressive membrane forces develop in the top layer of the slab resulting in an arching action. To study this change from bending to arching it was deemed necessary to provide strain gauges within the thickness of the slab at strategic locations. Concrete embedment gauges with a nominal resistance of 350 Ω were selected for this purpose. Concrete embedment gauges are foil type strain gauges installed within a fiber reinforced polymer carrier. The gauge typically, has an overall cross-section of 20 x 9 mm and is 190 mm long. The surface of the gauge is heavily indented to provide adequate bond to the surrounding concrete. To measure the variation in concrete strain within the thickness of the slab, three sets of three embedment gauges each were provided along the transverse centre-line of one of the load pads in each panel as shown in Figure 4.12.

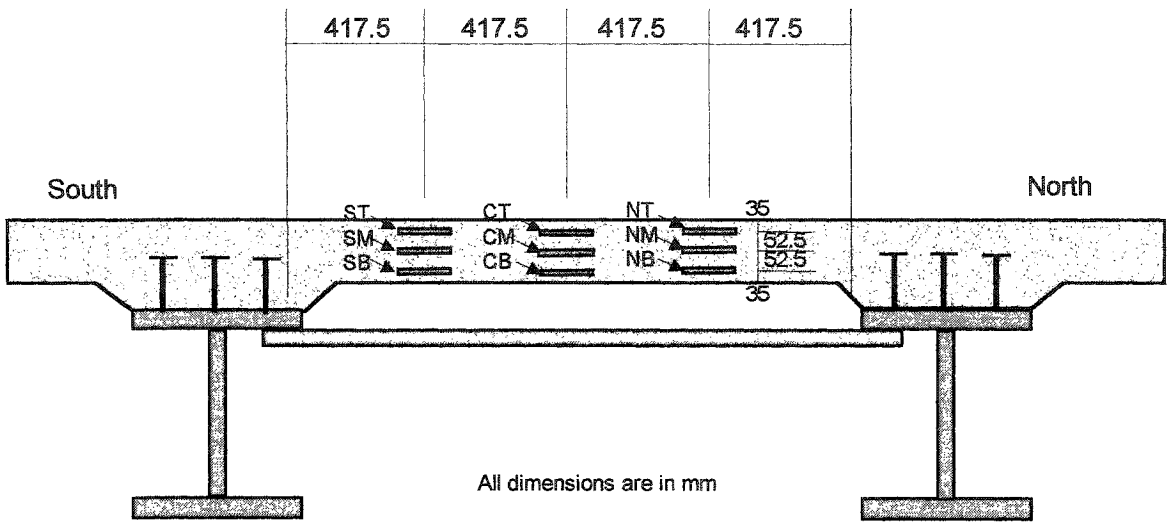

Figure 4-12 Cross-Section of Model through Embedment Gauges

As shown in Figure 4.13, the three embedment gauges in a set were installed in a vertical ladder pattern at each designated location. The gauges were installed on a purpose built carrier. The carrier comprised two plexiglass brackets with three pre-drilled holes to accommodate the embedment gauges. The embedment gauges were then inserted in the brackets and the brackets screwed-down to the formwork. The gauges were wedged in the holes to prevent rotation during concreting operation. Plexiglass was selected, as it did not have sufficient stiffness to affect the strain in the gauges. The top gauge was placed 35 mm from the top surface of the slab. The middle gauge was placed at the mid-depth of the slab. The bottom gauge was placed 35 mm from the bottom surface of the slab.

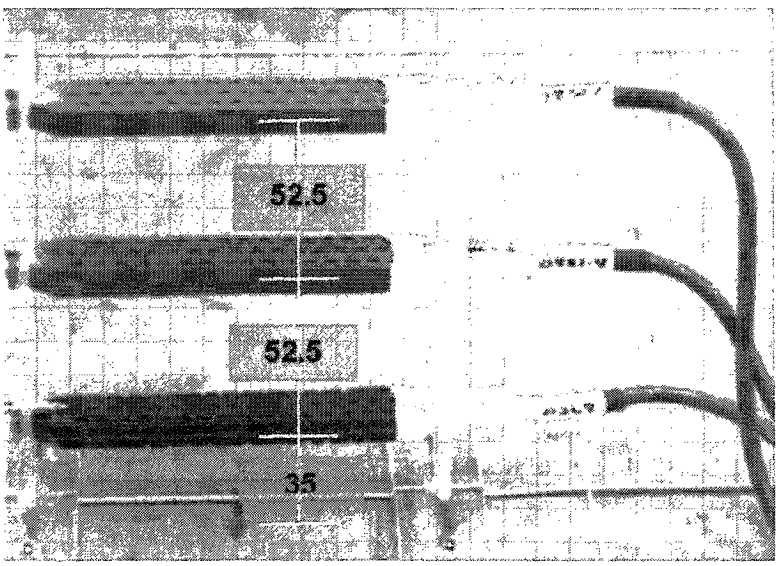

Dimensions are in mm

Figure 4-13 Close-Up View of a Set of Concrete Embedment Gauges

4.1.14.4 Crack Detection Gauges and Crack Propagation Gauges

Crack detection gauges are single filament strain gauges. They are used to detect the initiation of a crack. Typically, these types of gauges are bonded to the external surface of the structure. However, in the case of this research, the crack detection gauges were bonded to 6 mm thick concrete plates as shown in Figure 4.14 and then embedded within the thickness of the deck slab. The concrete plates were sliced from the fiber reinforced concrete cylinder prepared from the trial mix which was subsequently also used for the model. Thus, the plates had properties similar to those of the deck concrete. Figure 4.15 presents the cross-section of Panel-A showing the location of crack detection and propagation gauges. The cluster of three crack-propagation gauges is identified as CPG. Individual functioning crack-propagation gauges are identified as CPL1, CPL2, CPU2, representing Lower Gauge1, Lower Gauge2 and Upper Gauge2, respectively. CD-2 and CD-4 represent a group of two crack-detection gauges and a group of four crack-detection gauges, respectively.

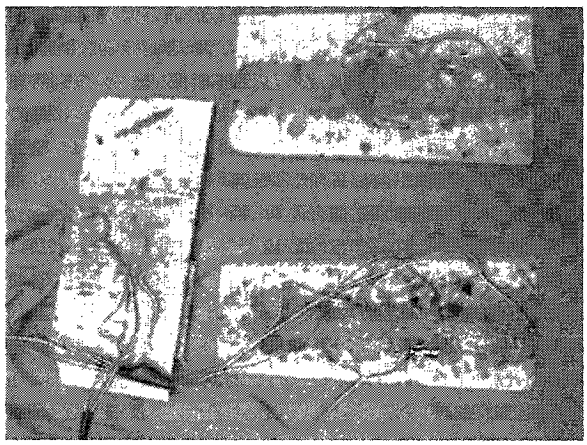

Figure 4-14 Crack Detection and Propagation Gauges Bonded to Concrete Plates

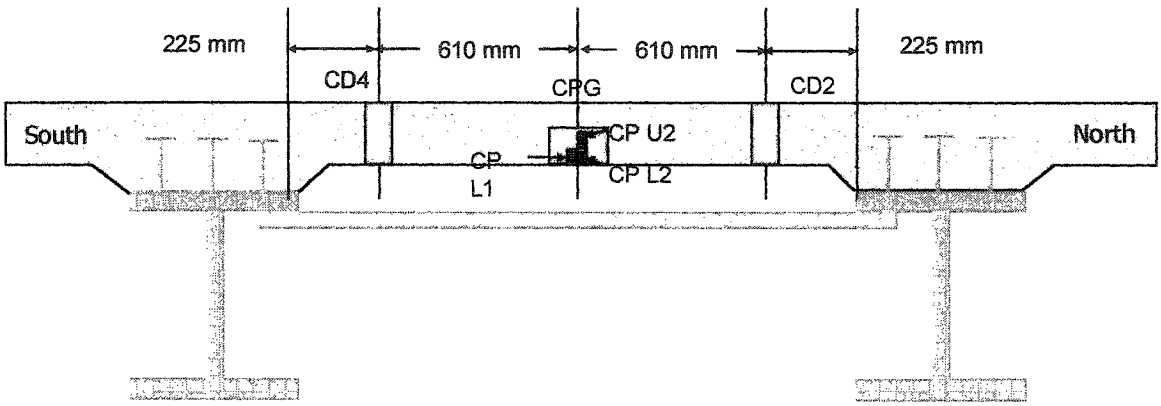

Figure 4-15 Cross-Section of Panel-A at Centre Showing Positions of Crack Detection and Crack Propagation Gauges

The gauge, in series with a light emitting diode (LED), is connected to a power source. The LED glows under normal conditions. When a crack develops within the length of the gauge, the filament ruptures. When the continuity of the circuit is broken, the LED stops

glowing. Crack propagation gauges are multi-filament gauges with filaments spanning two elongated tabs. An unbroken gauge has certain known resistance. As a crack initiates it may rupture one or more filament thus increasing the resistance of the gauge. As the crack progresses through the gauge assembly, the gauge resistance continues to increase until all the filaments are ruptured and the circuit is interrupted. The crack propagation gauges were also bonded to concrete biscuits and embedded within the thickness of the slab. Crack propagation gauges require a sensitive Ohmmeter to detect very small changes in the gauge resistance caused by the rupture of individual filaments. As it was not feasible to procure such a device, these gauges were also connected to the LEDs and therefore served as crack detection gauges. The bank of LED indicators is shown in Figure 4.16.

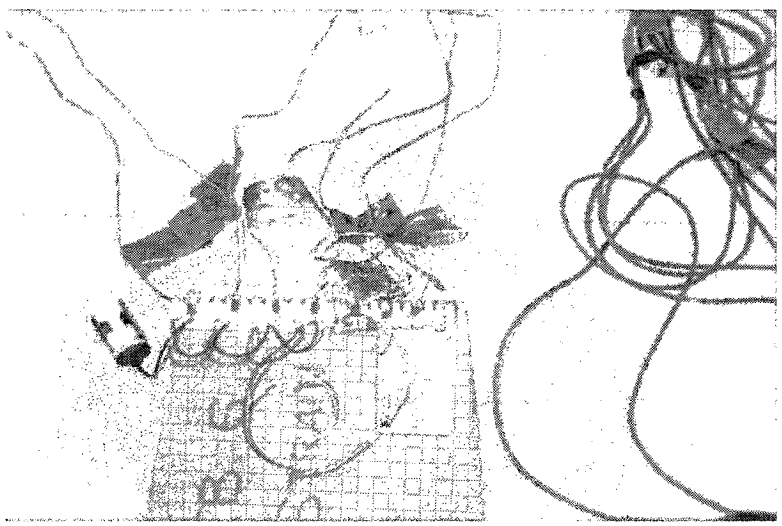

Figure 4-16 A View of LED Indicators

4.1.14.5 Instrumentation of Reinforcing Bars

Nominal crack control reinforcement was provided in Panels C and D. To assess the participation of crack control reinforcement in arching action, one reinforcing bar in each panel was instrumented with five, 350-Ω strain gauges, equally spaced, between the girders. Bondable foil gauges were provided on a GFRP reinforcing bar in Panel-C, while

weldable strain gauges were provided on the steel reinforcing bar in Panel-D. The strain gauges were protected by a four-layer protection system comprising the following:

1. teflon tape
2. butyl rubber compound
3. PVC tape
4. Aluminum adhesive foil

A close-up of the instrumented GFRP bar in shown in Figure 4.17.

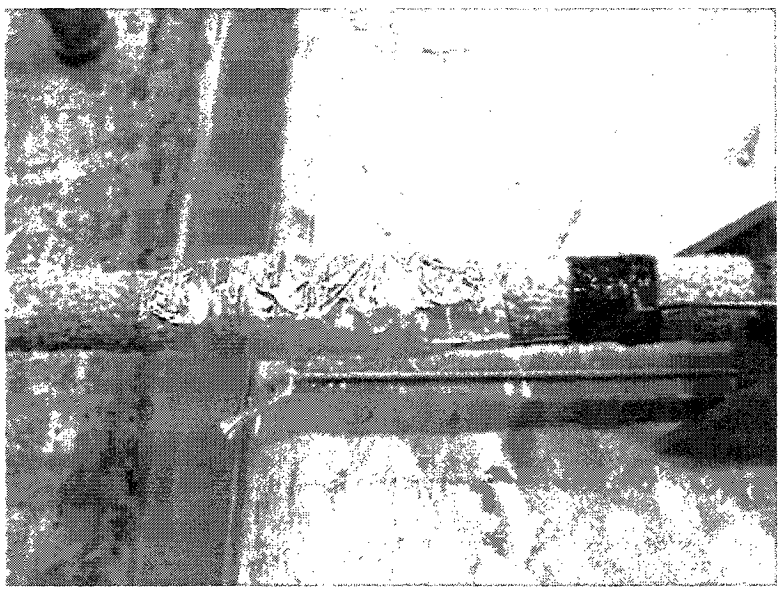

Figure 4-17 Strain Gauge Protection of Instrumented GFRP Bar in Panel-C

4.1.14.6 Displacement Transducers (DTs)

Displacement transducers (DTs) were used to measure the displacements during testing. These sensors had a range of ± 25 mm and sensitivity of 0.01 mm. During the first phase of testing, one DT was provided on each of the two load pads for the panel under test to measure the deflection of the slab with respect to the girders. Near each load pad one 100 x 50 mm SHC (Structural Hollow Section) spanning the two girders

was placed on knife-edge supports positioned along the centre line of the girders. The DT was mounted on the SHC using magnetic stand with the plunger resting on the load pad. One DT was also placed under each girder at the transverse centre line of the panel under test.

On Panel-B, the loading was applied only at one load pad and therefore only one DT was used for measuring the deflection of the slab. However, the load pad was placed asymmetric on one side of the pre-induced crack. Two DTs were placed vertically on opposite sides of the crack to detect any possible vertical differential movement along the crack. Further, a DT each was placed horizontally across the longitudinal crack at the top and the bottom of the slab to monitor its closing and opening under cyclic loading. The monitoring of the crack opening/closing is discussed in detail in section 4.3.4.5.1.

In the second phase of testing, load was applied at one load pad in each panel and only one DT was used to measure the deflection of the slab. One DT was placed under each girder. During the testing of Panel-A, a gradual shifting of the load pad was noticed under repeated loading. This resulted in an erratic pattern in the slab deflection. It was therefore decided to place a second DT on the other side of the load pad.

During the testing of Panels A and D, DTs were also placed across transverse cracks to measure the relative movement of various segments of the deck slab.

4.1.14.7 Pressure Transducer

An Omega series 302 pressure transducer, with a range of 0-67,000 kPa (0-10,000 psi), was used to measure the load applied by the hydraulic system. The in-line fluid pressure is multiplied by an appropriate gauge factor to obtain the applied load.

4.1.14.8 Main Data Acquisition System

The main data acquisition system comprised National Instruments SCXI 1001 chassis with nine SCXI 1121 signal-conditioning modules and one SCXI 1200 12-bit data acquisition module. Each signal-conditioning module (SCXI 1121) provided 3.3-v or 10-v excitation to four sensors, acquired and conditioned the incoming signals. The data acquisition module (SCXI 1200) gathered data from each of the nine signal-conditioning modules and transmitted to a laptop computer through a parallel port. Signal conditioning eliminates the need for post-processing. The system could accommodate 24 strain gauges, 8 DTs and one pressure transducer, and continuously display the acquired data on the computer screen. A scan-rate of 4000 to 8000 scans per second and sample averaging of 120 to 240 samples, depending on the total number of sensors connected simultaneously, was used to provide a smooth data pattern.

4.1.14.9 Data Acquisition System for Fibre Optic Sensor

The fibre optic sensor was connected to a single-channel Roc-Test FIZ 10 read-out unit. FIZ 10 converts light signals to electrical signals and transmits to a Personal Computer through a serial port. The acquired data were stored as text files which were later converted to Excel files as required.

4.1.14.10 Acoustic Attenuation System

The acoustic system used during the testing comprised two acoustic sensors mounted on the underside of the panel under test, a pendulum type acoustic source mounted on the side of the slab and a PC-based digitizing and storage module. The acoustic sensors had a frequency response range of 30 to 150 kHz and were placed so that one sensor would be beyond the expected main crack and the other close to the acoustic source. Recording of the waveforms detected by both sensors was triggered by a threshold signal level on the sensor nearest to the acoustic source and each waveform was digitally recorded at a sampling rate of 500 kHz. The sensors were attached to the slab using quick-setting epoxy, which also functioned as acoustic couplant.

Except for Panel-A, the acoustic source and the sensors were mounted close to the transverse centreline of the panel with the acoustic sensors positioned approximately 300 mm on either side of the longitudinal centreline. The positioning of acoustic sensors was strategic in that the expected region of major damage under the loading pads was expected to lie between the sensors. In this arrangement, the waveform detected by the near sensor, termed the reference sensor, would serve as a reference signal to be compared with the waveform detected by the far sensor, termed the active sensor, after it had passed through the major damaged zone. This signal comparison was facilitated by computing the ratio of the integrated amplitudes under the rectified waveforms for the reference sensor and the active sensor. An increase in this ratio would indicate an increase in the level of attenuation in the region between the two sensors. In accordance with the assumptions underlying this technique, an increase in the level of attenuation would correspond to an increase in the level of damage in that region of the deck slab. In addition, since both waveforms were recorded to the same timescale, the direct measurement of the travel time between the sensors, and hence acoustic wave velocity, could also be computed for comparison to the attenuation measurements.

Since in Panel-A, the acoustic sensors were on significantly divergent ray-paths from acoustic source, changes in the amplitude ratios could indicate that additional damage has occurred in the deck. The location, however,of the damage could not be determined as precisely as for the other panels.

4.2 Construction of Model

4.2.1 General

The construction of the model was carried out in the heavy structures lab at Dalhousie University. With the exception of placing and finishing of concrete the complete construction was carried out using in-house personnel.

4.2.2 Installation of Support Blocks, Laminated Rubber Bearings and Sliding Mechanism

4.2.2.1 Support Blocks

The concrete support blocks were placed at the predetermined positions on the strong floor and aligned correctly with respect to the proposed centerline of the model. The support blocks were spaced at 11.6 m centres in the longitudinal direction and at 2 m centres in the transverse direction. Each block has two partly embedded guide bars. The support blocks on the western end of the model were designed to support the sliding end of the model while the blocks at the eastern end of the model were designed to support the non-sliding end of the model.

4.2.2.2 Bearing Pad Installation

A layer of non-shrink high-strength leveling grout was spread on the top surface of the support blocks and leveled to set-in the bearing pads. The bearing pad was positioned and aligned correctly on the prepared surface. It was ensured that the elevation of the four bearing pads was same. The water content of the grout was kept to a minimum possible level to avoid any settlement. To avoid direct contact between the mortar and the bearing pad a vapour barrier was provided. The grout was allowed to cure for a period of seven days.

4.2.2.3 Sliding Mechanism

One thin galvanized iron sheet was placed on top of each of the bearing pad positioned at the sliding end of the model. The top surface of the galvanized iron (GI) sheet was lubricated with heavy-duty grease and covered with a second GI sheet. A 16 mm thick steel base plate, measuring 450 x 550 mm, with pre-drilled slots for the guide bars, was placed on the second sheet. The frictional force between the upper GI sheet and the base plate was sufficient to allow them to slide freely over the lower GI sheet. At the non-sliding end, one galvanized sheet was placed over the bearing pad and the base plate was installed directly over it (Figure 4.8).

4.2.2.4 Installation of Girders, Diaphragms, Edge Beams and Straps

The girders, the edge beams and the central diaphragm were assembled on the floor and then lifted and placed in position on the support blocks. After aligning the girders correctly, the base plates were first tack-welded to the girders. Before carrying out the continuous fillet welding, one end of the model was raised above the bearing to avoid any damage to the laminated rubber bearing due to the heat generated by the welding. The raised end was lowered back into position after the heat had dissipated. The straps were positioned in place and tack-welded to the underside of the top flanges of the girder. Continuous fillet welding was carried out subsequently. Due care was exercised to avoid development of curvature in the straps during the welding process. However, some straps did develop a hogging profile along their length which could not be rectified completely.

4.2.3 Design and Construction of Formwork

The formwork was designed to be supported on the girders. Continuous wooden runners were installed on the bottom flanges of the girder. Cross beams were placed on the lower runner, at every 900 mm. The cross beams supported the 50 x 100 mm runners which in turn supported the wooden decking panels. For the cantilevered portion of the

deck slab special triangular brackets were wedged between the top and the bottom flanges of the girders. The ends of the brackets were provided with additional supports to prevent significant movement. The brackets supported the wooden decking panels. Chamfers were installed along the edge of each flange. After the formwork for the decking was completed, the longitudinal and transverse centrelines of the panels and the load pads were set out on the decking panels. The entire surface of the decking was divided into 305 x 305 mm grids with the gridlines coinciding with the transverse and the longitudinal centrelines of the panels and the load-pads. The decking was covered with a layer of polyethylene sheeting to act as a barrier between the decking and the concrete. The sheeting was stretched over the decking to provide a smooth surface on the soffit. Twine strings were stretched over the entire grid pattern and stapled to the formwork at regular intervals. Upon removal of the forms, the impression left by the twine threads on the concrete soffit replicated the grid patterns on the soffit, which were used to map the cracks without any ambiguity.

4.2.4 Installation of Crack Trainer and Crack Control Reinforcement

The prefabricated crack trainer, together with the transition pieces, was aligned along the longitudinal centreline of Panel-B and screwed down to the decking. Two threaded steel bars were provided across each transition piece at its end to arrest the propagation of the pre-induced longitudinal crack into Panel-A and Panel-C. One of the threaded bars, the crack trainer, and the transition piece, are shown in Figure 4.18.

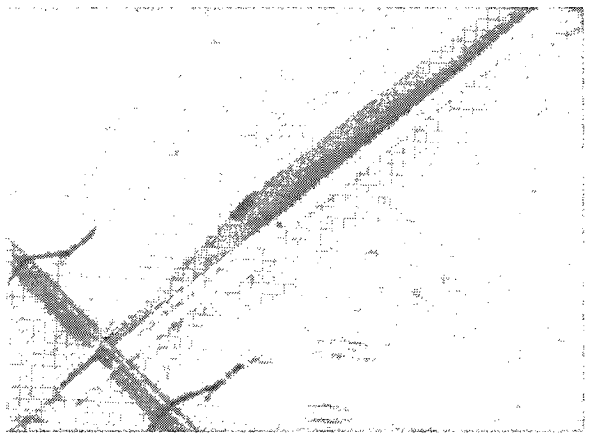

Figure 4-18 A Close-Up View of Threaded Bar Across Crack Trainer

For Panel-C, the GFRP crack control reinforcement was laid-out on the decking and tied together using PVC cable ties. To ensure that the bars had adequate and uniform cover, PVC spacers were placed under the bars. The density of GFRP is much lower than the density of the fresh concrete and there was a possibility that the bars could float while the fresh concrete was being placed. Therefore, the reinforcing mesh was anchored to the formwork at regular intervals. GFRP mesh in Panel-C is shown in Figure 4.19. Note the bank of concrete embedment gauges and the strain gauge identification on the instrumented bar.

Steel reinforcement was laid out and tied and provided with PVC spacers to provide adequate concrete cover. The tied up steel reinforcing mesh in Panel-D is shown in Figure 4.20.

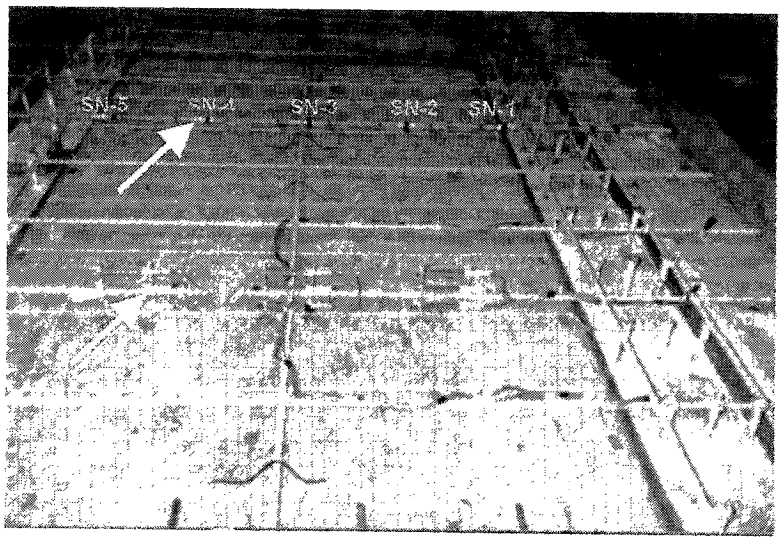

Figure 4-19 A View of GFRP Crack-Control Reinforcement in Panel-C

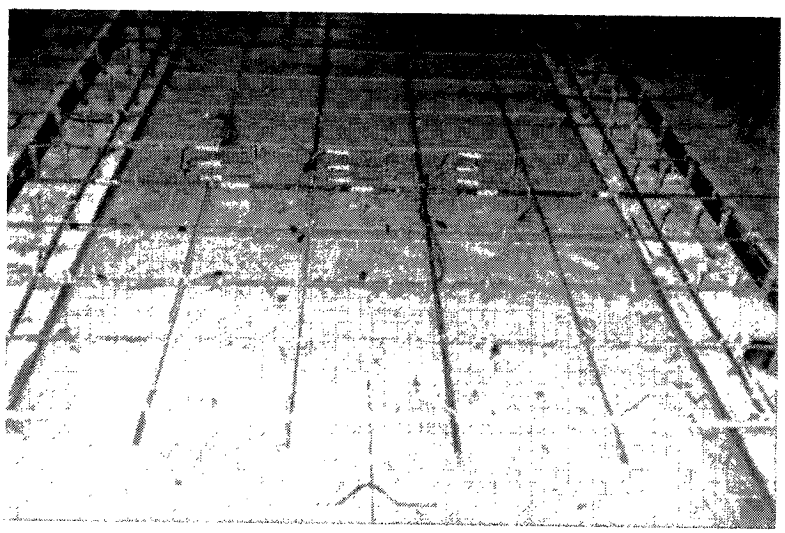

Figure 4-20 A View of Steel Crack-Control Reinforcement in Panel-D

4.2.5 Installation of Embedded and Fixed Instrumentation

The cyclic load was applied at two load pads in each panel. One set of nine-embedment gauges was installed under one load pad in each panel to measure the internal strains in concrete. The embedment gauges were installed under Pad-2, Pad-4, Pad-6, and Pad-7 in Panel-A, Panel-B, Panel-C, and Panel-D, respectively. The instrumented GFRP bar was positioned along the transverse centreline of Pad-5 in Panel C, while in Panel-D, the instrumented steel bar was placed along the transverse centreline of Pad-7. The load pad posoitons are shown in Figures 4.26 and 4.35.

The strain gauges on each of the 12 straps were welded, wired and protected before the commencement of the formwork. The fiber optic sensors to be placed on the middle strap of each panel were also bonded and protected prior the commencement of the formwork. The layout of instrumentation is shown in Figure 4.21.

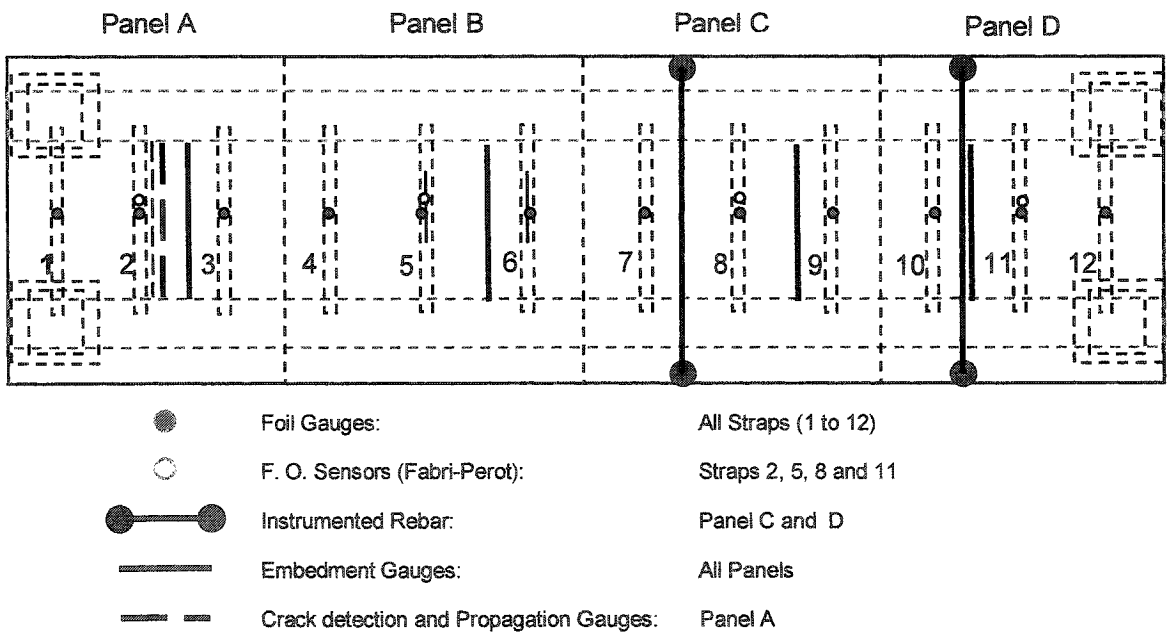

Figure 4-21 Instrumentation Layout

4.2.6 Selection of Fibers

Grace Structural Fiber, GSF-1, was selected after conducting tests on a trial mixture that was used earlier to construct the four support blocks for the support of the steel girders. As shown in Figure 4.22, the fibers partially fibrillate during the mixing process. A fiber volume fraction of 0.75% was adopted. The mechanical properties of fibers are shown in Table 4.2.The concrete mixture proportions and the results for the trial mixture are discussed in Section 4.2.8.3.

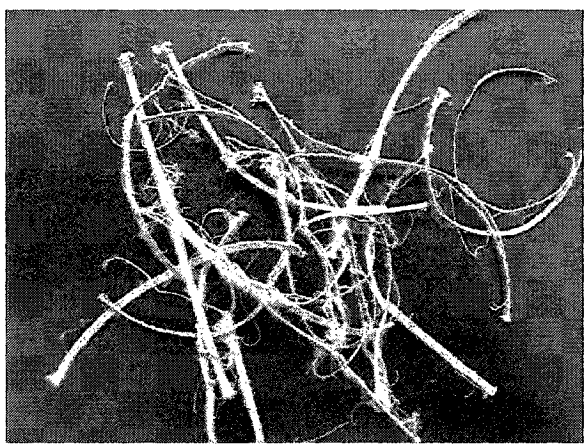

Figure 4-22 A Close-up of Partially Fibrillated Fibers

Table 4-2 Mechanical Properties of GSF-1

Specific Gravity	0.92
Modulus of Elasticity (GPa)	4.3
Tensile Strength (MPa)	370

4.2.7 Placing, Finishing and Curing of Concrete

The concrete for the deck slab was placed on February 20th, 2000. The concrete was supplied in two ready-mix concrete trucks. The supplied concrete was inspected and preliminary tests were conducted on the fresh concrete. Samples of the fresh concrete were taken before the addition of the required fiber dosage. After the fibers are added to

concrete, the workability of the mixture is reduced considerably. To enable easy handling and the placing of concrete admixtures have to be added. The additives in this case had to perform two functions: a) improving the workability of the mixture, and b) reducing the total water content of the mixture. After the addition of fibers, the concrete was thoroughly mixed and the workability of the concrete was assessed. High-range water reducing admixture was added to achieve the desired workability. Samples of the concrete were collected to conduct tests on the hardened concrete. Then the concrete was unloaded in a crane bucket, hoisted and discharged at the desired location. The placing of the concrete began for the far end (Panel-D) and proceeded towards Panel-A. The concrete biscuits with crack detection and propagation gauges were inserted in the fresh concrete. The slab surface was power-floated to a smooth finish. The concrete slab surface was covered with wet burlap and polyethylene sheet to retain the moisture within. The slab was wet cured for more than seven days. The formwork was removed after the concrete had reached the desired strength. Figures 4.23 and 4.24 show the finished deck slab and the curing of concrete, respectively.

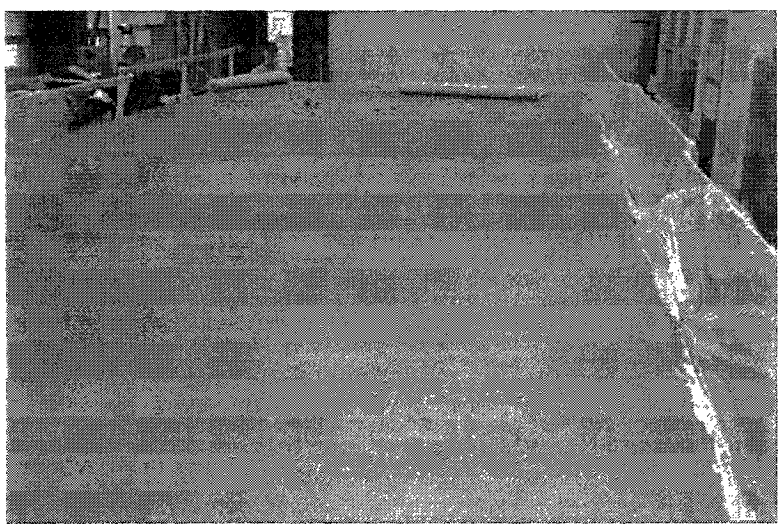

Figure 4-23 A View of Finished Deck Slab

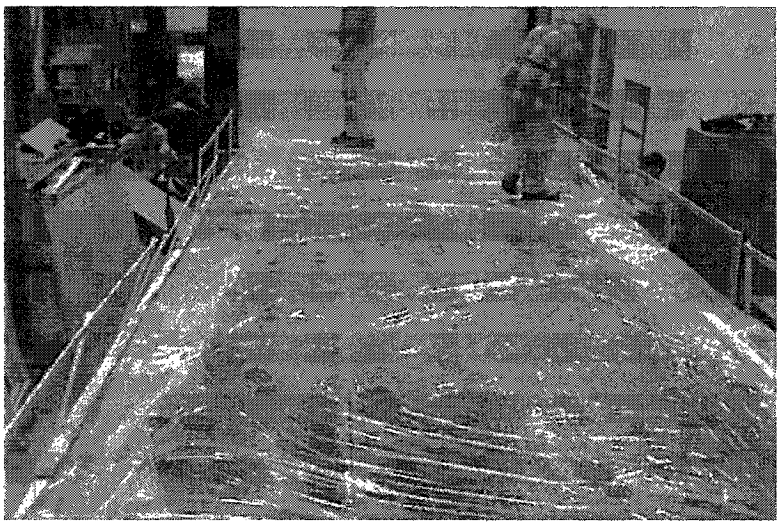

Figure 4-24 A View of Deck Slab during Wet Curing

4.2.8 Quality Control

4.2.8.1 General

The main materials used for the model were steel, concrete and GFRP rods. The tests on concrete were conducted in the Material Testing Laboratory at Dalhousie University.

The reinforcing bars used as crack control reinforcement conformed to CSA Standards with a minimum yield strength of 400 MPa. The steel girders used for the model were used successfully for the previous three test models (Newhook 1997; Thorburn 1998; Khanna 1999).

The properties of steel straps, concrete and the GFRP rods have been shown in the following section.

4.2.8.2 Structural Steel

The mechanical properties of steel straps are given in Table 4.3.

Table 4-3 Mechanical Properties of Steel Strap

Grade	CSA G40.21 44W
Size of straps (mm)	50 x 16
Yield Stress (MPa)	386.6
Tensile strength (MPa)	511.8
% Elongation	25

4.2.8.3 Concrete Mixture Design

As per Clause 16.6.1 of CAN/CSA-S6-00, the fiber-reinforced concrete for bridge deck slabs must have a residual strength index (R_i) of at least 0.30. Trial batches of concrete were mixed using a mixture design that was previously used for the airport apron replacement at the Halifax International Airport and had provided satisfactory workability and strength. Laboratory tests conducted indicated that the average R_i for the trial mixture was 0.44, which exceeded the code requirements. The mixture design adopted for the deck slab is shown in Table 4.4.

Table 4-4 Concrete Mixture Design

Cement Type 10	365 kg/m^3
20 mm Coarse Aggregate	1,040 kg/m^3
Fine Aggregate	825 kg/m^3
Water	160 kg/m^3
W/C Ratio	0.44
Fibers @0.75 by volume	6.9 kg/m^3
Air Entrainment (micro-air)	160 ml/m^3
Superplasticiser (WRDA 19)	1.5 l/m^3

4.2.8.4 Tests on Fresh Concrete (February 21, 2000)

On arrival of the concrete trucks at the Heavy Structures Laboratory, samples from the delivered concrete were taken and standard tests were conducted for temperature, slump, and the air-content. After it was ascertained that the delivered concrete was acceptable, the predetermined quantity of synthetic fiber was added to the truck and thoroughly mixed. Addition of fiber also necessitated the addition of water reducing admixture to improve the slump back to a workable level. The test results on fresh concrete are given in Appendix-B.

4.2.8.5 Tests on Hardened Concrete

The cylinder specimens from the trial mixture were tested at 7 days, 28 days and 180 days after casting. The results of these tests are similar to those of the actual concrete mix used. Concrete beams were tested to confirm compliance with the CAN/CSA-S6-00 requirements for fiber reinforced concrete.

Compressive tests on cylinder specimen were carried out at 7 and 28 days. In addition, compressive tests were also carried out when the load testing of the model was commenced and after the conclusion of the entire testing program.
The summary of the test results is presented in Table 4.5. The details of individual tests are given in Appendix-B.

Table 4-5 Summary of Concrete Test Results

Age (days)	Type of test	Average result	Comments
7	compressive	24.8 MPa	(Plain Tr-2) 7-day test
7	compressive	28.1 MPa	(FRC Tr-2) 7 day test
28	compressive	35.3 MPa	(Plain Tr-2) 28-day test
28	compressive	35.7 MPa	(FRC Tr-1) 28 day test
28	compressive	35 MPa	(FRC Tr-2) 28 day test
28	Young's Modulus	22,264 MPa	(FRC Tr-2)
28	OHBDC index	0.45	
167	compressive	41.5 MPa	(FRC-Tr-2) transverse crack
167	tensile	3.5 MPa	(FRC Tr-1) transverse crack
167	tensile	2.5	(FRC Tr-2) transverse crack
240	compressive	42.7 MPa	(Plain-Tr-2) test start
240	compressive	48.6 MPa	(FRC Tr-2) test start
927	compressive	46.7 MPa	(FRC Tr-1) test completion
927	compressive	48.4 MPa	(FRC Tr-2)test completion
927	tensile	3.6 MPa	(FRC Tr-2)test completion

4.2.9 Transverse Cracks in Slab

4.2.9.1 General

The concrete for the deck slab was poured on February 20, 2000. After 142 days (on July 15, 2000) a full-depth transverse crack, across the entire width of the deck slab, appeared in Panel-A. An audible loud noise accompanied the appearance of the crack. The crack path was approximately located along the transverse centre line of Load Pad-2. It is to be noted that an array of 9 concrete embedment gauges was located along the crack path. The testing of these gauges immediately after the cracking revealed that three embedment gauges, SB, CB, and NB were damaged. Prior to the cracking, all the embedment gauges were tested and were found to be functional. An interesting point to be noted is the fact that at each of the three locations there were three embedment gauges located one above the other. However, only one gauge failed at each location.

This indicates that the crack had by-passed, although slightly, the other undamaged gauges. At the commencement of the test, gauge CB was once again found to be functional but failed within the first ten load cycles. All the remaining embedment gauges continued to function except gauges SM and CM, which failed within the first 100 load cycles during Phase-I of the testing.

A second transverse crack appeared also approximately along the transverse centre line of Load Pad-5 in Panel-C after 159 days (August 10, 2000). The transverse cracks in Panel-A and Panel-C are shown in Figure 4.25.

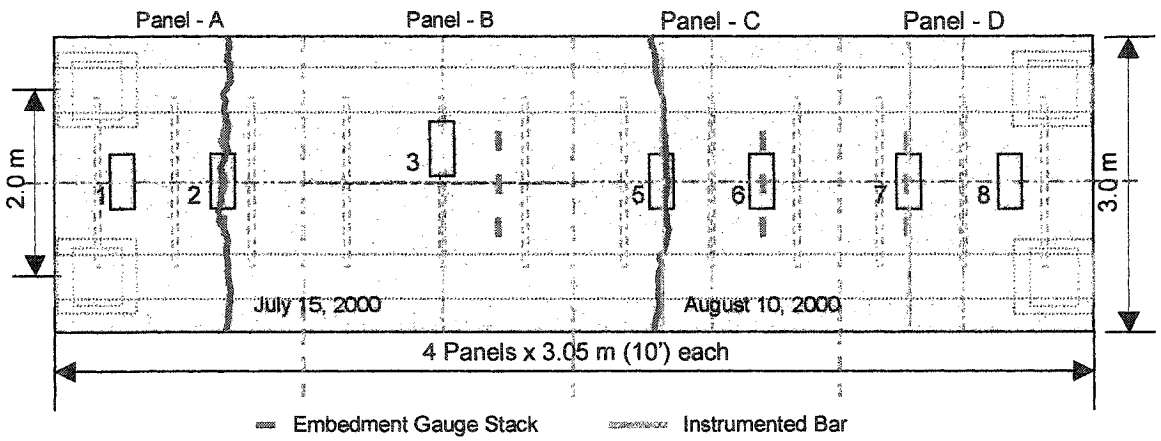

Figure 4-25 Transverse Cracks in Panels-A and C

4.2.9.2 Probable Causes of Transverse Cracks

Initiation of the transverse cracks in the test model can be attributed to a combination of the following factors:

- large drying-shrinkage strains,
- reduction of cross-section due to embedment gauges,
- under-compaction of concrete around embedment gauges.

4.2.9.2.1 Large Shrinkage Strains

One of the most obvious reasons of cracking in any concrete structure is the development of large shrinkage strains caused by drying shrinkage of concrete.

The drying shrinkage is the decrease in the volume of hardened concrete with time, which is caused by the evaporation of water from the concrete, and the hydration of cement. The shrinkage begins as soon as the moist curing of the concrete is discontinued. At this stage, the concrete is fully saturated. The migration of the water from concrete to the atmosphere is influenced by the relative humidity of the atmosphere surrounding the concrete. Initially, the increase in the shrinkage strains is very high. As the moisture in the concrete continues to decrease, the rate of increase of the shrinkage strains also declines and, at a later stage, there is no further increase in the shrinkage strains. The final value of shrinkage strain is termed as ultimate shrinkage strain (Neville, 1996).

The shrinkage strain at any time in the interim can be calculated by various methods specified by the codes. The Euro International Concrete Committee (CEB) has recommended one of the most detailed methods to calculate shrinkage strains. Factors affecting shrinkage such as specified compressive strength, type of cement, relative humidity of the surrounding, ratio of the area of cross-section to the exposed perimeter of the member etc. have been taken into account.

MacGregor and Bartlett (2000) also have adopted the Eurocode method for computing shrinkage strains. However they have recommended that computed shrinkage strains be increased by 20% to account for North American concretes.

The Canadian Precast Concrete Institute (CPCI) specifies a detailed procedure for calculating the shrinkage strain in concrete. However, it leads to a significantly higher value of shrinkage strain compared to the other methods. The charts for the computation of shrinkage strains in concrete by Reynold (1988) lead to a lower bound value.

The first transverse crack appeared 142 days after the deck concrete was poured. The second crack appeared in Panel-C after 159 days. The values of shrinkage strain computed by above-mentioned procedures are shown in Table 4.6. Detailed calculations for the shrinkage strains are given in Appendix-C.

Table 4-6 Shrinkage Strain in Concrete after 142 and 159 Days

Age (days)	Transverse Crack Location	Method			
		CEB	MacGregor & Bartlett	CPCI	Reynolds
142	Panel A under Load Pad-2	186×10^{-6}	223×10^{-6}	457×10^{-6}	170×10^{-6}
159	Panel C Under Load Pad-5	198×10^{-6}	235×10^{-6}	467×10^{-6}	

Although the value of shrinkage strain computed by various methods varies considerably, it is obvious that even the lowest value of shrinkage strain is sufficient to crack concrete. Under pure tensile loading, the tensile strain at peak stress is about 0.0001 (MacGregor and Bartlett 2000). Micro-cracking occurs in the vicinity of the highest stress, referred to as "fracture process zone", tensile capacity of the concrete decreases with the increase in elongation in the fracture process zone accompanied by unloading in the other parts of concrete.

4.2.9.2.2 Role of Fibers

In a conventionally designed deck slab, the resistance against shrinkage stresses in the transverse direction is provided by the longitudinal reinforcement. The isotropic reinforcement required by Cl. 8.18.4 -Empirical Design Method of CAN/CSA-S6-00 is expected to provide adequate resistance against large shrinkage stresses.

For steel-free deck slabs, which are referred to as FRC Deck Slabs, CAN/CSA-S6-00 Clause 16.7 permits the use of randomly distributed fibers to offer resistance against

shrinkage cracking. The shear connectors used to ensure monolithic action between the deck slab and the girders also resist the shrinkage stresses. Although, the test results for the fiber-reinforced concrete exceeded the requirements of the code, the cracking could not be prevented. However, one important factor that needs to be considered is the age of the concrete of the deck slab when the cracks appeared. Previously, in almost all the deck slab tests, the concrete was not left to dry for a prolonged period of time after casting and the tests were conducted soon after the concrete attained 28 days strength (Khanna 1999; Thorburn 1999; Bakht and Selvadurai 1997). Therefore, the occurrence of transverse cracks was not observed. Table 4.7 shows the shrinkage strains at 28 days.

Table 4-7 Shrinkage Strains in Concrete after 28 Days

Age - days	CEB	MacGregor & Bartlett	CPCI Method	Reynolds
28 days	72.2×10^{-6}	86.6×10^{-6}	335×10^{-6}	70×10^{-6}

4.2.9.2.3 Reduction in Cross-Section

The other mitigating factor was the presence of nine embedment strain gauges at the location of the transverse crack. Each strain gauge occupies 200 x 9 mm of the deck cross-section within the two main girders. The section is further reduced in this region due to signal cable attached to each gauge and passing on to one side of the slab. It is believed that the reduction of the concrete section due to the presence of stacked embedment gauges was the main reason for transverse cracks.

4.2.9.2.4 Under-Compaction of Concrete

During the concreting operation extra care was taken to protect the gauges against any damage due to concrete vibrator. A smaller size poker vibrator was used to compact the concrete in the vicinity of the embedment gauges while a larger vibrator was used to compact the concrete in the other areas of the slab. Thus a zone of relatively weaker concrete may have been created at each location of the embedment gauges.

4.3 Test Program

4.3.1 General

The testing program was carried out in two phases. In the first phase, each panel was subjected to an equal number of load cycles to compare their performance. In the second phase, three panels were tested to failure under cyclic load, while one panel was tested to failure under static loads. The entire program was conducted under slow speed cyclic loading. The testing in Phase I began on October 11, 2000, almost eight months after the deck slab was concreted. It is well known that the concrete compressive strength continues to increase beyond the age of 28 days. If the fatigue testing is carried out immediately after 28-day period, the results can be influenced by the continual gain in the concrete strength. Poorman (1966) recommends a six-month period before the commencement of the fatigue tests on concrete. As shown in Table 4.4, the average compressive strength of the concrete of the deck slab increased from 35 MPa to 48.6 MPa between 28 days and 220 days when the testing was commenced. However, between commencement of the testing program and its completion after 946 days, the compressive strength of concrete remained virtually unchanged at 48 MPa. Although the delay was unintended, it helped eliminate one major factor that could have influenced the fatigue test.

4.3.2 Test setup

It was decided to adopt a slow-speed loading regime using hydraulic jacks coupled to an electrically operated hydraulic pump, which was controlled manually. The pump was capable of producing hydraulic pressures of up to 69 MPa (10,000 psi). A review of available literature showed that the majority of the tests were either conducted under dynamic loading at frequencies over 0.1 Hz or under monotonic loading. The loading method that was adopted was unique in the sense that during each load cycle, the deck model underwent a complete cycle of displacement, followed by a complete recovery, before the next load cycle was applied. This was contrary to the high frequency loading under which the displacement of the deck slab is out of synch with the load application.

The slow speed loading provided an excellent opportunity to study the propagation of cracks as the test progressed. It is also more representative of field conditions.

As initially planned, each panel had two loading pads situated at 610 mm on either side of transverse centreline of the panel. However, as explained in sub-section 4.3.4.5, the position of load pad for Panel-B differed from the other three panels. The load pads, each measuring 710 x 305 x 50 mm thick, were placed over the deck slab. A smaller steel plate measuring 500 x 250 x 50 mm thick was placed on top of this load pad to reduce excessive bending of the load pad under high load levels. One 90-t hydraulic jack was placed over each pad. Each jack reacted against the girder of a loading frame. The loading frame comprised a heavy-duty compound girder bolted to two steel columns that were anchored to the strong floor of the testing lab. The loading frame is shown in Fig.4.26.

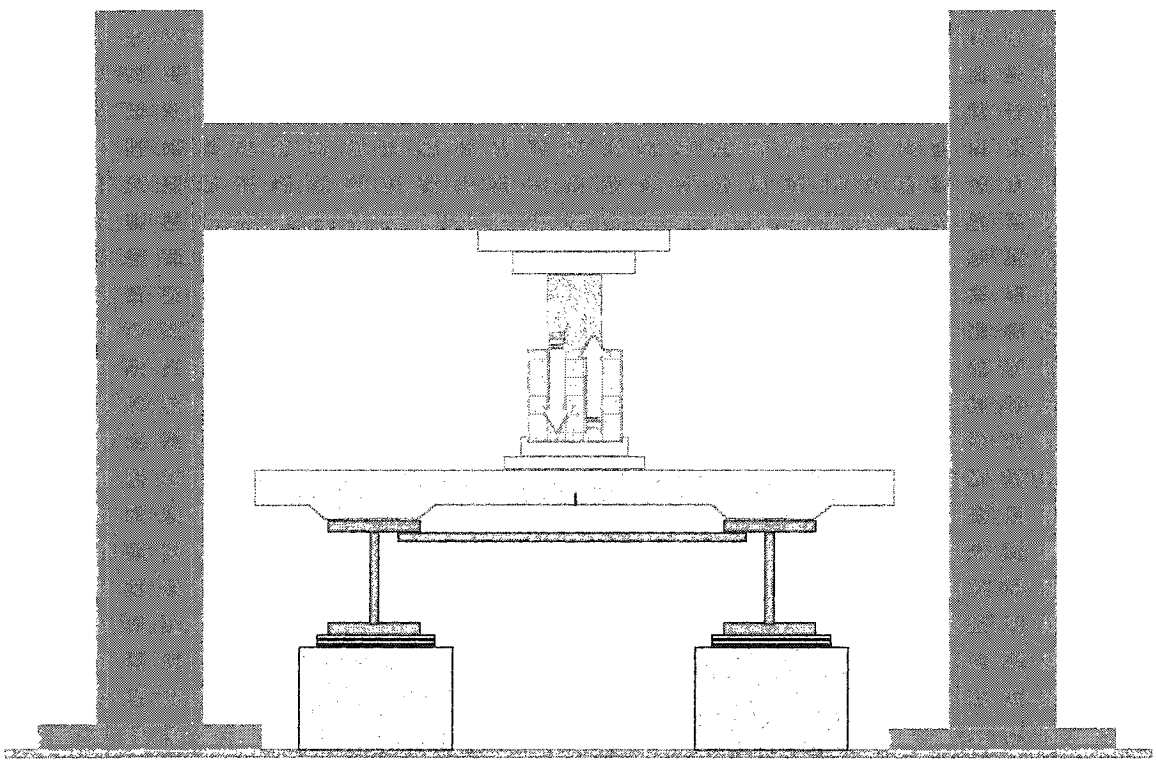

Figure 4-26 A View of Loading Setup

4.3.3 Testing Procedures

4.3.3.1 General

The testing of the experimental model commenced on October 11, 2000 and was concluded on June 27, 2002. The testing was conducted in two phases.

In the first phase, each panel was tested under cyclic loading with a nominal peak value of 400 kN, for the same number of load cycles.

In the second phase, Panels-A, C, and D were tested under cyclic loading until failure. The peak value of the cyclic load was varied in each panel according to its internal configuration. The peak value of the load at failure varied from 900 kN to 1100 kN. The testing procedure as originally planned required each of the four panels to be tested to failure under cyclic load with a peak value of 400 kN each. However, due to constraints placed by the loading apparatus the peak load was subsequently increased. Panel-B was tested under static loading conditions to calibrate the experimental model for punching strength.

The testing procedures in each phase of the testing are described in the following sections.

4.3.4 Testing - Phase-I

4.3.4.1 General

The testing of panels in the first phase of commenced on October 11, 2000 and continued until May 17, 2001. The panels were tested in the following sequence.

1. Panel A
2. Panel C
3. Panel D
4. Panel B

Two load pads were used to apply the cyclic loading on Panels A, C, and D. The load pads were placed along the longitudinal centreline of the model at 610 mm on either side of the transverse centreline of each panel. On Panel-B, only one load pad was used to apply the cyclic load. The load pad was placed along the transverse centreline of the panel mid-way between the pre-induced longitudinal crack and the inner edge of the North girder. The layout of the load pads is shown in Fig. 4.27.

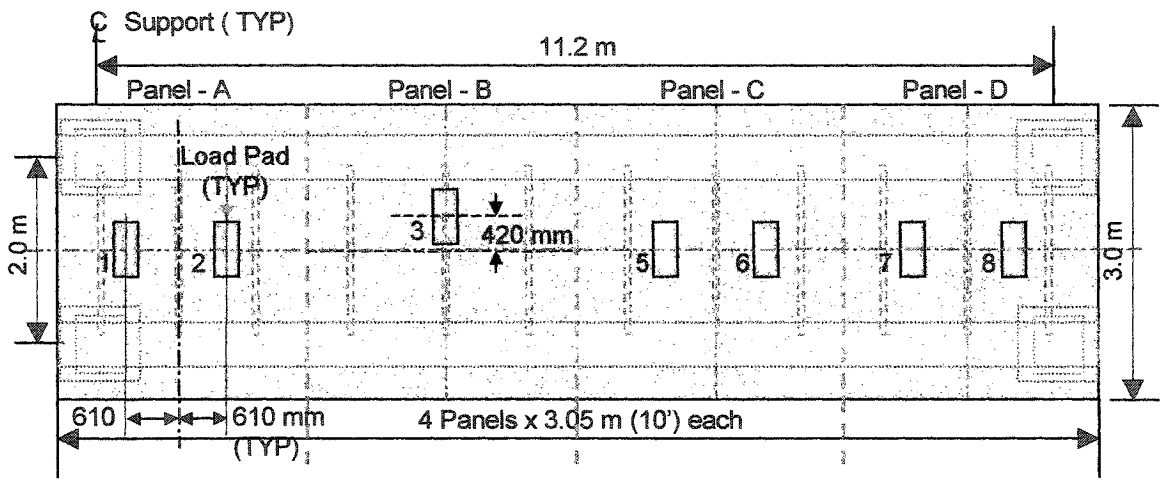

Figure 4-27 Layout of Load Pads for Phase-I

It was decided to apply a cyclic load with a peak value of about 400 kN. This value of the peak load corresponds to 40 percent of the theoretical static punching failure load. PUNCH Program (Mufti et al. 1997) was used for predicting the punching strength of the panel. As described in the procedures for the second phase, the predicted failure load was found to be too conservative. This necessitated re-evaluation of the magnitude of the available transverse confinement and recalculation of the punching strength.

4.3.4.1.1 Loading Procedure

Tests conducted by Mufti et al. (2001) showed that the cyclic load applied at only one location did not cause the soffit cracks in the vicinity of the load to propagate to the top surface of the slab. A moving load on the other hand, induced full-depth cracks (Matsui

et al. 2001). For each panel, the cyclic load was to be applied through two load pads with the intention of creating a kneading effect on the panel. It was expected that alternating load positions between the two pads would cause the longitudinal crack to extend from one load pad to another and then propagate to the top surface of the deck slab. Ideally, the loading position should have been alternated after each cycle, however, for practical reasons the loading position was alternated after every 100 load cycles. This also afforded the opportunity to inspect the panel under test and survey the crack patterns after each 100 load cycles. Figure 4.28 shows the typical loading sequence for a panel. The testing of each panel is described in sub-sections 4.3.4.2 to 4.3.4.5.

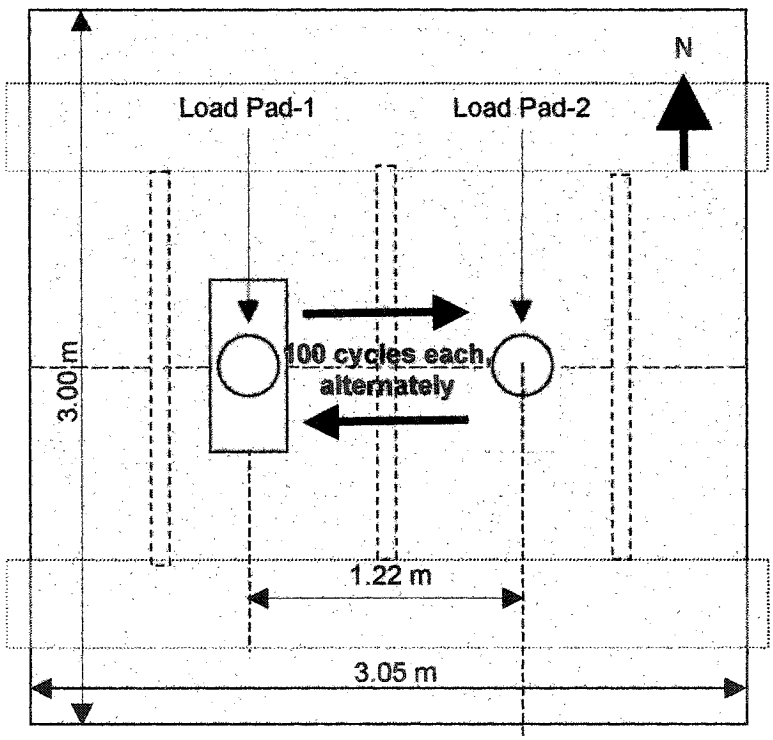

Figure 4-28 Typical Loading Sequence of Panels-A, C, and D

4.3.4.2 Panel-A

The testing of Panel-A commenced with identifying and mapping of all visible cracks on the top and the bottom surfaces of the Panels A, B, C and D. As described in sub-

section 4.2.10, well before the commencement of the testing, a full-depth transverse crack had appeared in Panel-A running approximately along the transverse centreline of the second load pad. The crack patterns are shown and discussed in Chapters 5 and 6.

After ten load cycles on Load Pad-1, it was observed that a longitudinal crack had developed on the underside of Panel-A starting from the junction with panel-B and extending up to the centre of Load Pad-1. This crack bifurcated into a Y-shaped crack in the direction of, and extending into, the edge beam. At this stage, the cracks were measured and mapped. The loading was recommenced and a total of 100 load cycles were applied on Load Pad-1. Representative crack patterns are shown in Section 5. A detailed discussion of crack patterns follows in Section 6.

The loading set up was adjusted and 100 load cycles were applied on Load Pad-2. The loading of the panel was continued by alternately applying 100 load cycles, on Load Pads 1 and 2. After completion of each 100 load cycles, the top and the bottom surfaces of the panel were inspected for visible cracks and any other sign of deterioration. The cracks were measured and mapped. The loading of the panel was continued until the longitudinal crack that had appeared within the first ten load cycles on the soffit of the panel extended up to the top surface of the panel between the two load pads on the panel. At this stage, a total of 1,700 load cycles were applied on Panel-A with 900 cycles on Load Pad-1 and 800 cycles on Load Pad-2. The first phase of the testing of panel-A was considered completed at this stage.

As originally planned, Panel-B was to be tested next. However, it was found that during testing of Panel-A, a longitudinal crack developed on the top surface of Panel-B. This crack extended from the centre of the panel up to its junction with Panel-A. It may be recalled that a 75 mm high longitudinal crack trainer was provided in Panel-B, which reduced the overall thickness of the deck slab at the centre from 175 mm to 100 mm. This was the likely cause of this premature appearance of the crack. It was therefore decided to move the test set-up to Panel-C.

4.3.4.3 Panel-C

Shortly after the transverse crack described in the foregoing section had appeared in Panel-A, a similar transverse crack of smaller width also appeared in Panel-C. Interestingly, this crack was also located approximately in the vicinity of the transverse centreline of Load Pad-5 where an instrumented transverse reinforcing bar was located. Another transverse crack extending over only over a part of the width of the panel appeared along the centreline of Load Pad-6.

Before commencing the testing of Panel-C the top and the bottom surfaces were inspected and all the existing cracks mapped.

Panel-C was subjected to 1,700 load cycles with 900 and 800 load cycles being applied on Load Pad-5 and Load Pad-6 respectively. It noted that after completing 1,000 load cycles, the loading set up was modified by installing a by-pass valve in the hydraulic line to permit faster unloading. This increased the overall pace of the testing considerably.

Crack patterns for the top and the bottom surface of the panel were mapped after first 20 and 100 load cycles and then after every 100 load cycles until the end of the test.

At the completion of 1,700 load cycles on Panel-C, the longitudinal crack in the soffit did not extend to the top surface of the panel, thus indicating the effectiveness of crack control mesh.

4.3.4.4 Panel-D

The test set-up was moved to Panel-D. The loading jacks were positioned on Load Pad-7 and Load Pad-8. First 100 load cycles were applied on Load Pad-7.

A grid of very fine cracks had formed on the bottom surface of the panel in the vicinity of the load pad within first 20 cycles. The cracks had formed under the bottom layer of the crack control reinforcement. The main longitudinal crack, however, which had formed in Panel-A and Panel-C within first ten load cycles and which is typically formed in a steel-

free deck slab, had not appeared. The next 100 load cycles were applied on Load Pad-8. After the application of first 20 load cycles on Load Pad-8, a Y-shaped crack, starting from one of the finer longitudinal cracks under Load Pad-8 and extending up to the edge beam, had appeared on the bottom surface of the panel. It is noted that this crack appeared only when the load was applied on pad 8, which was in close proximity of the edge beam. In Panel-A, Load Pad-1 was also closer to the edge beam and the Y-shaped crack had appeared within the first ten load cycles.

1,700 load cycles were applied on panel-D with 900 and 800 load cycles being applied on Load Pad-7 and Load Pad-8, respectively. At the completion of test, there was no single predominant longitudinal crack that was wider than the other longitudinal cracks. The overall width of cracks was significantly less than that of cracks in Panel-A, and none of the cracks in the soffit extended up to the top surface of the deck slab.

4.3.4.5 Panel-B

After the completion of the testing of Panel-D, the loading set-up was moved over Panel-B. The pre-induced longitudinal crack had propagated to the top surface of the panel. The crack at the top extended from the border of Panel-A up to the transverse centreline of Panel-B. It was realized that the pre-existing full depth longitudinal crack in Panel-B provided with a unique opportunity to study the behaviour of a panel with full-depth crack under asymmetric loading conditions. It was therefore decided to apply load at only one load pad that would be placed on one side of the longitudinal crack. This load pad was designated as Load Pad-3 (Figure 4.27). The aim of this testing was to study the fatigue resistance of the crack zone under cyclic loading. As discussed in 4.1.14.6, two DTs were placed to study the relative movement of two segments of the panel separated by the longitudinal crack. One DT each was placed across the longitudinal crack at the top and the bottom surface of the panel to measure the opening and the closing of the longitudinal crack under the applied cyclic loading. Further details are provided in Section 4.3.4.5.1.

4.3.4.5.1 Panel-B - Crack Displacements

It may be recalled here that Load Pad-3 was placed midway between the inner edge of the flange of the North girder, and the crack trainer. Beginning with the 800th cycle, the full-depth longitudinal crack that extended from the edge of Panel-A to the load pad was instrumented to monitor the relative horizontal and the vertical movement of the two segments of the panel. The details of the top and the bottom instrumentation are shown in Figure 4.29 and Figure 4.30 respectively. The longitudinal crack is highlighted for clarity.

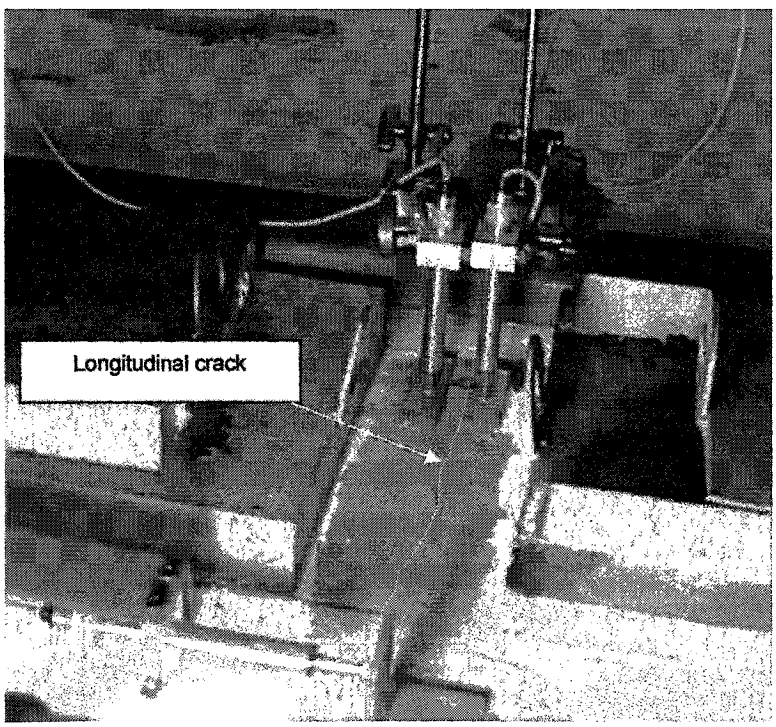

Figure 4-29 View Displacement Transducers Across Longitudinal Crack at Top

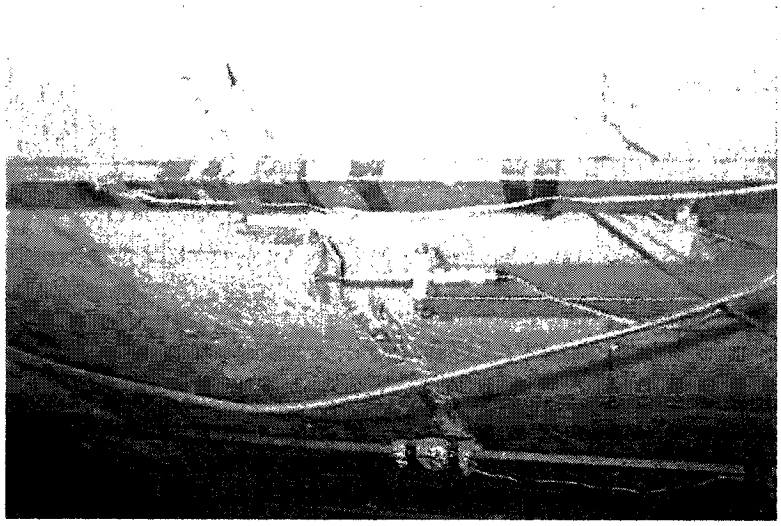

Figure 4-30 View of Displacement Transducer Across Longitudinal Crack on Soffit

4.3.4.5.2 Vertical Movement along Crack

One DT was installed above each segment as close to the crack as possible. The sensor recorded the displacement of the segment. The initial values of the displacement recorded by each sensor were compared. The segment on the North side was the loaded segment. Had there been a relative movement of the two segments with respect to each other under load, one of the sensors would have recorded a higher value of displacement, while the other sensor mounted on the opposite segment would have recorded a lower value of displacement. The displacement trends are shown in Figure 4.31.

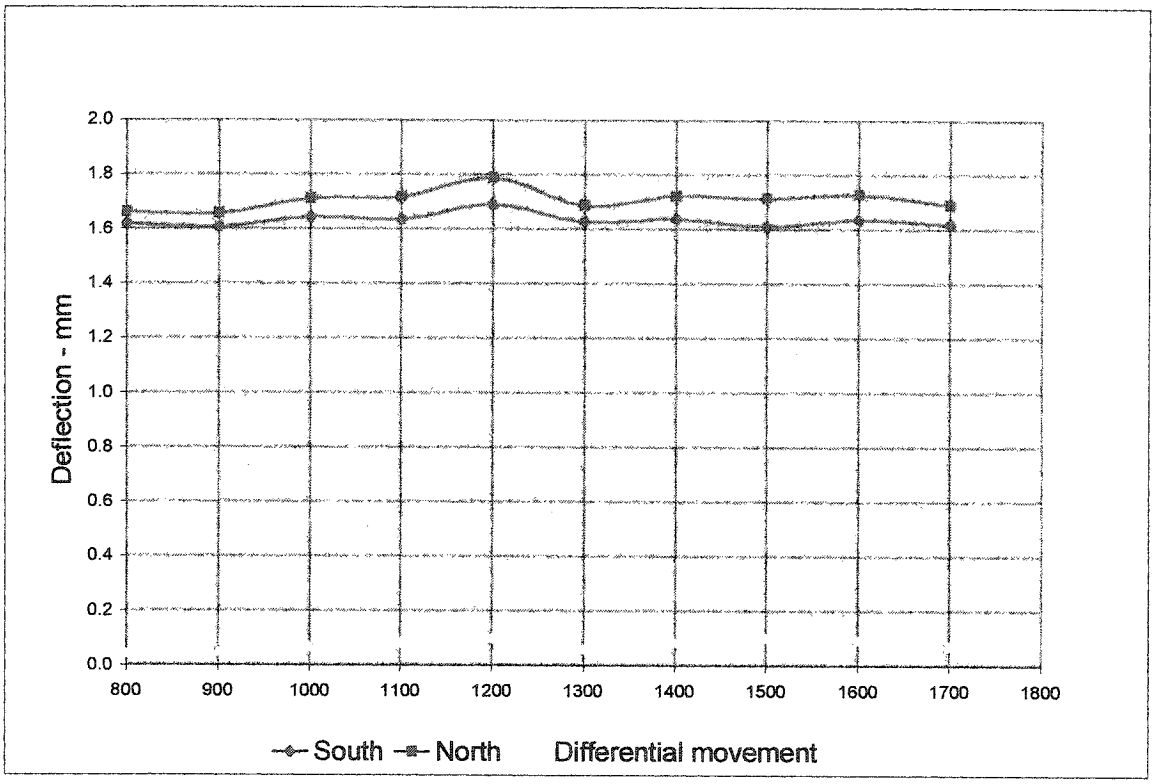

Figure 4-31 Panel-B: Deflection Trends of Panel Segments Under Load

The initial difference in the displacements recorded by the two sensors was 0.04 mm. This difference was taken as the base value, and was deducted from the differences calculated after each 100 load cycles to calculate the relative difference. Starting with the initial relative difference of zero at the 800th cycle, the relative difference increased to 0.06 mm at the 1,200th cycle. The value dropped to 0.02 mm at the 1,300th cycle and increased to 0.06 mm after 1,500 load cycles and then gradually reduced to 0.03 mm during the 1,700th load cycle. The relative displacement trend from 800 to 1,700 load cycles is shown in Figure 4.32.

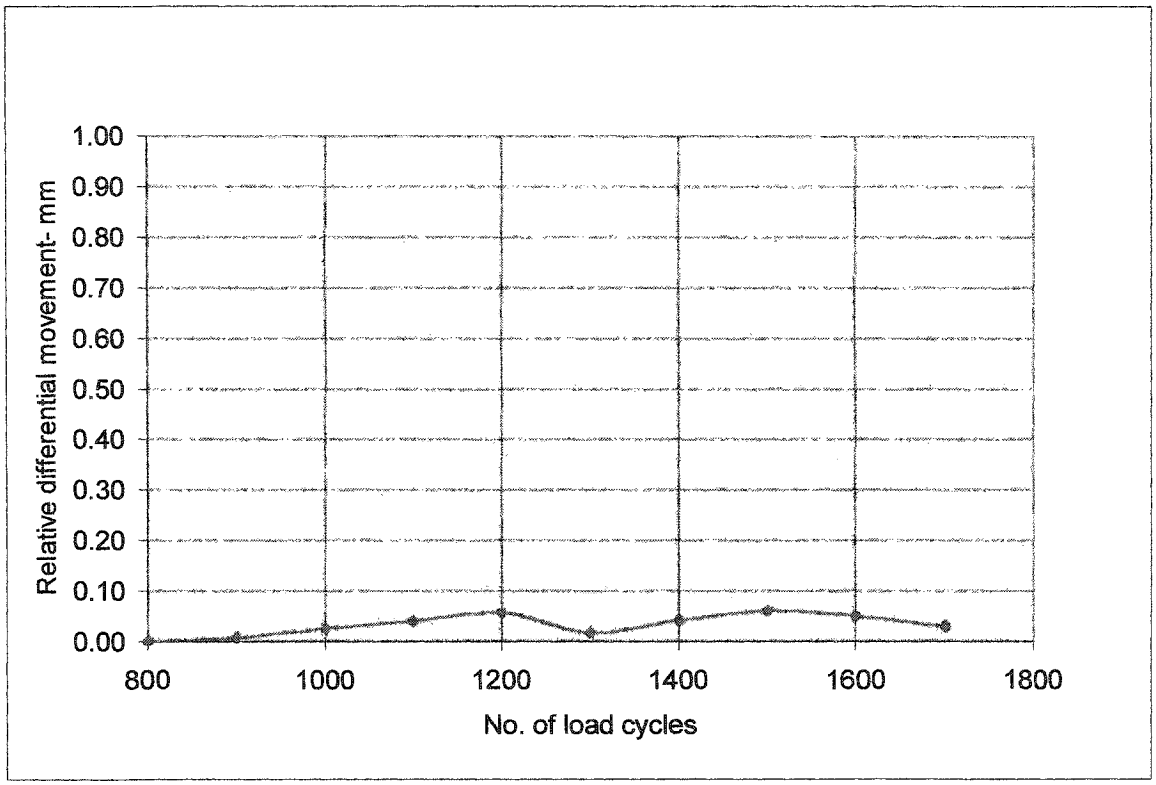

Figure 4-32 Variation in Relative Differential Displacement Across Longitudinal Crack under Load of 393 kN

The values of the relative difference are extremely small and under a load of 393 kN, which is significantly higher than even the factored wheel load at the ultimate limit state. It can therefore be concluded that vertical displacement between the two segments of the panel between 800 and 1,700 load cycles was negligible.

4.3.4.5.3 Horizontal Displacement – Opening and Closing of Longitudinal Crack

One DT was placed at the top and the bottom of the deck slab. Each DT was anchored at a point located on transverse centre line of the load pad, and monitored the displacement of a point on the opposing segment located on the edge of the crack. Under load, the longitudinal crack tended to close at the top and open at the bottom. By comparing the displacements recorded by the top and the bottom transducer, the depth of the compression zone can be estimated. Initially, the application of the load caused the crack to close completely. Any further displacement recorded at the top would indicate the compression of concrete. It can be seen from Figure 4.33 that there was a marginal increase in the opening of the crack at the bottom, while the movement at the top remained almost unchanged between 800 and 1,700 load cycles.

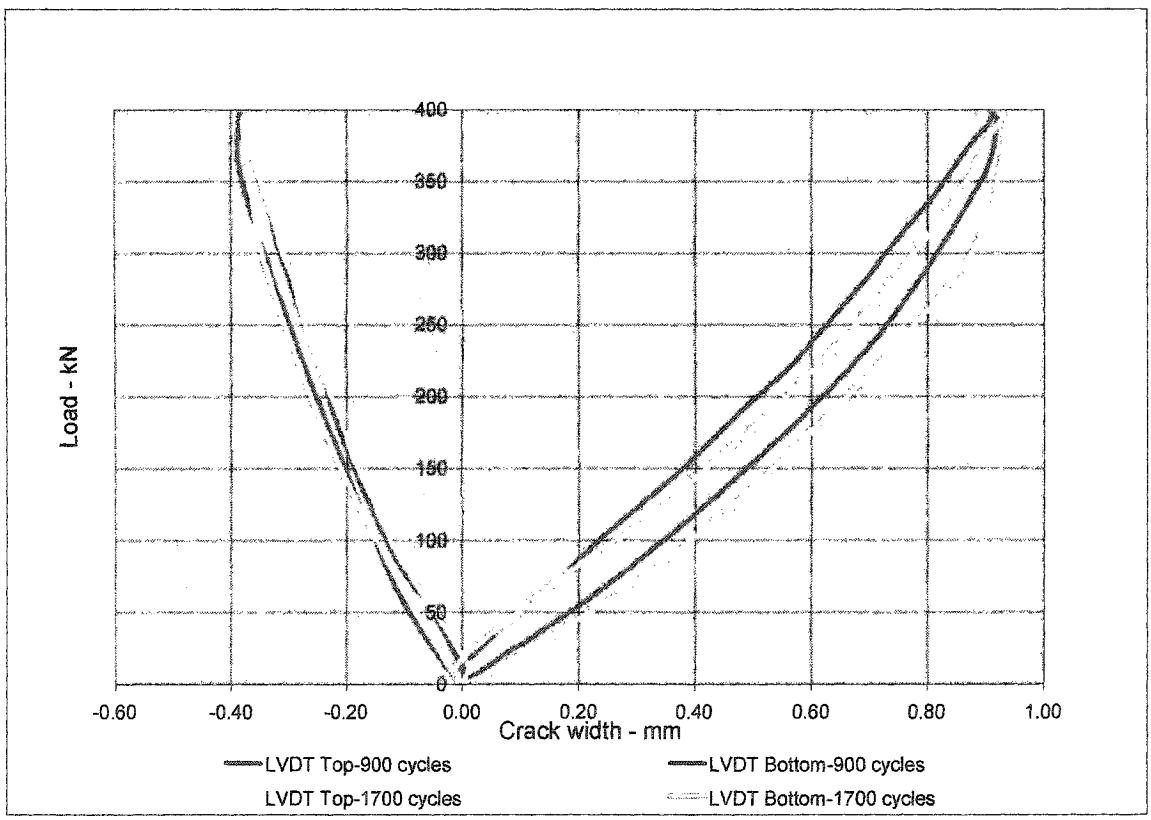

Figure 4-33 Displacements at Longitudinal Crack at Top And Bottom

Between 800 and 900 cycles, the compressive movement across of the crack increased from 0.35 to 0.39 mm, which is an increase of over 10%. From 900 cycles until the end of 1,700 load cycles, the displacement varied between 0.38 to 0.39 mm. The trends for the displacement patterns are shown in Figure 4.34.

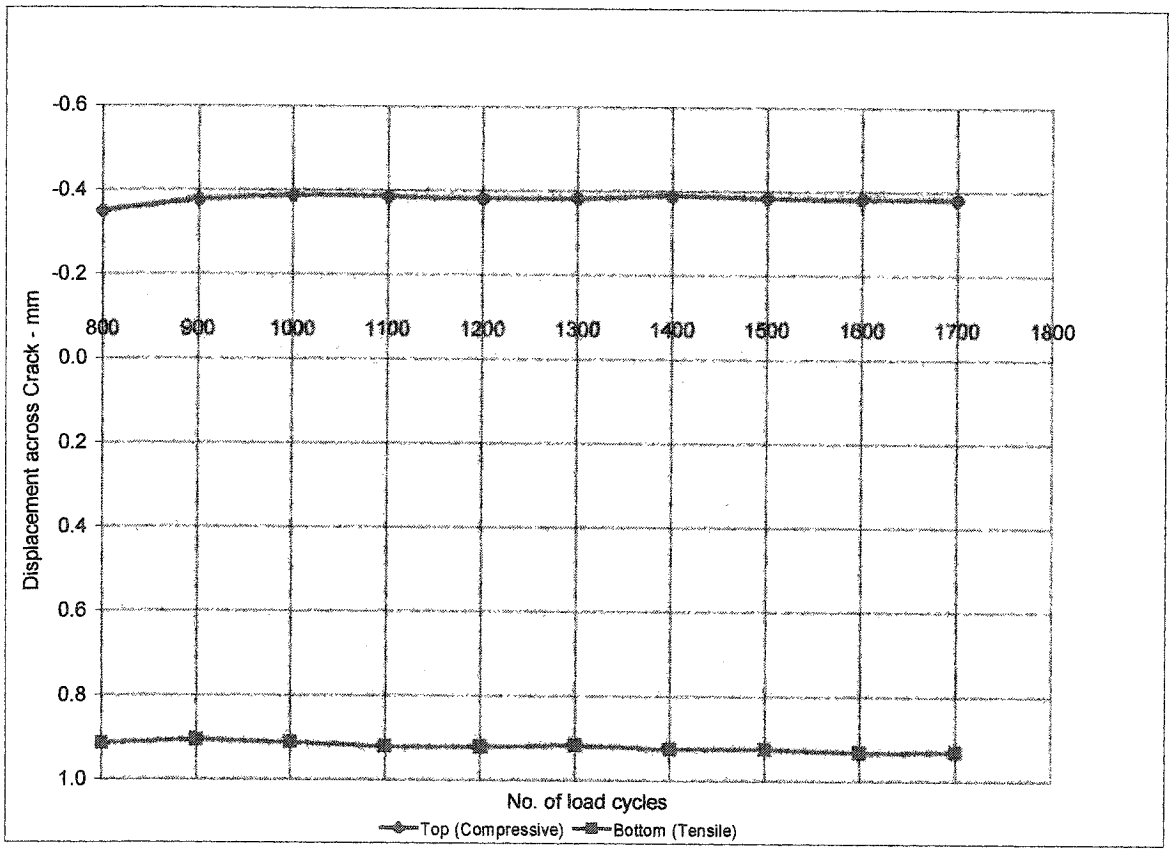

Figure 4-34 Panel-B: Displacement Patterns at Longitudinal Crack

4.3.4.5.4 Compressive Stress at Crack Interface

The recorded displacement at the bottom after 800 cycles was 0.91 mm. The displacement increased to 0.92 mm after 1,300 cycles and then gradually increased to 0.93 mm, after 1,700 cycles. Along the length of the longitudinal crack, out of a total slab thickness of 175 mm, the concrete in the lower 75 mm was separated by the crack trainer leaving a net concrete thickness of 100 mm. The DTs were mounted at 42.5 mm

and 50 mm from the top surface and the bottom surface of the slab, respectively. As the anchor point of the LVDT was on the transverse centre line of the pad, the recorded compressive displacement also included the elastic deformation of concrete between the anchoring point and the longitudinal crack. The elastic deformation can be estimated using the test data. To maintain the equilibrium of forces in the horizontal direction, the tensile forces developed in the straps would balance the compressive force developed in the deck slab along the longitudinal crack. Using the strain values for the three straps in Panel-B, the magnitude of the force for the central 1000-mm concrete section can be calculated. The weighted-average of the strains (1 x Strap-4, 2 x Strap-5, and 1 x Strap-6) in the three straps is 386 $\mu\varepsilon$. Using the cross-sectional area of the strap as 800 mm^2, and the modulus of elasticity of the steel as 200 GPa, this strain corresponds to a force of 61,760 N/1,000 mm length of the deck slab along the longitudinal crack. Further, it can be assumed that only $1/3^{rd}$ of the available 100 mm depth of the deck slab above the crack trainer would be in compression. The average compressive stress in concrete would be 1.85 MPa. Using E_{Conc} = 27,120 MPa, the elastic strain, $\varepsilon_{elastic}$, in concrete is 68.3 $\mu\varepsilon$, and the elastic shortening, $\delta_{elastic}$, of the 420 mm length of the slab, the distance between the anchoring point and the longitudinal crack, would be 0.03 mm. The net crack movement can be calculated by deducting this value from the recorded crack displacements.

Figure 4.35 shows the net crack displacements at 800, 900, 1,300 and 1,700 load cycles. There is an increase in the top displacement between 800 and 900 load cycles. The response is steady from 900 cycles to 1,700 load cycles.

The crack displacements at bottom had a different pattern. The crack opening decreased slightly from 800 to 900 cycles. This was followed by an increase up to 1,200 cycles. From 1,200 cycles to 1,700 load cycles the displacements increased gradually from 0.89 mm to 0.91 mm.

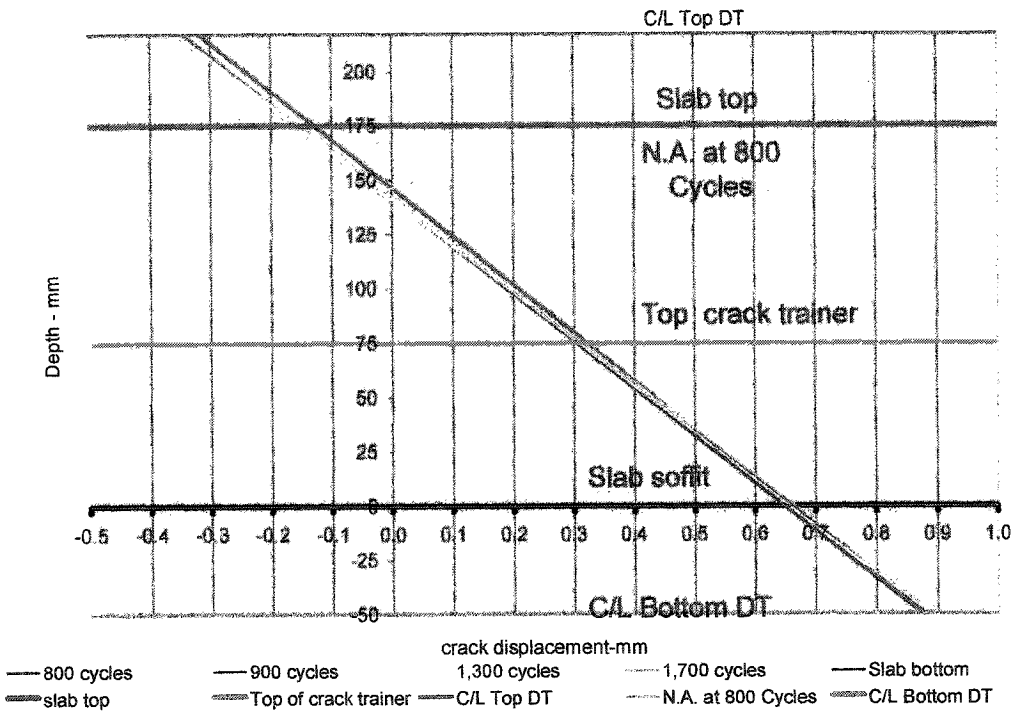

Figure 4-35 Panel-B: Longitudinal Crack Displacements Under Load

The compressive strength of the concrete varied between 43 to 48 MPa while the average compressive stress in concrete along the longitudinal crack at the peak load was 1.85 MPa. Considering a case of linear variation in the stress in concrete the maximum stress will be 3.7 MPa. Thus the stress range is 0 to 0.086 f'_c at 392.4 kN peak load.

The above values are based on the weighted average of strain in three straps. The peak value of the recorded strain in strap directly under load was 504 $\mu\varepsilon$. Considering this value would result in an average compressive stress of 2.42 MPa, a maximum stress of 4.84 MPa, would correspond to a stress range of 0 to 0.11 f'_c. Ople and Hulsbos (1966) concluded that the stress gradient had a significant positive effect on the fatigue strength of concrete.

From the above discussion it can be concluded that asymmetric loading conditions did not affect the performance of Panel-B with a full depth longitudinal crack.

There were concerns about a possible grinding action between the two segments of the panel under asymmetric cyclic loading. However, no significant differential movement of the two segments was observed during Phase-I of the test. As in the case of other panels, test on Panel-B was terminated after 1,700 load cycles at 392.4 kN peak load. It is therefore recommended that similar tests be carried out until failure.

The stress range for the compressive fatigue loading across the crack was well below the maximum recommended value of 0.4. The recommended value is for concrete in uniaxial compression. Around the crack interface, the concrete is in triaxial compression, which would result in even better fatigue performance. Therefore, the possibility of failure due to fatigue by loading on one side of a full-depth crack is not likely.

4.3.5 Testing - Phase II

4.3.5.1 General

Phase-2 of the testing was commenced in May 2001 and completed by June 2002. This comprised of testing of Panels A, C and D under cyclic loading until failure. Panel-B was tested under monotonically increasing load to failure. In each panel, the load was applied at one load pad throughout the test. The layout of the load pads is shown in Figure 4.36.

The testing was conducted in the following sequence:

1. Panel A – Cyclic loading
2. Panel D - Cyclic loading
3. Panel B – Static loading
4. Panel C - Cyclic loading

The testing procedure is discussed in Sections 4.3.6.2 through 4.3.6.5.

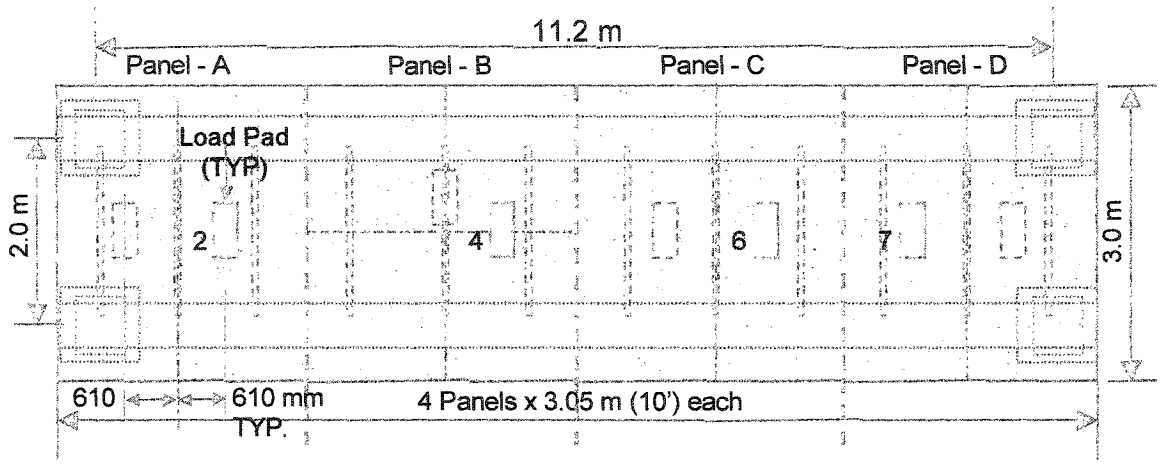

Figure 4-36 Location of Load Pads-Phase-II

4.3.5.2 Panel-A

Testing of Panel-A was commenced on May 31, 2001. The nominal load level of 393 kN (40 t), as in case of Phase-I, was maintained. Initially it was estimated that the failure of the panel would occur at about 13,000 load cycles, however, after 13,000 load cycles the response of the deck was linear under load and various strap strains were well below the yield strains. Recalculation showed that the number of load cycles required to initiate the failure of the panel, at the current load level of 393 kN, exceeded several million cycles. The testing at the same load level was however continued. The response of deck was continuously monitored throughout the test. After application of 50,000 cycles, the peak load level was raised to 635 kN (65 tons) and 10,000 load cycles were applied at this load level. The peak load value was further raised to 785 kN (80 tons) and 2,000 load cycles were applied. Finally, the peak load level was raised to 883 kN (90 t), which was estimated to be about 90% of the static failure load. The testing continued until Panel-A failed in punching shear after 1,243 load cycles.

4.3.5.3 Panel-D

After the failure of Panel-A, the testing set-up was moved over to Load Pad-7 on Panel-D. In addition to the external straps this panel was provided with a layer of steel crack control grid. The transverse reinforcing bars increased the axial stiffness of the transverse confinement system, and consequently the punching strength of the deck slab. The static punching strength of the slab was estimated to be about 1,450 kN. It was therefore decided to commence the test with a peak load level of 883 kN (90 tons). The testing was commenced on April 11, 2002, and 5,000 load cycles were applied without any sign of failure. The peak load was increased to 981 kN (100 tons) and 41 load cycles were applied. The load was again raised to 1,030 kN (105 tons) and 55 load cycles were applied. The peak load was once again raised to 1,079 kN (110 tons). The panel failed after 108 cycles.

4.3.5.4 Panel-B

After the completion of fatigue tests of Panel-D and before commencing of the fatigue test of Panel-C, Panel-B was subjected to static failure test to compare the static failure load that was computed analytically. The load was applied on load Pad-4 as shown in Figure 4.36. The position of this load pad was similar to the position of load pads in the other panels. However, it is noted that during the first phase of testing of Panel-B the load was applied at Load Pad-3.

The load was applied at the load pad through two hydraulic jacks placed in parallel. In the first cycle the panel was loaded up to 400 kN and then the load was released. During the next three load cycles the peak value of the load was increased by 200 kN after each load cycle, and released until a peak load value of 1,000 kN was reached. The panel did not show any signs of failure. In the final load cycle; the load was increased gradually until the failure occurred in punching shear at 1,218 kN.

During the entire duration of the test, acoustic data generated by the damage occurring in concrete was collected by the system. Further, to monitor the changes in the acoustic attenuation characteristics of the deck slab until failure, acoustic signals were also

generated by the external source at regular intervals and recorded. However, during the final load cycle, the external signal could not be generated due to safety concerns, as it would have required the operator to stand very close to the deck slab panel. The strain levels in all of the 12 straps were monitored during this test.

4.3.5.5 Panel-C

Panel-C was tested last. Extensive damage was caused to Panel-C during the failure of Panels B and D. The cyclic load could only be applied at Pad-6, the slab under which was relatively free of damage. The peak value of the cyclic load was 883 kN (90 t). As the loading was commenced it became evident that the time required to apply one load cycle was considerably longer than that was required for Panel-A and Panel-D. This resulted in very large data files for each 100 load cycles. The testing was temporarily discontinued and the problem was investigated. It was found that the stiffness of the cross-beam of the load frame was not adequate. A trial test showed that applied load caused the cross beam to deflect upward considerably before causing any noticeable deflection of the model. As well, the failure of Panel-B had resulted in a reduction in the overall stiffness of the model. The load frame was replaced with another frame that had a stiffer cross-beam. Also, one intermediate support was provided under each girder to reduce the effective span of the model. The supports were positioned at such locations that there was no significant uplift of the girders at far ends.

The testing was resumed thereafter. After the application of 300 load cycles, cracking was noticed around the load pad. The panel failed in punching shear after 304 load cycles at 887 kN peak load.

4.3.6 Post Failure Acoustic Survey

To assess the effectiveness of the acoustic attenuation technique in detecting severe damage in concrete, an acoustic survey of the entire deck slab was carried out. As discussed earlier, the top surface of the deck slab was whitewashed for easy identification of the cracks. The entire surface was divided into small squares with each square measuring 305 x 305 mm, starting from the center of the model. The grid system

helped to map the cracks accurately. The same grid pattern was used to position the acoustic sensors.

4.3.6.1 Acoustic System

The system for the survey comprised a mechanical sound source, two acoustic sensors, a PC based acoustic signal digitizing and recording system and custom data processing software. Steel strike plates, measuring 75 x 75 mm were bonded to the sides of the deck slab at mid-depth using quick setting epoxy. A ball-peen hammer was used to strike the steel plates to generate the acoustic signal. The location of the sensor was at the junction of two orthogonal gridlines. The top surface of the slab was scraped and the sensors were mounted using vacuum grease as an acoustic couplant.

4.3.6.2 Survey Procedure

The acoustic survey was conducted along each transverse gridline with the readings taken at the junction of each longitudinal line. The first survey line was located at 305 mm from the transverse edge of Panel-D. The survey procedure is given below.

1) One acoustic sensor (the reference sensor) was positioned at 305 mm from the edge of the panel.
2) The second sensor (the active sensor) was initially positioned by the side of the sensor.
3) The hammer source was struck on the steel plate, and the system recorded the same waveform as it propagated past the reference and the active sensors. Multiple hammer strikes were made and the acquired signals averaged during data processing.
4) The active sensor was moved to a new position 305 mm away and Step 3) was repeated.
5) Step 4) was repeated until the active sensor was positioned in its final location at the longitudinal centerline of the deck slab.

Steps 1) through 5) were then repeated for the next transverse gridline. After the survey was completed along one side of the deck slab the procedure was repeated on the other

side of the deck with the final position of the active sensor ending at the longitudinal centerline of the deck. A schematic view of the sensor positioning is shown in Figure 4.37.

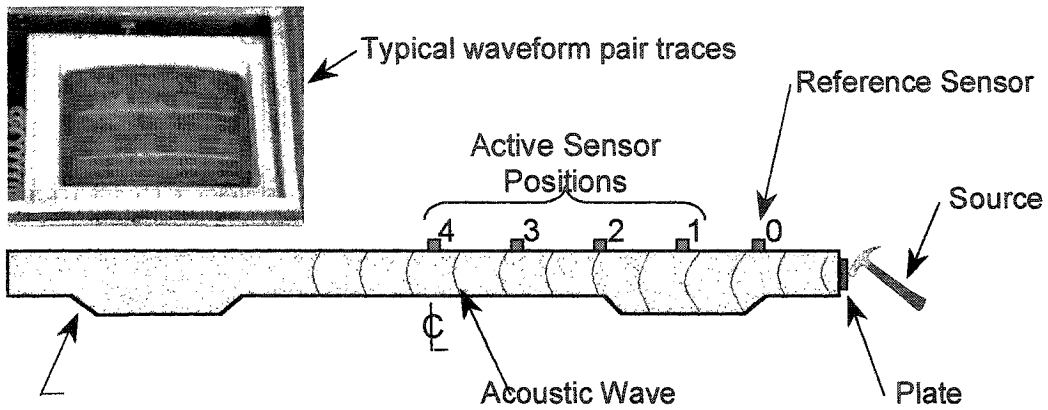

Figure 4-37 A Schematic View of Acoustic Survey Set-Up on the Cross-Section of Deck Slab

4.3.7 Recording and Processing of Data

The test data from the main data acquisition system were recorded in text format. The test data were recorded for each and every load cycle applied during the entire testing program. Only one data file, covering twenty load cycles applied during Phase-I, was lost due to a loss of power to the computer.

The text files were later reviewed and converted to specially formatted excel files. Each file showed the relevant details of the test such as the date of the test, the range of load cycles applied, load pad identification number, position of each displacement transducer and strain gauge, and any other comment that was deemed necessary to be included.

The data from the fiber optic sensor that was placed on the middle strap in each panel were acquired and recorded on a separate computer. The data were processed separately and were used to compare the strain values obtained through the main data acquisition system.

The details of the acoustic attenuation system recording and processing have been provided separately.

4.3.8 Statistics of Loading

The load control was manually operated. To asses the effectiveness of load control, peak load values of 20 consecutive load cycles after 100, 900, and 1,700 load cycles in Phase-I were analyzed statistically. The statistical results are shown in Table 4.8.

Table 4-8 Statistical Details of Loading

	Peak Load		
	Mean (kN)	Standard Deviation (kN)	Coefficient of Variance
Panel-A	397.0	4.83	0.0122
Panel-C	395.5	2.28	0.0058
Panel-D	397.7	3.86	0.0097
Panel-B	395.4	2.24	0.0056
All Panels	396.5	3.80	0.0096

5.0 TEST RESULTS

5.1 General

The testing of the experimental model was carried out in two phases. Each phase was planned to examine one of the two specific performance requirements:

Phase-I - Comparative performance,

Phase-II – Fatigue life and comparative performance.

5.2 Presentation of Test Results

A summary of the test results for Phase-I and Phase-II of the testing are presented in Sections 5.3 and 5.4, respectively. The detailed test results are presented and discussed in Chapter 6. Therefore, the results presented in this section are representative in nature, to avoid duplication. They however, provide the reader an overview of the outcome of the experimental work.

5.3 Results - Phase-I – Comparative Performance

5.3.1 General

In order to compare the performance of all the panels, Panel-A (the Control) was tested first under cyclic loading. As expected, the panel developed a longitudinal crack on the soffit within the first 10 load cycles. The loading continued until the longitudinal crack grew and gradually propagated upwards through the thickness of the slab and was visible to the naked eye on the top surface. The crack was first noticed on the top surface after 1,700 load cycles. The Phase-I testing of Panel-A was discontinued at this stage. Thereafter, the remaining three panels were also subjected to the same number of load cycles. The load positions for Panel-C and Panel-D were identical to the load positions for Panel-A. Panel-B was tested at one asymmetric load position for the reasons that have been discussed elsewhere in this document.

The response from internal and external sensors was complimented by the results from acoustic attenuation and visual observations in the form of crack surveys, which were carried at regular intervals. The test results have been divided into three separate categories; a) response of conventional instrumentation, b) acoustic attenuation, and c) visual observations. Each of the three sets of results has been discussed in sub-sections 5.3.1.1, 5.3.1.2, and 5.3.1.3.

5.3.1.1 Conventional Instrumentation

Data were acquired for all the load cycles during the testing and were analyzed at regular intervals and reviewed. The data are presented in two formats.

- Load versus sensor response
- Sensor response versus number of load cycles applied

In the first format, various instrument responses have been plotted against the applied load. Each chart shows the response of one particular sensor at three different stages during the test. This provides an overview of the change that occurred during the test. For example, a change in the slope of load-deflection curves for a panel at three different stages would represent a change in the stiffness of the panel.

In the second format, the response of each sensor has been plotted against the total number of load cycles completed. Such diagrams show the trends in the change of response as the testing proceeded. Any abnormal increase or decrease would indicate some unusual changes in the structural behavior. For each panel, the response of various sensors was examined at the first, tenth, and at intervals of 100 load cycles thereafter, until the conclusion of the test on that particular panel. The cyclic load was controlled manually and therefore the exact magnitude of the applied load varied from cycle to cycle. The statistical details have been provided in Section 4. In order to make a rational and correct comparison of various responses, the nominal peak load value of 393 kN, corresponding to 40-t, was adopted as the peak load for comparison. All instrument responses corresponding to 393 kN load were calculated. The sensor responses that were recorded are shown in Table 5.1.

Table 5-1 Instrumentation for Phase-I

Deflection under load pad/s	All Panels
Deflection under girder/s	All Panels
Crack Displacement - (Horizontal and Vertical)	Panel-B
Differential Displacement across longitudinal crack	Panel-B
Strap strains	All Panels
Strains in instrumented reinforcing bar	Panel-C and Panel-D
Strains in concrete embedment gauges	All Panels
Strains in central strap (Fiber-optic sensor)	All Panels

The patterns of sensor response over the entire duration of the test were plotted for each functioning sensor except the fiber-optic sensor.

Representative load-deflection and load-strain curves for each panel are shown in the following section. The values of the deflection and strains for the entire duration of the test are shown and discussed in Chapter 6.

5.3.1.2 Acoustic Attenuation

The acoustic attenuation results show the acoustic parameters that were compared during the test. The data presented here are the waveforms for the artificially generated signals at recorded regular intervals. The waveform patterns changed as the testing proceeded. The strength of the signal diminishes as the medium through which the acoustic signal propagates deteriorates under repeated loading. An increase in the differential arrival time, which represents a reduction in the velocity of the signal wave, indicates an increase in damage within the concrete slab. Representative waveforms, recorded during the test are shown for each panel.

5.3.1.3 Crack Patterns

The top and the bottom surfaces of the panel under test were inspected a) before the commencement of the test, b) after 10 load cycles, and c) after each 100 load cycles. The crack widths were measured and the crack-patterns plotted at each stage. The cracks recorded during the previous surveys are shown with blue coloured lines, while the cracks observed after the previous surveys are shown with magenta coloured lines. The widths of crack is shown in millimeters. Representative crack patterns are shown in the following sections, while significant changes in the crack patterns during the test are discussed in Chapter 6. However, all the crack patterns recorded for all the panels are given in Appendix-J.

5.3.2 Loading Sequence

The instrumentation response changed when the loading position was changed from one load pad, to another. The responses for each loading position must be compared separately. In order to review the results it is necessary to explain the sequence of loading for each panel. For ease of identification, the odd numbered load pad in each panel was the first pad while the even numbered pad was the second pad. The loading position was changed after every 100 load cycles. The load pad locations and the loading sequence are shown in Figures 4.26 and 4.27. The sequence of load application on the first pad and the second pad for Panels A, C and D is shown in Table 5.2.

Table 5-2 Loading Sequence: Panels A, C, and D

First Pad	Pad-1, Pad-5, Pad-7	0-100	201-300	401-500	601-700	801-900*
Second Pad	Pad-2, Pad-6, Pad-8	101-200	301-400	501-600	701-800*	———

* Total number of load cycles on each panel was (900 + 800 = 1,700 cycles)

At the completion of the test on Panel-A, 900 and 800 load cycles were applied at Pad-1 and Pad-2, respectively. Similarly on Panel-C, 900 and 800 load cycles were applied at Pad-5 and Pad-6 respectively, and on Panel-D, 900 and 800 load cycles were applied at Pad-7 and Pad-8 respectively. On Panel-B, all 1,700 load cycles were applied at Pad-3.

5.3.3 Embedded Instrumentation

The embedded instrumentation such as the embedment gauges and the instrumented bars were placed under a load pad in each panel. The response of the instruments changed when the loading position was moved from one load pad to another. Table 5.3 identifies the position of instrumentation relative to the closest load pad in each panel.

Table 5-3 Position of Embedded Instrumentation in All Panels

Panel	Embedment gauges under	Instrumented bar under
Panel A	Pad 2	NA
Panel B	Pad-4*	NA
Panel C	Pad-6	Pad-5
Panel D	Pad-7	Pad-7

Note: Pad-4 was not used for loading during Phase I

5.3.4 Results: Panel-A

5.3.4.1 Conventional Instrumentation

Deflection

The load-deflection curves for Panel-A at Load Pad-2 are shown in Figure 5.1. A significant increase in the deflection is seen between 100 and 900 load cycles. However, between 900 and 1,700 load cycles the increase is marginal.

Strap Strain

The load-strain curves for Strap-2 are shown in Figure 5.2. There is significant increase in strain level between 100 and 900 load cycles. The curves for 900 and 1,700 load cycles are almost identical with only a minimal increase between 900 and 1,700 load cycles.

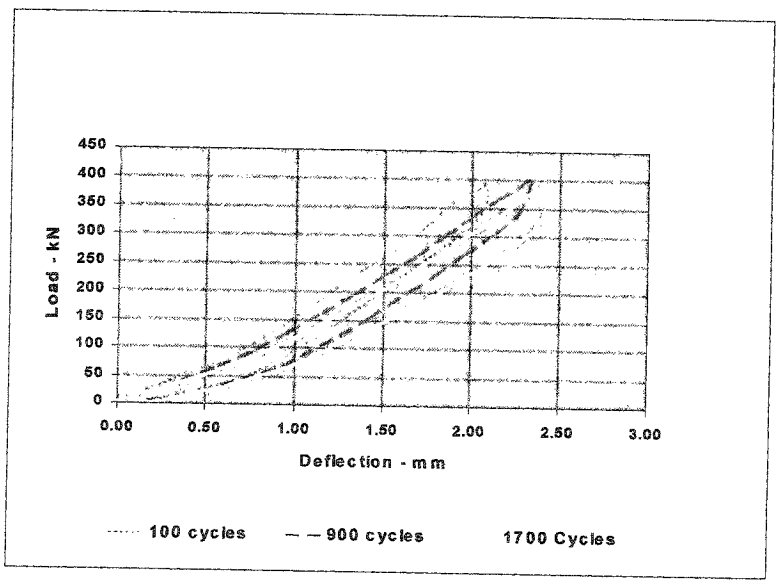

Figure 5-1 Panel-A: Load-Deflection Curves

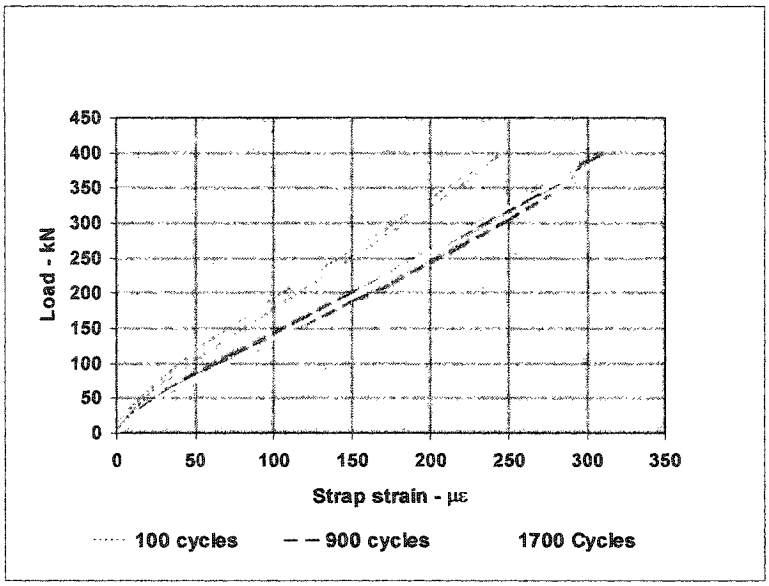

Figure 5-2 Panel-A: Load-Strap Strain Curves

5.3.4.2 Panel-A: Acoustic Waveforms

Acoustic waveforms after 100, 900, and1,700 load cycles are shown in Figures 5.3, 5.4, and 5.5, respectively. In each figure, the upper waveform shows the signal recorded by the reference sensor S1, and the lower waveform shows the signal recorded by the active sensor, S2. The large reduction in the signal received by the reference sensor between 100 and 900 load cycles indicates significant damage in the concrete. The change in the waveform between 900 and 1,700 load cycles is minimal. Although a better indicator of damage is the change in the ratios of integrated amplitudes, the ratios of peak amplitudes also serves as an indicator of damage. The ratios of peak amplitude of the reference sensor and that of the active sensor calculated at 100, 900, and 1,700 load cycles are 3.88, 8.86 and 8.12, respectively which indicates significant damage between 100 and 900 load cycles, and minimal damage thereafter. These ratios are based only on the waveforms shown on the next page.

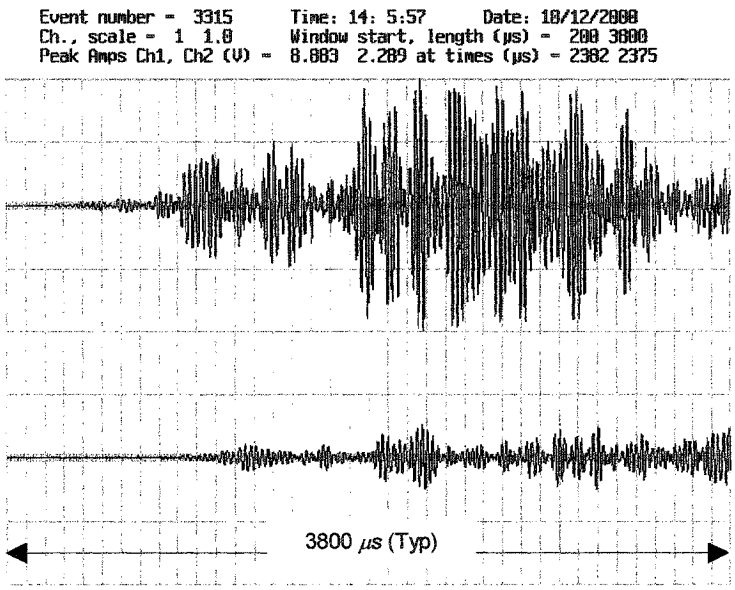

Figure 5-3 Panel-A: Waveforms after 100 Load Cycles

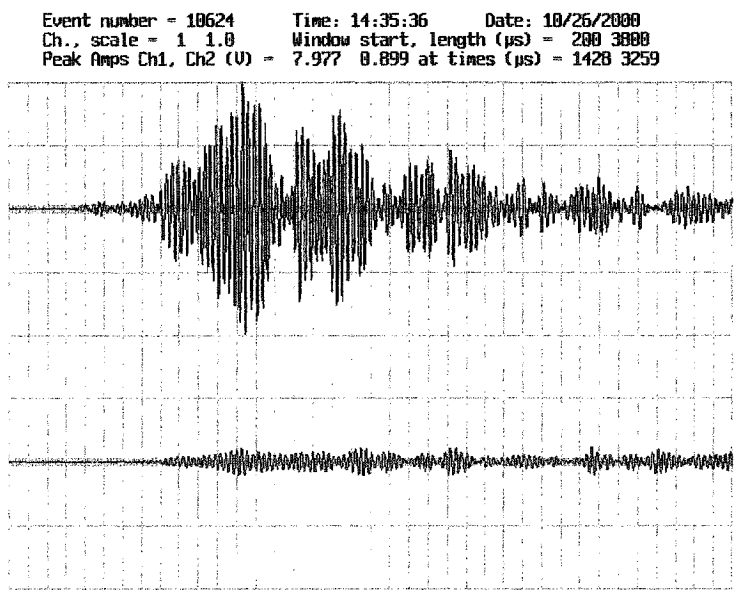

Figure 5-4 Panel-A: Acoustic Waveforms after 900 Load Cycles

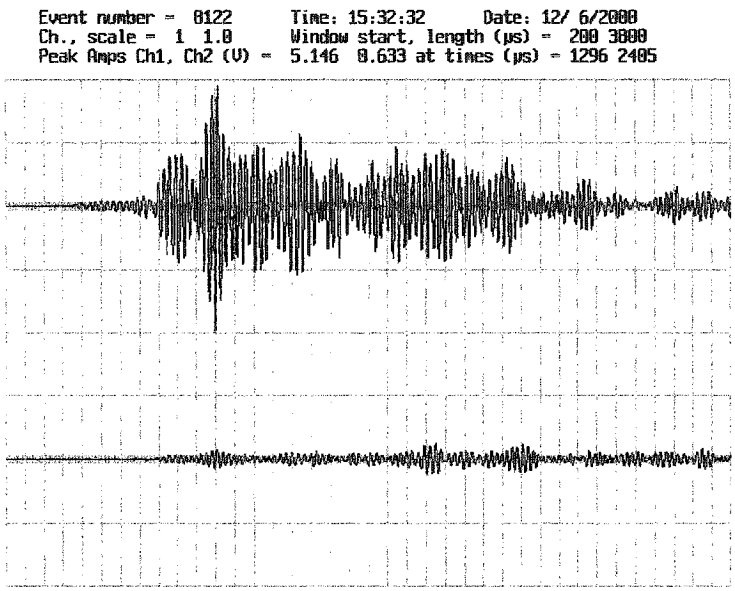

Figure 5-5 Panel-A: Acoustic Waveforms after 1,700 Load Cycles

5.3.4.3 Panel-A: Crack Patterns

Crack patterns on the top and the soffit are shown in Figures 5.6 through 5.11 after 100, 900, and 1,700 load cycles. There is no significant cracking on the top surface except one transverse crack between 100 and 900 load cycles and one longitudinal crack that propagated to the top just before 1,700 load cycles. On the soffit, the longitudinal crack, a Y-shaped crack and radial cracks under the load pads are seen. The growth of cracks is limited to the soffit.

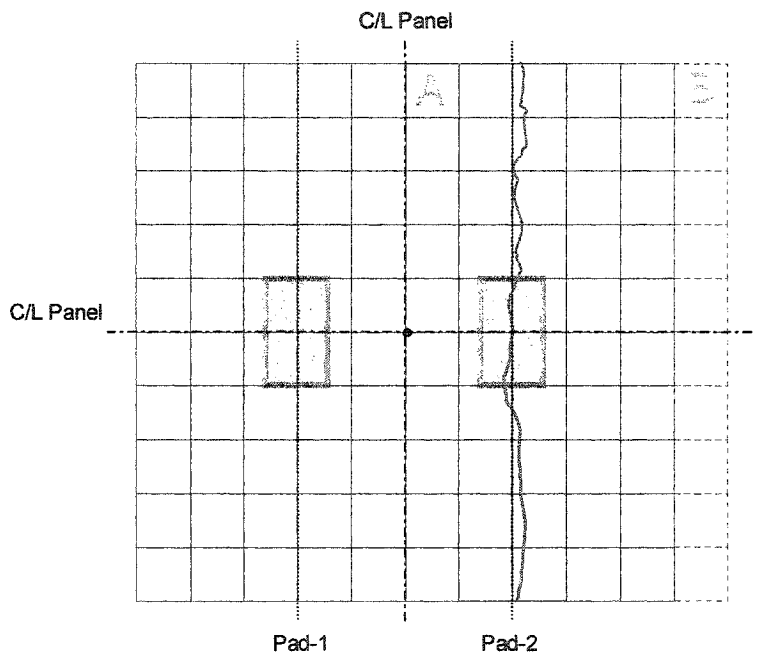

Figure 5-6 Panel-A: Crack Patterns on Top after 100 Load Cycles

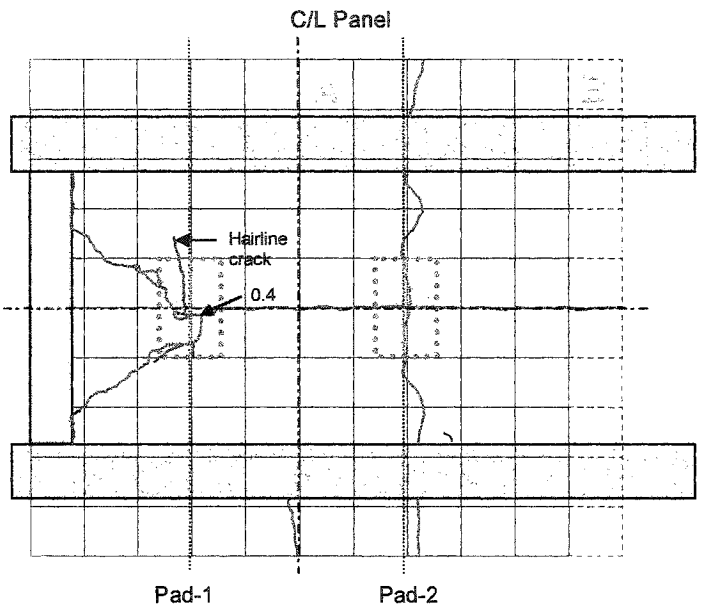

Figure 5-7 Panel-A: Crack Patterns on Soffit after 100 Load Cycles

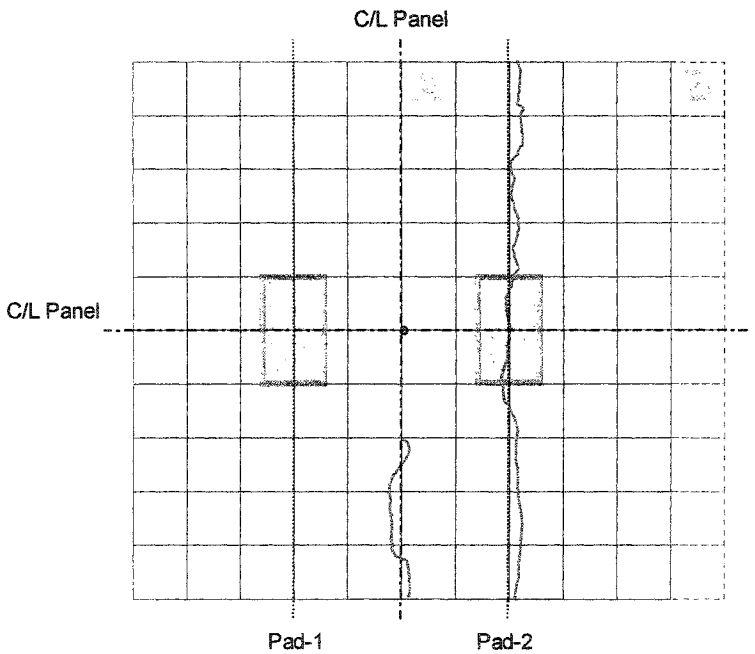

Figure 5-8 Panel-A: Crack Pattern on Top after 900 Load Cycles

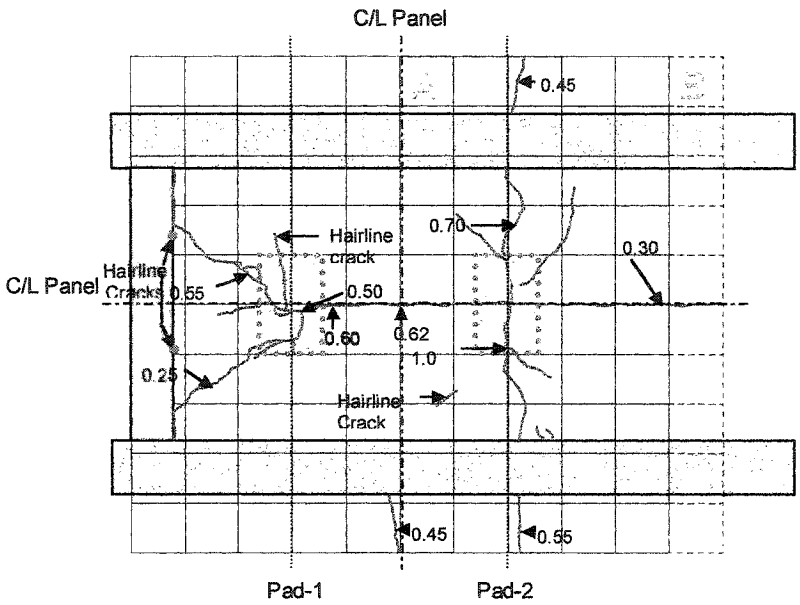

Figure 5-9 Panel-A: Crack pattern on Soffit after 900 Load Cycles

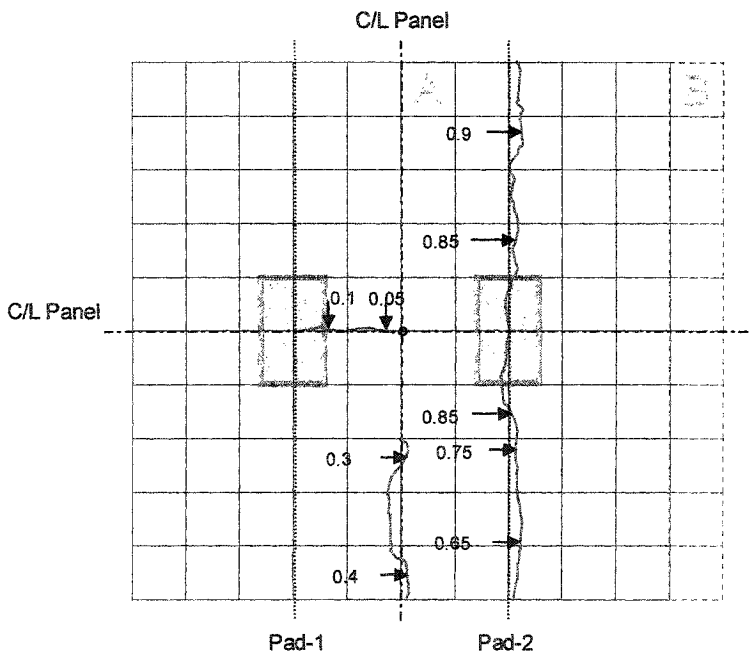

Figure 5-10 Panel-A: Crack Pattern on Top after 1,700 Load Cycles

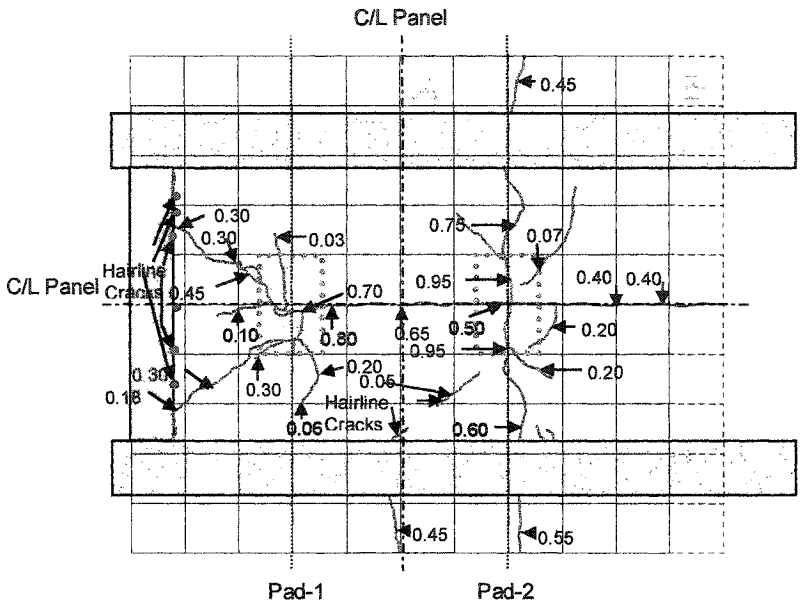

Figure 5-11 Panel-A: Crack Pattern on Soffit after 1,700 Load Cycles

5.3.5 Results: Panel C

5.3.5.1 Panel C: Conventional Instrumentation

Deflection

Load-deflection curves are shown in Figure 5.12. The deflection increased between 100 and 900 load cycles indicating, a softening of the deck slab. There was no change in the deflection between 900 and 1,700 load cycles, indicating a stable behaviour.

Strap-Strains

Load-strain curves for Strap-8 are shown in Figure 5.13. The curve at 100 load cycles is entirely in the compressive strain zone due to the fact that Strap-8 had an initial hogging curvature which straightened under load and caused compressive strain at top surface where the gauge was located. There is significant change in the strain at peak load between 100 and 900 load cycles. The change between 900 and 1,700 load cycles is relatively small.

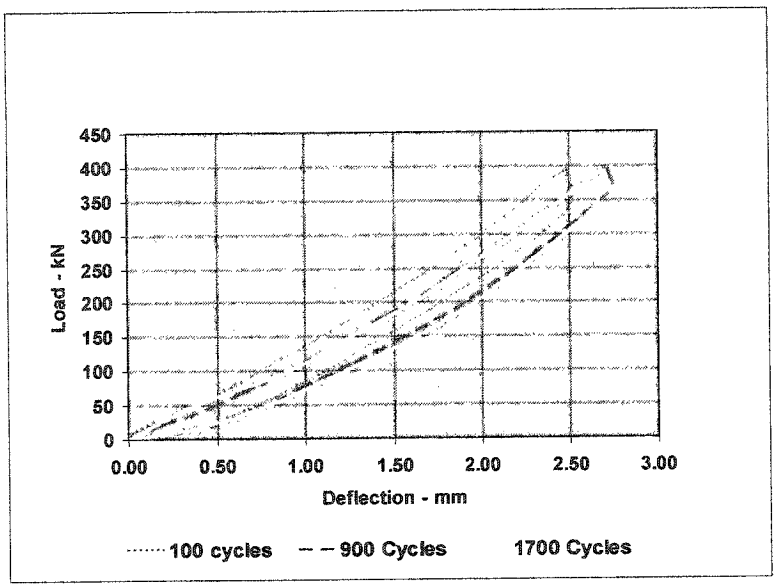

Figure 5-12 Panel-C: Load-Deflection Curves

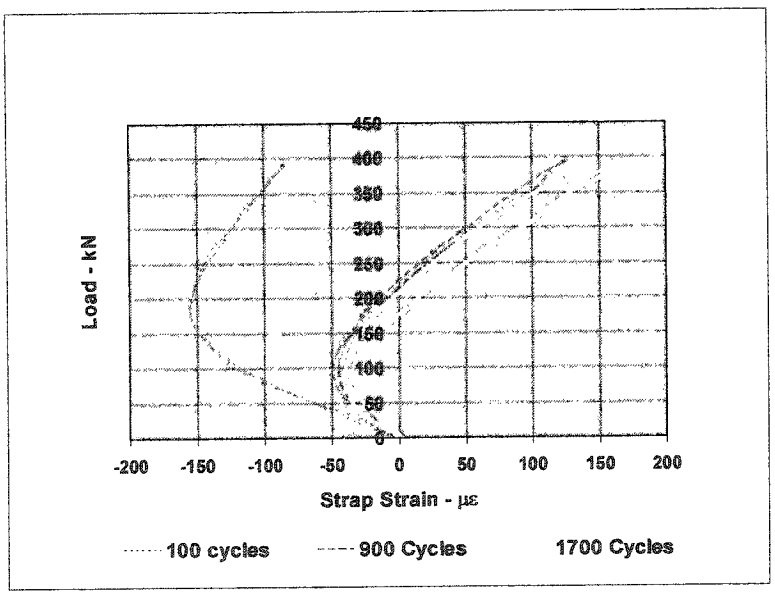

Figure 5-13 Panel-C: Load-Strap Strain Curves

5.3.5.2 Panel-C: Acoustic Waveforms

Acoustic waveforms before testing, after 900, and 1,700 load cycles are shown in Figures 5.14, 5.15, and 5.16, respectively. In each figure, the upper waveform shows the signal recorded by the reference sensor, and the lower waveform shows the signal recorded by the active sensor. There is significant change in the signal received by the active sensor from before the start of testing and after 900 load cycles, indicating damage in the concrete bounded by the sensors. The change in the waveform between 900 and 1,700 load cycles is also noticeable. The ratios of peak amplitude of the reference sensor and that of the active sensor calculated before test, at 900, and 1,700 load cycles are 1.2, 1.9, and 2.4 which indicates significant damage before 900 load cycles, and lesser damage thereafter. These ratios are based only on the waveforms shown below. It is noted that the positioning of the sensors in Panel-C was different and closer as compared to the sensor position in Panel-A. The raypaths to sensors in Panel-A crossed several cracks while the raypaths to sensors in Panel-C covered mainly the area in the vicinity of the longitudinal crack.

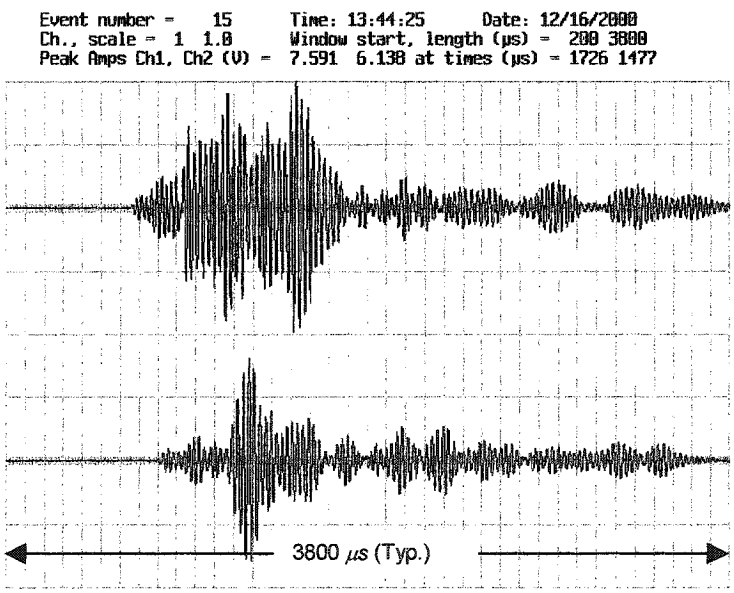

Figure 5-14 Panel-C: Acoustic Waveforms before Test

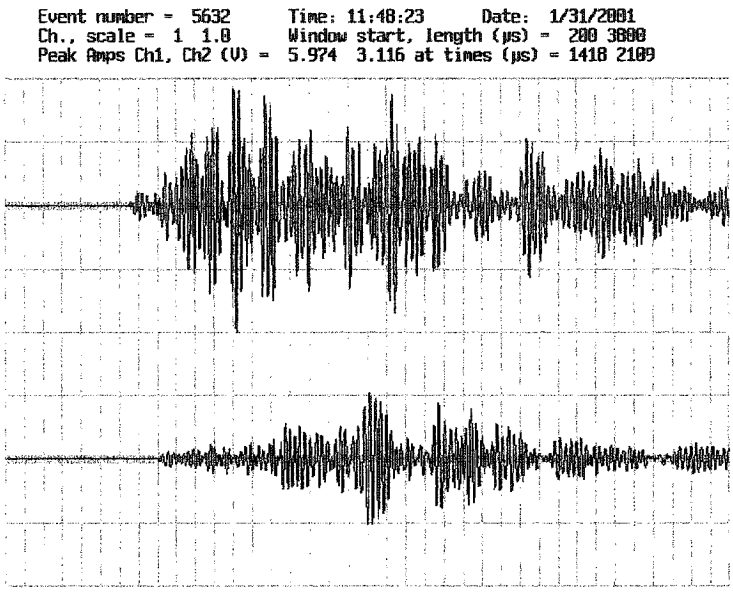

Figure 5-15 Panel-C: Acoustic Waveforms after 900 Load Cycles

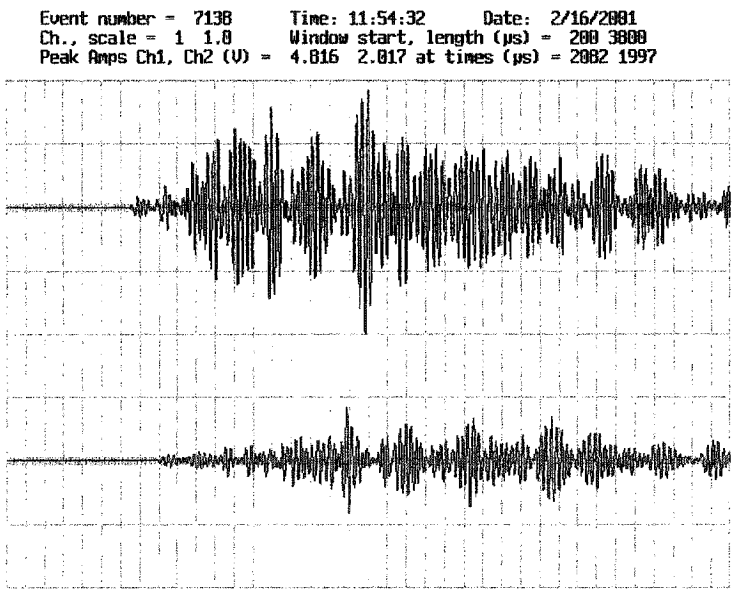

Figure 5-16 Panel-C: Acoustic Waveforms after 1,700 Load Cycles

5.3.5.3 Panel-C: Crack Patterns

The crack patterns after 100, 900, and 1,700 load cycles are shown in Figures 5.17 through 5.22. During the first 100 load cycles, only one small transverse crack developed on the top surface and a longitudinal crack developed on the soffit. Between 900 and 1,700 load cycles, the transverse crack extended from the entire width of the panel and another radial crack also developed from Load Pad-6. Radial cracks had also developed under both the load pads. The extent and width of cracks in Panel-C were considerably lesser than those of Panel-A.

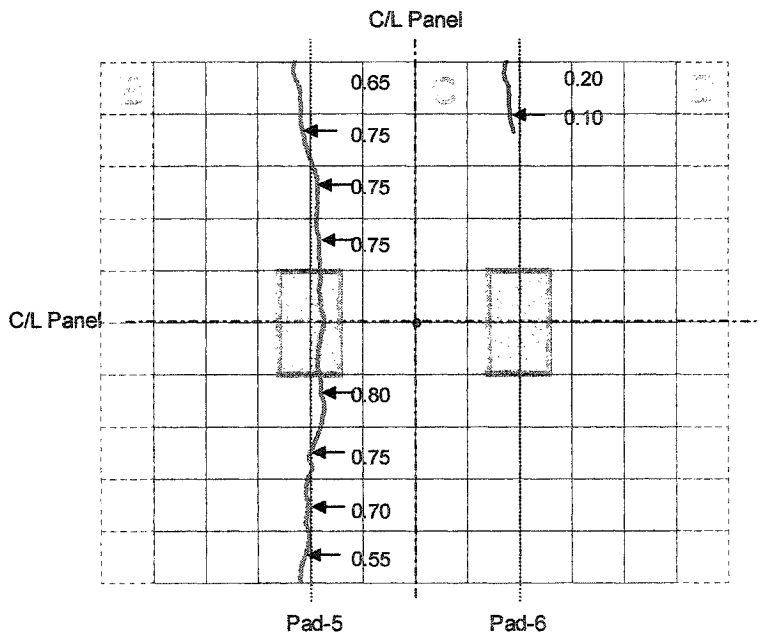

Figure 5-17 Panel-C: Crack Pattern on Top after 100 Load Cycles

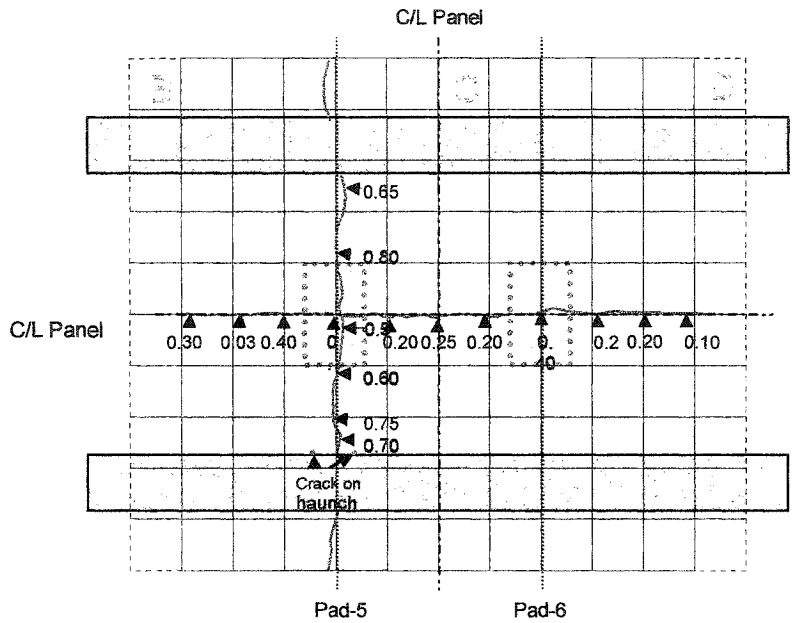

Figure 5-18 Panel C: Crack Pattern on Soffit after 100 Load Cycles

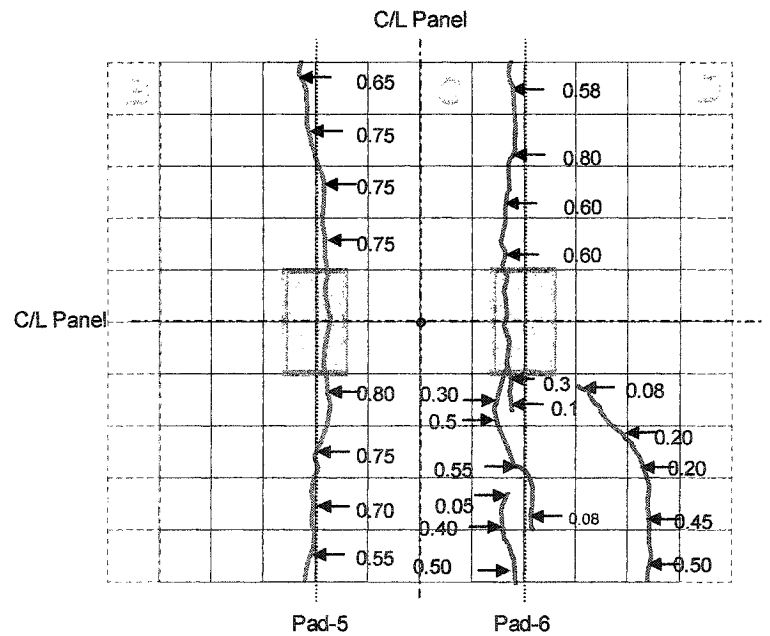

Figure 5-19 Panel C: Crack Pattern on Top after 900 Load Cycles

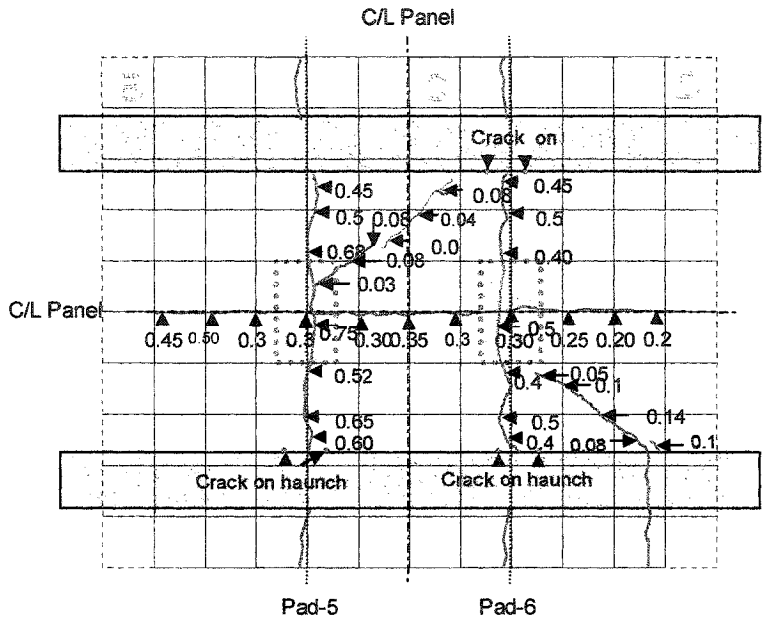

Figure 5-20 Panel C: Crack Pattern on Soffit after 900 Load Cycles

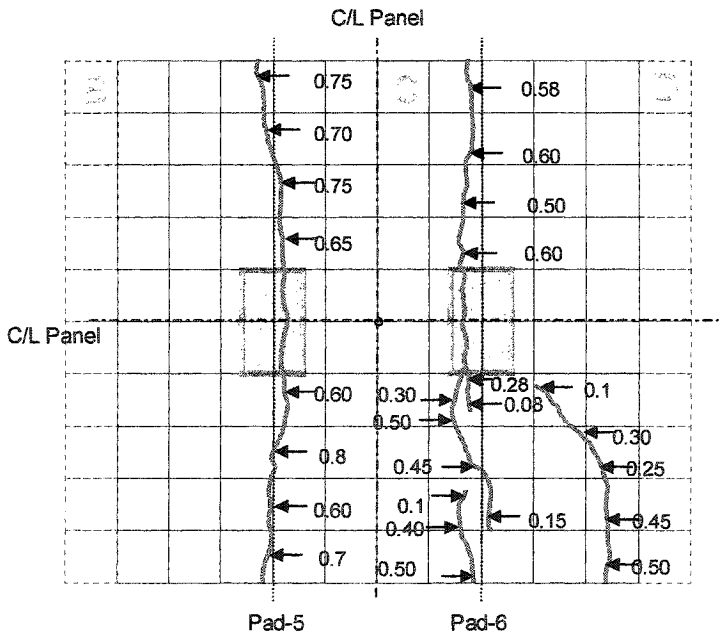

Figure 5-21 Panel C: Crack Pattern on Top after 1,700 Load Cycles

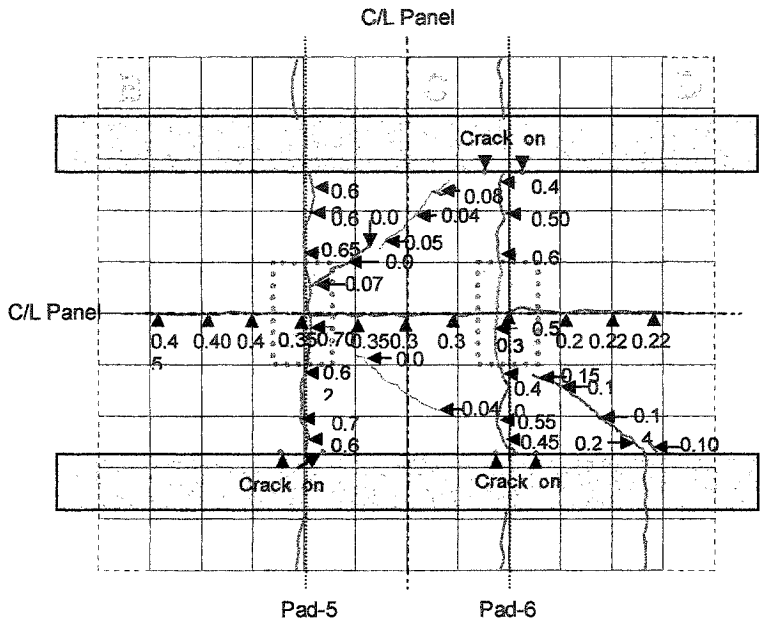

Figure 5-22 Panel C: Crack Pattern on Soffit after 1,700 Load Cycles

5.3.6 Results: Panel-D

5.3.6.1 Conventional Instrumentation

Deflection

The load-deflection curves under Load Pad-7 are shown in Figure 5.23. The deflection increased between 100 and 900 load cycles. There was no change from 900 to 1,700 load cycles.

Strap-Strain

The load-strain in Strap-11 is shown in Figure 5.24. There was a significant increase in strain between 100 and 900 load cycles. Between 900 and 1,700 load cycles the strain level, however, remained unchanged.

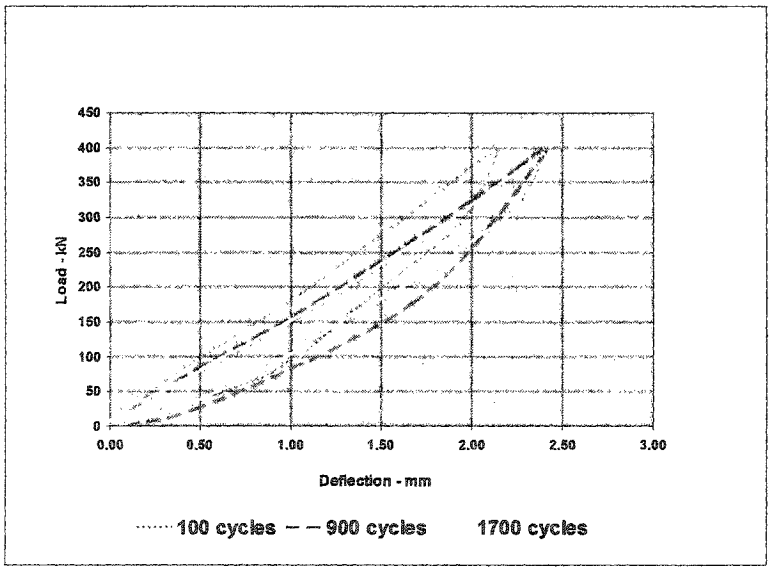

Figure 5-23 Panel-D: Load-Deflection Curves

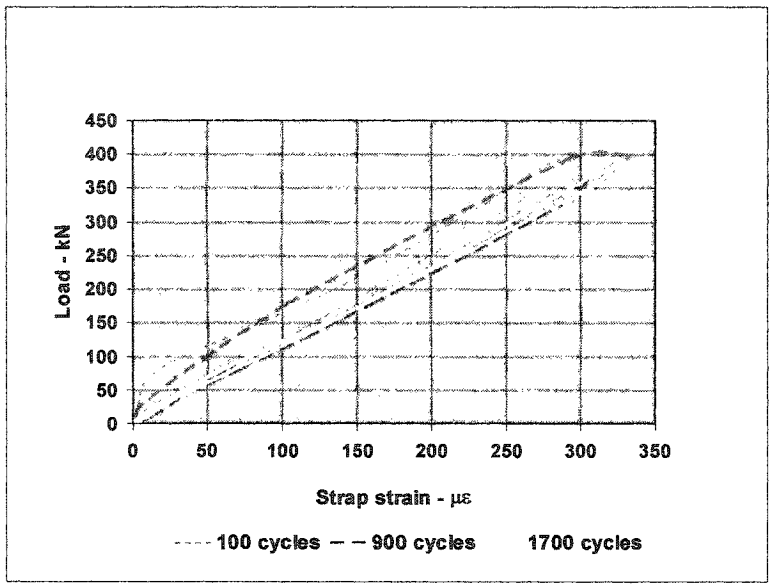

Figure 5-24 Panel-D: Load-Strap Strain Curves

5.3.6.2 Acoustic Attenuation Results

Acoustic waveforms before test, after 900, and 1,700 load cycles are shown in Figures 5.25, 5.26, and 5.27, respectively. In each figure, the upper waveform shows the signal recorded by the reference sensor, and the lower waveform shows the signal recorded by the active sensor. There is a noticeable change in the signal received by the reference sensor before the test and after 900 load cycles, indicating some damage in the concrete bounded by the sensors. The change in the waveform between 900 and 1,700 load cycles is also evident. The ratios of the peak amplitude of the reference sensor and that of the active sensor calculated before test, at 900, and 1,700 load cycles are 3.55, 3.6 and 4.5. This indicates minor damage before 900 load cycles and significant damage thereafter. These ratios are based only on the waveforms shown.

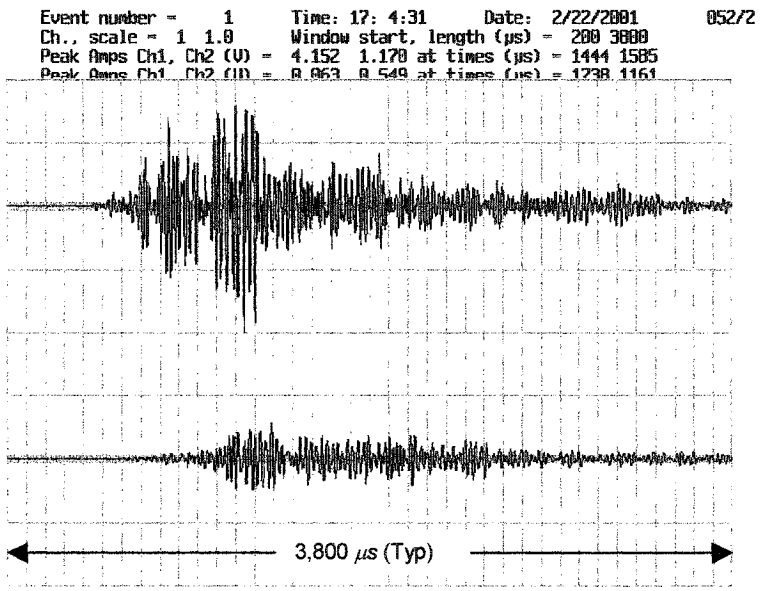

Figure 5-25 Panel-D: Acoustic Waveforms before Test

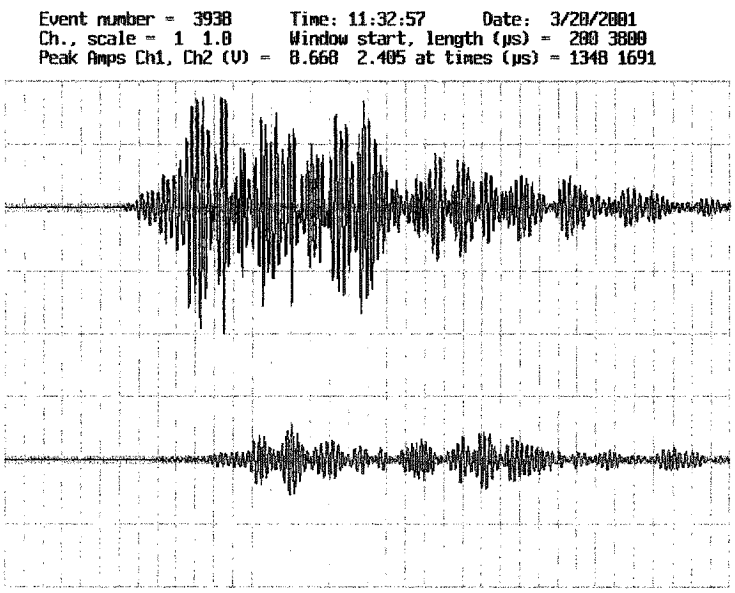

Figure 5-26 Panel-D: Acoustic Waveforms after 900 Load Cycles

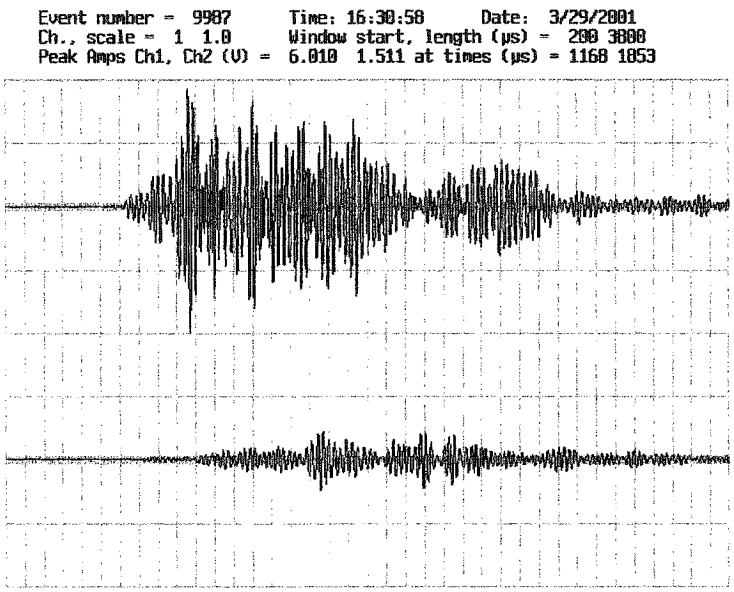

Figure 5-27 Panel-D: Acoustic Waveforms after 1,700 Load Cycles

5.3.6.3 Crack Patterns

The crack patterns for the top surface and the soffit after 100, 900, and 1,700 load cycles are shown in Figure 5.28 through 5.33.

On the top surface, there was only one transverse crack for the part width of the panel. The crack pattern on the soffit is different from Panel-A and Panel-C. Most of the cracks have occurred in an orthogonal pattern below the steel crack control reinforcement. The crack widths are significantly smaller than those of other panels.

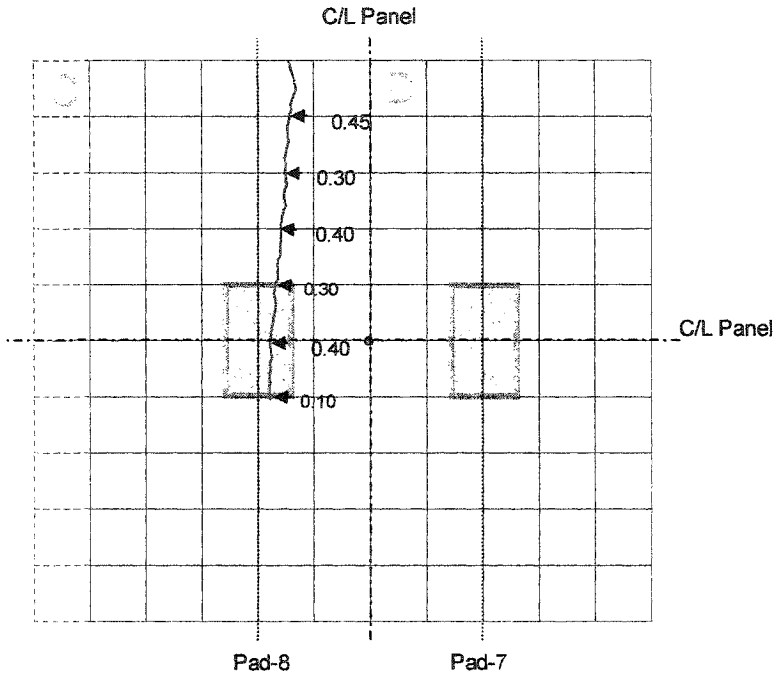

Figure 5-28 Panel-D: Crack Patterns at Top after 100 Load Cycles

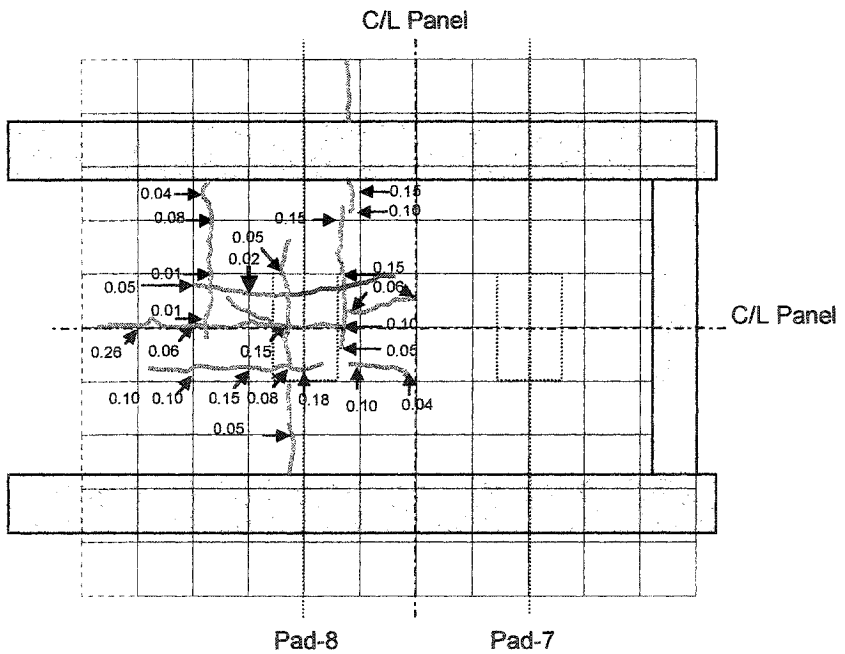

Figure 5-29 Panel-D: Crack Patterns on Soffit after 100 Load Cycles

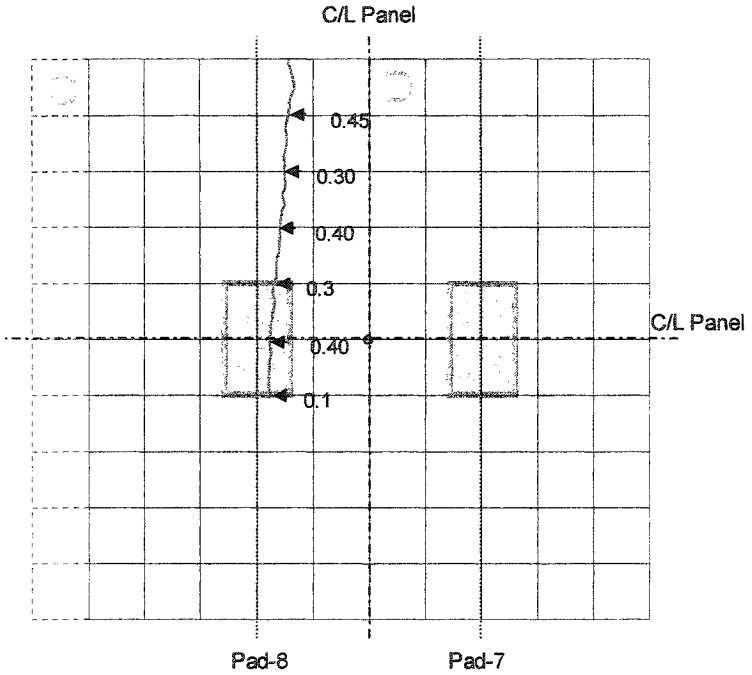

Figure 5-30 Panel-D: Crack Patterns on Top after 900 Cycles

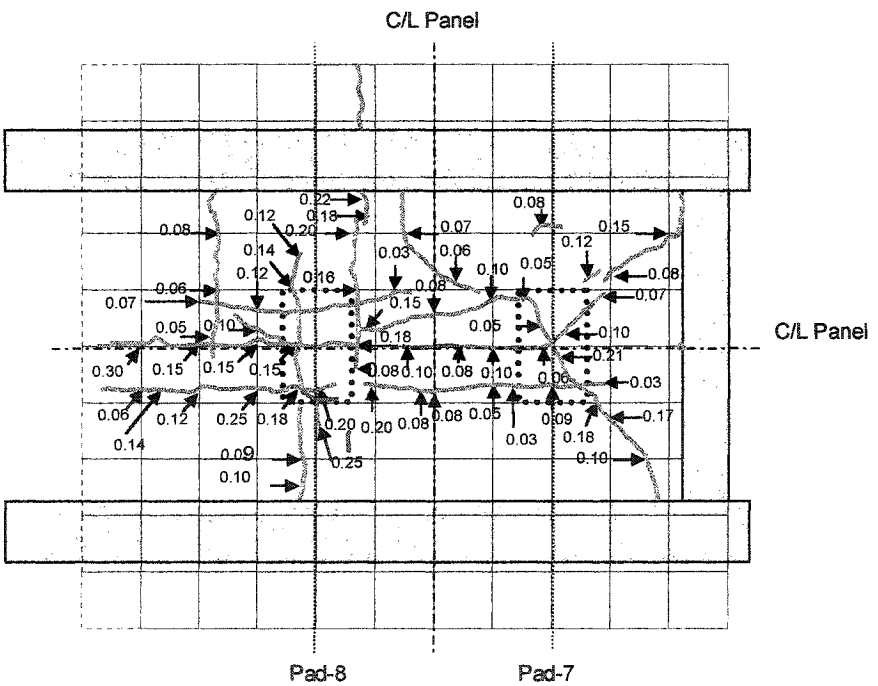

Figure 5-31 Panel-D: Crack Patterns on Soffit after 900 Load Cycles

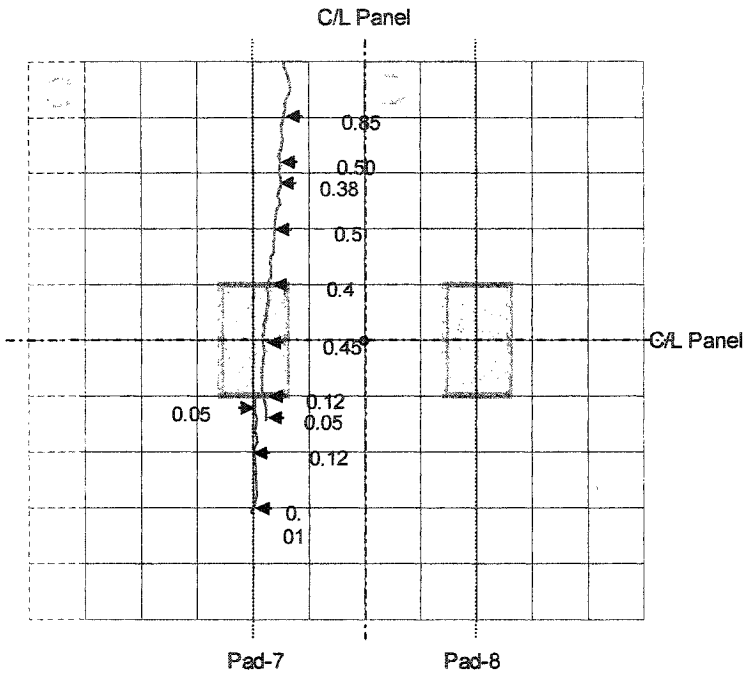

Figure 5-32 Panel-D: Crack Patterns on Top after 1,700 Load Cycles

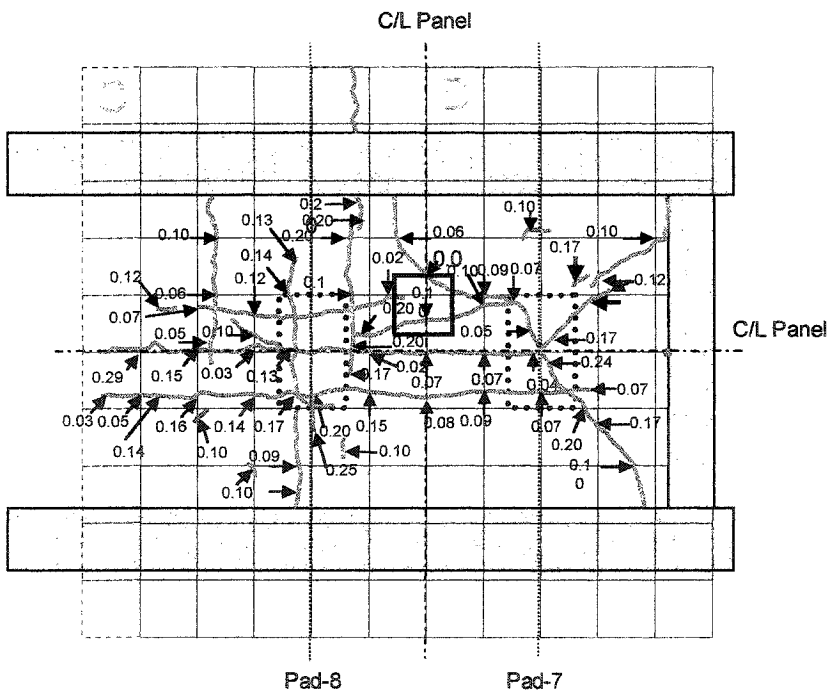

Figure 5-33 Panel-D: Crack Patterns on Soffit after 1,700 Load Cycles

5.3.7 Results: Panel-B

5.3.7.1 Conventional Instrumentation

Deflection

The load-deflection curve is shown in Figure 5.34. In the case of this panel, the deflection pattern is reversed. The deflection after 900 load cycles is marginally less than the deflection after 100 load cycles and the deflection after 1,700 load cycles is again less than that after 900 load cycles. This marginal reduction is possibly due to the initial closure of the full depth longitudinal crack under asymmetric loading. The deflection was measured at the centre of the load pad.

Strap Strain

The load-strain curves for Strap-5 are shown in Figure 5.35. All the three curves coincide indicating no change in strain during the 1,700 load cycles applied on the panel. The strain levels are significantly higher as the load pad was placed directly over Strap-5.

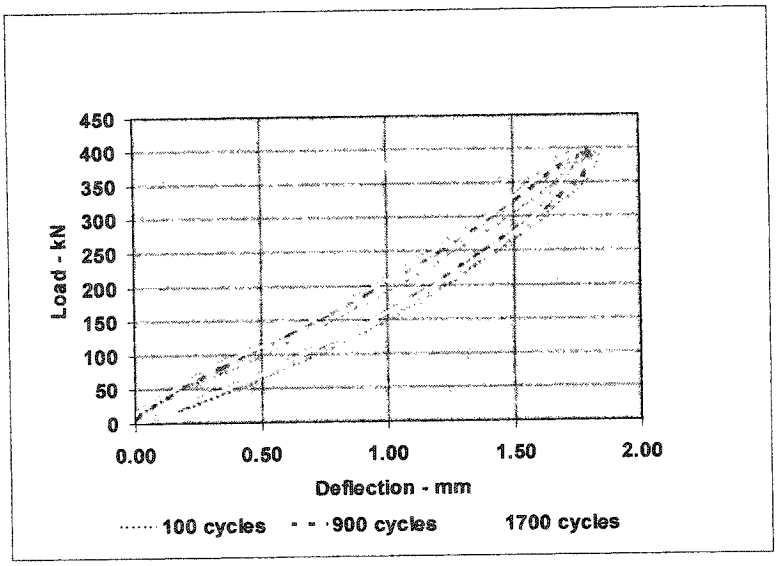

Figure 5-34 Panel-B: Load-Deflection Curves

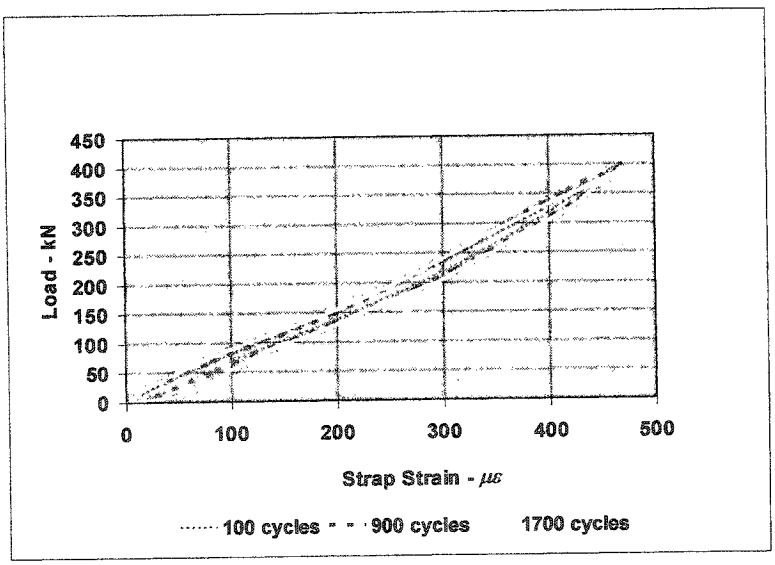

Figure 5-35 Panel-B: Load-Strap Strain Curves

5.3.7.2 Panel-B: Acoustic Waveforms

Acoustic waveforms after 320, 900, and 1,700 load cycles are shown in Figures 5.36, 5.37, and 5.38, respectively. In each figure, the upper waveform shows the signal recorded by the reference sensor, and the lower waveform shows the signal recorded by the active sensor. The large reduction in the signal received by the reference sensor between 320 and 900 load cycles indicates significant damage in the concrete. The change in the waveform between 900 and 1,700 load cycles is minimal. Although a better indicator of damage is the change in the ratios of integrated amplitudes, the ratio of peak amplitudes also serves as an indicator of damage. The ratios of peak amplitude of the reference sensor and that of the active sensor calculated at 320, 900, and 1,700 load cycles are 3.43, 3.63 and 5.08 which indicate marginal damage between 100 and 900 load cycles and significant damage thereafter. These ratios are based only on the waveforms shown below. Acoustic waveforms are further discussed in Chapter 6.

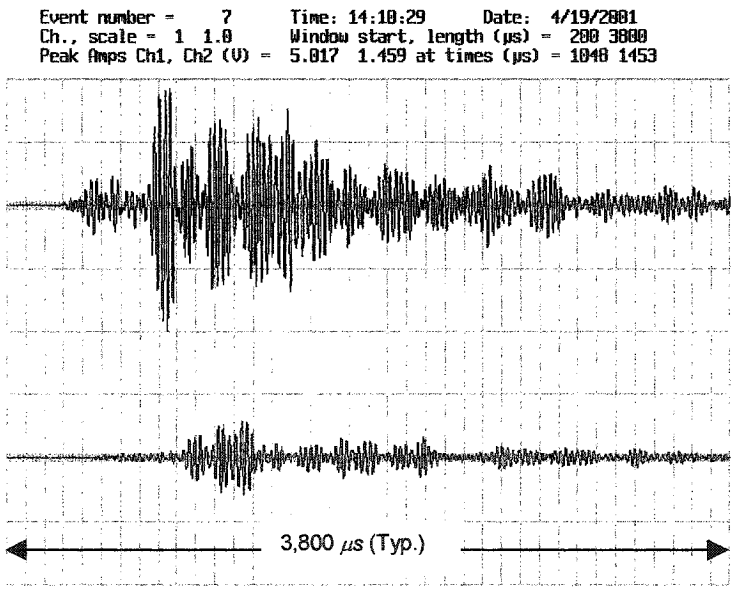

Figure 5-36 Panel-B: Acoustic Waveforms after 320 Load Cycles

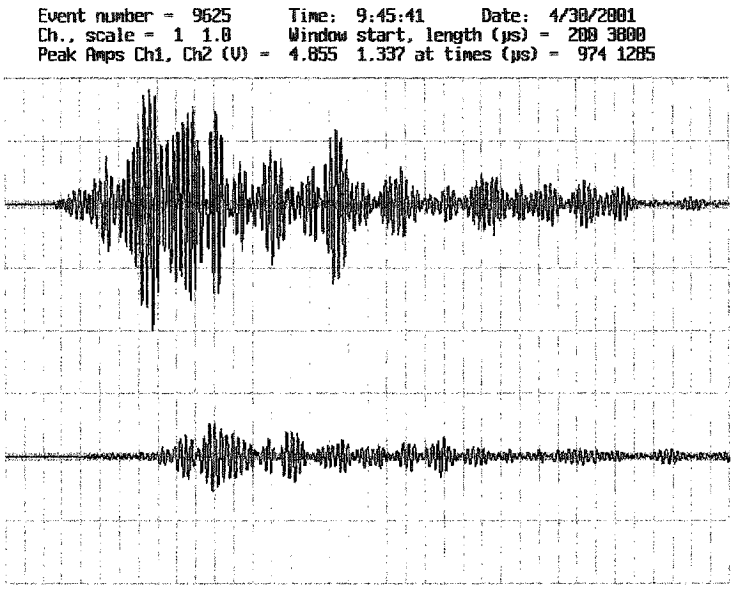

Figure 5-37 Panel-B: Acoustic Waveforms after 900 Cycles

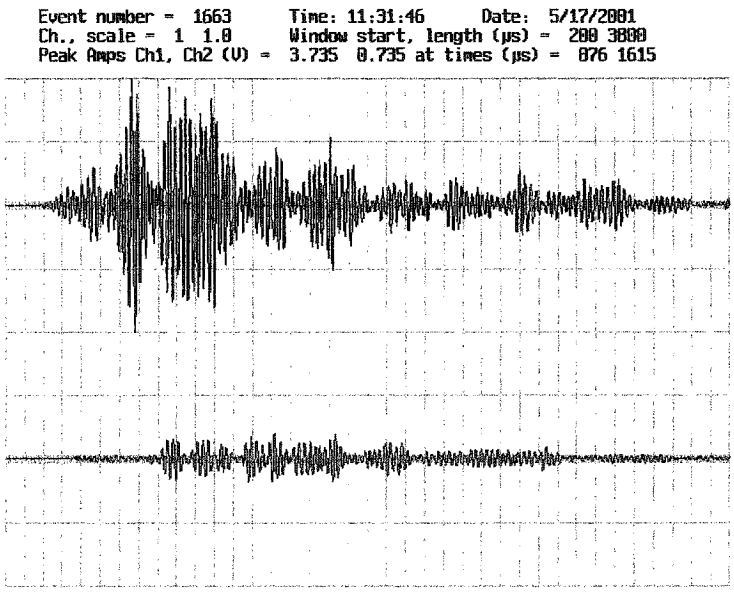

Figure 5-38 Panel-B: Acoustic Waveforms after 1,700 Cycles

5.3.7.3 Panel-B: Crack Patterns

Crack patterns on the top surface and the soffit after 100, 900, and 1,700 load cycles are shown in Figures 5.39 through 5.34. Panel-B had the most cracking on the top surface among all the panels. The radial cracks on the soffit were concentrated under the load pad. The crack width was less than that in Panel-A.

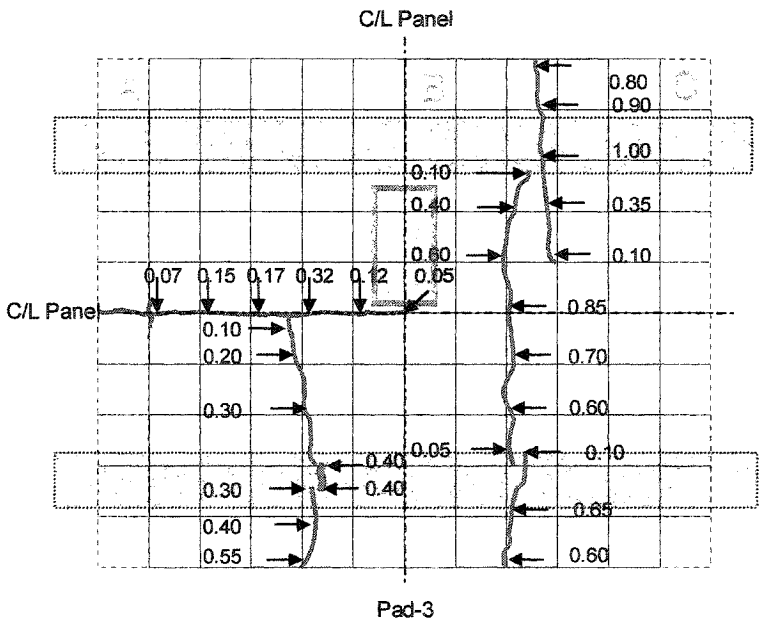

Figure 5-39 Panel-B: Crack Patterns on Top after 100 Load Cycles

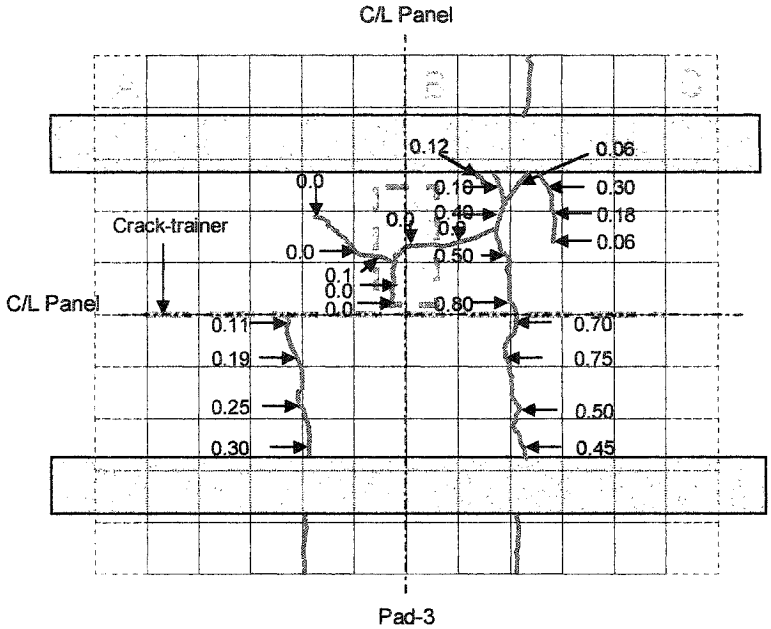

Figure 5-40 Panel-B: Crack Patterns on Soffit after 100 Load Cycles

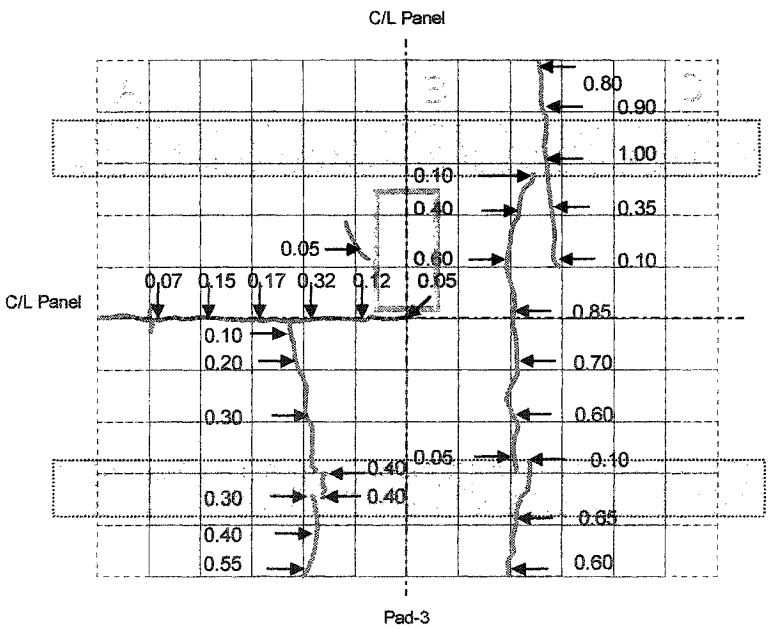

Figure 5-41 Panel-B: Crack Pattern on Top after 900 Load Cycles

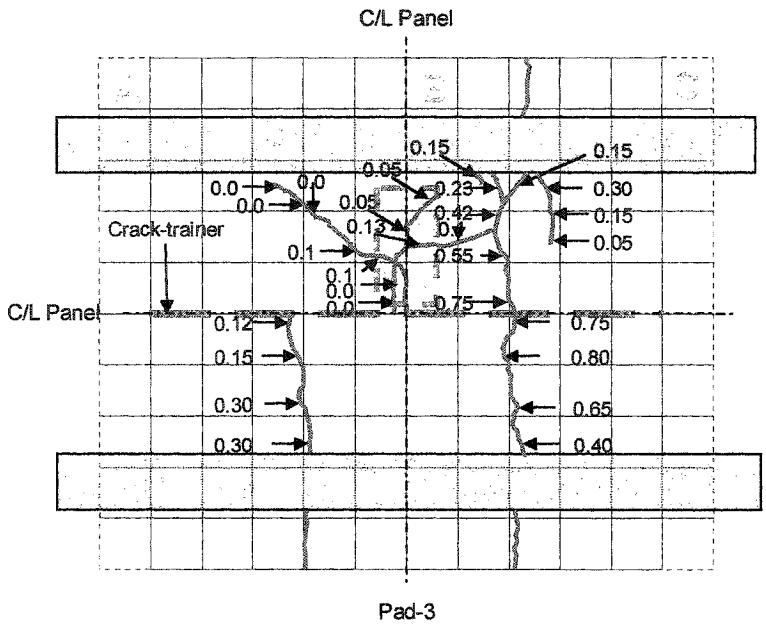

Figure 5-42 Panel-B: Crack Pattern on Soffit after 900 Load Cycles

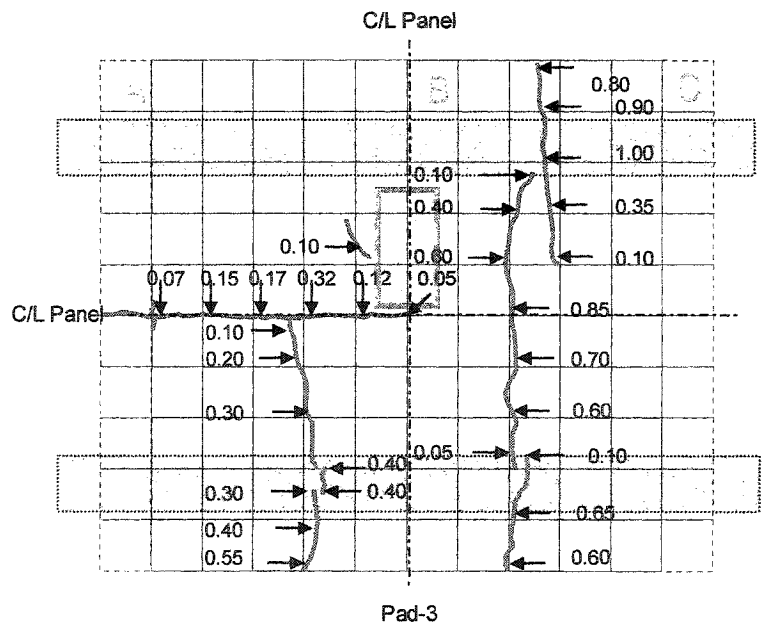

Figure 5-43 Panel-B: Crack Patterns on Top after 1,700 Load Cycles

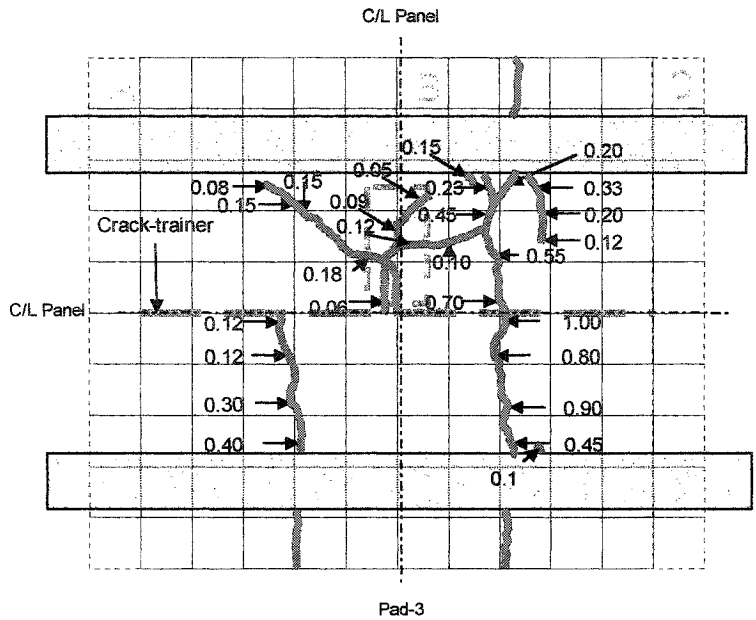

Figure 5-44 Panel-B: Crack Patterns on Soffit after 1,700 Load Cycles

5.4 Results: Phase II – Fatigue and Comparative Performance

5.4.1 General

The goals of Phase-II of the testing program were to a) ascertain the fatigue life of each configuration, b) study the change in deck panel response over the entire test-span, and c) to evaluate the effectiveness of each configuration under fatigue loading.

Panel-A was tested the first under pulsating loading, followed by Panel-D. Panel-B was then tested under static loading conditions to ascertain the punching strength of the panel. (It may be recalled here that Panel-B was identical to Panel-A, but had a pre-induced 75 mm high longitudinal crack, which had grown into a full-depth crack by the end of Phase-I). Panel-C was tested the last under pulsating load. Cyclic loading was applied on each panel through only one load pad.

The pulsating load ranged from 0-400 kN to 0-900 kN for Panel-A, and from 0-900 kN to 0-1100 kN for Panel-D. Due to varying magnitudes of the peak load, it was essential to establish a method to evaluate the change in response at various stages of testing. To

compare the response of various sensors over the entire fatigue life of a panel, their values corresponding to the lowest applied load of 392.4 kN (40 t) were calculated from the test data and plotted against the total number of load cycles applied. The plots were updated on a continual basis as the testing proceeded. The plots, termed as 'the response patterns", have been plotted for all sensors. The response patterns clearly show the three distinct phases in the fatigue life of a given panel.

The data from the internal and external sensors gathered by the conventional instrumentation were complemented by acoustic attenuation data and visual observations in the form of crack inspection and surveys. Then test results are divided into three separate categories; a) response of conventional instrumentation, b) acoustic attenuation, and c) visual observations. Each of the three results has been discussed in sub-sections 5.4.1.1, 5.4.1.2, and 5.4.1.3.

5.4.1.1 Conventional Instrumentation

Data were acquired for all the load cycles during testing and were analyzed at regular intervals and reviewed. The data have been presented in the following two formats.

- Load versus sensor response
- Sensor response versus number of load cycles

In the first format, various instrument responses have been plotted against the applied load. Each chart shows the response of one particular sensor at several different stages over the entire test period at 393 kN peak load. This provides an overview of the change that occurred during the test period. The data in the first format have been presented in this chapter.

In the second format, the response of each sensor has been plotted against the total number of load cycles completed. This diagram would show the trends in the change of response as the testing proceeded. For each panel, the response of various sensors was calculated after each 1,000 load cycles until the failure of that panel. The peak value

of the load was raised during the test as discussed in 5.4.1. In order to make a rational and correct comparison of various responses, the instrument responses corresponding to a 392.4 kN load, were extracted from the test data. The data in this format have been presented and discussed in Chapter 6.

The sensor responses that were recorded are listed in table 5.4

Table 5-4 Instrumentation for Phase-II

Deflection under load pad	All Panels
Deflection under girder/s	All Panels
Transverse Crack Displacement- (Horizontal and Vertical)	Panel-A
Strains in straps	All Panels
Strains in instrumented reinforcing bar	Panel-C and Panel-D
Strains in concrete embedment gauges	All Panels
Strains in central strap (Fiber-optic sensor)	All Panels

In each panel, the main parameters that were closely followed were a) the strain patterns of straps, and b) the deflection patterns at the load pads. It was noticed that, while the strain patterns of the straps were consistent, the values of deflection at the load pad occasionally exhibited fluctuations that were inconsistent with the recognized trends of damage growth. On investigation, it was found that the load pads tended to move laterally under repeated loading. The problem was addressed by frequent realignment of the load pad and adding one additional displacement transducer at the load pad.

In all the panels, the signs of impending failure were apparent only shortly before the actual failure. The changes in slab behaviour were characterized by a sudden and a

large variation in the sensor-response over a relatively small number of load cycles. The load versus sensor-response curves at failure have been plotted to highlight that change. The entire range of curves for sensor responses is given in Appendix-I.

5.4.1.2 Acoustic Attenuation

The acoustic attenuation results show the acoustic parameters that were compared during the test. The data presented here are the waveforms for the artificially generated signals at recorded regular intervals. The waveform patterns changed as the testing proceeded. The strength of the signal diminishes as the medium through which the acoustic signal propagates deteriorates under repeated loading. An increase in the differential arrival time, which represents a reduction in the velocity of the signal wave indicates an increase in the damage within the concrete slab. Representative waveforms, recorded during the test, have been shown for each panel.

5.4.1.3 Crack Patterns

The top and the bottom surfaces of the panel under test were inspected a) before the commencement of the test, and b) at regular intervals thereafter. The crack widths were measured during these inspections. The crack patterns were plotted when new cracks were noticed or there was an extension of the existing cracks. All the crack patterns recorded during the test have been included in Appendix-J.

5.4.2 Results: Panel-A

5.4.2.1 General

Initially in this phase, 48,300 load cycles with a peak value of about 393 kN were applied. The peak value of the load was raised to 638 kN and 10,000 load cycles were applied at that load level. The peak value of the load was then further raised to 800 kN and 2,000 load cycles were applied. Finally, the peak value was raised to 883 kN and the panel failed after 1,243 load cycles.

5.4.2.2 Conventional Instrumentation

Deflection

Load-deflection curves for deflection under Load Pad-2 at various stages are shown in Figure 5.45. The curves are shown for load levels of about 393 kN load level. The gradual softening of the deck slab up to the first cycle at 883 kN load level is evident. A greater effect is seen during the final load cycle.

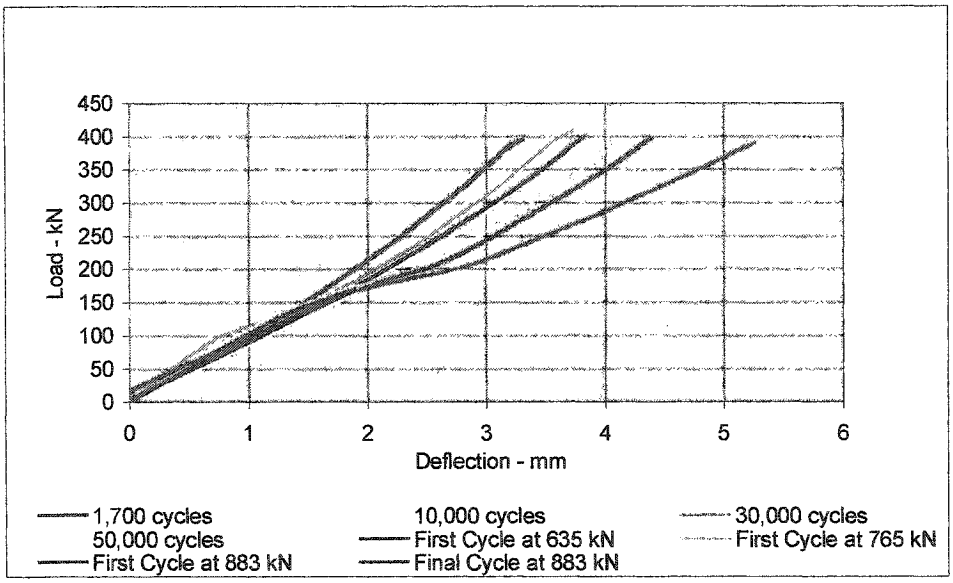

Figure 5-45 Panel-A: Load-Deflection Curves

Strap Strains

Load-strain curves for Strap-2 and Strap-3 are shown in Figure 5.46 and Figure 5.47 respectively. For both straps, a gradual increase in strain can be seen. However, the strain in both straps in the final load cycle at 883 kN is less that that recorded during the first cycle at that load level. This phenomenon is discussed in Chapter-6.

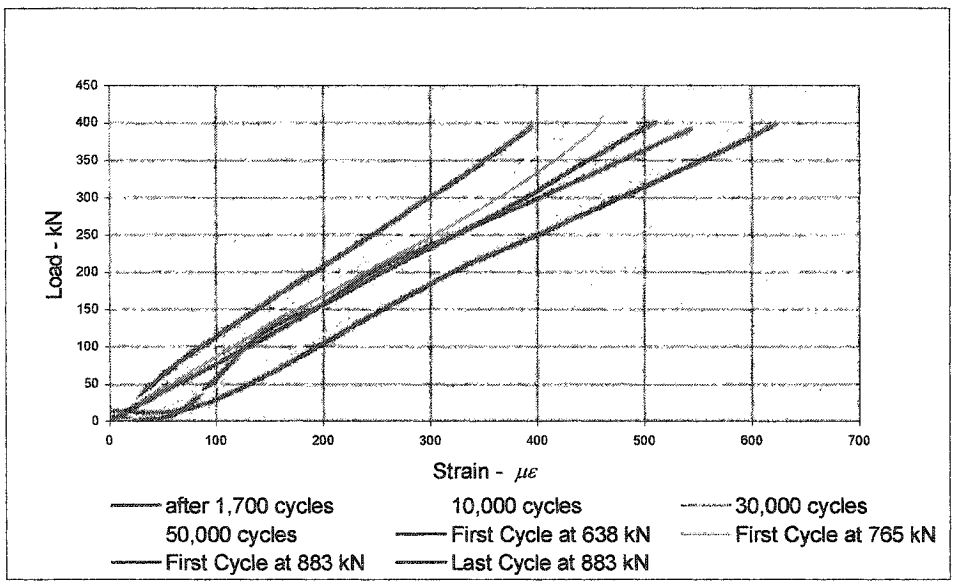

Figure 5-46 Panel-A: Load-Strain Curves for Strap-2

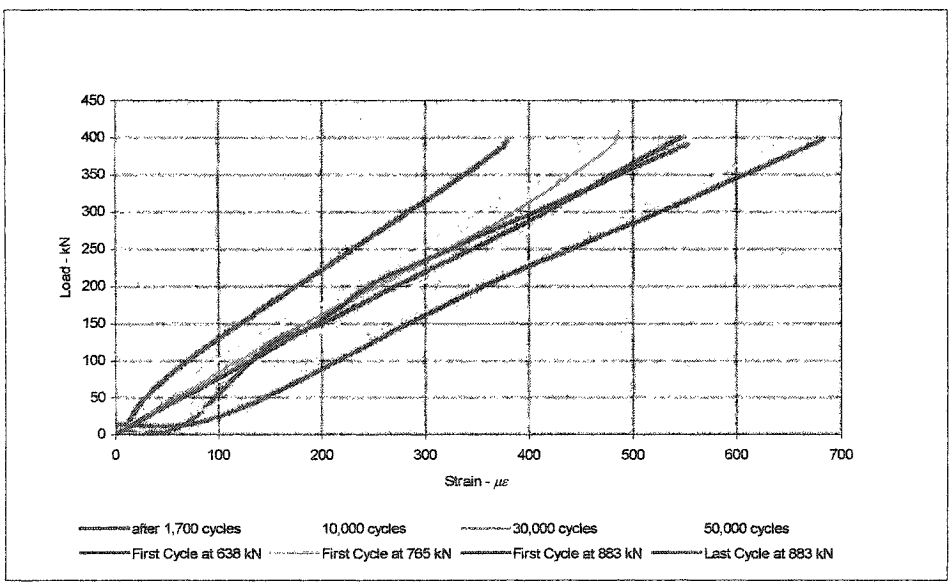

Figure 5-47 Panel-A: Load-Strain Curves for Strap-3

5.4.2.3 Acoustic Waveforms

Acoustic waveforms at various stages of testing are shown in Figures 5.48 through 5.51. A change in the waveforms with the progress of loading is seen. The upper waveform represents the signal received by the reference sensor S1, and the lower waveform represents the waveform recorded by the active sensor S2 in Figures 5.48 through 5.50. After 50,000 load cycles due to a change in location and the type of the signal source, the functions of the sensors S1 and S2 were interchanged. Therefore in Figure 5.51, the upper waveform represents the singal received by the active sensor S1, while the lower waveform represents the signal recorded by the reference sensor S2.

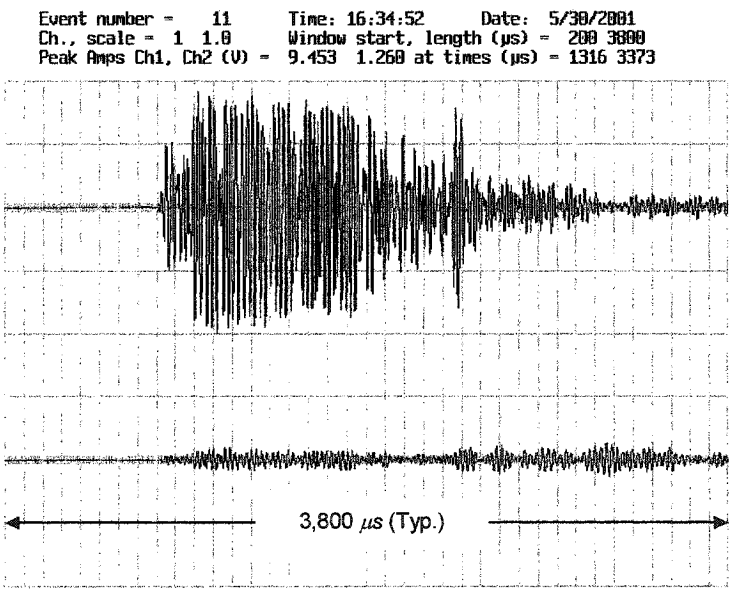

Figure 5-48 Panel-A: Acoustic Waveforms after 1,700 Cycles

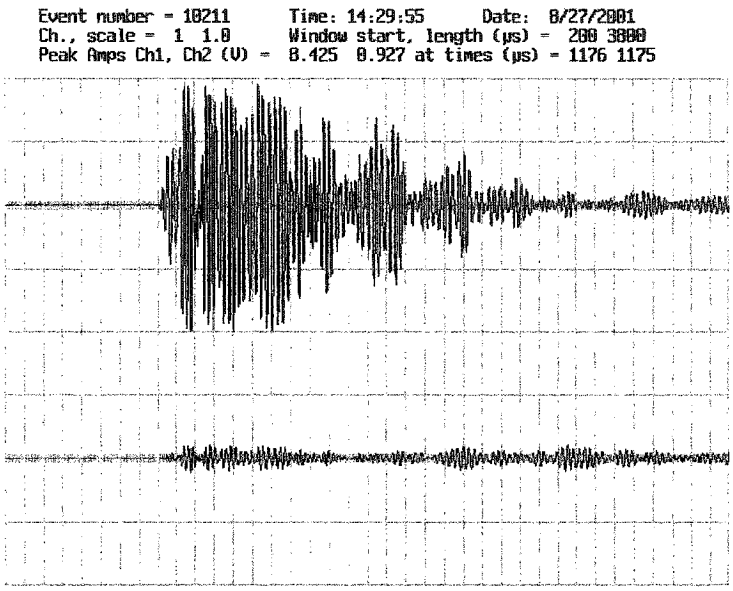

Figure 5-49 Panel-A: Acoustic Waveforms after 30,000 Load Cycles

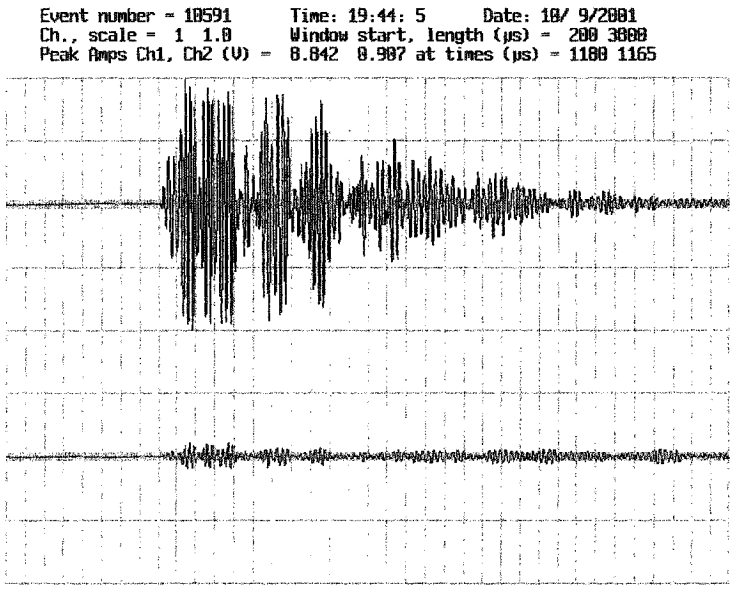

Figure 5-50 Panel-A: Acoustic Waveforms after 50,000 Load Cycles

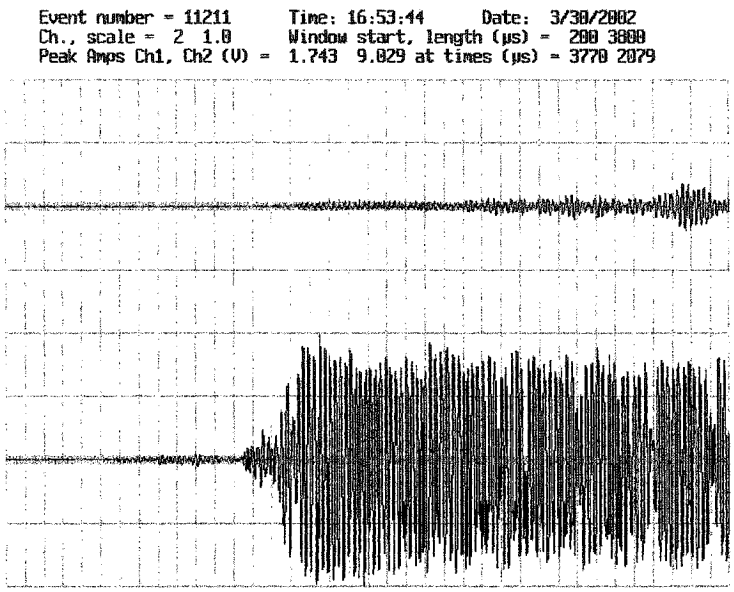

Figure 5-51 Panel-A: Acoustic Waveforms after Failure

5.4.2.4 Crack Patterns

Crack patterns on the top surface and the soffit shown in Figures 5.52 through 5.57, provide an overview of the crack development up to failure. The development of circular crack on the top was almost complete by 30,000 load cycles.

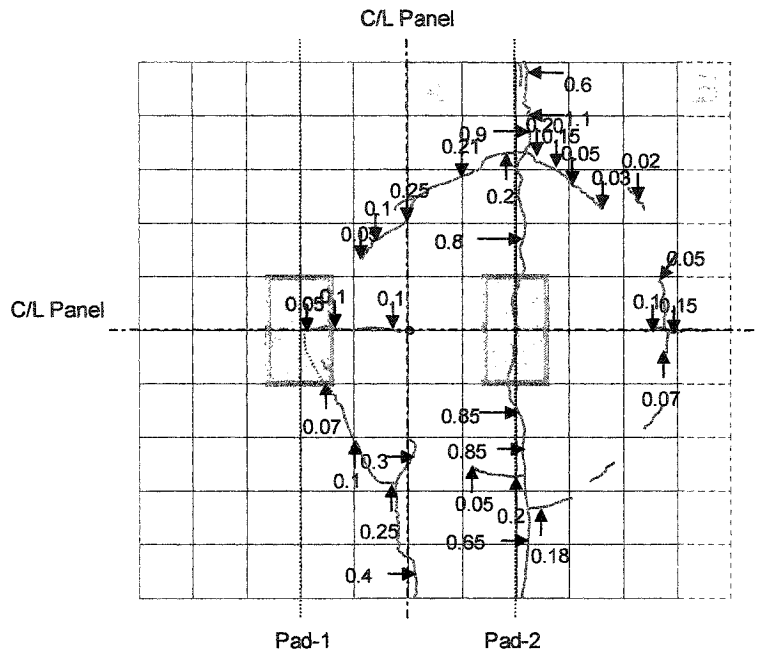

Figure 5-52 Panel-A: Crack Pattern at Top after 9,400 Load Cycles

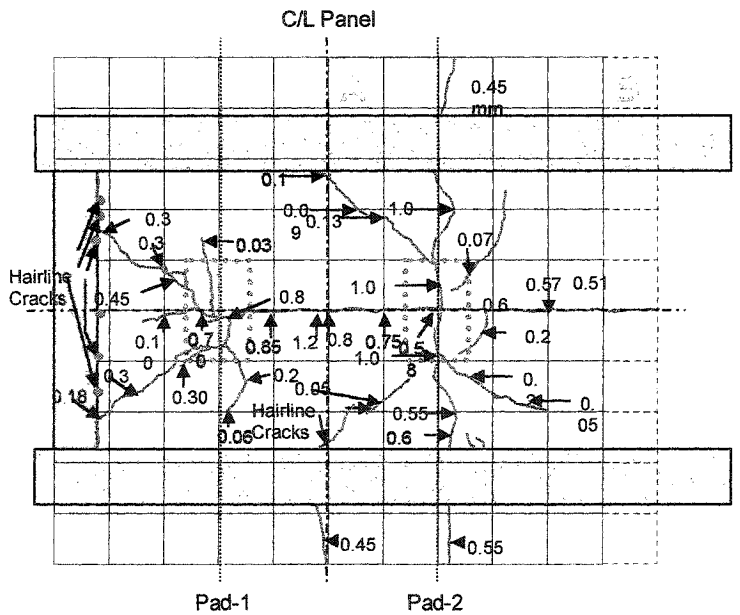

Figure 5-53 Panel-A: Crack Pattern on Soffit after 9,400 Load Cycles

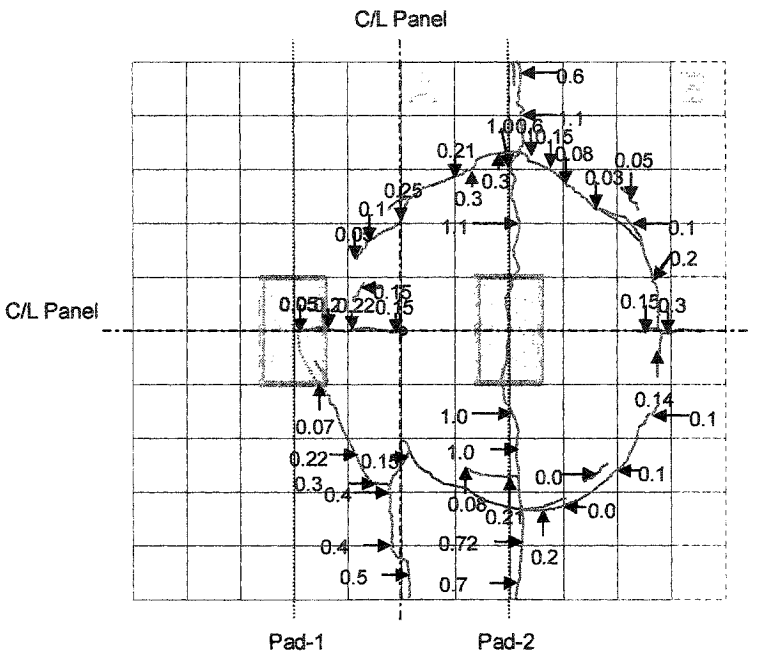

Figure 5-54 Panel-A: Crack Pattern on Top after 30,000 Load Cycles

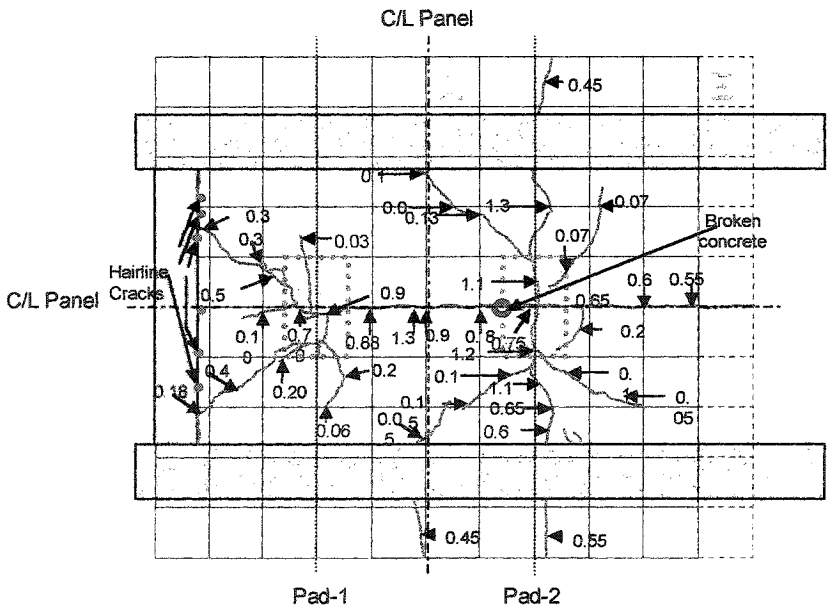

Figure 5-55 Panel-A: Crack Pattern on Soffit after 30,000 Load Cycles

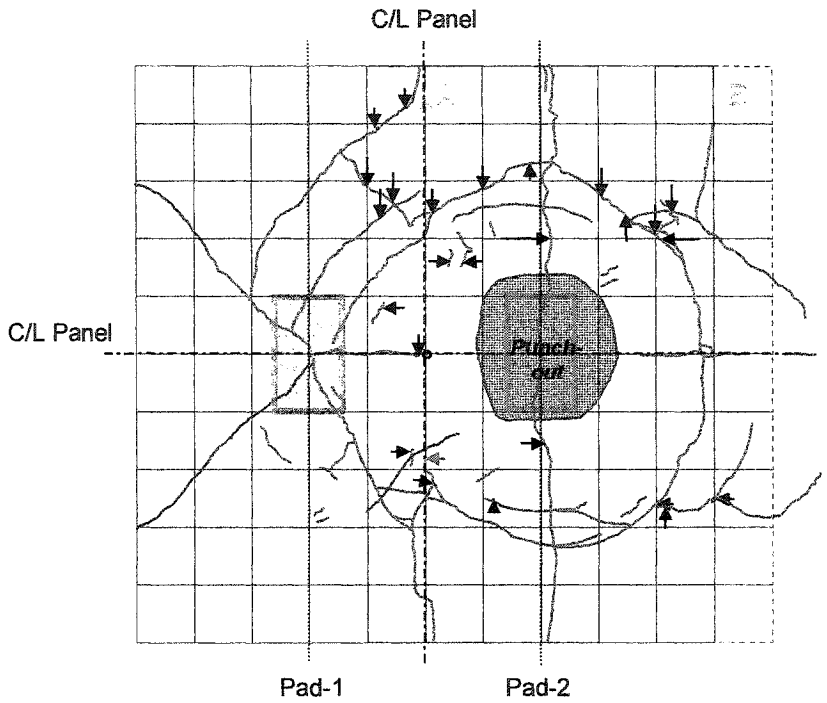

Figure 5-56 Panel-A: Crack Patterns on Top after Failure (63,243 Load Cycles)

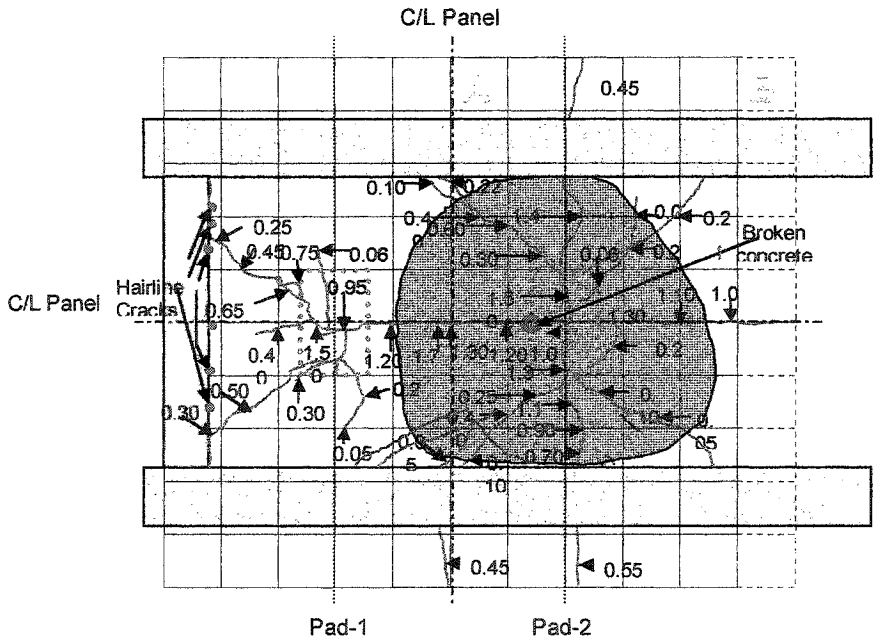

Figure 5-57 Panel-A: Crack Patterns on Soffit after Failure (63,243 Load Cycles)

5.4.3 Results: Panel-D

5.4.3.1 General

For Panel-D, 5,000 load cycles were applied with a peak value of 883 kN. The peak value was subsequently raised to 981 kN and 1,050 kN and 45 and 55 load cycles respectively were applied. The peak value of the load was then raised to 1,079 kN and failure occurred after the next 108 load cycles.

5.4.3.2 Panel D: Conventional Instrumentation

Deflection

The load-deflection curves for deflection under Load Pad-8 at various stages are shown in Figure 5.58. The first load cycle in Phase-I was applied at a 393 kN peak load, followed by 5,000 load cycles at 883 kN peak load. There is a significant increase in the deflection as the peak load is increased, followed by a stable behaviour. Once again, the deflection increases substantially at failure.

Strap Strains

Load-strain curves for Strap-10 and Strap-11 are shown in Figures 5.59 and 5.60, respectively. There is a steep increase in the strains in both the straps as the load is raised to 883 kN, followed by a relatively stable behaviour. As observed in the case of Panel-A, the strain levels in both the straps decline at failure; this phenomenon is discussed in Chapter-6.

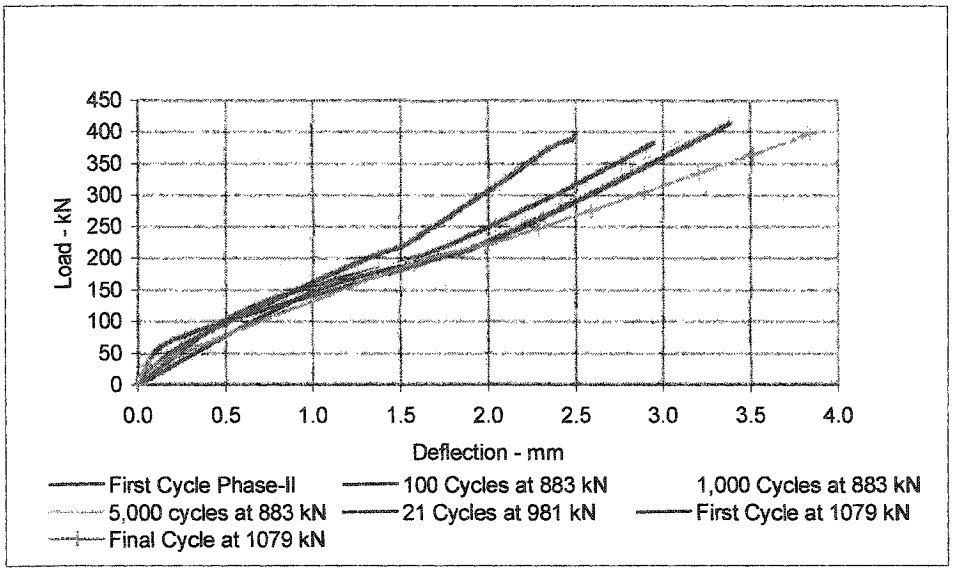

Figure 5-58 Panel-D: Load-Deflection Curves

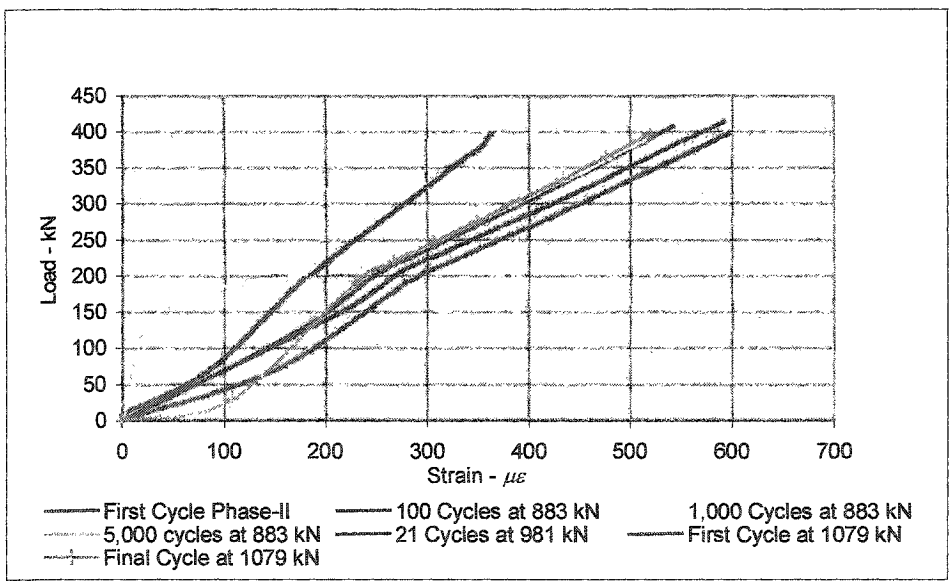

Figure 5-59 Panel-D: Load-Strain Curves for Strap-10

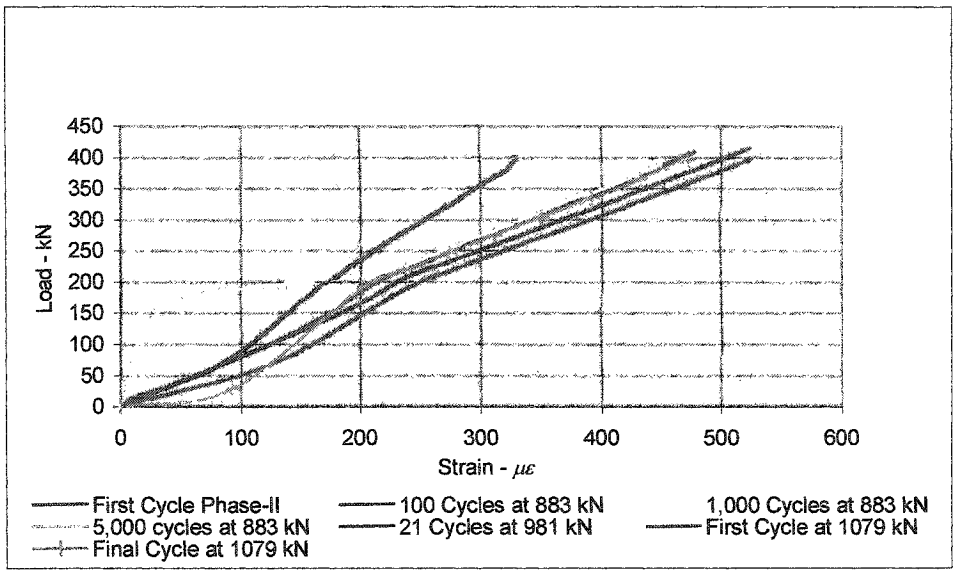

Figure 5-60 Panel-D: Load-Strain Curves for Strap-11

5.4.3.3 Panel-D: Acoustic Waveforms

The acoustic waveforms at three different stages are shown in Figures 5.61 through 5.63. It is seen that the strength of the signal diminished significantly after failure.

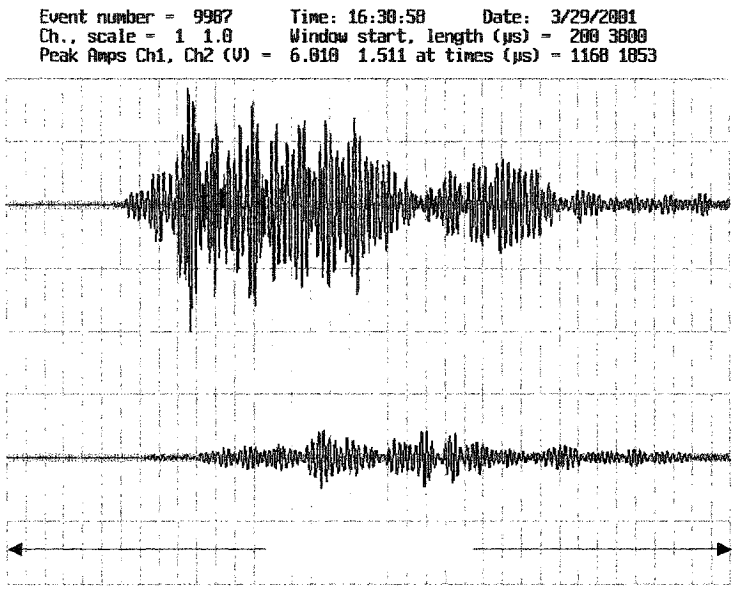

Figure 5-61 Panel-D: Acoustic Waveforms before Test

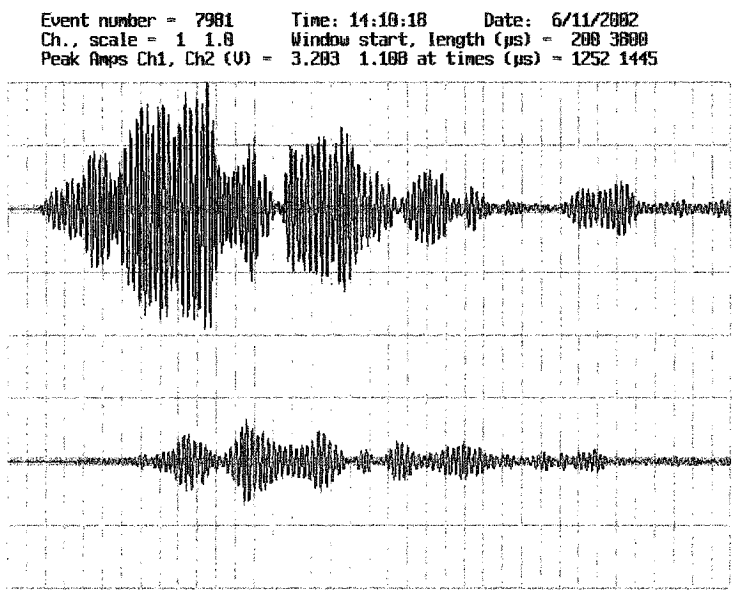

Figure 5-62 Panel-D: Acoustic Waveforms after 5,000 Load Cycles at 883 kN

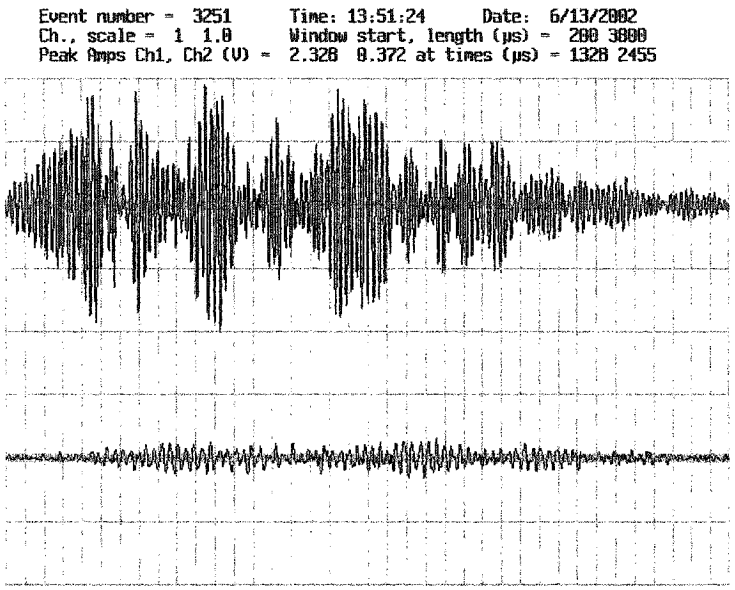

Figure 5-63 Panel-D: Acoustic Waveforms after Failure

5.4.3.4 Panel-D: Crack Patterns

Crack patterns after 500, and 5,000 load cycles, and after failure are shown in Figures 5.64 through 5.69. The circular crack on the top surface did not develop fully up to the failure of the panel. There was significant crack development on the soffit within the first 500 load cycles. Radial cracks developed under the load pad in this phase of testing. In Phase-I, the crack pattern on soffit was mostly orthogonal.

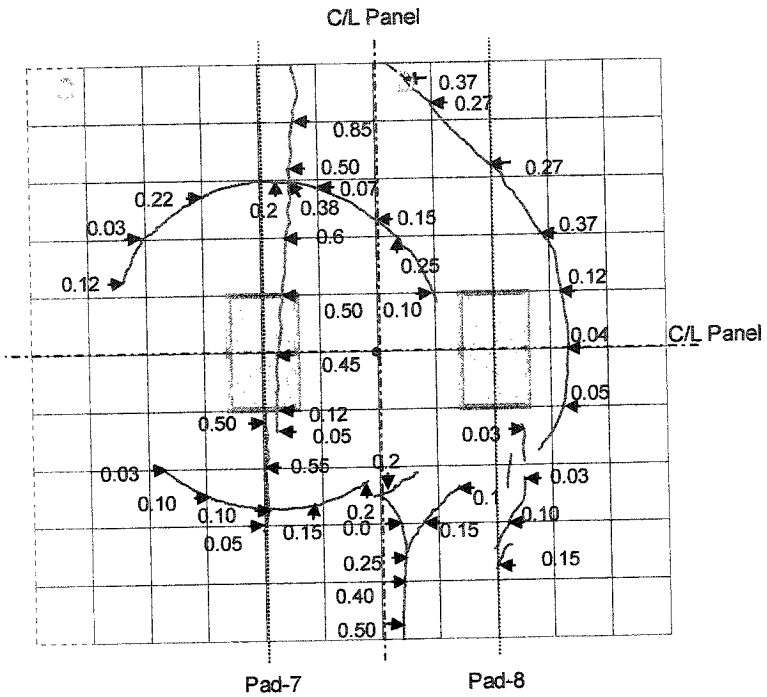

Figure 5-64 Panel-D: Crack Patterns on Top after 500 Load Cycles at 883 kN

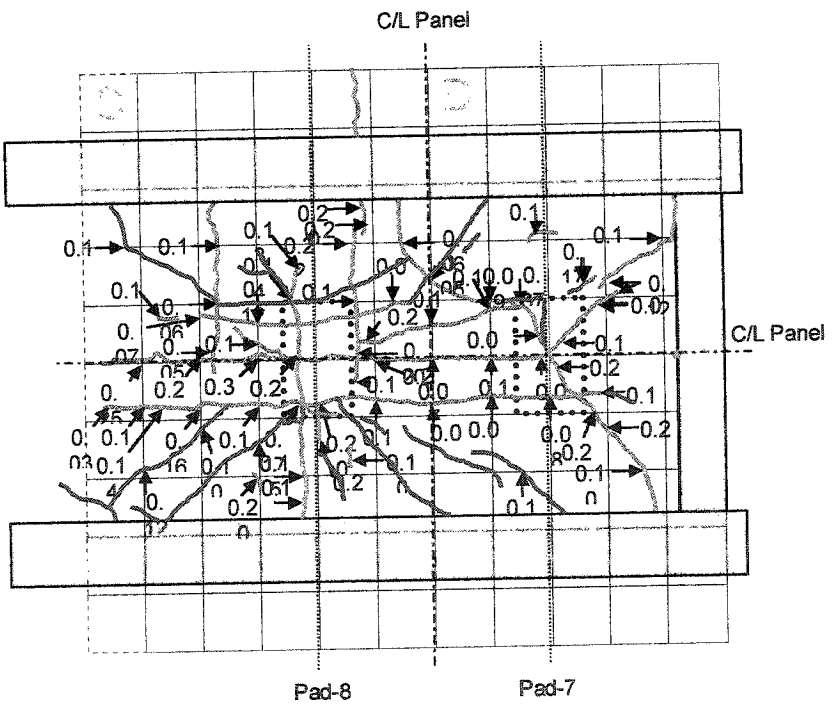

Figure 5-65 Panel-D: Crack Pattern on Soffit after 500 Load Cycles at 883 kN

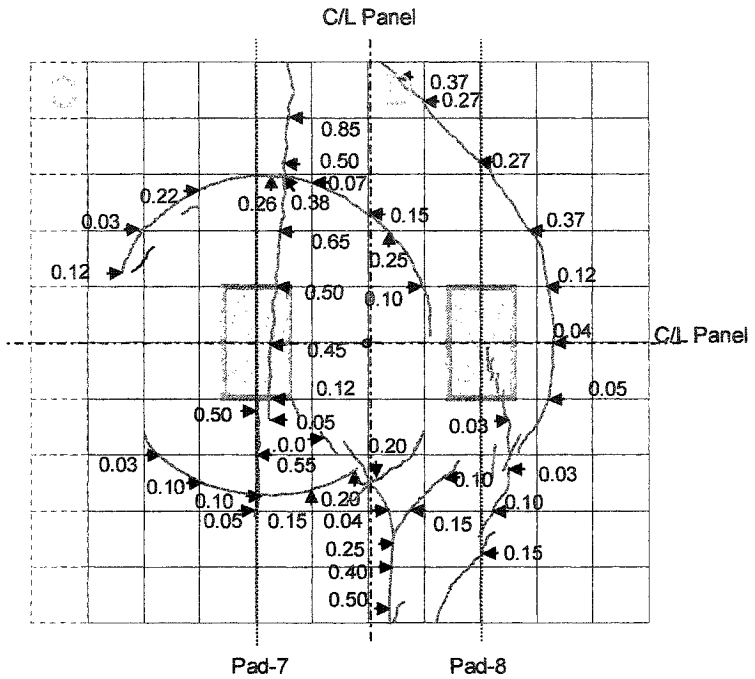

Figure 5-66 Panel-D: Crack Pattern on Top after 5,000 Load Cycles at 883 kN

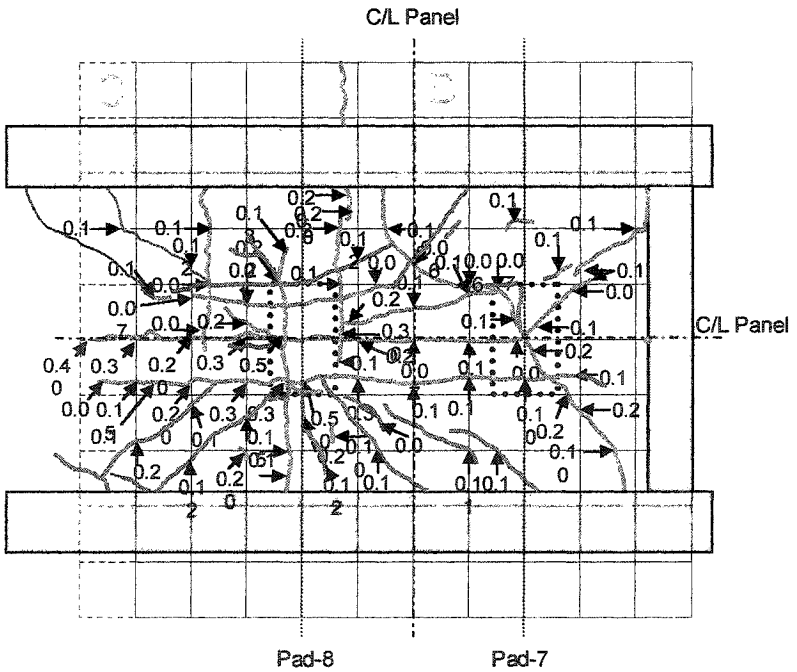

Figure 5-67 Panel-D: Crack Patterns on Soffit after 5,000 Load Cycles at 883 kN

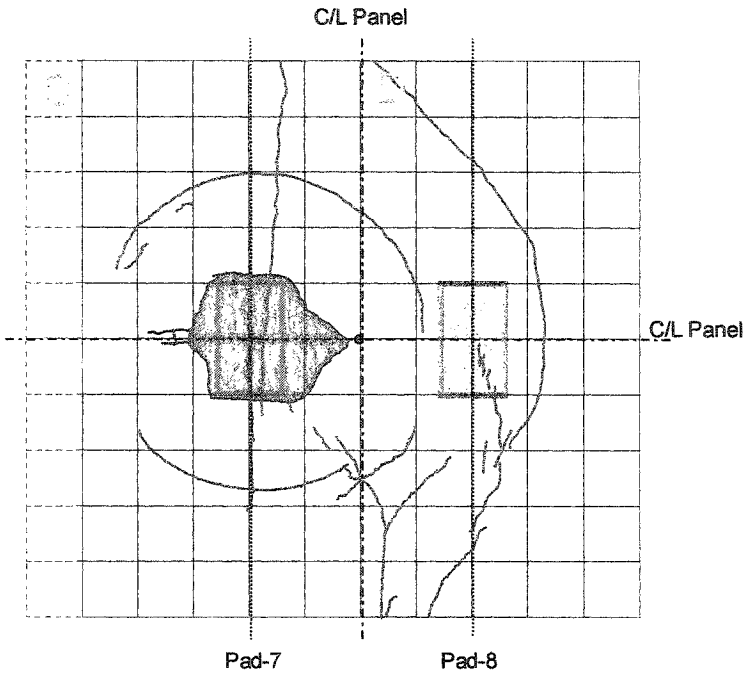

Figure 5-68 Panel-D: Crack Pattern on Top after Failure

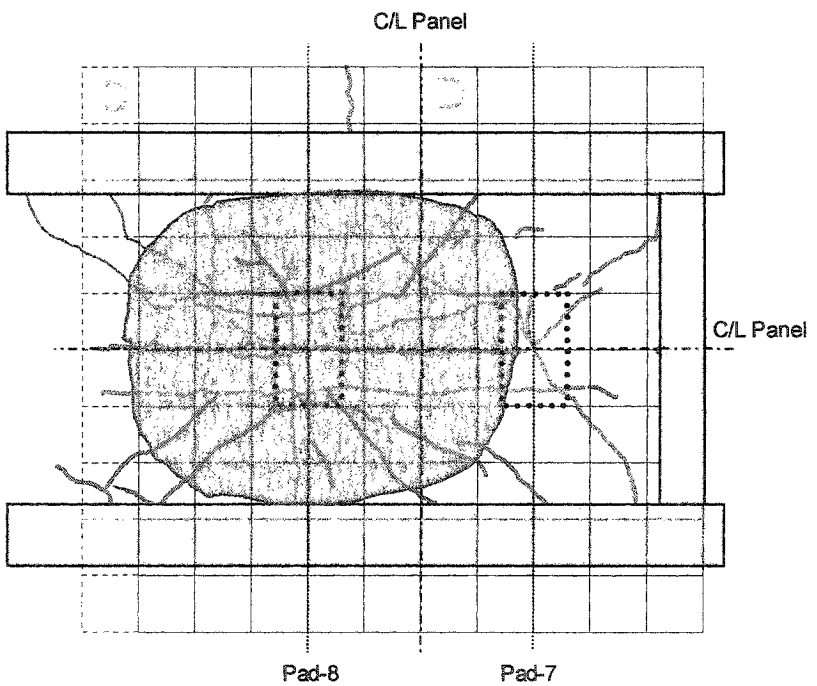

Figure 5-69 Panel-D: Crack Pattern on Soffit after Failure

5.4.4 Results: Panel-B

5.4.4.1 General

Panel-B was tested under static loading conditions to validate the static failure load of the panel that was computed theoretically. The load was applied in five cycles. In the first four load cycles, the peak value was raised from 400 to 1,000 kN, in steps of 200 kN. In the fifth and the final load cycle, the load was raised until the failure occurred at 1,218 kN.

5.4.4.2 Panel-B: Conventional Instrumentation

Deflection

The load-deflection curve at failure is shown in Figure 5.70. The behaviour of the deck is nearly linear up to 1,000 kN and then becomes nonlinear up to failure.

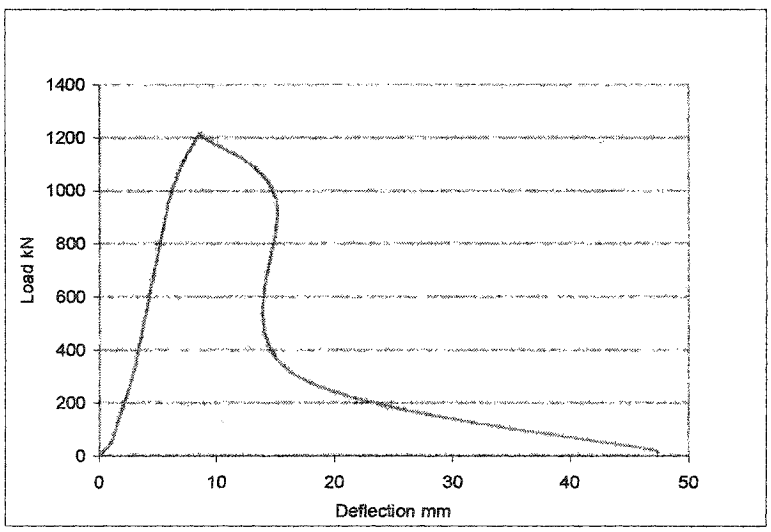

Figure 5-70 Panel-B: Load – Deflection Curve at Failure

Strap Strains

Load-strain curves for Straps 2 through 8 are shown in Figure 5.71. The linear behaviour of straps, particularly those adjacent to Load Pad-4, up to 1,000 kN load is evident. Load Pad-4 was 610 mm and 406 mm from Strap-5 and Strap-6, respectively. The nonlinear behaviour of Strap-7, and strap-8 is due to their initial curvature.

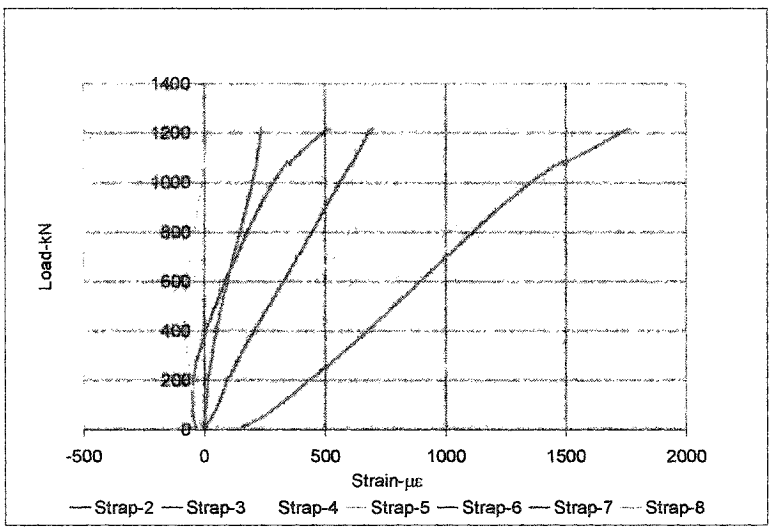

Figure 5-71 Panel-B: Load–Strap Strain Curves at Failure

5.4.4.3 Panel-B: Acoustic Waveforms

Acoustic waveforms before and after the failure of the panel are shown in Figure 5.72 and 5. 73 respectively. It is seen that the amplitude ratio has changed substantially, from 8.6 before test, to 22.2 after failure.

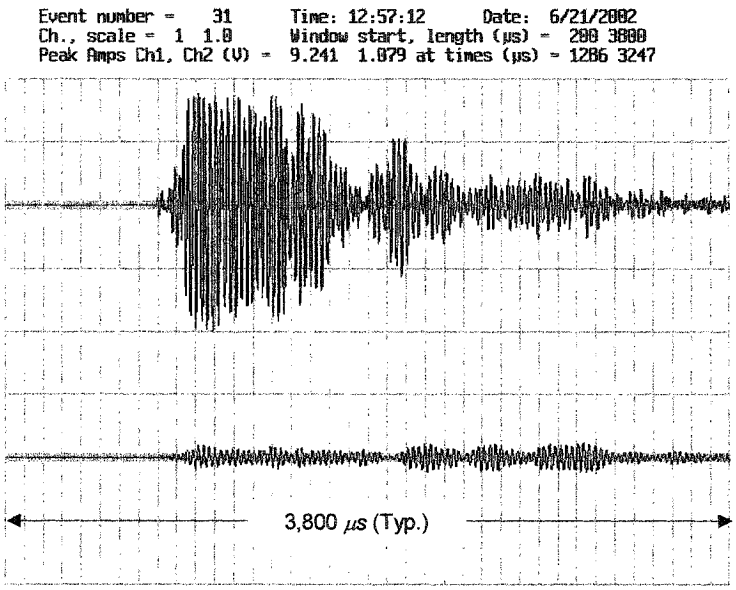

Figure 5-72 Panel-B: Acoustic Waveforms at Start of Test

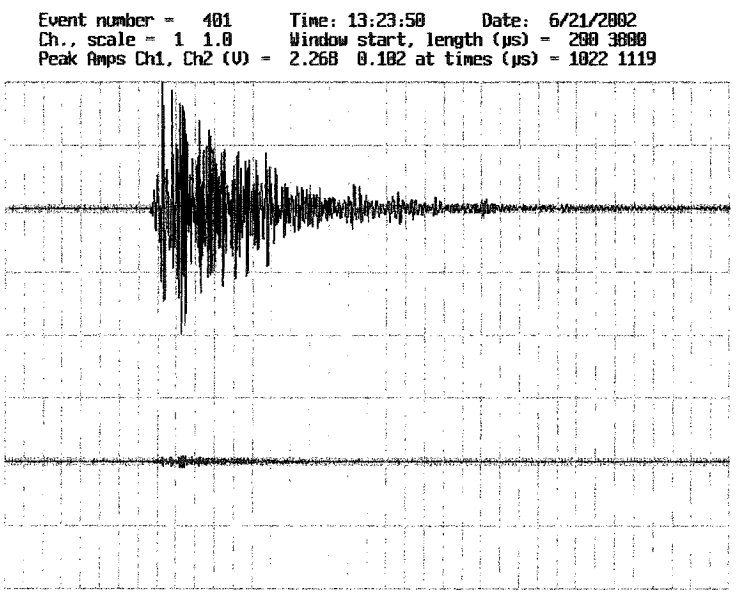

Figure 5-73 Panel-B: Acoustic Waveforms after Failure

5.4.4.4 Panel-B: Crack Patterns

The crack patterns on the top surface and the soffit are shown in Figure 5.74 and 5.75, respectively. The extent of cracking is relatively less than those of Panels A and D.

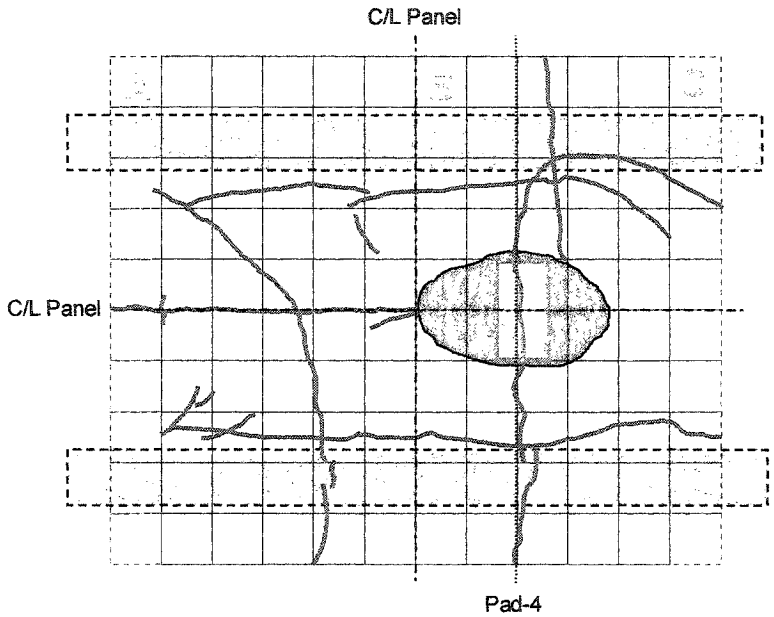

Figure 5-74 Panel-B: Crack Pattern on Top after Failure

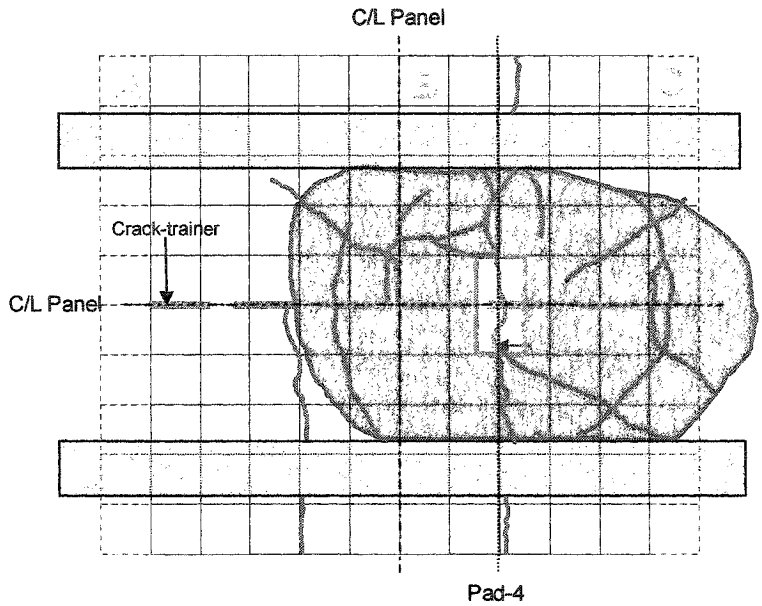

Figure 5-75 Panel-B: Crack Pattern on Soffit after Failure

5.4.5 Results: Panel-C

5.4.5.1 General

Before commencement of the test, the panels on the either side of Panel-C (Panel-B and Panel-D) had already been tested to failure. These failures caused significant damage to concrete in Panel-C.

It was decided to apply the cyclic load with a peak value of 900 kN. During the test, it was noticed that the overall deflection of the model at 392.4 kN (load level during Phase-I) was 15% higher than previously recorded values. Considerably longer time was required for each load cycle to achieve the peak load. To expedite the loading process, the loading frame in use was replaced by another frame of larger stiffness. Additional supports were also introduced under the main girders to reduce their effective span.

5.4.5.2 Panel-C: Conventional Instrumentation

Deflection

The load-deflection curves for the first and the final four cycles are shown in Figure 5.76. The gradual increase in the deflection over the final four cycles is clearly seen. The failure of the Panel-C is gradual in contrast to the failure of Panel-B shown in Figure 5.70.

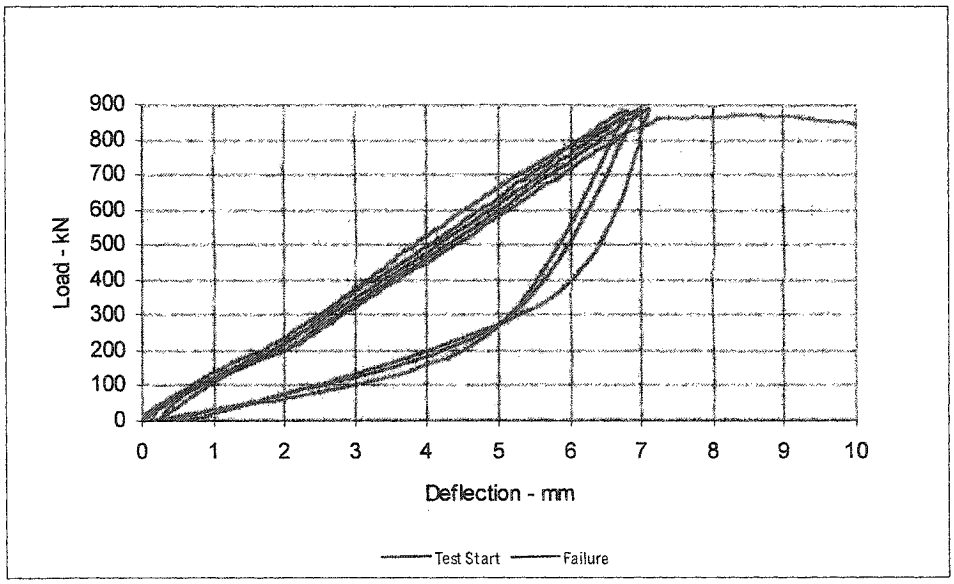

Figure 5-76 Panel-C: Load-Deflection Curves

Strap Strains and Bar Strains

The load-strain curves for Strap-8 and Strap-9 at the beginning of the test and the final four load cycles are shown in Figure 5.77. The strain gauge on Strap-8 stopped functioning before failure of the panel. There is a significant increase in strain in Strap-9 at failure, however, its behaviour is stable up to the failure of the panel. Similarly, the load- bar strain curve for strain gauge SN-4 as shown in Figure 4.19, shows substantial

increase but a stable behaviour up to the penultimate cycle. The sudden surge in strain occurs as the panel fails and the bar ruptures.

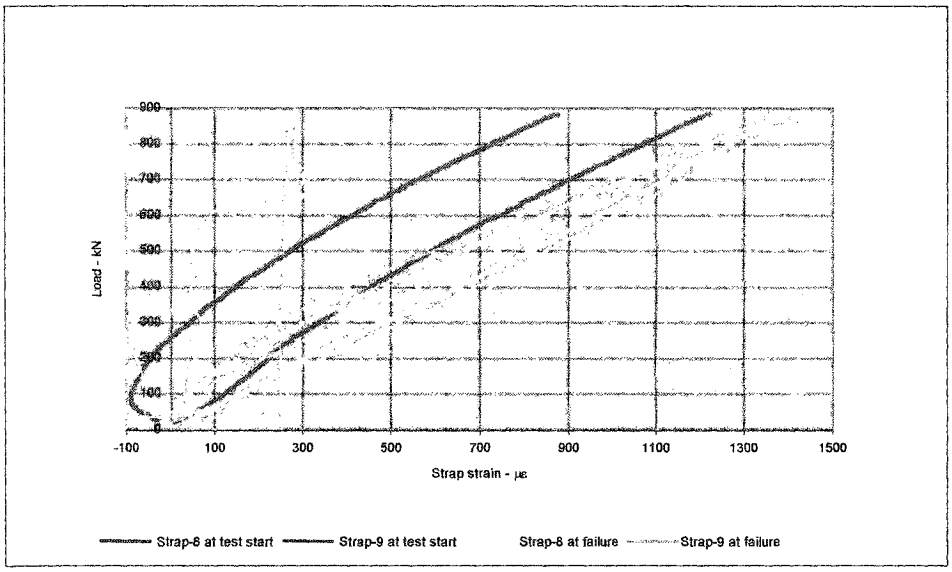

Figure 5-77 Panel-C: Load-Strap Strain Curves

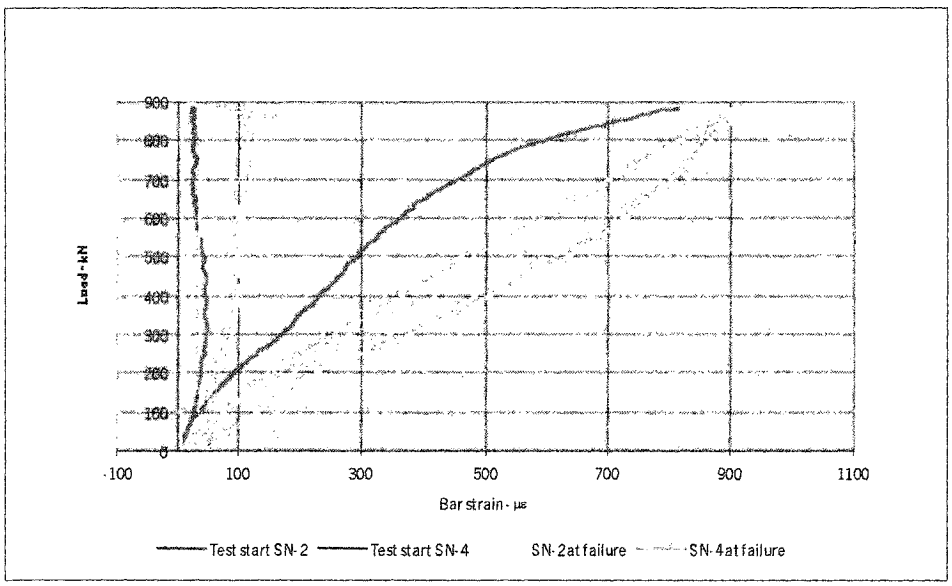

Figure 5-78 Panel-C: Load–Bar Strain Curves

5.4.5.3 Panel-C: Acoustic Waveforms

The acoustic waveforms at the beginning of the test and after failure are shown in Figure 5.79 and Figure 5.80, respectively. There is a significant difference in the two waveforms. The amplitude ratios before test and after failure are 2.9 and 41.9, respectively indicating extremely severe damage.

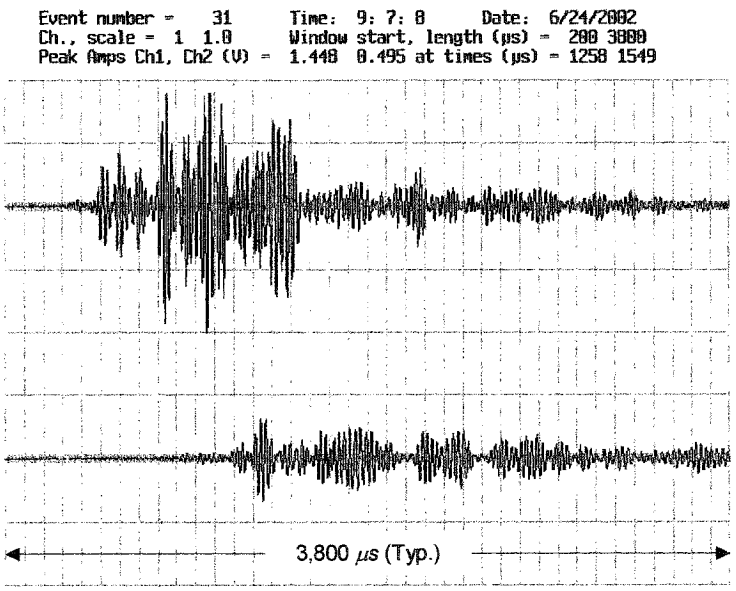

Figure 5-79 Panel-C: Acoustic Waveforms at Test Start

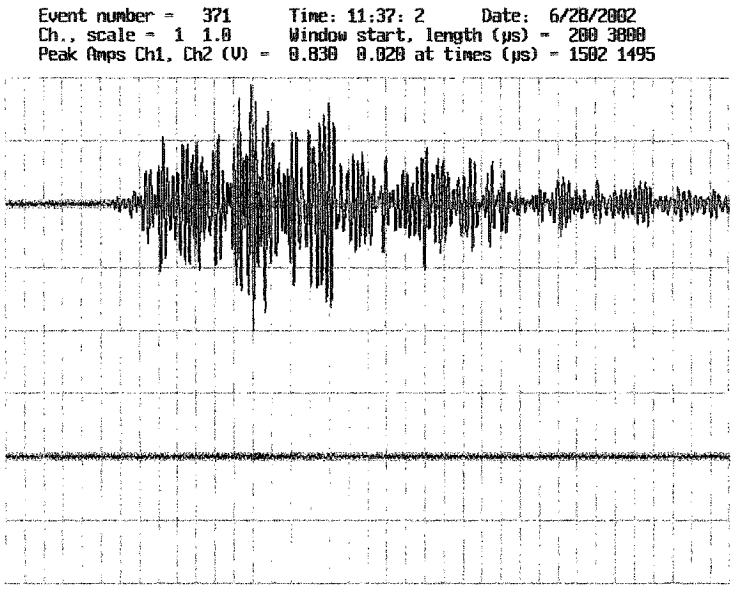

Figure 5-80 Panel-C: Acoustic Waveforms after Failure

5.4.5.4 Panel-C: Crack Patterns

Crack patterns on the top surface and the soffit at the beginning of the test and after failure are shown in Figures 5.91 through 5.94. The damage to Panel-C before the start of the test can be clearly seen in Figure 5.91 and Figure 5.92. Despite prior damage, the failure is caused by punching shear. The crack pattern on the top surface is different from that in Panel-A and Panel-D.

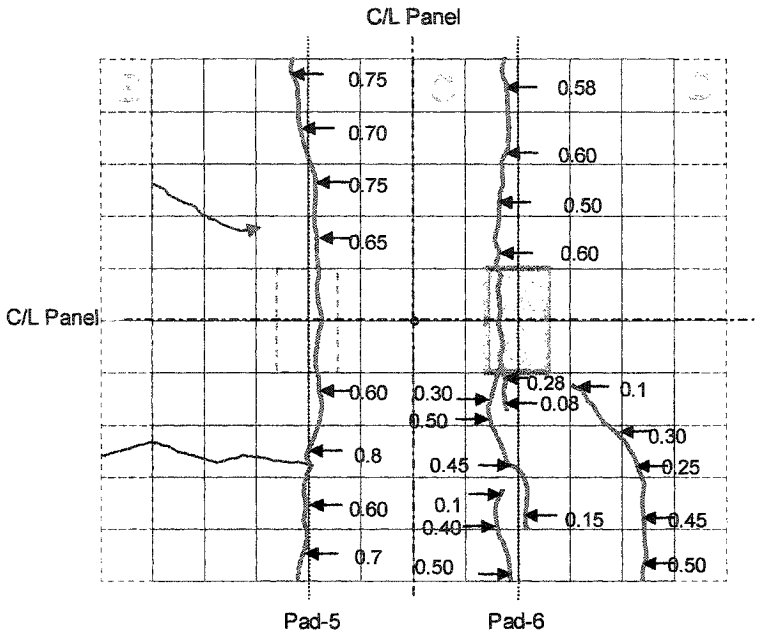

Figure 5-81 Panel-C: Crack Patterns on Top at Test Start

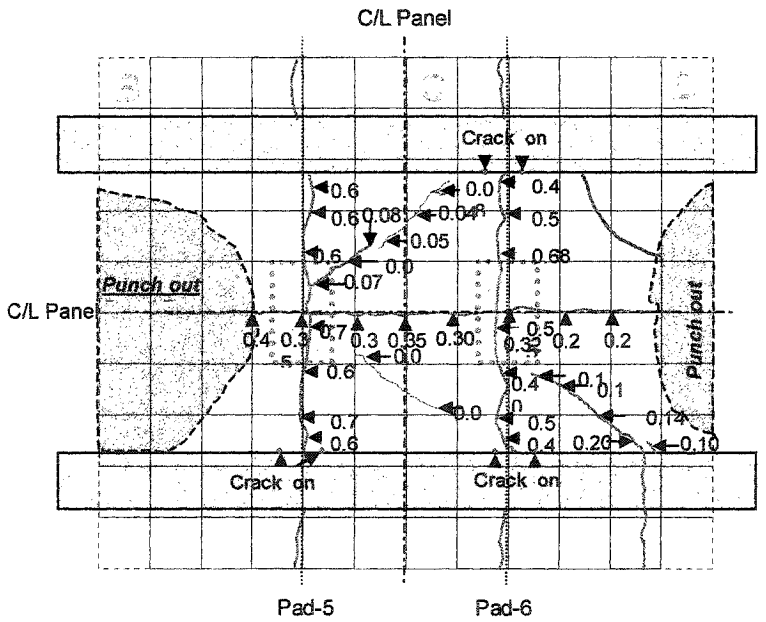

Figure 5-82 Panel-C: Crack Patterns on Soffit at Test Start

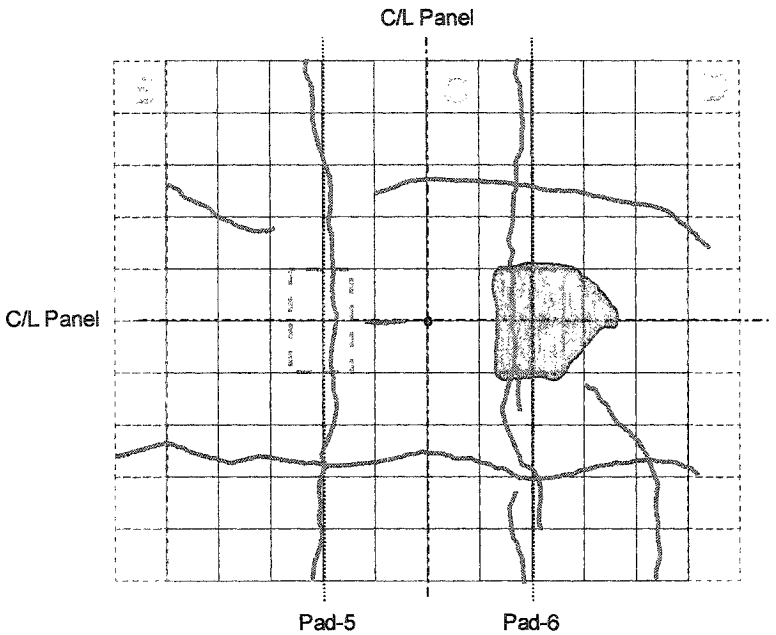

Figure 5-83 Panel-C: Crack Patterns on Top after Failure

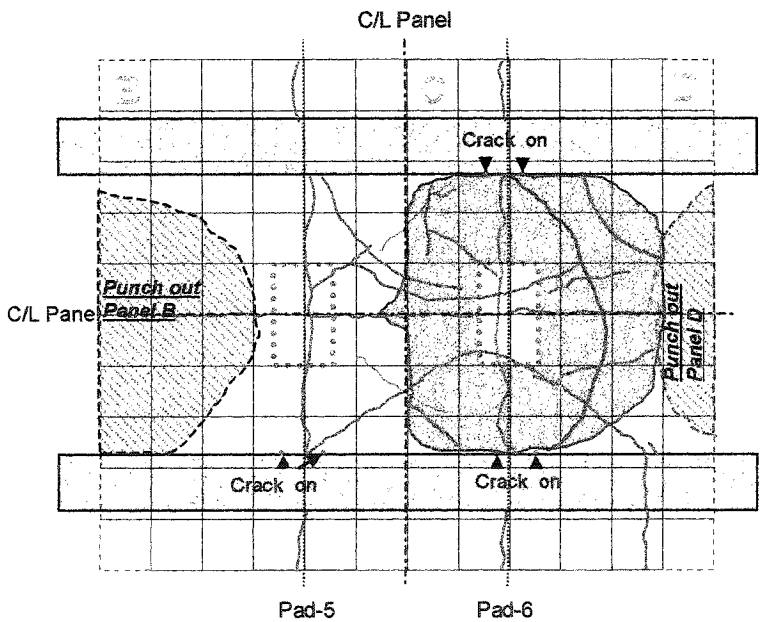

Figure 5-84 Panel-C: Crack Patterns on Soffit after Failure

5.5 Post-Failure Acoustic Survey

As discussed in Section 4.3.7, an acoustic survey of the deck slab was carried out at the end of the test program to assess internal damage in concrete. Relative attenuation image of the deck surface was generated showing the extent of the damage.

The view of the deck slab after failure of all the four panels is shown in Figure 5.85, while the tomographic images are shown in Figures 5.86 and 5.87.

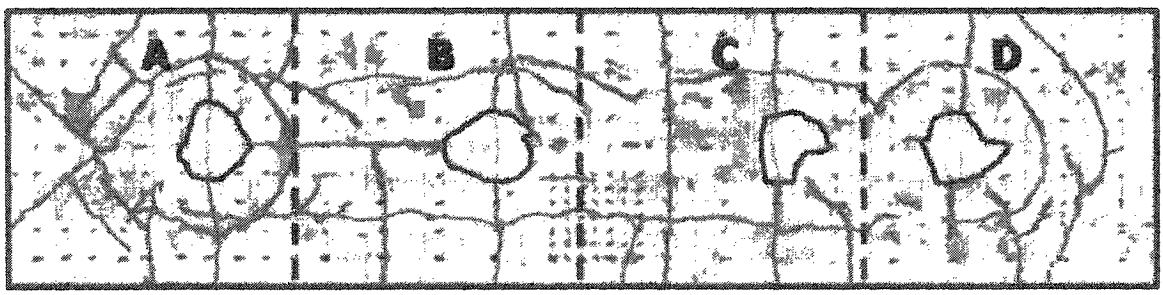

Figure 5-85 Composite Image of Deck Slab

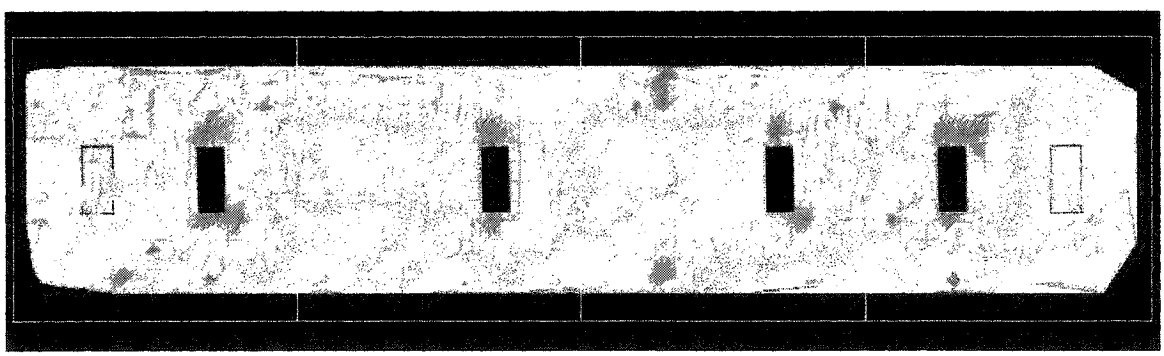

Figure 5-86 Relative Attenuation Image of Deck Slab

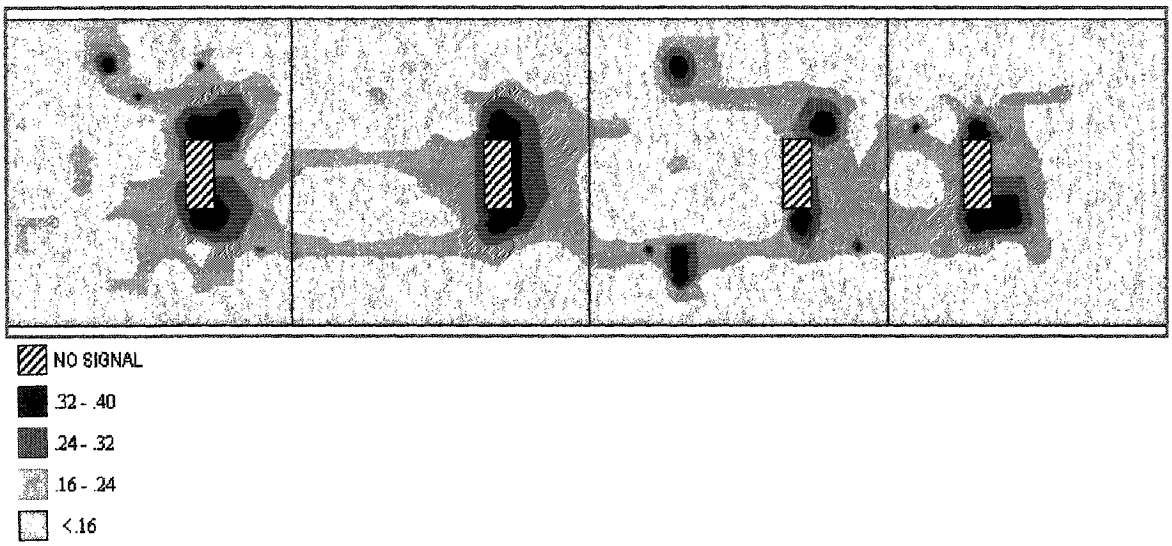

Figure 5-87 Relative Attenuation Image of Deck Slab Showing Extent of Damage

Discussion

Comparing Figures 5.85 and 5.87, it is evident that there is an obvious correlation between the regions of highest acoustic attenuation shown in Figure 5.87, and many of the damaged regions visible on the top deck surface.

1. Each of the four punch-out cones is surrounded by a zone of greater than 16% relative attenuation, which increases to up to 40% relative attenuation immediately adjacent to detached concrete slab segments.
2. Several longitudinal cracks are imaged as zones of greater than 16% relative attenuation. The full-depth crack over the crack trainer in Panel-B as well as the longitudinal cracks along the girder are clearly visible.
3. Several other cracks are partially imaged as zones of greater than 16% attenuation such as the full-depth transverse crack in Panel-C and several radial and circumferential cracks in Panel-A.

The cracks that are not imaged well include the discontinuous longitudinal crack running from Panel-A to Panel-D near the north girder and most of the transverse cracks. The discontinuous longitudinal crack did not have a consistently wide aperture (as compared to the longitudinal cracks that were well imaged) suggesting that it was shallower and thus would be expected to have a lower level of relative attenuation. The transverse cracks are in a direction parallel to the survey direction and thus are not crossed by the acoustic wave raypath between the sensors.

An important aspect of these imaging results is that there are no regions with high levels of relative attenuation that do not have corresponding damage. In other words, the acoustic imaging technique does not generate false positives indicating damage where there is none. This aspect of the acoustic imaging technique makes it suitable to correctly identify the locations where damage is present.

It can be seen that the cracks that are at perpendicular to the direction of the survey were detected correctly while the cracks that ran parallel to the survey direction were not imaged. This leads to the conclusion that a multidirectional survey will help in obtaining a better acoustic image of the damage in concrete.

5.6 Summary of Test Results for Phase-I and Phase-II

In Phase-I, all the panels were subjected to 1,700 load cycles of 393 kN peak load. In Phase-II, Panel-A, Panel-D, and Panel-C were tested to failure under cyclic loading conditions, while Panel-B was tested under static loading conditions. The magnitude of the peak load was increased in the case of Panel-A, and Panel-D. All the panels failed in punching shear. The details of the cyclic and static test have been summarized in Table 5.5.

Table 5-5 Summary of Failure Data for Panels

	Number of load cycles							
Peak load (kN) (t)	393 (40)	638 (65)	785 (80)	883 (90)	981 (100)	1030 (105)	1079 (110)	1218 (124)
Panel A	50,000*	10,000	2,000	1,243 (F)	-----			
Panel D	1,700*	----------	--------	5,000	41	50	108 (F)	
Panel C	1,700*	----------	--------	304 (F)				
Panel B	1,700*	1	1	--------	1		1	1(F)

* 1,700 load cycles applied in Phase-I.
(F) Denotes failure at that peak load

6.0 DISCUSSION OF TEST RESULTS

6.1 General

The testing in Phase-I focussed on comparing the performance of the four panels after subjecting each of them to an equal number of load cycles of the same magnitude. The testing in Phase-II focussed mainly on determining the fatigue life of each configuration. The discussion of results has been divided in two separate sections: Phase-I and Phase-II.

As discussed in Chapter 4, during Phase-I, all the panels were subjected to cyclic load with a nominal peak value of 392.4 kN. During Phase-II however, the peak loads varied from 393 kN to 1,079 kN. In order to compare the response of all the panels at varying load levels, values of strains and displacements were extracted at 393 kN load level from each data file. Therefore, the values of various responses discussed in this section are not the maximum values. The maximum values, where shown, are clearly identified.

6.2 Parameters for Discussion

During the test, five parameters were identified that reflected the state of fatigue damage in the test model. Those factors were:

- strain in the straps (particularly for straps located on either side of the load pad),
- slab deflection,
- acoustic attenuation,
- crack patterns,
- concrete internal strains.

A summary of the results for each parameter is presented in Sections 6.2.1 to 6.2.5, followed by a detailed discussion in Sections 6.3, and 6.5. The discussion of the results is based mainly on these factors. The variation in concrete strains is also briefly discussed.

6.2.1 Overview of Strap Strain Results

As the test progressed, there was a marked increase in the strain levels of the straps that were located adjacent to the load pad. Generally, the strains followed a pattern consistent with the three fatigue stages described by many researchers (Do et al. 1993). The maximum magnitude of the strap-strains during the fatigue tests also indicates the possibility of failure due to yielding of straps.

6.2.2 Overview of Slab Deflection Results

The deflection of the slab was continuously monitored during the test. The deflection pattern was indicative of the damage occurring in the concrete deck slab. During the test, however, it was noticed that under repeated loading and unloading, the load pads tended to move gradually out of position, thus, adversely affecting the deflection values. Once detected, the problem was corrected by frequently checking and adjusting the load pad, and by installing an additional displacement transducer to monitor the deflection of the slab.

6.2.3 Overview of Acoustic Attenuation Results

In those cases where the probable zone of damage was clearly identified, acoustic attenuation could be used effectively as an independent tool for detecting damage within the concrete mass. While any substantial damage in the concrete can be detected by a significant increase in strains and deflections, and by visual inspection, acoustic attenuation can help detect initiation of damage at the microscopic level. The internal damage in the concrete can otherwise be detected only when a crack or a defect within the body of the concrete grows and propagates to the surface. In the case of steel-free deck slabs, it is known that a longitudinal crack develops midway between the two adjacent girders. Therefore, the instrumentation was placed to monitor the zone of damage. Throughout the test, acoustic attenuation provided information that was

consistent with the data collected by conventional instrumentation and the visual observations.

6.2.4 Overview of Crack Patterns

Cracks were measured and mapped after the 10^{th} load cycle and then after each 100 load cycles during Phase-I of the test. During Phase-II, the cracks were inspected after each 100 load cycles and were mapped whenever new cracks appeared, or the existing cracks had either widened or propagated further. The crack patterns also followed a trend similar to the strain patterns. The cracks were found to grow at a faster rate initially, and appeared to have stabilized for most of the duration of Phase-II. There was a minor increase in the extent of the cracks. One important difference between the crack patterns mapped during Phase-I and Phase-II of the testing was the location of cracks. In Phase-I, most of the cracking appeared to have taken place on the soffit or the bottom surface of the deck slab, while, in Phase-II, the majority of cracking occurred on the top surface. Just prior to the ultimate failure, the shear cracks defining the perimeter of the punch cone appeared on the soffit.

6.2.5 Overview of Concrete Internal Strains

The response of the embedment gauges has been plotted against the number of load cycles applied. Each figure showed the response of three embedment gauges, placed vertically one above another, at one of the three locations as shown in Figure 6.1 a) south side b) central, and c) north side. Each gauge has a two-letters identification code. The first letter denotes the position of the gauge group on the panel. S, C, and N, stand for south, centre, and north, respectively. The second letter identifies the vertical position of a gauge in the group. T, M and B, stand for the top, middle, and bottom gauges respectively. Figure 6.1 illustrates the gauge nomenclature.

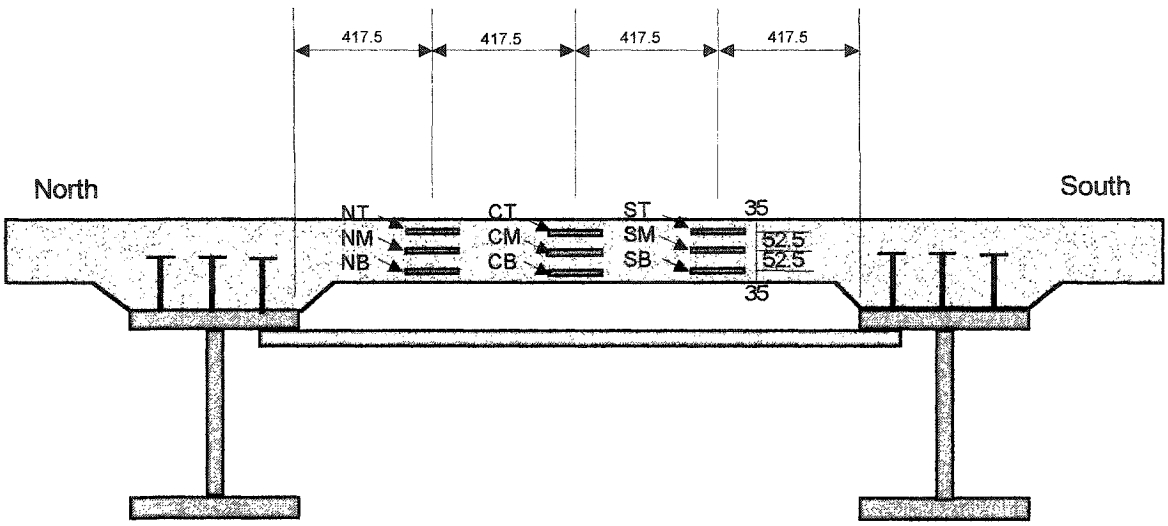

Figure 6-1 Embedment Gauge Identification

6.2.6 Bar Strains (Panel-C and Panel-D)

Each instrumented bar had five strain gauges along its length. Each strain gauge was identified by a number preceded by the letters SN, indicating that the gauge numbers beginnning from the southern girder gauge. Thus, gauge SN-1 was closest to the south girder and gauge SN-5 was closest to the north girder. Figure 6.2 shows the position of strain gauges on the instrumented bar.

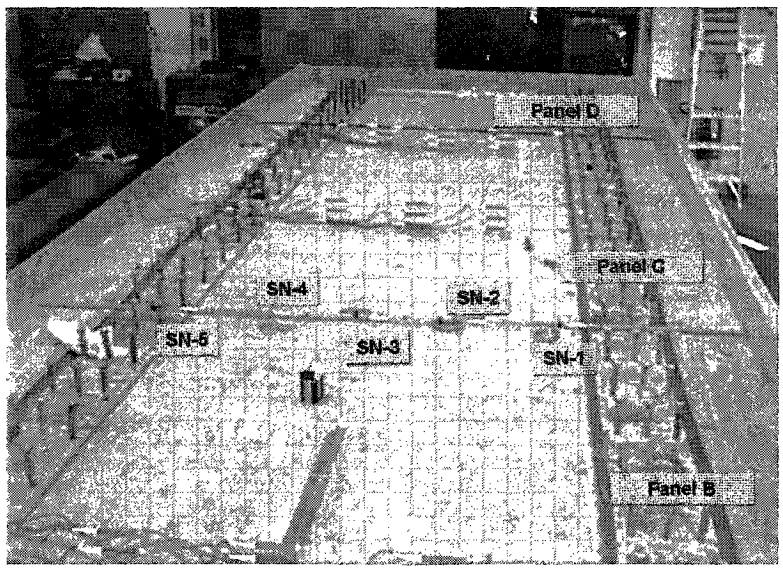

Figure 6-2 Identification of Strain Gauges on Instrumented Bar

6.3 Discussion - Phase-I

6.3.1 General

The cyclic loading was alternately applied at two load pads on Panels A, C, and, D, and only on one load pad on Panel-B. The sequence of loading on each load pad is summarized in Table 5.2. In the following discussion, the load pad at which the cyclic loading was applied has been termed as the active load pad, while the other load pad has been termed as the passive load pad. The trends in variation in deflection, strap strains, concrete internal strains, and bar strains in Panel-C and Panel-D, for the first load pad were different from those of the second load pad. This resulted from the change in the relative position of various sensors when the load position was changed from one load pad to another. For each panel except Panel-B, the discussion has been limited to the effects of load applied at the load pad that was also used on Phase-II. The crack patterns, and acoustic attenuation are discussed for the entire span of the test for each panel.

6.3.2 Strap Strains

The trends in the strap strains in Panel-A, Panel-C, Panel-D, and Panel-B are shown in Figures 6. 3 through Figure 6.6. The strap strain levels in Panel-A and Panel-C show a pattern of higher increases up to 600 load cycles followed by a gradual and continual growth until the end of the test. However, in Panel-D and Panel-B, the strain levels show significant fluctuations within the first 300 load cycles followed by a stable behaviour up to the end of 1,700 load cycles. As Load Pad-3 was positioned directly above Strap-5 in Panel-B, the strain in Strap-5 was significantly higher than the other straps. It is noted in Panel-B, the load pad was asymmetrically placed on one side of a full-depth longitudinal crack.

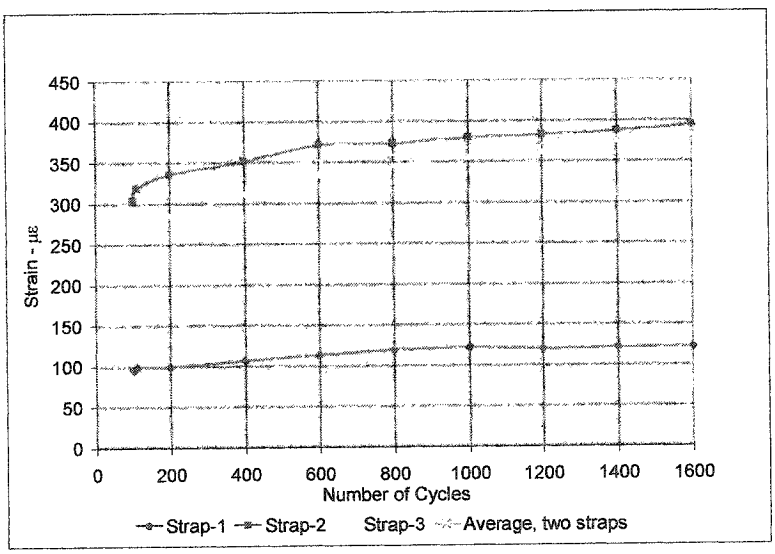

Figure 6-3 Panel-A: Active Load Pad-2, Strap-Strain Patterns

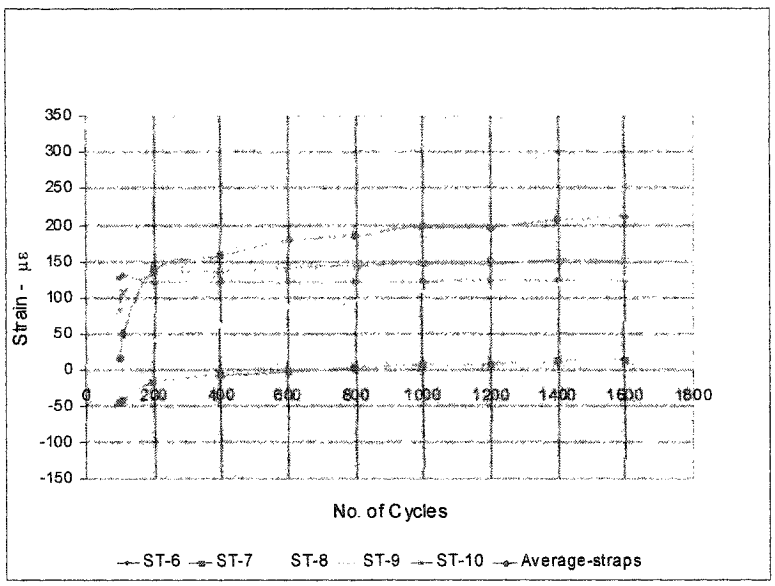

Figure 6-4 Panel-C, Active Load Pad-6: Strap-Strain Patterns

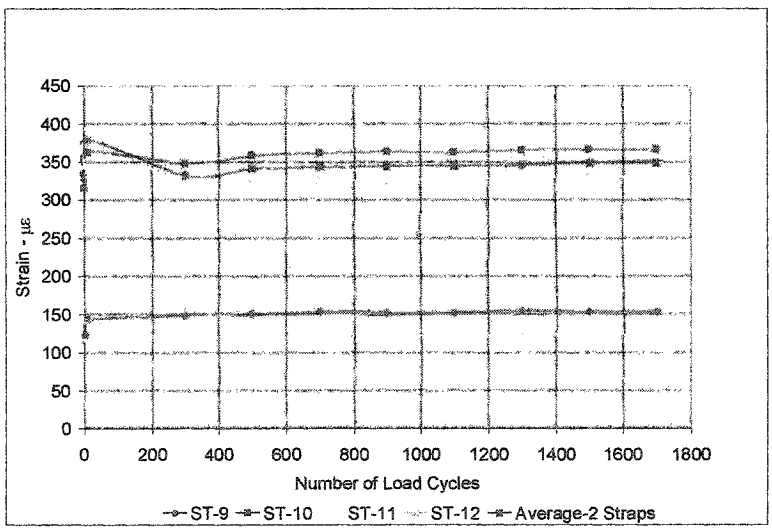

Figure 6-5 Panel-D, Active Load Pad-7: Strap-Strain Patterns

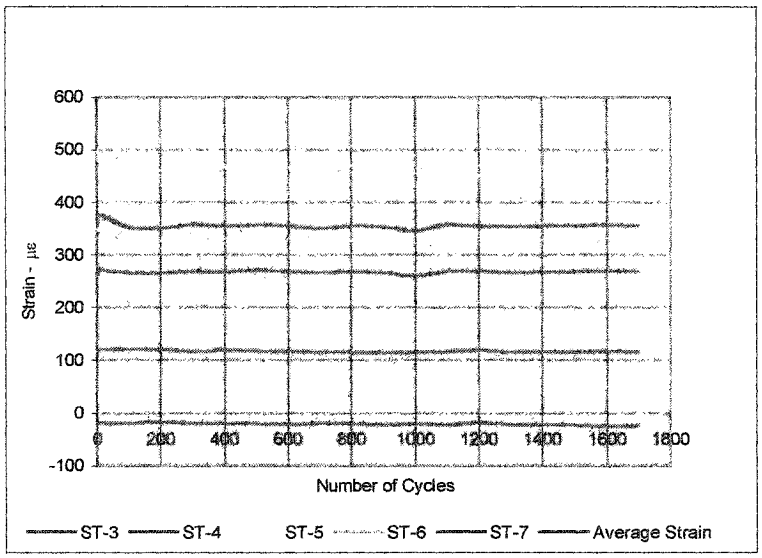

Figure 6-6 Panel-B, Active Load Pad-3: Strap-Strain Patterns

6.3.3 Deflection

The trends in slab deflection under load pads for Panel-A, Panel-C, Panel-D, and Panel-B are shown in Figure 6.7 through Figure 6.10. In the case of Panel-A and Panel-C, the deflection increased gradually up to the end of the test. The magnitude of deflection in Panel-A was the highest, followed by the deflection in Panel-C. The deflection in Panel-D was the smallest, which can be attributed to the presence of crack-control reinforcement. The deflection in Panel-B cannot be compared as the deflection was measured under the load pad that was positioned away from the centre of the panel. Following an initial sharp drop, the deflection pattern shows a gradual reduction up to 1,000 load cycles and subsequent stable behaviour. The drop in deflection in Panel-B can be attributed to the initial closure of the full-depth crack under load. This is also reflected in the acoustic attenuation results of Panel-B which are discussed in Section 6.3.5.

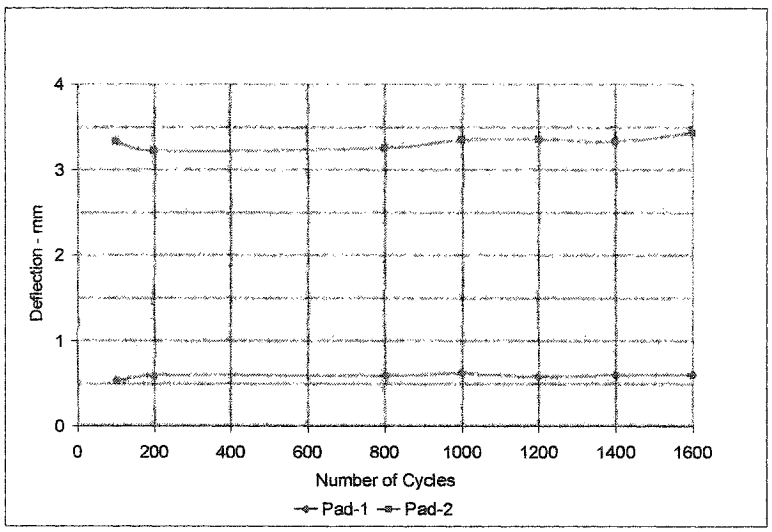

Figure 6-7 Panel A: Active Load Pad-2: Deflection Patterns

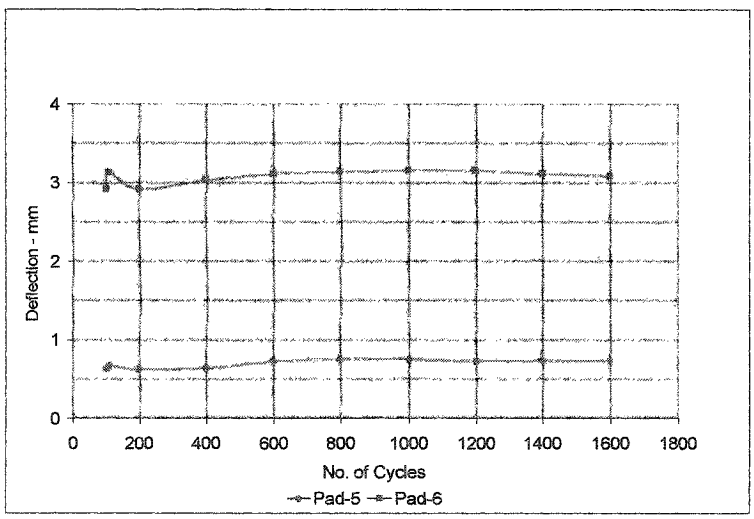

Figure 6-8 Panel-C, Active Load Pad-6: Deflection Patterns

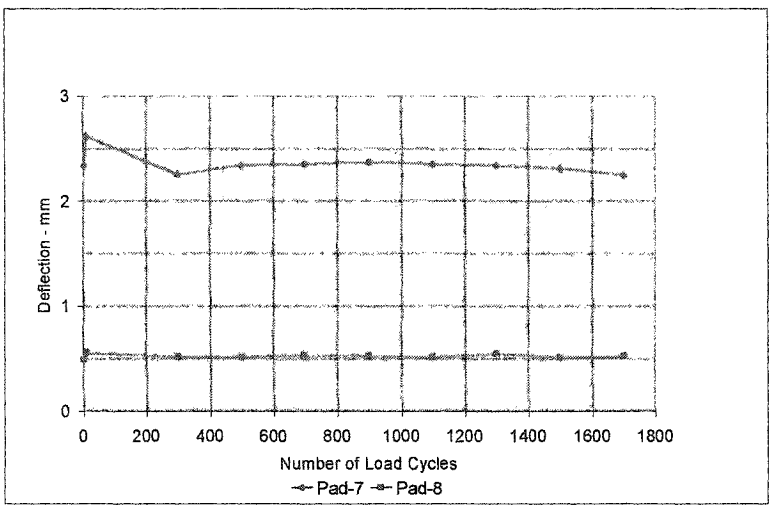

Figure 6-9 Panel-D, Active Load Pad-7: Deflection Patterns

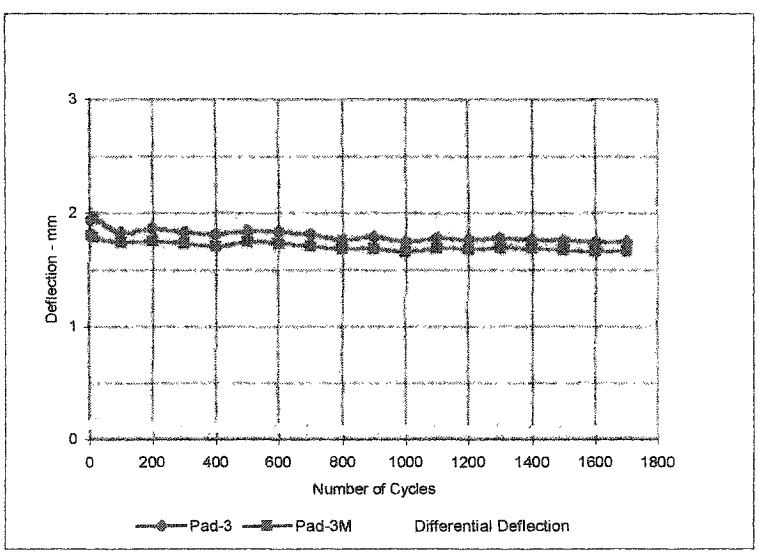

Figure 6-10 Panel-B, Active Load Pad-3: Deflection Patterns

6.3.4 Concrete Internal Strains

The trends in concrete internal strains for Panel-A, Panel-C, Panel-D, and Panel-B are shown in Figure 6.11 through 6.17. The main purpose of presenting these trends is to compare the strain levels and the survival of gauges in each panel. The strain levels stabilized within the first 100 load cycles in Panel-A, Panel-C, and Panel-B. In Panel-D, the strains stabilized within the first 300 load cycles. All panels exhibited stable behaviour up to the end of the test. The strain levels in Panel-A were the highest while those in Panel-D were the lowest. The strains under asymmetric loading in Panel-B, also stabilized and remained nearly unchanged from 1,100 to 1,700 load cycles. Concrete under a load pad is highly stressed. The embedment gauges at the centre of the panel, CT, CM, and CB, failed in Panels A, C and B. The gauge CT in Panel-C survived for 1,500 load cycles. However, all the embedment gauges in Panel-D survived for most part of Phase-II. The spacing of GFRP crack-control reinforcement in Panel-C was larger than that of steel crack-control reinforcement in Panel-D. The crack-control reinforcement appears to have a positive effect on the strain levels within the deck slab.

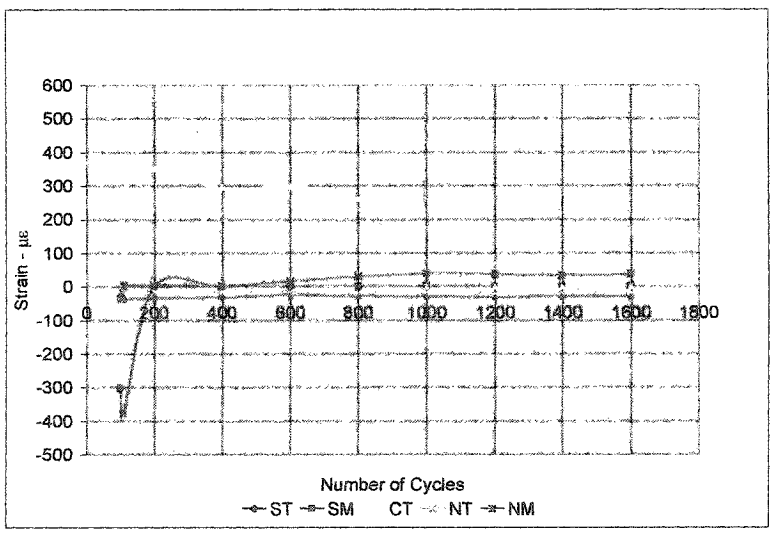

Figure 6-11 Panel A, Active Load Pad-2: Concrete Strain Patterns

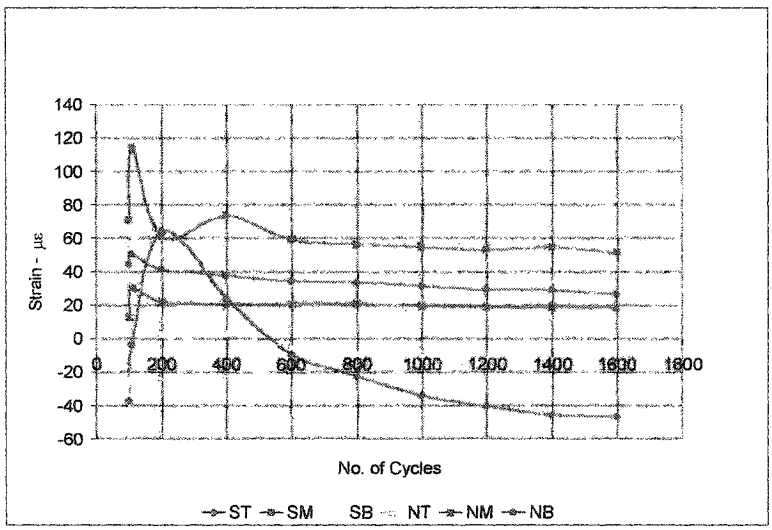

Figure 6-12 Panel-C, Active Load Pad-6: Concrete Internal Strain Patterns for South and North Gauges

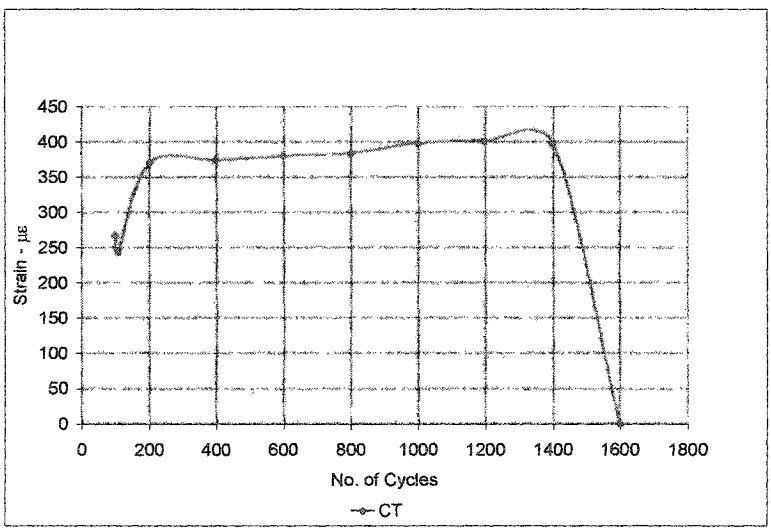

Figure 6-13 Panel-D Active Load Pad-6: Concrete Internal Strain Pattern CT

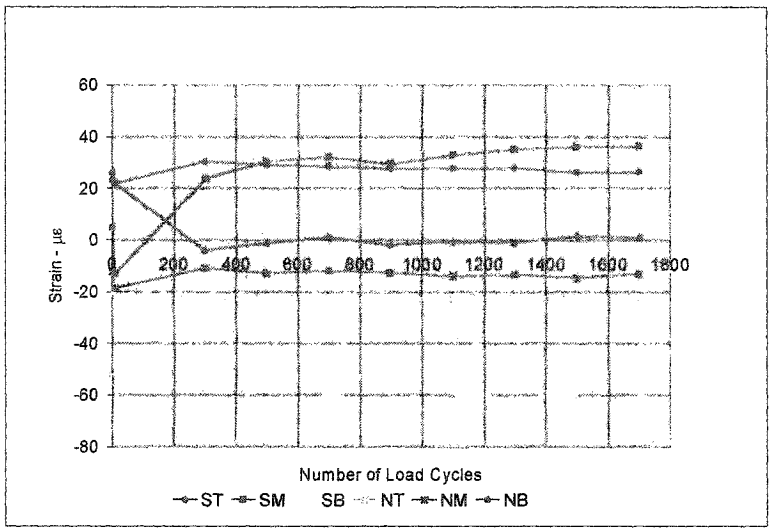

Figure 6-14 Panel-D, Active Load Pad-7: Concrete Internal Strain Patterns ST, SM, SB, NT, NM, and NB

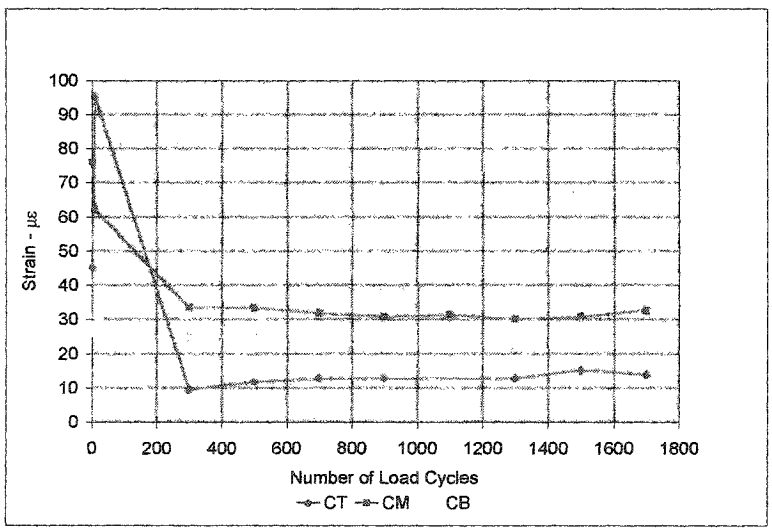

Figure 6-15 Panel-D, Active Load Pad-7: Concrete Internal Strain Patterns CT, CM, and CB

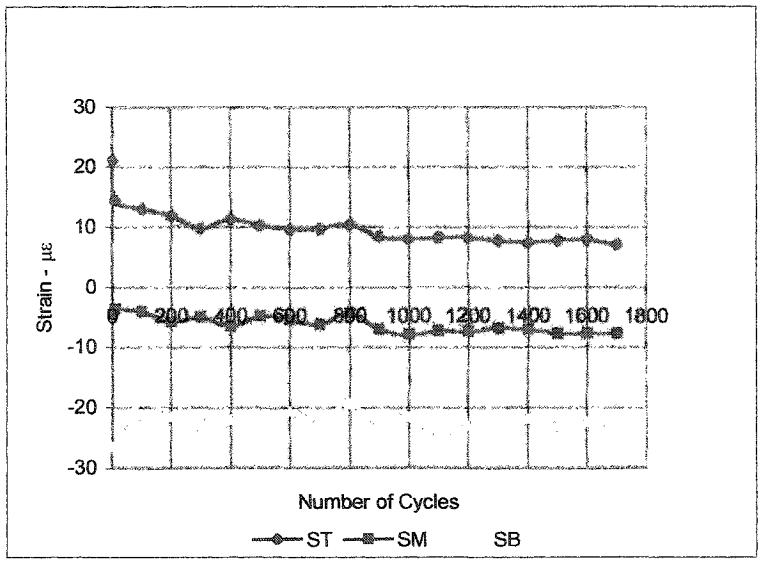

Figure 6-16 Panel-B: Concrete Internal Strain Patterns, ST, SM, and SB (Side Not Loaded)

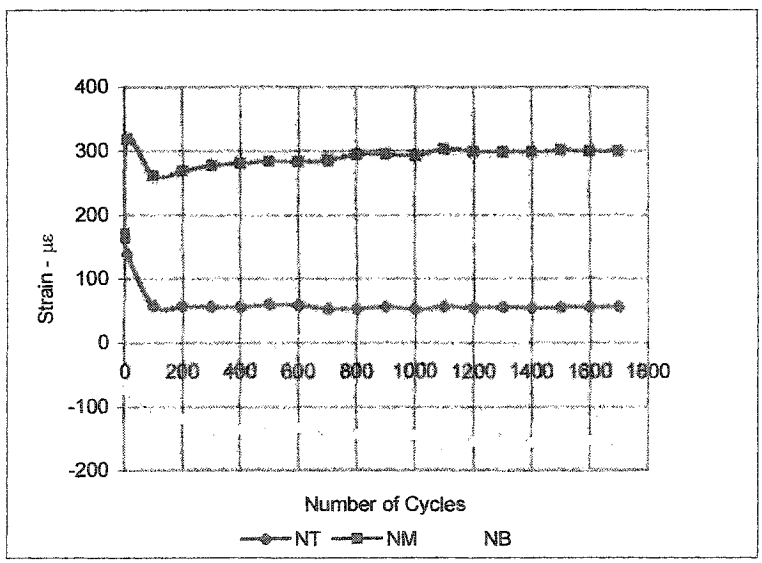

Figure 6-17 Panel-B: Concrete Internal Strain Patterns, NT, NM, and NB (Loaded Side)

6.3.5 Acoustic Attenuation Results

The acoustic attenuation results presented here exhibit trends that are similar to those observed through conventional instrumentation as discussed in Sections 6.3.1 through 6.3.4. An increase in the integrated amplitude ratio is associated with a corresponding damage growth within the concrete. In each case, there was a significant increase in the ratios at the commencement of the test, followed by a gradual growth of damage. The results for each panel are discussed briefly in Sections 6.3.5.1 through 6.3.5.4.

6.3.5.1 Panel-A (Figure 6.18)

1. A sharp change in the amplitude ratio during the first few loading cycles indicates an immediate increase in damage.
2. Fluctuating amplitude ratios over the first 400 to 600 load cycles indicates a relatively high level of damage accumulation.
3. The relatively stable amplitude ratios during the subsequent loading cycles indicate that the damage accumulation was gradual.

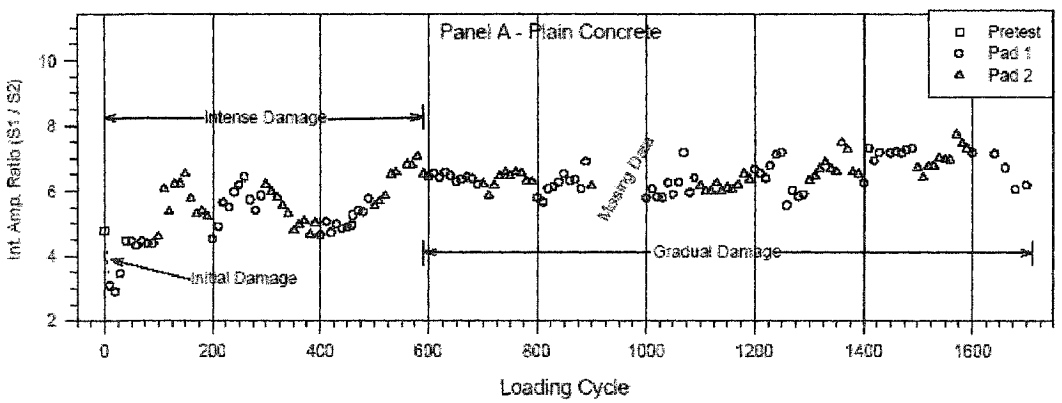

Figure 6-18 Panel-A: Integrated Amplitude Ratios

6.3.5.2 Panel-C (Figure 6.19)

1. A sharp change in amplitude ratio during the first few loading cycles indicates an immediate increase in damage.
2. There was significant increase in damage when the loading position was changed from Pad-5 to Pad-6.
3. The relatively stable amplitude ratios during the subsequent loading cycles indicate that the damage accumulation was gradual.

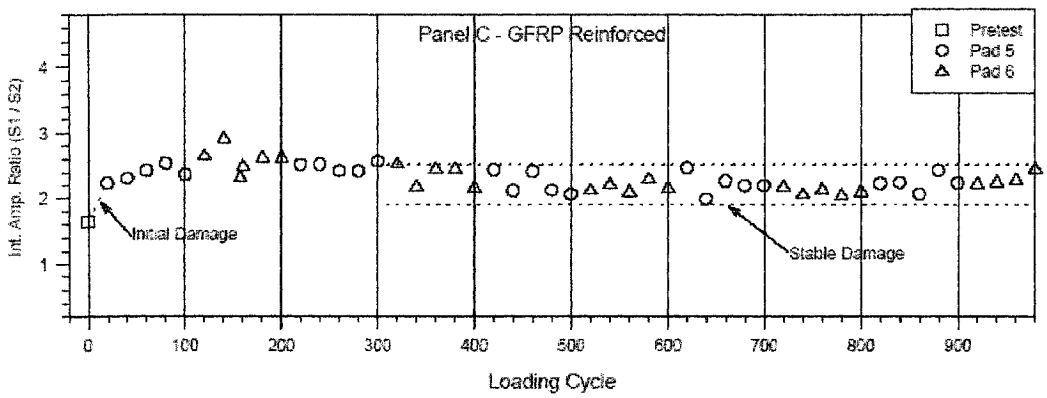

Figure 6-19 Panel-C: Integrated Amplitude Ratios

6.3.5.3 Panel-D (Figure 6.20)

1. There was an initial episode of cracking at the start of loading
2. There was another episode of cracking when loading was first switched from Pad-7 to Pad-8.
3. Most of the significant damage occurred over the first 300 to 400 load cycles.
4. From approximately 500 to 1,700 load cycles, there was continual but gradual increase in the extent of cracking.

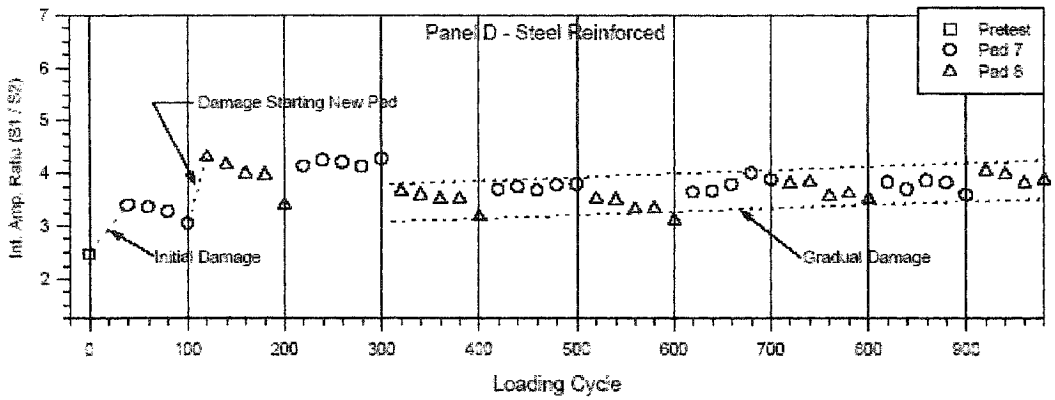

Figure 6-20 Panel-D: Integrated Amplitude Ratios

6.3.5.4 Panel-B (Figure 6.21)

Contrary to the trend observed in other panels, the integrated amplitude ratio showed a marked decline after the first 20 load cycles. A probable cause for this anomaly was the closure of a pre-existing longitudinal crack in Panel-B, which had developed when the two adjacent panels were being tested. Panel-B was constructed with a 75 mm deep, pre-induced longitudinal crack along the centerline of the panel. The crack propagated to the top surface when Panel-A was being tested and extended from the border of Panel-A, to the mid-point of Panel-B. Apparently, the initial application of the load caused the crack to close partially.

The following key interpretations are made from these data:

1. There was initial permanent closure of the pre-induced crack during the first 20 load cycles as indicated by the sharp decrease in ratios.
2. There was continued damage to the panel after 300 load cycles as indicated by the gradual but continual increase in ratios.
3. There was also a continual and similar increase in "Under load" ratios.
4. The pre-induced crack goes into elastic compression during loading, as evidenced by the clear and consistent decrease in ratios as compared to the ratios when no load was applied.

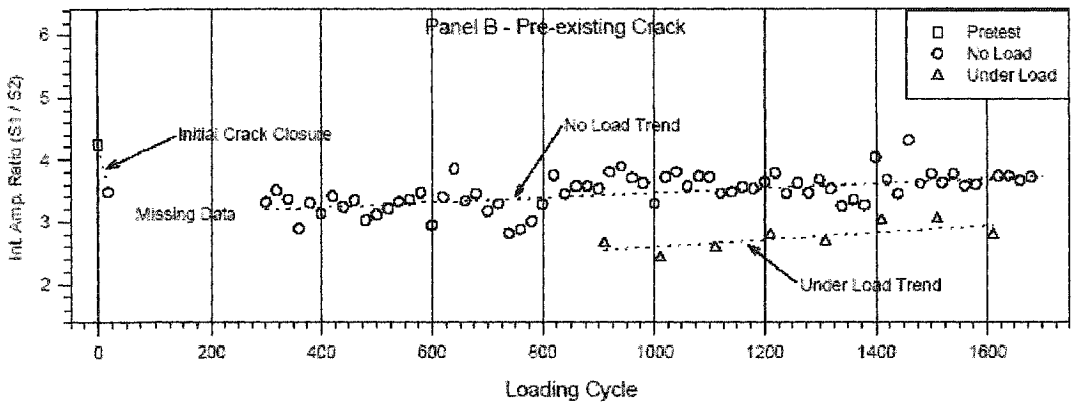

Figure 6-21 Panel-B: Integrated Amplitude Ratios

6.3.6 Crack Patterns

The crack patterns and the width of cracks after Phase-I tests for Panel-A, Panel-C, Panel-D and Panel-B are shown in Figures 6.22 through 6.25. The crack-widths are shown in millimeters. All panels except Panel-D had developed a predominant longitudinal crack on the soffit. Panel-A and Panel-D developed a Y-shaped crack near the edge beam. The crack widths were significantly smaller in the panels with crack-control reinforcement. The crack widths were the largest in Panel-A, and the smallest in Panel-D. The crack widths in Panel-C were larger than those in Panel-D but smaller than those in Panel-A. It can be concluded that crack control reinforcement contributes to reducing crack widths.

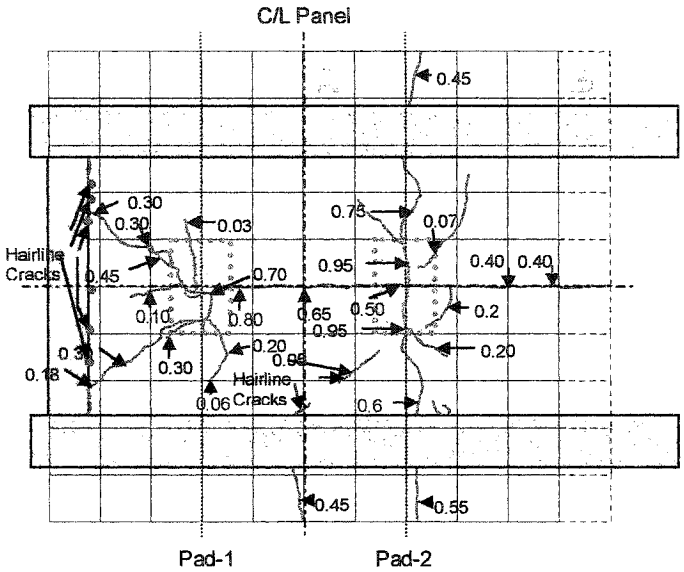

Figure 6-22 Panel-A: Crack Pattern on Soffit after 1,700 Load Cycles

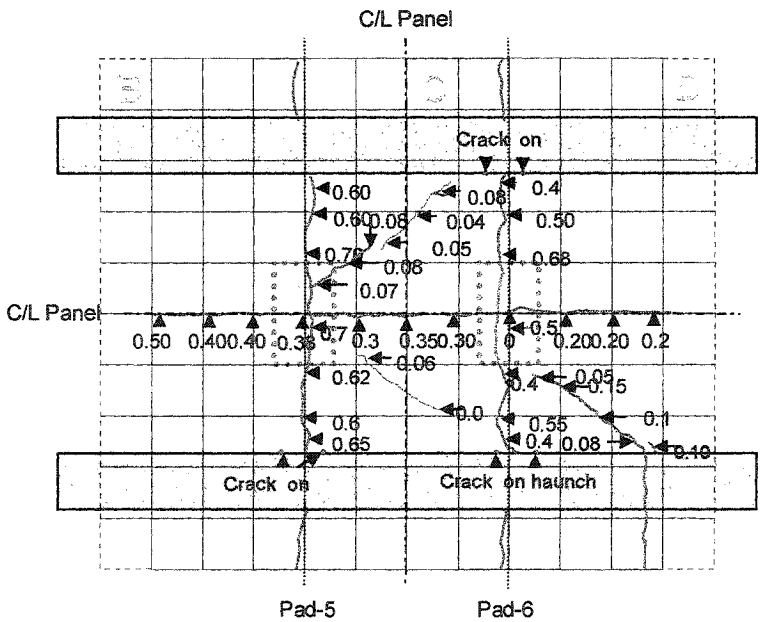

Figure 6-23 Panel-C: Crack Pattern on Soffit after 1,700 Load Cycles

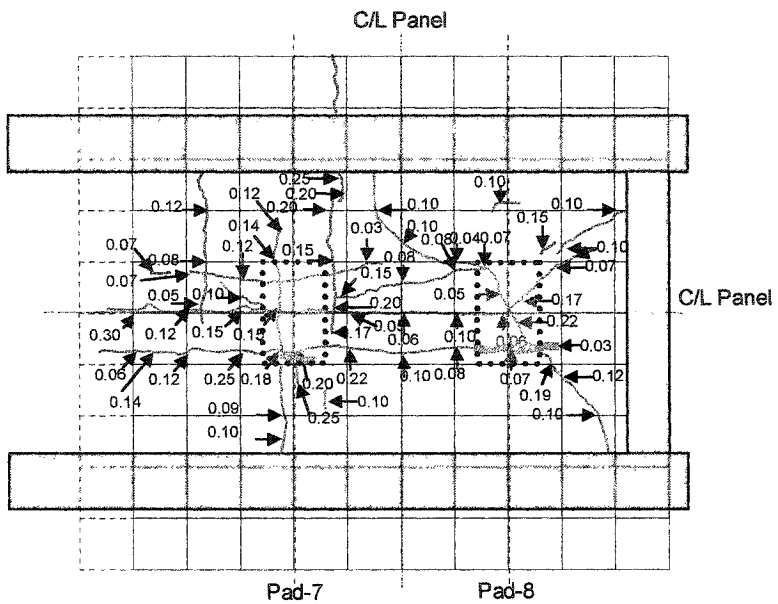

Figure 6-24 Panel-D: Crack Pattern on Soffit after 1,700 Load Cycles

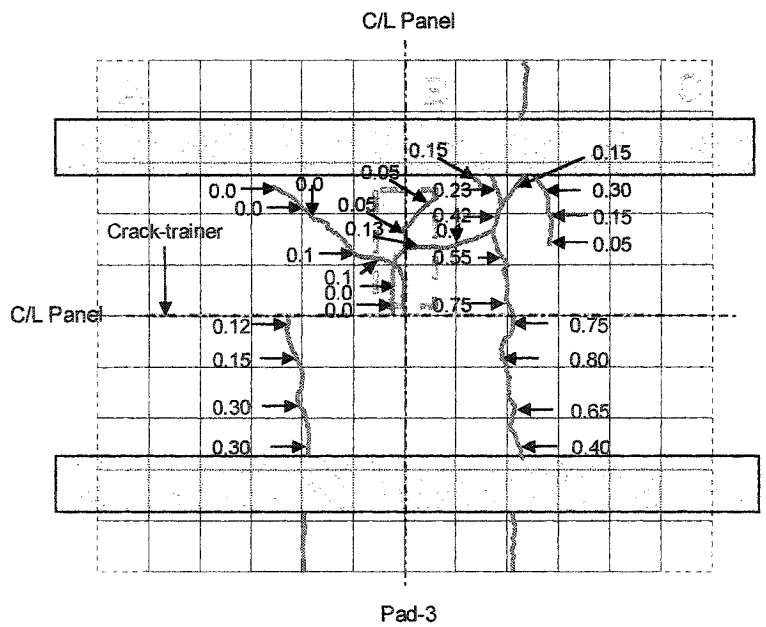

Figure 6-25 Panel-B: Crack Pattern on Soffit after 1,700 Load Cycles

6.4 Discussion - Phase-II

6.4.1 General

In this phase of testing, each panel was tested to failure. Panels A, D, and C were tested under cyclic loading and Panel-B was tested under static loading. The load was applied at only one load pad in each panel. Panel-A was subjected to the largest number load cycles (63,243 cycles) with peak loads ranging from 393 kN to 883 kN, while Panel-C was subjected to the least number of load cycles (304 cycles), with a single peak load value of 883 kN. The trends in variation of deflection and strap strains are plotted against the number load cycles applied. The crack patterns and acoustic attenuation results are discussed for the test.

The test data shows that each increase in the peak load level was accompanied by a corresponding increase in the damage. The extent of damage is reflected by the increase in the strain in the straps located on the either side of the load pad, an increase in the deflection under the load pad, and an increase in acoustic attenuation.

As discussed in Section 6.1, the value of the peak load was varied during the testing of the panels. In order to compare the response of the panels at varying load levels, values of strains and displacements at 393 kN load, corresponding to a 40 t wheel load, were extracted from the test data. Maximum values of strap strains recorded during the first, penultimate, and the final load cycle have also been shown separately. The fatigue test results for Panels A, D, and C are grouped together for discussion, while the static failure of Panel-B is discussed separately.

6.4.2 Strap Strains

Strain patterns for straps in Panels A, D, and C are shown in Figures 6.26 through 6.29. In each panel, a sharp increase in the strains indicating damage is followed by a steady behaviour. Increase in the magnitude of peak load is accompanied by an increase in strain in Panels A and D. At failure, the strain in the straps closest to the load pad (at 610 mm and 406 mm) drops as shown in Figure 6.26 and 6.27, while the straps that are 1.02 m away form the these straps, show a corresponding increase in strain as shown in the case of Panel-D. This shift in load path is an indicator of impending failure. To highlight this change in strain patterns, the strain profiles for the last 297 load cycles on Panel-D are shown in Figure 6.28. Strain patterns during static failure of Panel-B are shown separately.

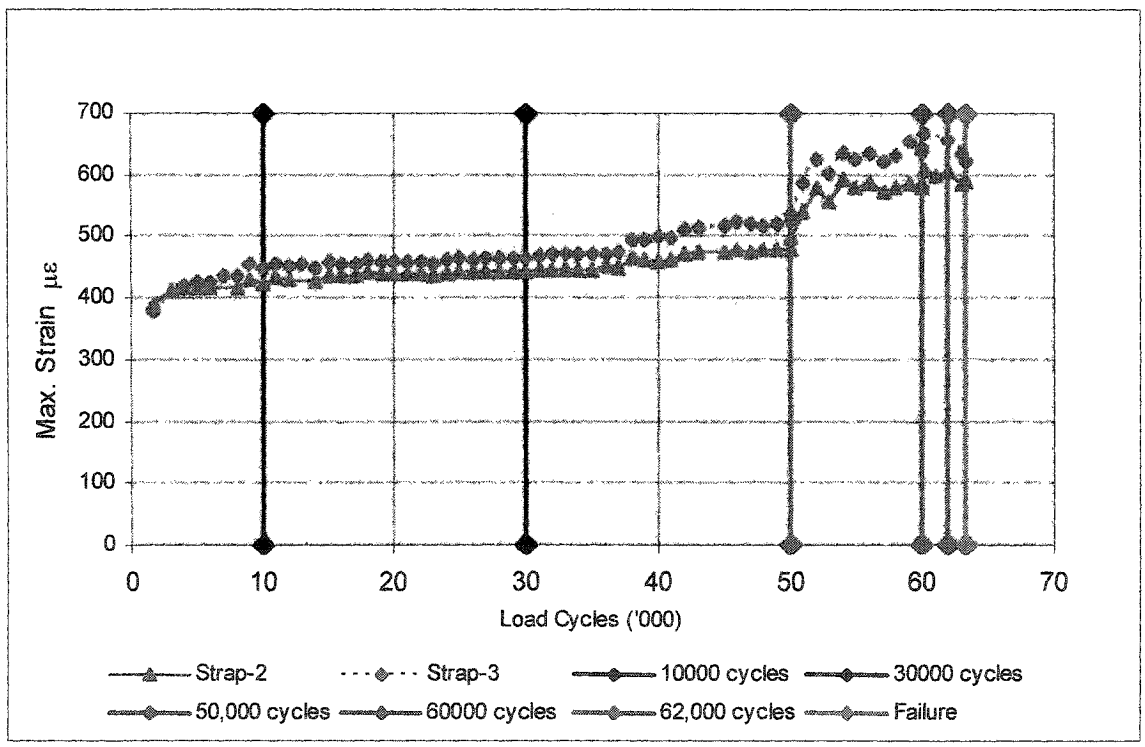

Figure 6-26 Panel-A: Trends in Strains in Strap-2 and Strap-3

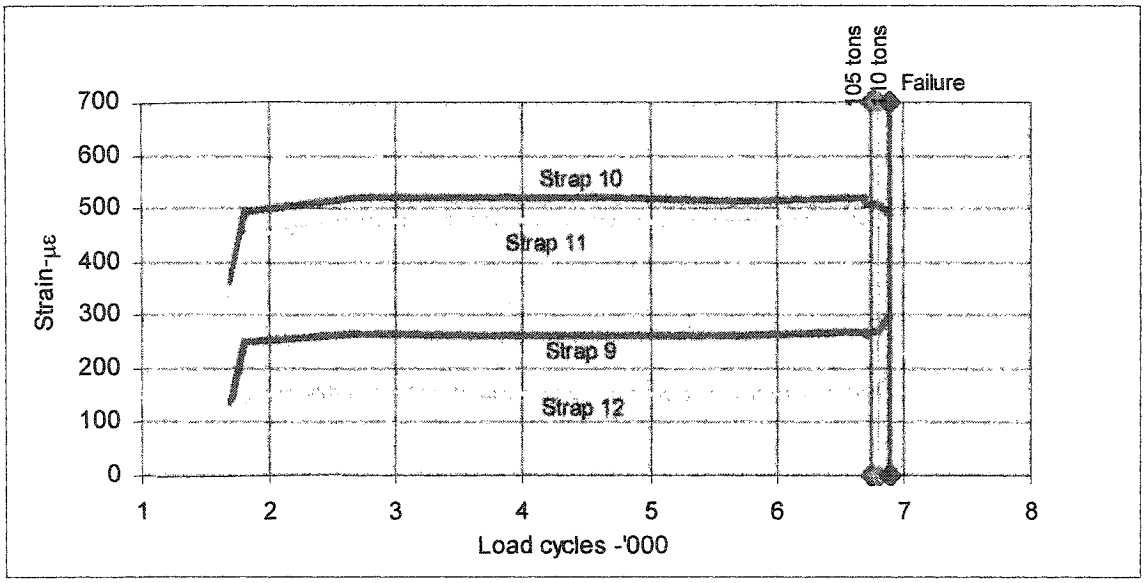

Figure 6-27 Panel-D: Trends-Strain in Straps 9, 10 11, and 12

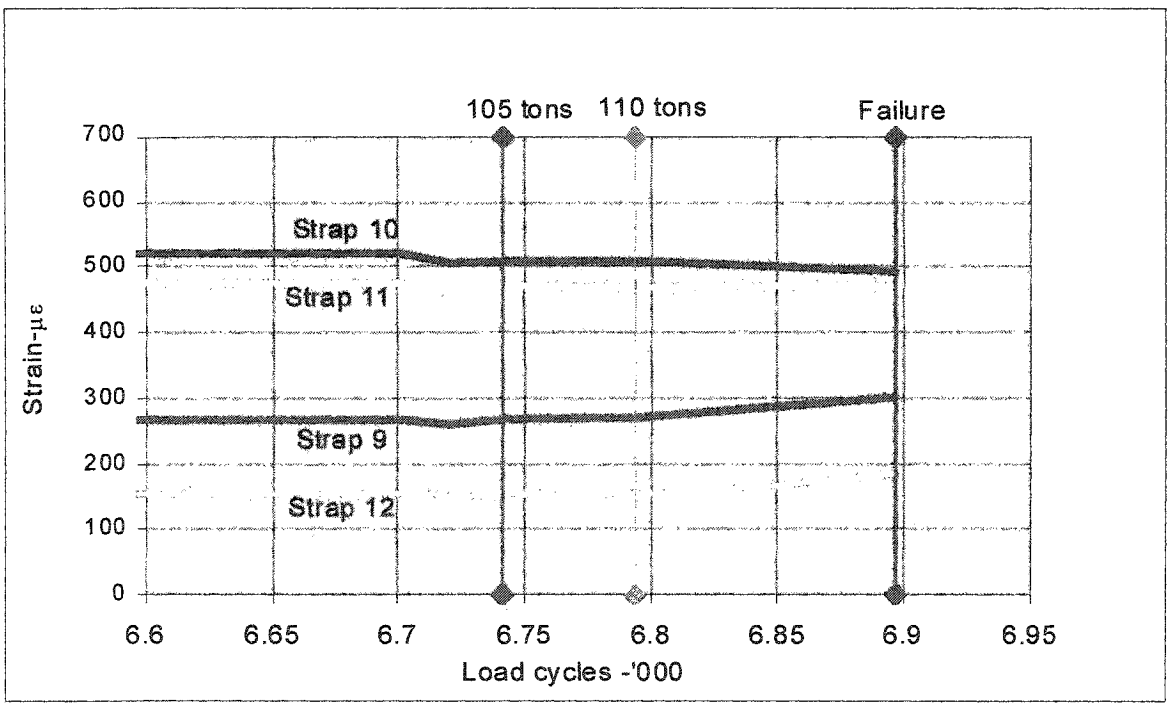

Figure 6-28 Panel-D: Strap Strain Profiles over Final 297 Load Cycles

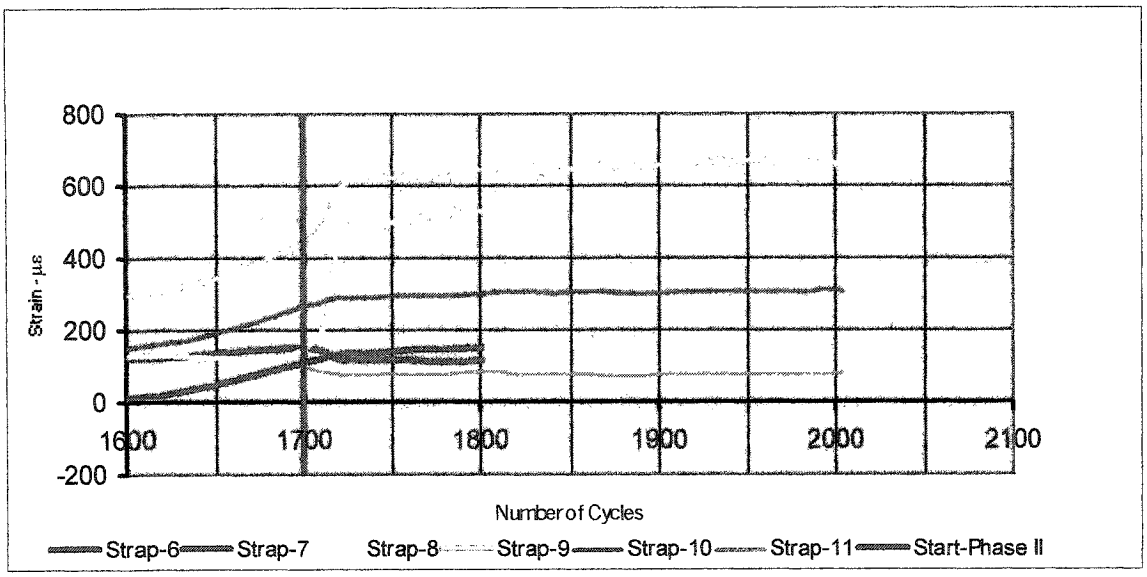

Figure 6-29 Panel-C: Trends-Strap Strain

6.4.3 Deflection

The deflection trends in shown in Figures 6.30 through 6.32 follow a pattern that is similar to that observed for the straps. As the magnitude of the load was increased there was a sharp increase in deflection followed by a stable behaviour. The gradual increase in deflection is quite evident in the case of Panels A and C, while the significant changes in deflection in Panel-D occurred only during the last four cycles. This is possibly due to the fact that the four load cycles at 1,079 kN peak load caused damage that was equivalent to the damage caused by several million load cycles at 196 kN.

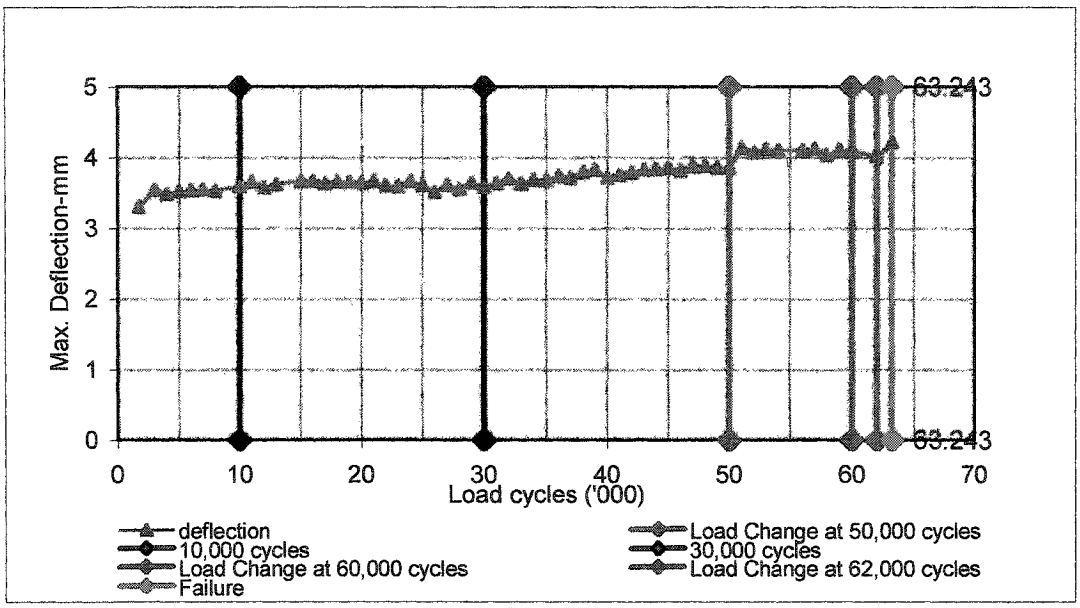

Figure 6-30 Panel-A: Trends-Slab Deflection at 393 kN

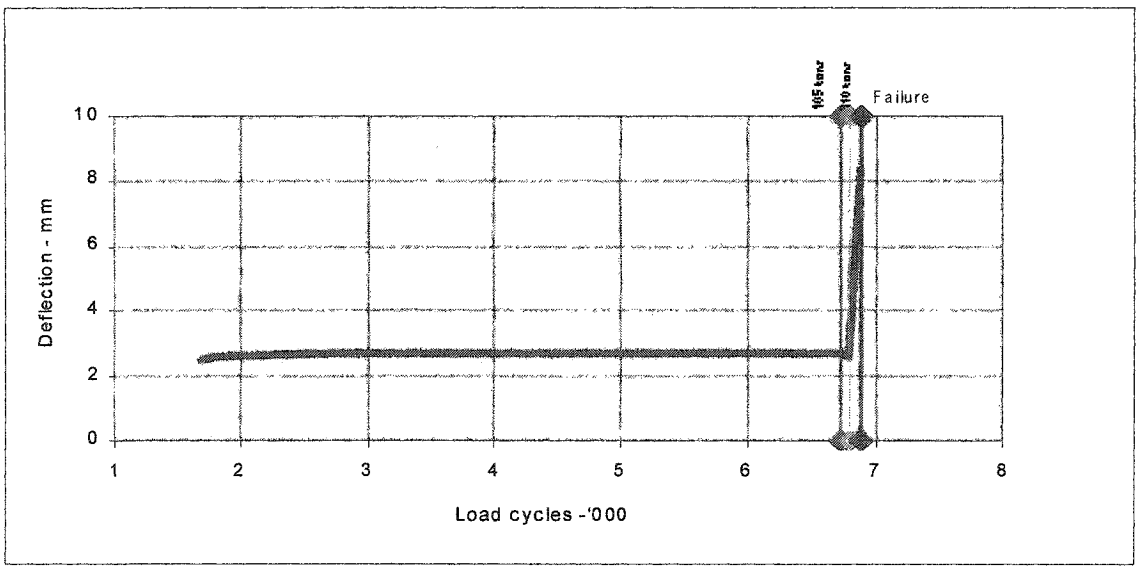

Figure 6-31 Panel-D: Trend in Slab Deflection

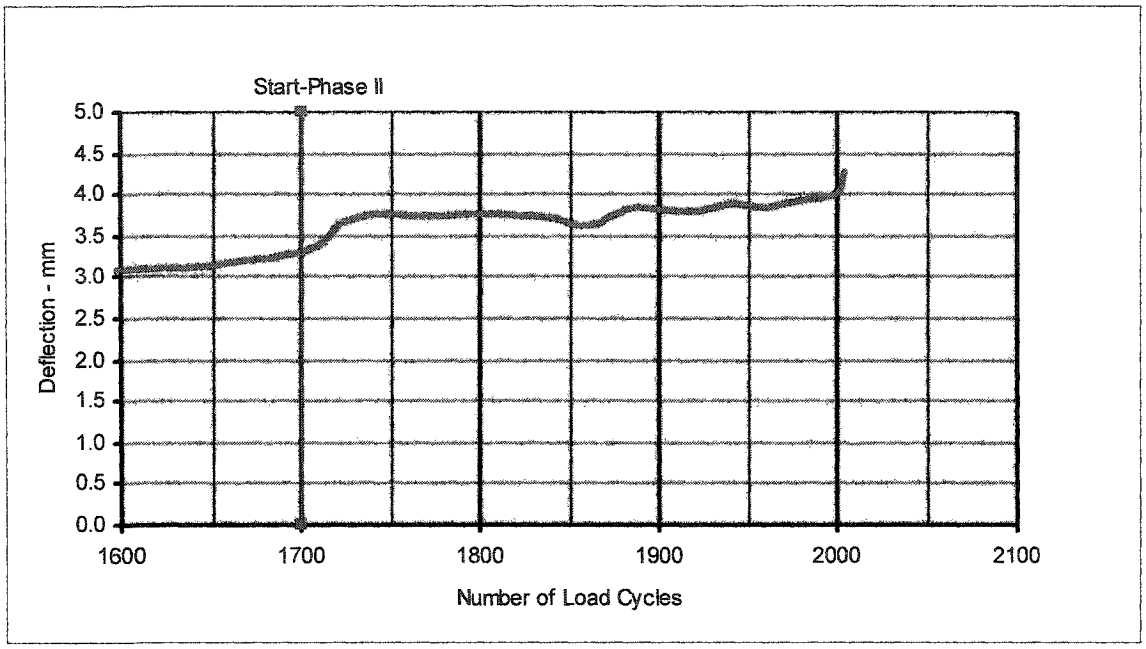

Figure 6-32 Panel-C: Trend-Slab Deflection

6.4.4 Sequence of Failure

To examine the sequence of failure, the applied load, strap strains, and the slab deflection are plotted against the time intervals covering the failure period. Figure 6.33 shows the failure sequence for Panel-A. The changes in sensor responses over the last 24 load cycles on Panel-D are shown in Figure 6.34. It is evident that during the last four load cycles, the strains and deflections begin to increase at an accelerated pace.The sequence of failure for Panel-D, Panel-B, and Panel-C, are shown in Figures 6.35 through 6.37. It can be seen that just before impending failure, the strain in straps adjacent to the load pad declined while the strain in straps further away continued to increase suggesting a change in the load path. In Panel-A, the load declined marginally and deflection continued to increase for one time interval even after all the straps did not carry any load. Each time interval is approximately 0.78 second. The failure of Panel-C appears to be more gradual as compared to the other panels.

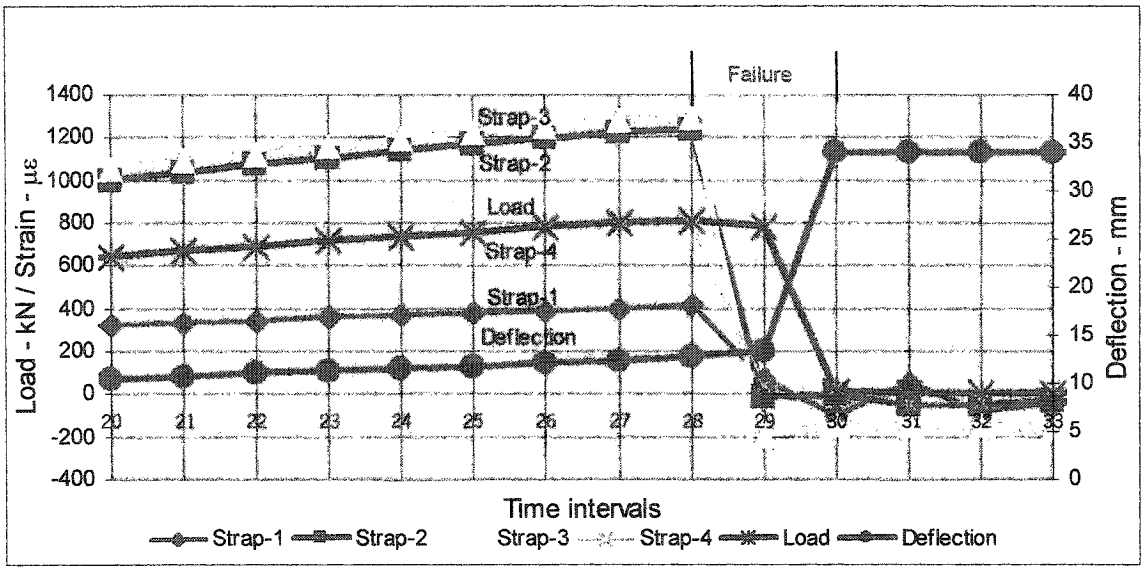

Figure 6-33 Panel-A: Sequence of Failure

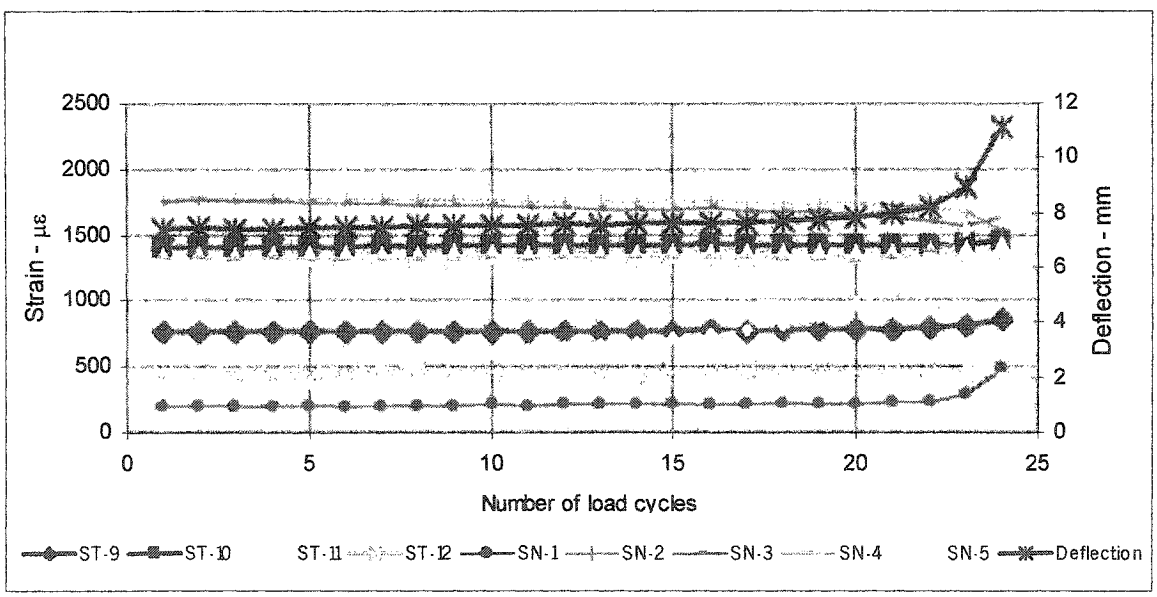

Figure 6-34 Panel-D: Sensor Response Patterns during Final 24 Load Cycles

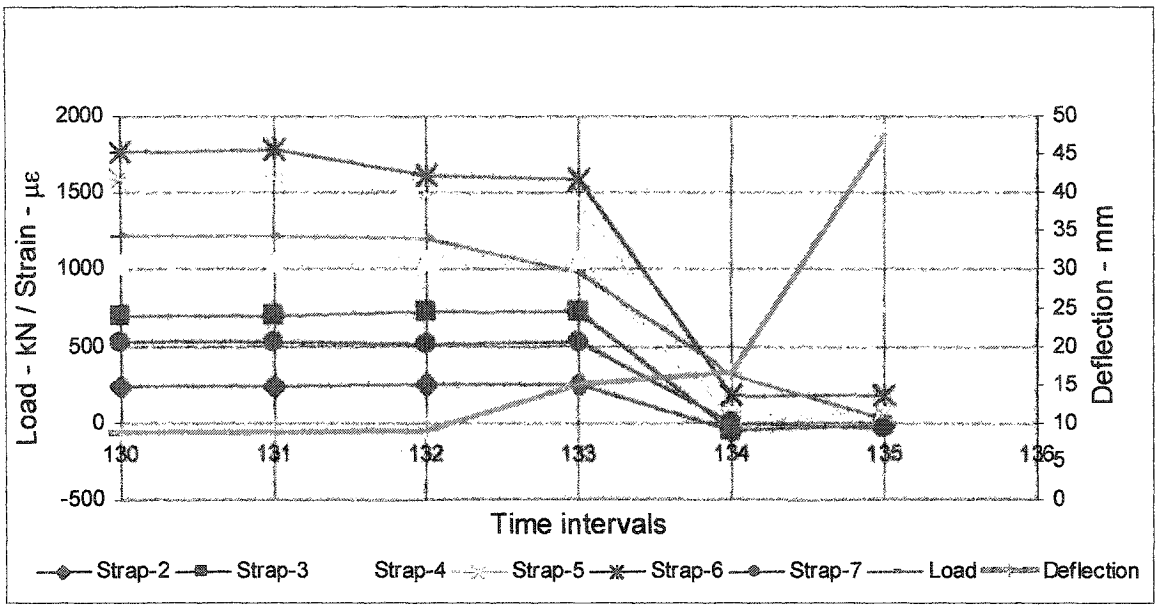

Figure 6-35 Panel-D: Sensor Response at Failure

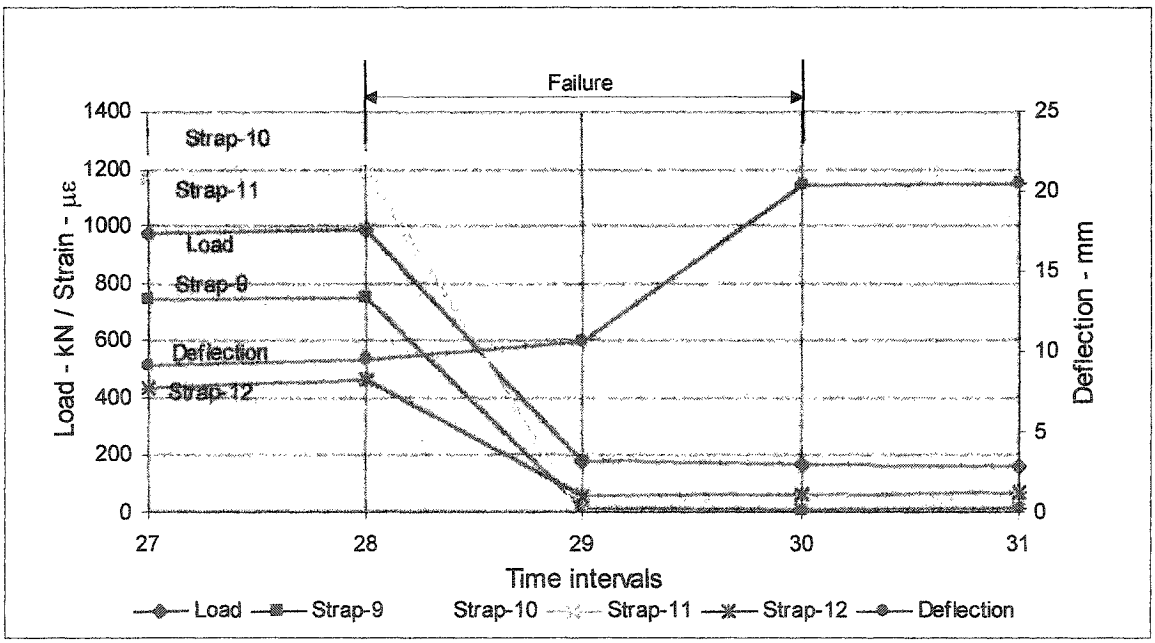

Figure 6-36 Panel-B: Sensor Response at Failure

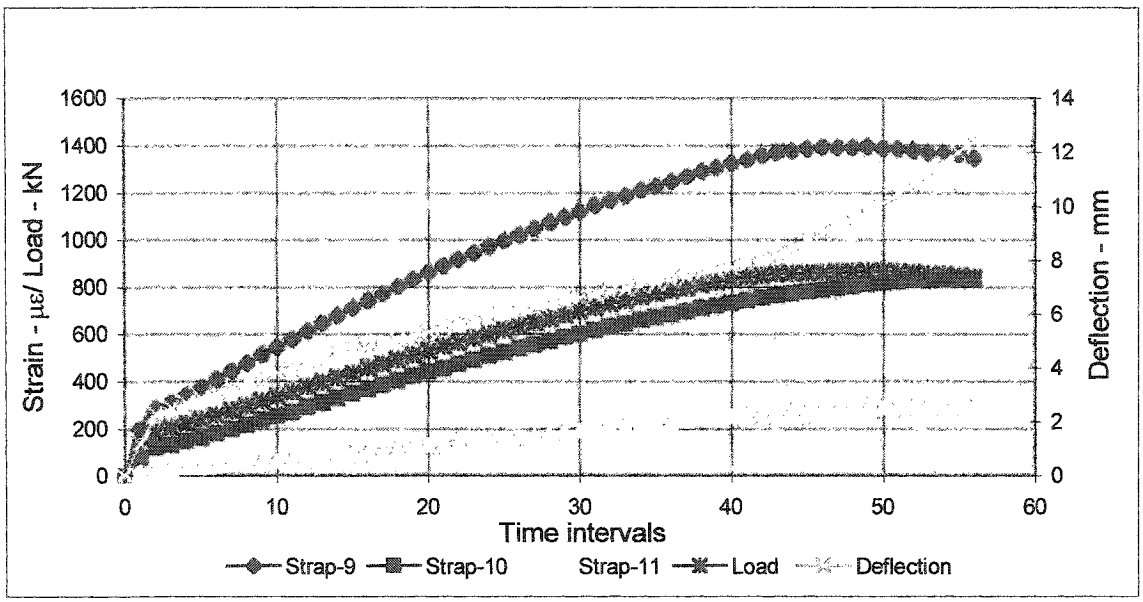

Figure 6-37 Panel-C: Sensor Response at Failure

6.4.5 Strain Values at Failure

The values of strap strains during the first, penultimate, and final load cycles for Panels A, D, and C are shown in Tables 6.1 through 6.3. The values during the penultimate load cycle are interpolated for 883 kN peak load from the test data. At failure, the share of the two straps adjacent to the load pad, expressed as percentage of the sum of strains in straps, shows a decline, while the share of the straps away from the load pad shows a corresponding gain. The percentage gains between the first and the penultimate load cycle for each strap are also shown. In Panel-C, the strap stains show a sudden increase between the penultimate and the final cycle.

Table 6-1 Panel-A: Maximum Strap Strains

Load Cycle	Strap-1 ($\mu\varepsilon$)	Strap-2 ($\mu\varepsilon$)	Strap-3 ($\mu\varepsilon$)	Strap-4 ($\mu\varepsilon$)
1st at 883 kN	335	1,239	1,364	769
(% Share)	(9.04)	(33.42)	(36.08)	(20.74)
Penultimate at 883 kN	433	1,350	1,429	864
(% Gain)	(29%)	(9%)	(4.5%)	(12%)
(% Share)	(10.62)	(33.12)	(35.06)	(21.20)
Final at 808 kN	413	1,230	1,283	793
(% Share)	(11.1)	(33.07)	(34.50)	(21.33)

Table 6-2 Panel-D: Maximum Strap Strains

Load Cycle	Strap-9 ($\mu\varepsilon$)	Strap-10 ($\mu\varepsilon$)	Strap-11 ($\mu\varepsilon$)	Strap-12 ($\mu\varepsilon$)
1st at 1,079 kN	729	1,380	1,227	416
(% Share)	(19.4)	(36.8)	(32.7)	(11.1)
Penultimate cycle at 1,079 kN	808	1,437	1,391	484
(% Gain)	(11)	(4)	(13.5)	(16.5)
(% Share)	(19.6)	(34.9)	(33.8)	(11.7)
107th (last) cycle at 988 kN	751	1,236	1,189	463
(% Share)	(20.6)	(34)	(32.7)	(12.7)

Table 6-3 Panel-C: Maximum Strap-Strains at Failure

Load Cycle	Strap-9 ($\mu\varepsilon$)	Strap-10 ($\mu\varepsilon$)	Strap-11 ($\mu\varepsilon$)
1st at 883 kN	1,225	733	291
Penultimate Cycle at 883 (% Increase)	1,379 (12.6%)	799 (9%)	272 (-6.5%)
304th (last) cycle at 869 kN (% Increase)	1,393 (13.7%)	876 (19.5%)	303 (4%)

6.4.6 Acoustic Attenuation

The plots of integrated amplitude ratios for Panels A, D, B and C are shown in Figures 6.38 through 6.41. In Panel-A, the growth of damage is rapid as the magnitude of the load is increased. The increase in ratios after failure is highest in Panel-C, indicating the greatest damage. In Panel-A, the increase after failure is substantially large., In Panel-D, however the increase in integrated ratio after failure is the smallest.

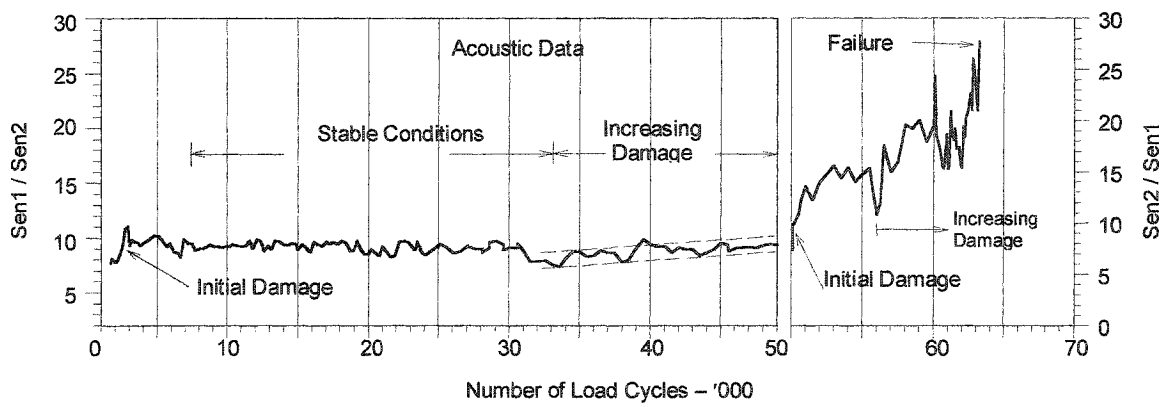

Figure 6-38 Panel-A: Integrated Amplitude Ratios

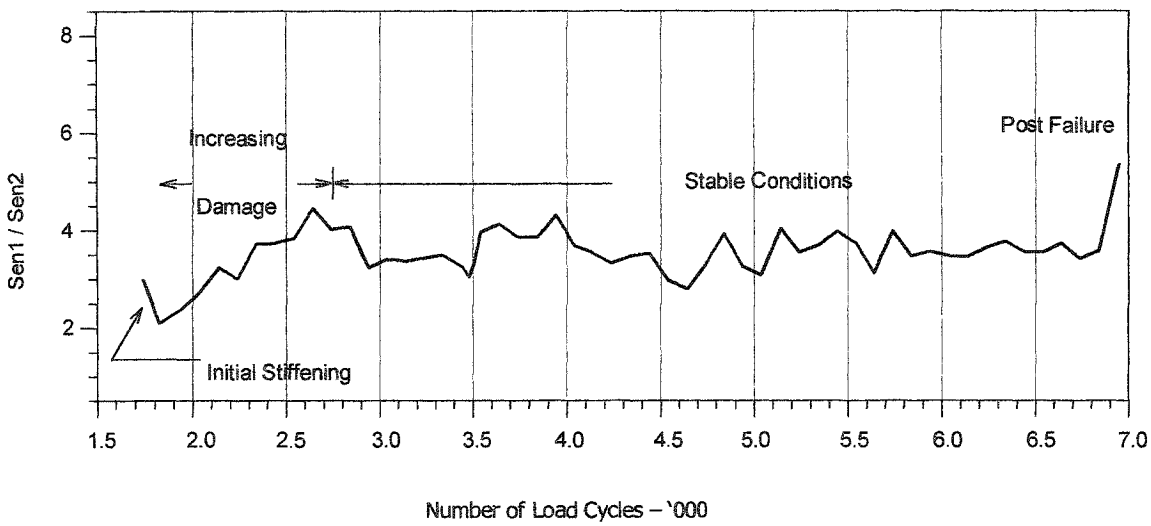

Figure 6-39 Panel-D, Integrated Amplitude Ratios

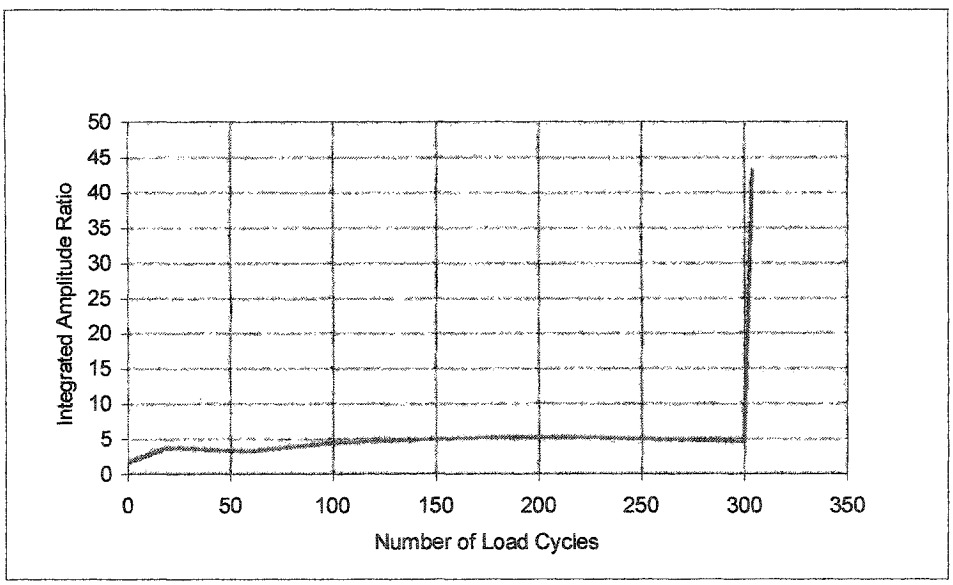

Figure 6-40 Panel-C: Integrated Amplitude Ratios

6.4.7 Crack Patterns

The crack patterns on the top and the bottom surface of Panels A, D, B, and D are shown in Figures 6.41 through 6.48. The crack-widths are shown in millimeters. All the panels failed by punching shear. The crack patterns for Panel-A at failure shows that the failure mode and the shape of the punch cone were not affected by the pre-existing full-depth transverse crack. This observation is in close agreement with the observations of Toulemonde and Ranc (2001) made in respect of full-depth transverse cracks in reinforced concrete bridge deck slabs. The two segments of the slab structurally acted as one single unit under load. The transverse crack between the two segments was instrumented to monitor their relative movement. It was found that during the initial part of the loading, the two segments moved independently towards each other until the crack was closed completely at the top. During the subsequent part of the load cycle, the two segments acted as one single unit. The damage after fatigue failure was localized.

The overall crack pattern on the top surface of the Panel-D was similar to that in Panel-A. The profile of the circumferential crack in Panel-D was more circular than that in Panel-A. The crack pattern on the soffit, however, was significantly different from that observed in Panel-A. The crack pattern on the soffit in Panel-A was mostly radial under the load pads, whereas the crack pattern in Panel-D was a combination of radial and orthogonal cracks.

Extensive damage caused by the failure of Panels D and B did not change the failure mode of Panel-C.

The extent of cracking was the least in Panel-B, and greatest in Panel-A .Crack widths were largest in Panel-A and smallest in Panel-D. The crack widths in Panel-C were significantly smaller than those in Panel-A but greater than those in Panel-D.

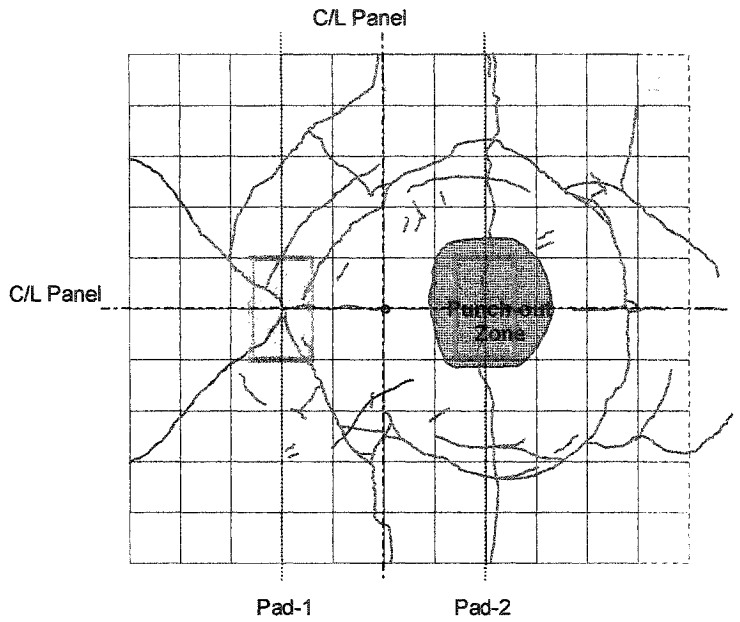

Figure 6-41 Panel-A: Crack Patterns at Top after Failure

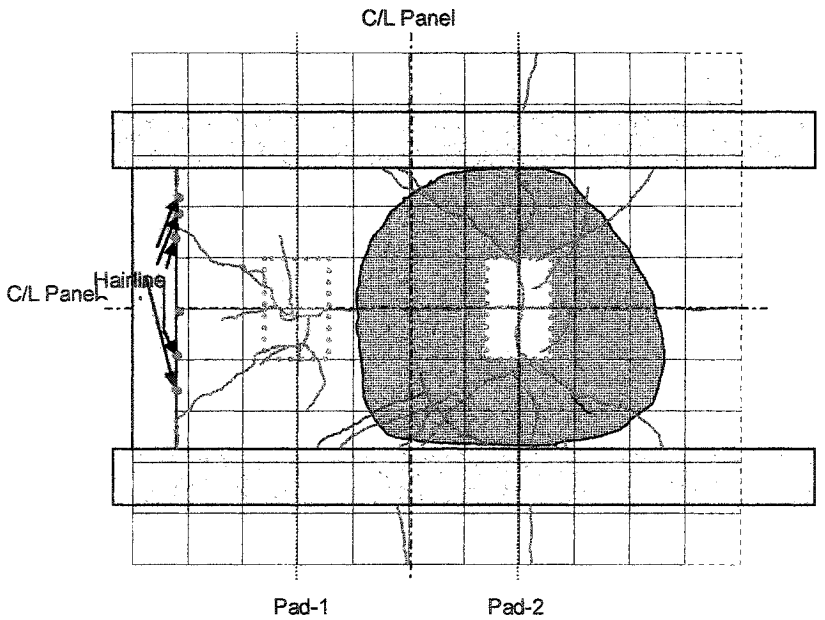

Figure 6-42 Panel-A: Crack Pattern on Soffit after Failure

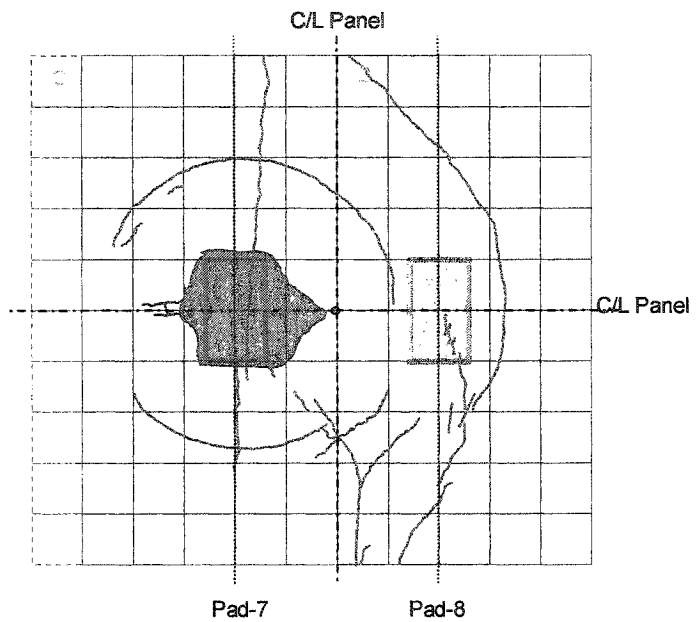

Figure 6-43 Panel-D: Crack Patterns on Top after Failure

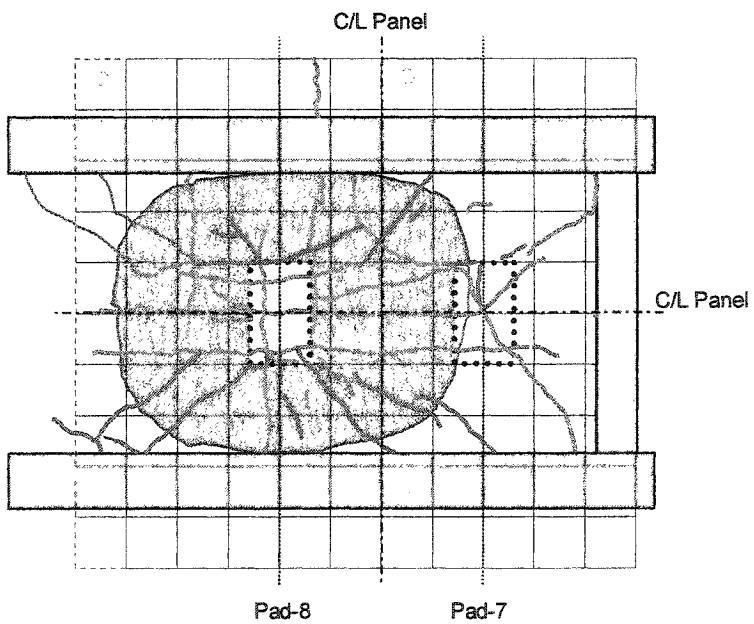

Figure 6-44 Panel-D: Crack Pattern on Soffit after Failure

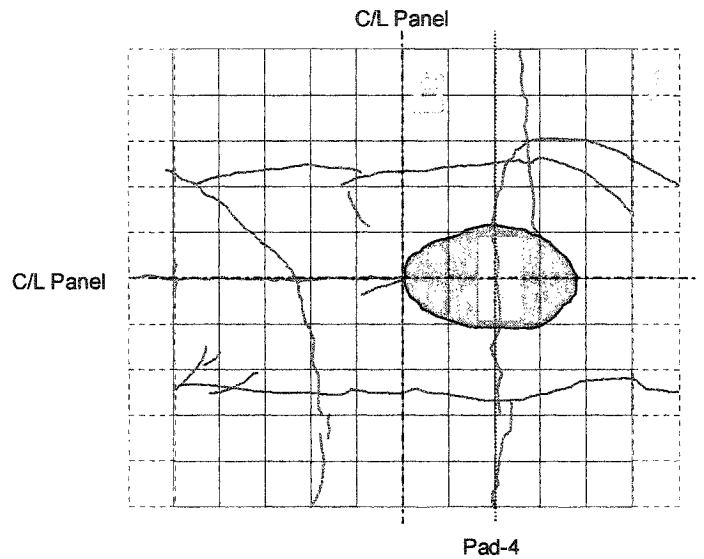

Figure 6-45 Panel-B: Crack Pattern on Top after Static Failure

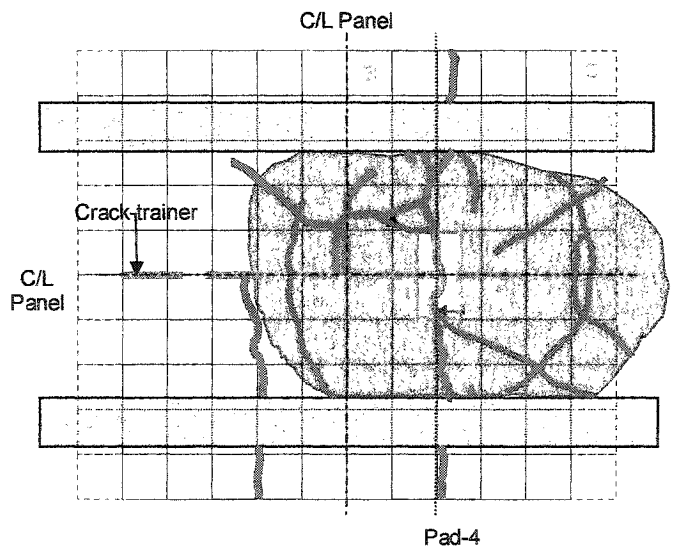

Figure 6-46 Panel-B Crack Pattern on Soffit after Static Failure

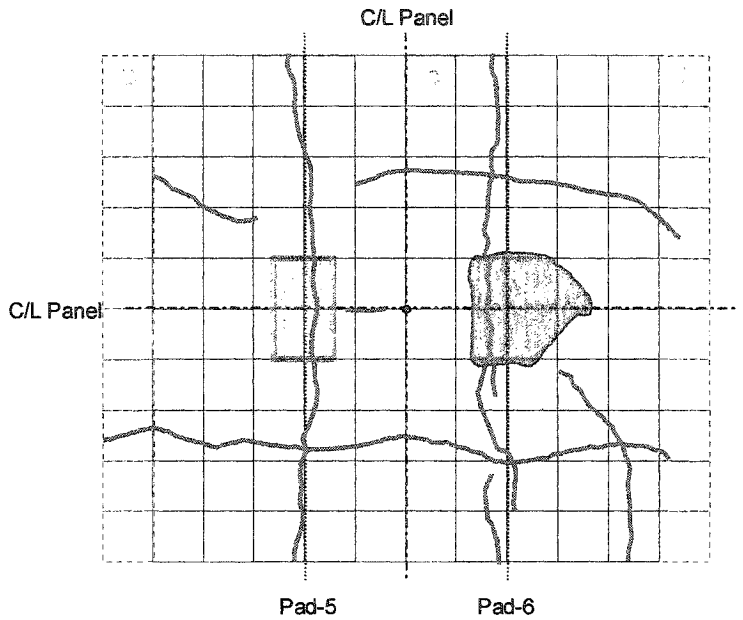

Figure 6-47 Panel-C: Crack Pattern on Top after Failure

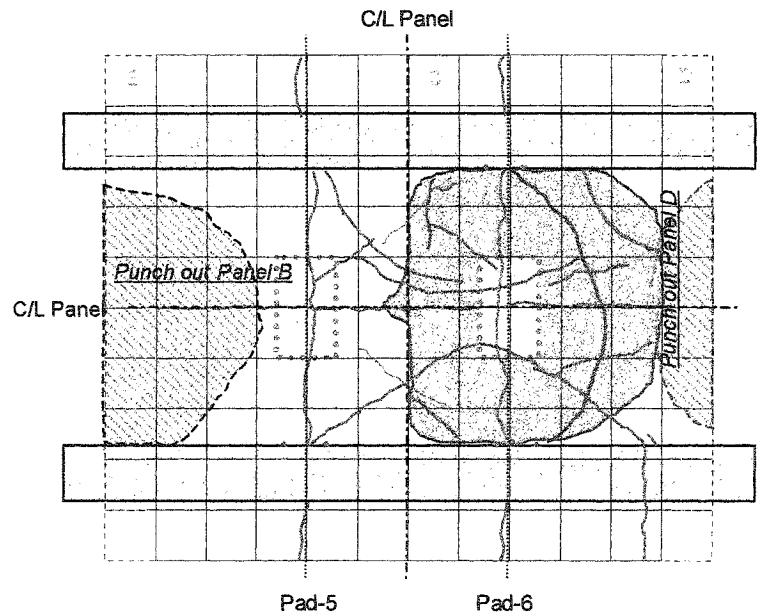

Figure 6-48 Panel-C: Crack Pattern on Soffit after Failure

6.4.7.1 Panel-A: Change in Width of Longitudinal and Y-Shaped Cracks

Longitudinal crack widths were monitored regularly. The crack widths varied along the length of the crack. The average crack-width is the average value of the crack widths measured along the entire length of that particular crack. The changes in the average width of the longitudinal crack, and the Y-shaped crack over the span of the test are shown in Figure 6.49. The curve for the longitudinal crack distinctly shows the three phases in the fatigue life of Panel-A under cyclic loading. The increase in the average width of Y-shaped crack was gradual for most part of the test. The crack width shows an increase after the magnitude of the peak load was increased and then remained unchanged until failure. The Y-shaped crack originated under the centre of Load Pad-1 and propagated towards the edge beam.

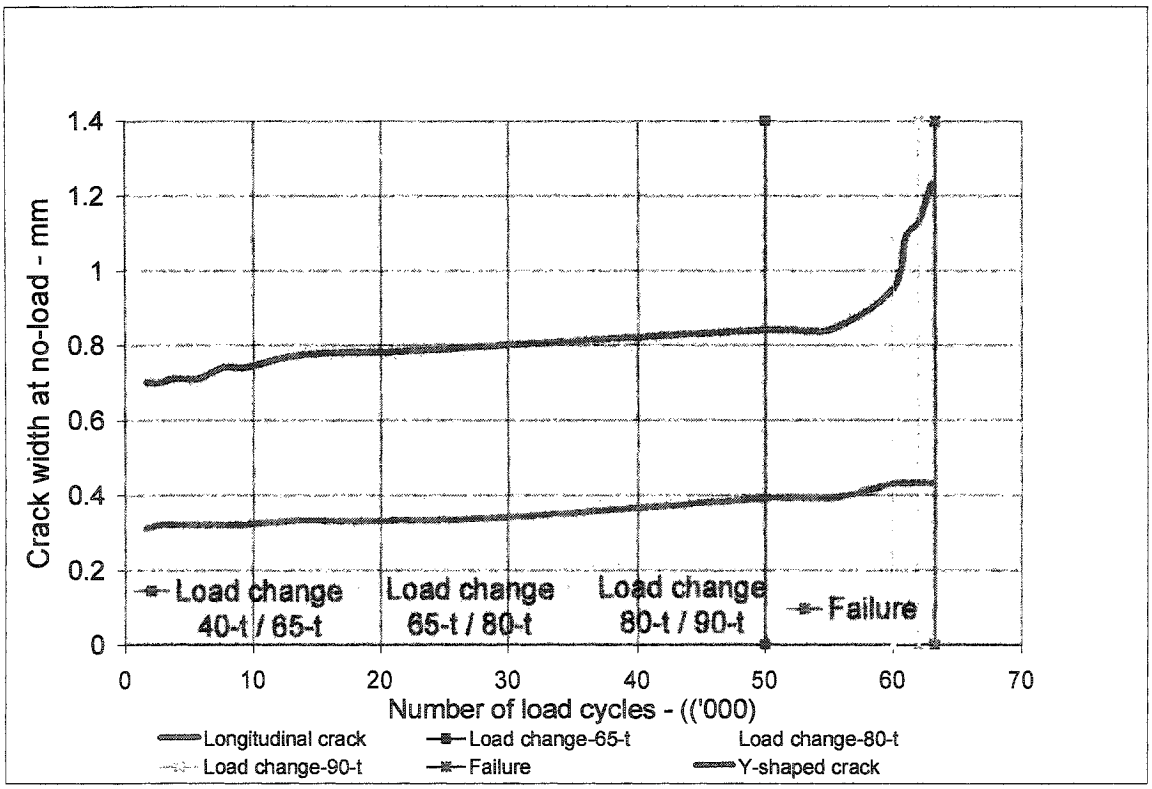

Figure 6-49 Panel-A: Crack-Width Patterns up to Failure

6.4.7.1.1 Panel-A: Crack-Width Range

In Table 6.4, column 2, and column 3 show the range of crack widths and the average crack width, respectively, for the longitudinal crack. Column 4, and column 5 show the range of crack widths and the average crack width, respectively, for the Y-shaped crack.

Table 6-4 Panel-A: Crack-Width Variation

Peak Load (kN)	Number of load cycles	Longitudinal crack		Y-shaped crack between Pad-1 and edge-beam	
		Width range (mm)	Average width (mm)	Width range (mm)	Average width (mm)
393	1,700	0.45-1.00	0.70	0.18-0.45	0.31
393	2,700	0.45-1.00	0.70	0.18-0.45	0.32
	3,700	0.45-1.20	0.71	0.18-0.45	0.32
	4,700	0.45-1.20	0.71	0.18-0.45	0.32
	5,700	0.45-1.20	0.71	0.18-0.45	0.32
	7,700	0.51-1.20	0.74	0.18-0.45	0.32
	9,400	0.52-1.20	0.74	0.18-0.45	0.32
	13,000	0.52-1.20	0.77	0.18-0.45	0.33
	17,000	0.55-1.30	0.78	0.18-0.45	0.33
	20,000	0.55-1.30	0.78	0.18-0.45	0.33
	30,000	0.55-1.30	0.80	0.18-0.50	0.34
	50,000	0.70-1.30	0.84	0.25-0.50	0.39
638	55,000	0.70-1.30	0.84	0.25-0.50	0.39
	60,000	0.70-1.10	0.95	0.25-0.65	0.43
785	61,000	0.90-1.50	1.09	0.25-0.65	0.43
	62,000	0.95-1.70	1.13	0.25-0.65	0.43
883	63,000	1.00-1.70	1.23	0.25-0.65	0.43
	63,248	(failure)			

6.4.7.2 Panel-D: Changes in Longitudinal and Y-Shaped Cracks

As in the case of Panel-A, the crack widths in Panel-D also showed a pattern of growth as the cyclic loading progressed. This is shown in Figure 6.50. The width of the central crack increased substantially during the first 1,000 load cycles applied at 883 kN peak load. Thereafter, unlike Panel-A, the width stabilized up to the last crack survey. The width of the second longitudinal crack, running parallel to the central longitudinal crack, remained unchanged during the initial stages of test at 883 kN, and then increased substantially during the next 500 load cycles. This was followed by a gradual increase up to the end. The width of the Y-shaped crack increased only during the first 900 load cycles in Phase-I of the test and then remained unchanged until the end. The crack widths, however, are substantially smaller than those recorded for Panel-A.

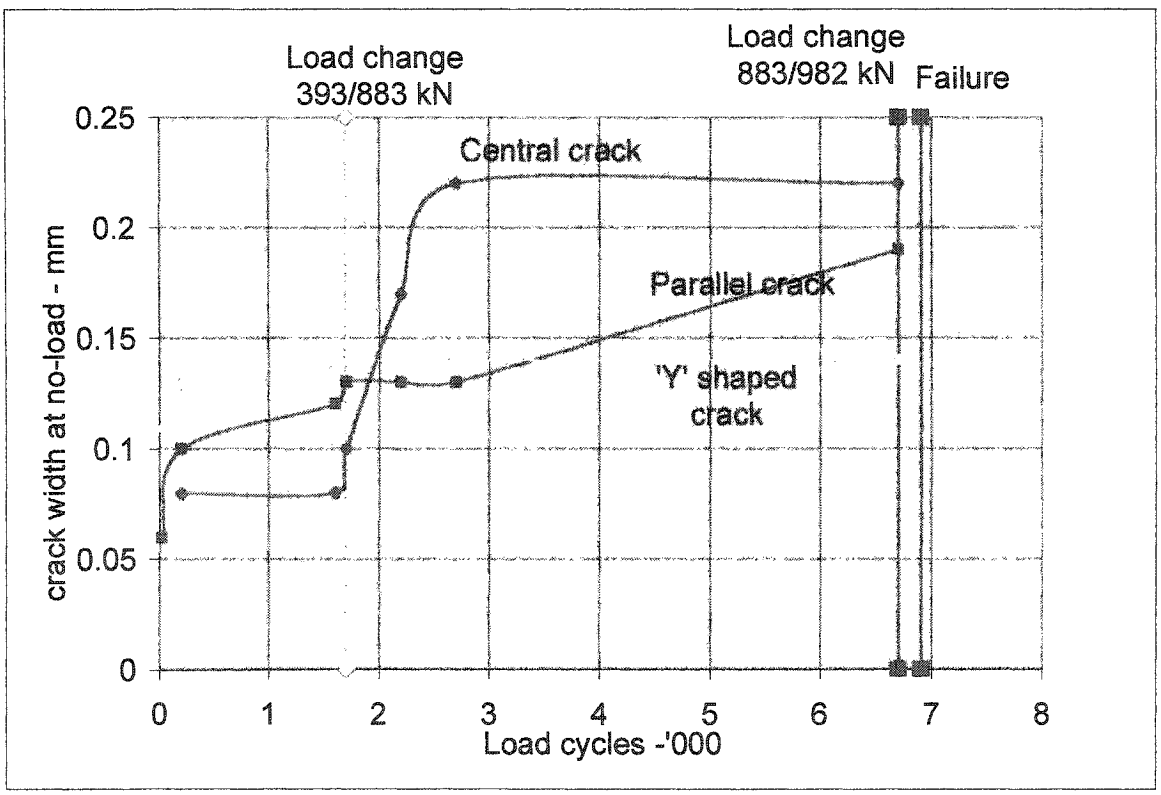

Figure 6-50 Panel-D: Crack-Width Patterns up to Failure

6.4.7.2.1 Panel-D: Crack-Width Range

The variation in crack widths in Panel-D is tabulated in Table 6.5. Cr-1 denotes the central longitudinal crack, while Cr-2 denotes the crack parallel to CR-1.

Table 6-5 Panel-D: Crack-Width Variation

Peak Load (kN)	Number of load cycles	Longitudinal cracks			Y-shaped crack near edge-beam	
		Width range (mm)	Average width (mm)		Width range (mm)	Average width (mm)
			Cr-1	Cr-2		
393	20	0.01-0.25	0.06	-	No crack	No crack
	200	0.03-0.26	0.08	0.10	0.01-0.20	0.11
	900	0.03-0.30	0.14	0.12	0.01-0.20	0.13
	1,600	0.02-0.30	0.08	0.13	0.05-0.24	0.14
	1,700	0.02-0.29	0.10	0.12	0.05-0.24	0.14
883	2,200	0.02-0.32	0.17	0.13	0.05-0.24	0.14
	2,700	0.02-0.50	0.22	0.19	0.05-0.20	0.14
	6,700	0.02-0.50	0.22	0.22	0.05-0.20	0.14
981, 1,030, 1,079	6,903 (failure)					

6.4.8 Panel-B

Panel-B was tested under monotonically increasing static load to failure. This punching failure load is assumed to be representative of the ultimate static load of the unreinforced deck.

6.4.8.1 Strains in Straps

The load versus strain curves for the final load cycle for Straps 2 to 8 are shown in Figure 6.51. The unloading paths of the curves have been omitted for clarity. Load Pad-4 was positioned between Strap-5 and Strap-6, at 610 mm and 406 mm, respectively. At failure, the strain levels in Strap-5 and Strap-6 approached the theoretical yield strain. The nonlinearity after approximately 1,050 kN is evident.

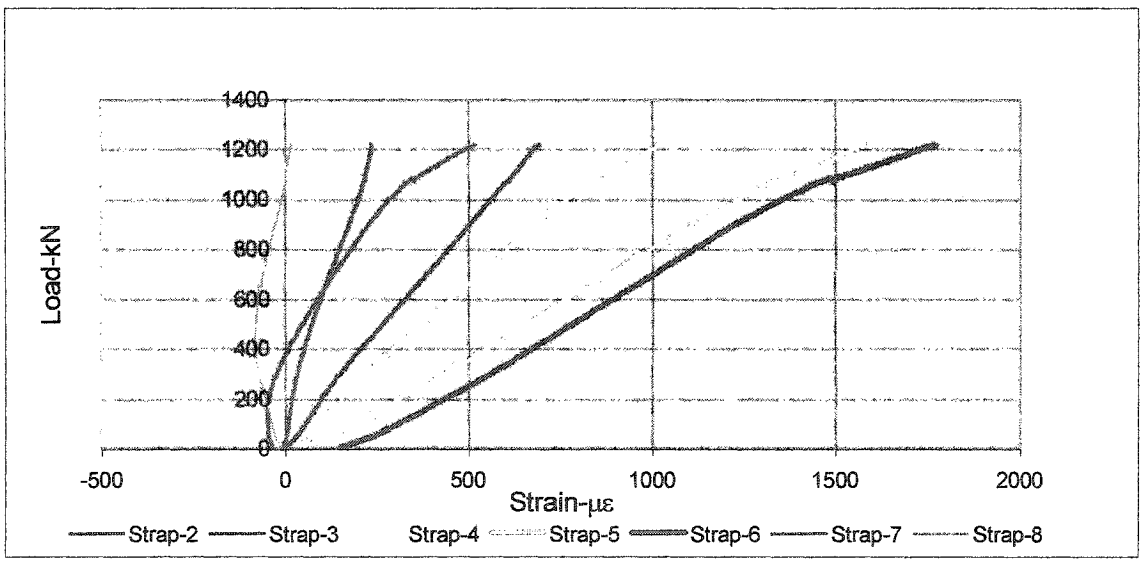

Figure 6-51 Panel-B: Load-Strain Curves for Straps

6.4.8.2 Strain Distribution in Straps

The strain distribution among all the 12 straps at various load levels is shown in Figure 6.52. It is seen that when the magnitude of the applied load was 53 kN, only Straps 4, 5 and 6 developed any significant levels of strain. At higher load levels, straps in other panels also started developing higher strains. The strain levels in Straps 2 and 3 in Panel-A, and Strap-7 in Panel-C, increased significantly with an increase in load. At lower load levels the distribution of load was localized. The load was dispersed over a larger area as the intensity of the applied load was increased.

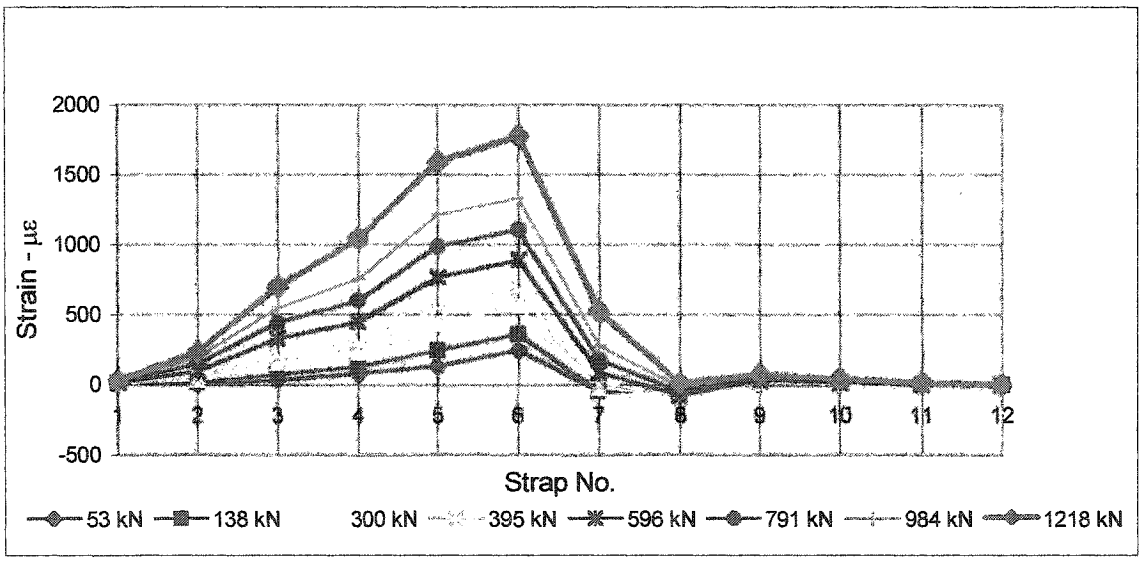

Figure 6-52 Panel-B: Strap-Strain Distribution

To compare the distribution of load among various straps at various load levels, the strains in all the straps at each load level were summed up and the percentage share of each strap was calculated. The percentage distribution among all the 12 straps is shown in Figure 6.53. It is seen that as the load was increased, the relative share of the load taken by straps adjacent to the load pad decreased, while the share of the straps that

were away from the load pad increased. This shows that as the load increased, a larger length of the deck slab participated in transferring the applied load to the girders.

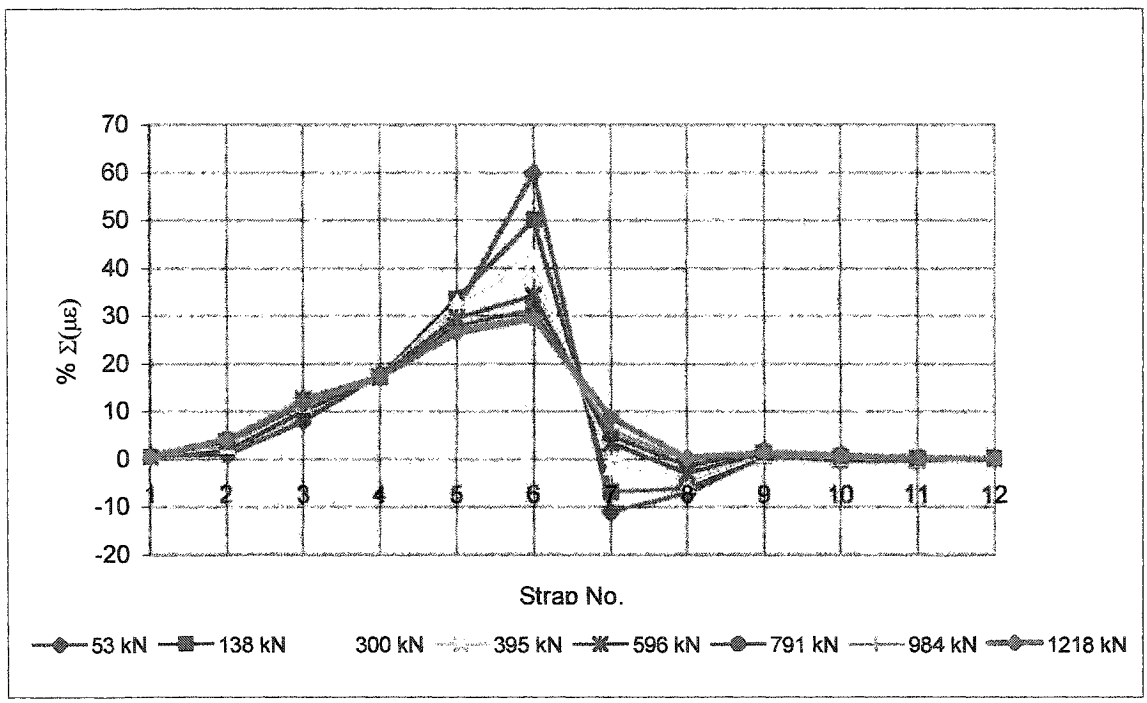

Figure 6-53 Panel-B: Percentage Distribution of Strain in Straps

The plot of sums of strap strains at various load levels is plotted against the applied load in Figure 6. 54. Although, the relationship between the applied load and the sum of strap strains is represented accurately by a sixth order polynomial, practically, it comprises two near linear segments. The first segment extends from 0 kN to approximately 1,000 kN load while the second segment stretches from 1,000 to 1,218 kN. The linear behaviour of the entire system is evident from this figure. The gentler slope of the second segment,however, indicates a reduction in the stiffness of the panel. Looking at the overall curve, it appears that the panel exhibited a nonlinear behaviour after approximately 890 kN. When this value of the applied load is compared with the maximum permissible wheel load of 200 kN on a bridge deck slab, it is evident that the

system has enough reserve strength to withstand an occasional overload without compromising permissible limits.

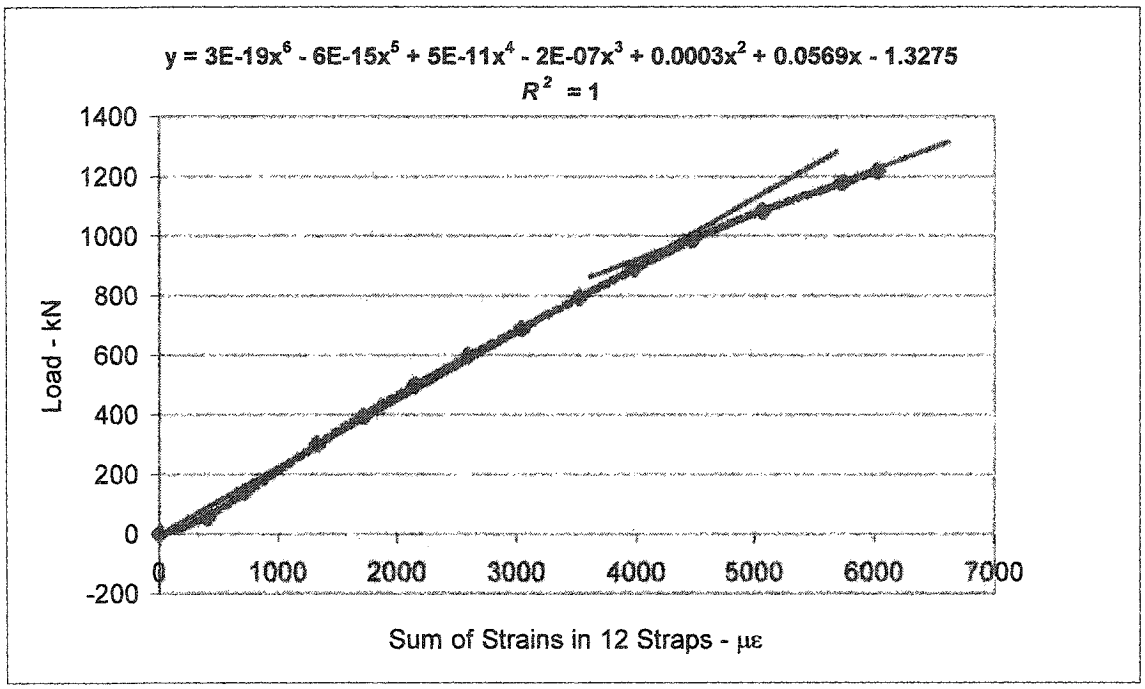

Figure 6-54 Panel-B: Load-Cumulative Strap Strain Curve

6.4.8.3 Deflection

The load deflection curve for Panel-B at failure is shown in Figure 6.55. In this case as well, the curve is linear up to approximately 1,000 kN load. A nonlinear behaviour is quite evident from 1,000 kN up to the failure load.

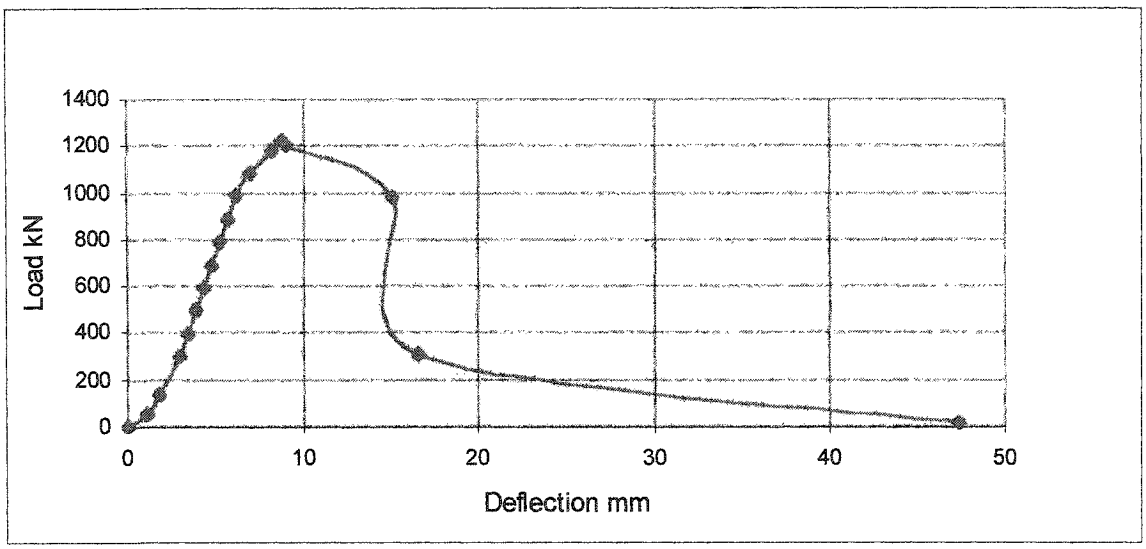

Figure 6-55 Panel-B: Load-Deflection Curve At Failure

6.4.8.4 Acoustic Attenuation

Integrated amplitude versus load curve is shown in Figure 6.56. As the loading progressed, acoustic pulses were generated and recorded at regular intervals up to about 1,000 kN load and discontinued for safety reasons. Thereafter, the acoustic signals were generated after the failure of the panel. There was gradual increase in the integrated amplitude ratios up to 1,000 kN. The ratio increased from about 8.3 to 14 reflecting a substantial damage due to static punching failure. The increase in the ratio is significantly higher than that seen in the case of Panel-D but lower than that in Panel-A.

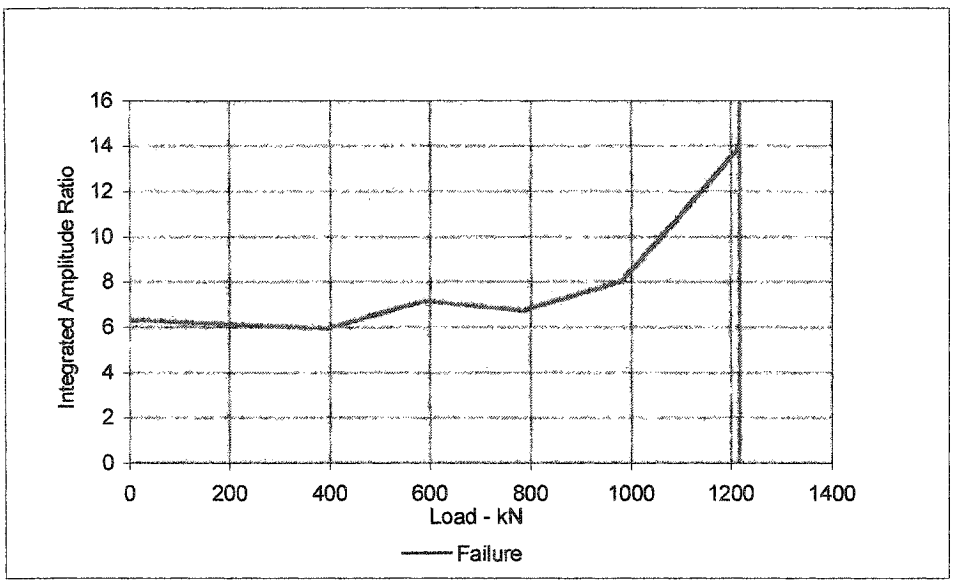

Figure 6-56 Panel-B: Integrated Amplitude Ratios

7.0 COMPARISON OF PERFORMANCE

7.1 General

The test model was conceptually divided into four segments, each with a different configuration, designated as Panel-A, Panel-B, Panel-C, and Panel-D. Panel-A was the control panel; Panel-B was identical to Panel-A with the inclusion of a 75 mm high, pre-induced longitudinal crack mid-way between the girders. Panel-C was provided with nominal GFRP crack-control reinforcement, and Panel-D was provided with nominal steel crack-control reinforcement, both near the bottom surface. The objectives of the testing were to assess the effectiveness of crack control reinforcement in inhibiting the initiation and growth of cracks on the soffit and to study the influence of a full-depth longitudinal crack on the performance of steel-free bridge deck slabs. The performance criteria for Phase-I and Phase-II differed from each other, and hence, the comparison has also been done separately for each phase.

7.2 Phase-I

There are three main parameters to compare the performance of the various configurations: (a) the strain in straps, (b) the slab deflection, and (c) the crack patterns. One indicator is the width of the cracks in general and the longitudinal crack in particular. The smaller the crack width on the soffit, the longer it would take for the crack to propagate to the top surface. The maximum strain level in a strap directly affects the stress range and hence the fatigue life of the panel. Similarly, the deflection is an indicator of the extent of rotation of the slab. The larger the rotation for successive load cycles, the higher the damage in the slab.

7.2.1 Comparison of Performance in Phase-I

- The extent of visible cracking in Panel-A and Panel-C was the least, with the cracks concentrated under and around the load pad, while the cracking in Panel-D was extensive and distributed over a significantly larger area of soffit of the panel.
- The crack-widths were the smallest in Panel-D, while the crack-widths in Panel-A were the largest. Panel-C had moderate crack-widths.
- All the configurations developed a longitudinal crack on the soffit, mid-way between the girders, within the first 10 load cycles at 393 kN load.
- The initial crack width was 0.3 mm, 0.2 mm, and 0.15 mm, in Panel-A, Panel-C, and Panel-D, respectively.
- At the conclusion of the Phase-I test, the maximum longitudinal crack width in Panel-A was the largest at 0.8 mm, while the maximum longitudinal crack width in Panel-D was the least, being 0.3 mm.
- Y-shaped cracks, originating from the soffit longitudinal crack, developed in both Panel-A and Panel-D within the first 10 load cycles, when the load was first applied at Load Pad-1 and Load Pad-8 which were closest to the edge beams.
- At the end of the test, the maximum width of the Y-shaped crack was 0.45 mm and 0.17 mm, in Panel-A and Panel-D, respectively.
- Panel-A and Panel-C had developed transverse cracks before the commencement of the test program. Panel-B and Panel-D developed transverse cracks during the testing of Panel-A and Panel C respectively
- Typically, the transverse cracks were located along the line of embedment gauges and the instrumented bar.
- Panel-B also had a full-depth longitudinal crack extending from Panel-A up to its centreline.
- The strap strains and the pad deflections stabilized after about 300 load cycles in each panel.
- The strap-strains in Panel-A and Panel-C showed continuous increase throughout the test. The increase in the strain levels was rather rapid over the first 300 load cycles in the case of Panel-C, while in the case of Panel-A the increase over the first

600 was relatively slower and followed by even smaller rate of increase up to end of the test.

- The strap-strains in Panel-B and Panel-D remained relatively stable after initial fluctuations over 100 and 300 load cycles, respectively. The average strap strain in Panel-D was about 350 $\mu\varepsilon$ and the bar strain was 803 $\mu\varepsilon$, while the average strap strain in Panel A at 389 $\mu\varepsilon$ was about 10% higher.
- The crack control reinforcement contributes positively in the arching action.
- The strains in concrete recorded by the embedment gauges were extremely high in Panel-A and Panel-C.
- Within the first 10 load cycles, three out of seven gauges were damaged in Panel-A and two out of nine embedment gauges were damaged inPanel-C. All the embedment gauges in Panel-D were functional up to the end of the test.
- The strain gauge CT in Panel-A and Panel-C, failed after 600 and 1400 load cycles, respectively. The recorded strains before failure were 300 $\mu\varepsilon$ and 398 $\mu\varepsilon$, respectively. The same gauge in Panel-D recorded a strain of only 13.8 $\mu\varepsilon$.
- The slab deflection at the end of the test was 3.43 mm, 2.69 mm, 2.25 mm for Panel-A, Panel-C, and Panel-D respectively. The slab deflection of Panel-B cannot be considered for comparison as the load pad was asymmetrically placed directly over the middle strap of the panel.
- In Panel-B, the cracking on the soffit was mainly limited to the area immediately below and around the load pad.
- In Panel-B, the strains recorded by embedment gauges NT, NM, and NB, located in the segment of the panel with the active load pad, were very high, while the gauges on the opposite side recorded low strain levels.

The values of strains in straps on either side of the load pad, slab deflection under load pad, integrated amplitude ratios, and the width of longitudinal and Y shaped cracks at the beginning and after completion of Phase-I are shown in Table 7.1.

Table 7-1 Phase-I: Comparison of Parameters for All Panels

Parameter Compared	Panel-A		Panel-B		Panel-C		Panel-D	
	Start	End	Start	End	Start	End	Start	End
Strap Strain ($\mu\varepsilon$)	ST-2 ∓ (304) ST-3† (265)	ST-2 ∓ (394) ST-3† (384)	ST-5 (478)	ST-5 (470)	ST-8 ∓ (-90) ST-9† (122)	ST-8 ∓ ∓ (126) ST-9† (296)	ST-10† (315) ST-11 ∓ (344)	ST-10† (366) ST-11 ∓ (328)
Deflection (mm)	3.33	3.43	1.8	1.67	2.92	3.08	2.34	2.35
Int. Amp. Ratio	5	6.18	3.4	3.8	2.25	2.29	2.4	4.15
Average Width Long. Crack (mm)	0	0.70	NA	NA	0.1*	0.33	0.06*†	0.44**
Average Width Y-Shaped Crack (mm)	0	0.31	NA	NA	NA	NA	0	0.14

∓ Strap position: 610 mm from load pad
† Strap position: 406 mm from load pad
* Crack only for 50% of the panel length
** Combined crack-width of three longitudinal cracks

Comparing the overall performance of the panels, the following conclusions can be drawn:

- The performance of all the panels was satisfactory.
- The width of cracks in general, and the longitudinal crack in particular, can be effectively reduced by the provision of a crack-control mesh near the bottom surface of the deck slab.
- The strains in the undamaged gauges, CT, CM, and CB, in Panel-D show that the overall strain levels in the highly loaded zone are considerably reduced by provision of crack-control mesh.
- The fact that all the embedment gauges in Panel-D were fully functional until the end of the test indicates that the concrete in Panel-D suffered the least internal damage.
- Although the spacing of the GFRP reinforcement in Panel-C was 67% wider than the spacing of the steel reinforcement in Panel-D, the crack widths were still lower than those in Panel-A, which did not contain any crack-control reinforcement.

- Asymmetrical loading of Panel-B with a full-depth longitudinal crack did not result in any differential movement at the crack.

Nominal crack control reinforcement increases the stiffness of the transverse confining system, resulting in smaller slab deflection.

7.3 Phase-II

7.3.1 Strap Strains

Strap strains at a common load level of 883 kN and failure for the straps closest to the active load pad are shown in Table 7.2. At 883 kN of load, the strain levels in the straps in Panel-B and Panel-D are comparable and lower than the strain levels in the straps in Panel-A. The lower strap-strains in Panel-D are possibly due to the contribution of crack control reinforcement. Panel-A and Panel-B had identical configurations except for a pre-induced longitudinal crack in Panel-B. While Panel-A was tested to failure under cyclic loading applied at Load Pad-2, Panel-B was subjected to only 1,700 load cycles at 393 kN peak load applied at asymmetrically positioned Load Pad-3 in Phase-I. It was tested to failure in Phase-II, under monotonically increasing static load that was applied at Load Pad-4. Therefore, the concrete in the vicinity of Load Pad-4 was relatively undamaged and the strain levels were lower.

Table 7-2 Comparison of Strap Strains at Failure

Panel	Panel-A		Panel-D		Panel-B†		Panel-C	
Strap	ST-2*	ST-3**	ST-10**	ST-11*	ST-5*	ST-6**	ST-8*	ST-9**
Strain at 883 kN ($\mu\varepsilon$)	1,350	1,429	1,175	1,138	1,154	1,286	No Data	1,379
Strain ($\mu\varepsilon$) Peak Load(kN)	1,350 883	1,429 883	1,437 1,079	1,391 1,079	1,593 1,218	1,775 1,218	No Data	1,379 883

* Strap position: 610 mm from load pad
** Strap position: 406 mm from load pad
† Tested under static loading conditions

7.3.2 Concrete Strains

The concrete strains were not discussed during the previous discussion. However, one important indicator is the number of strain gauges that were functional up to the end of the test in each panel. Panel-D had all nine embedment gauges surviving until the end of the test while Panel-A had the least number of functional gauges. Also, the strain levels in all the embedment gauges in Panel-D were significantly lower than the strain levels in the gauges in other panels. The status of embedment gauges in all the panels at the end of the test program is shown in Table 7.3.

Table 7-3 Status of Concrete Embedment Gauges in All Panels Just Before Failure

Gauge Designation →	ST	SM	SB	CT	CM	CB	NT	NM	NB
Panel-A	√	X	X	√	X	X	√	√	X
Panel-B	√	√	√	X	X	*	√	√	√
Panel-C	√	√	√	X	X	X	√	√	√
Panel-D	√	√	√	√	√	√	√	√	√

* CB in Panel-B replaced by crack trainer

√ Functional gauge

X Non-functional gauge

7.3.3 Acoustic Attenuation

The integrated amplitude ratios for all panels at the beginning of Phase-II, and after failure are shown Table-7.4. The acoustic attenuation results show that the integrated amplitude ratio at the commencement of Phase-II was highest for Panel-A and lowest in Panel-D. The increase in the integrated amplitudes ratios was significantly higher for Panel-A and Panel-B, while the ratios in Panel-C and Panel-D increased gradually until the end. After failure, the integrated amplitude ratio was highest for Panel-C, followed by Panel-A and then Panel-B. The ratio for Panel-D was the lowest.

Table 7-4 Integrated Amplitude Ratios for All Panels

Panel	Integrated Amplitude Ratio (Start - Phase-II)	Integrated Amplitude Ratio (Post-Failure)
A	8	28
B	6	14
C	5	43
D	3	6

7.3.4 Crack Patterns

The crack patterns show that the crack widths in Panel-A were the largest, while the crack widths in Panel-D were the smallest. The crack widths in Panel-C were moderate. The crack patterns on the top surface of Panel-A and Panel-D were similar. Both panels developed a circular crack around the load pad on the top surface. Panel-C did not develop such a crack. The probable reason was the damage caused during the failure of Panels D, and B. Table 7.5 shows the comparison of crack patterns in all panels.

Table 7-5 Comparison of Crack Patterns of All Panels

	Panel-A	Panel-B	Panel-C	Panel-D
Crack Control Reinforcement	Nil	Nil	GFRP	Steel
Width-Longitudinal Crack (mm)	1.23	NA	0.35	0.22
Y shaped Crack (mm)	0.43	NA	NA	0.14
Extent of Cracking – Top Crack Width	Extensive Large	Moderate Medium	Moderate Medium	Moderate Small
Extent of Cracking – Soffit Crack Widths	Extensive Large	Moderate Moderate	Moderate Moderate	Extensive Small

7.3.4.1 Proposed Crack Control Grids

The beneficial effect of crack control reinforcement on the widths of longitudinal and Y-shaped cracks is evident from Table 7.5. While the steel-crack control grid appears to have been more effective in controlling crack-widths, the GFRP crack-control grid is preferable for the following reasons:

- Smaller modulur ratio

The modulur ratio of GFRP bars(E = 40 GPa) and 45 MPa concrete (E = 27 GPa) is approximately 1.5, whereas the modulur ratio of steel (E = 200 GPa) and concrete (E = 27 GPa) is approximately 7.4. The stress differential at the GFRP-concrete interface would therefore be significantly less than the stress differential at the steel-concrerte interface. Thus under cyclic loading, the concrete in the GFRP-concrete interface zone would have a longer fatigue life due to a significantly smaller stress range.

- Corrosion Resistance

All concrete structures develop cracks during their service life, some of which may be full-depth cracks. Eventually, the salt laden water will penetrate to the bottom layer of crack-control grid. A potential deterioration of the deck can be avoided by using a GFRP crack control grid.

It is recalled that in Panel-C, the spacing of GFRP bars in the transverse direction was 500 mm as compared to the 300 mm spacing of steel bars in Panel-D. The axial stiffness of GFRP bars was 16,080 N/mm2, whereas the axial stiffness of the steel bars was 66,660 N/mm2, as shown in Appendix-D. A closer spacing of smaller diameter bars would more effective crack-control. A crack-control grid to control or distribute the longitudinal crack is proposed and shown in Figure 7.1. The deck slabs adjacent to the edge beams also develop Y-shaped cracks and are weaker than the remainder of the bridge deck (Youn and Chang 1998). The arrangement of the crack-control grid for the zone near the edge beams, is also shown in Figure 7.1.

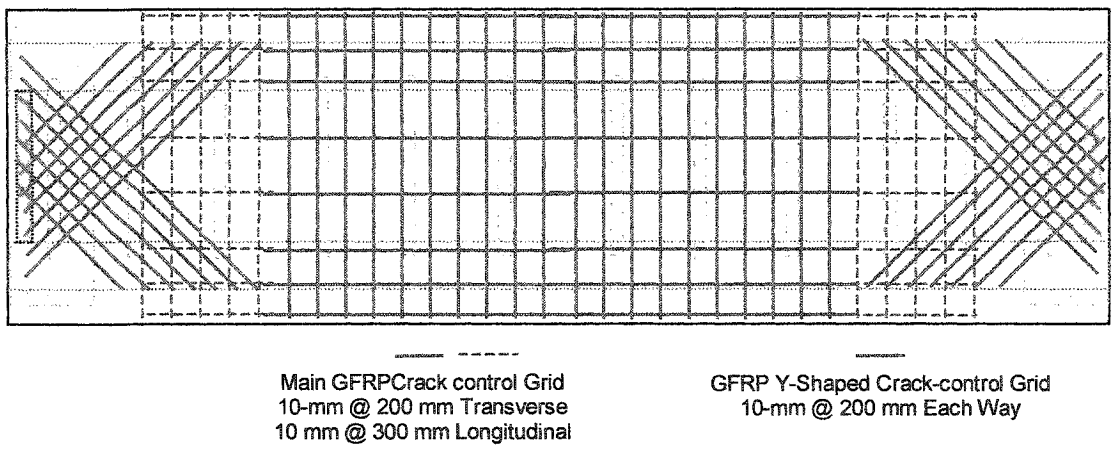

Figure 7-1 Proposed Arrangement of Crack-Control Reinforcement

7.3.5 Mode of Failure

All the panels failed in punching shear. The punch cone of Panel-D was largest and was influenced by the presence of the crack control reinforcement, while the punch cone of Panel-C was the smallest and was affected by the prior failure of adjacent panels. The failure mode of Panel-A was not influenced by the full-depth longitudinal crack that was approximately located along the transverse centre line of the active load pad. Toutlemonde and Ranc (2001) also reported similar results after conducting fatigue tests on transversely cracked reinforced concrete deck slabs.

7.3.6 Determination of Fatigue Life

To satisfy the fatigue resistance requirements of the design codes, a deck slab is required to withstand a certain number of load cycles, 2-million cycles, without failure. Commentary on CAN/CSA-S6-00 states, "*In real life, bridge components are subjected to variable load cycles. However, in design, the fatigue limit state is defined by the application of a specified number of cycles of a fixed characteristic transitory load such that the cumulative fatigue effect would be equal to that of the expected variable load cycles during the lifetime of the bridge structure without causing failure*". However, such

tests simply confirm compliance with the fatigue resistance requirements of the code and do not determine fatigue life.

To determine the fatigue life of a bridge deck slab, it would have to be tested under loading conditions that are similar to the field loading conditions. A highway bridge is subjected to a random combination of axle loads from a variety of light, medium and heavy vehicles. Consequently, there is a large variation in the axle loads and the frequency of their application. The highway bridge design codes specify the maximum expected design loads, which are based on actual wheel loads ranging from one country to another, and in the case of Canada, from one province to another, as shown in Table 7.6 (CAN/CSA-S6-00).

Table 7-6 Maximum Observed Axle Load in Canadian Provinces

Province	Ontario	Alberta	Saskatchewan	Quebec
Maximum axle load (kN)	314	150	134	159

Statistically, there is always a likelihood that during the lifetime of a bridge, the actual applied wheel loads will exceed the expected maximum wheel load. Based on traffic surveys, the range of axle loads on a bridge can be identified and categorized (Matsui, 2001). Table 10.17.2.3 (c) of CAN/CSA-S6-00 specifies a value of 4,000 for Average Daily Truck Traffic on a Class-A highway. The value of N_c, the specified number of design stress cycles, calculated in accordance with Clause 10.17.2.3 of CAN/CSA-S6-00, is 219 million cycles for a single lane. Mufti et al. (2002) calculated that one lane of a bridge, with a service life of 75 years, will be subjected to a maximum of 372 million passes of truck axles, based on the Average Daily Traffic (ADT) of 20,000 vehicles, with the Average Daily Truck Traffic ($ADTT_{SL}$) of 20%. Table 7.5 shows the statistical distribution of wheel loads as calculated by Mufti et al. (2002) based on observations by Matsui et al. (2001) in Japan.

Table 7-7 Statistical Distribution of Wheel Loads (Mufti et al. 2002)

Wheel load tonnes (kN)	Percentage of total wheel passes	Cumulative Total percentage	Number of wheel passes ($x10^6$)
1 (9.8)	21.25	21.25	79.05
2 (19.6)	32.06	53.31	119.26
3 (29.4)	21.61	74.92	80.39
4 (39.2)	12.60	87.52	46.87
5 (49.1)	6.48	94.00	24.11
6 (58.9)	3.24	97.24	12.05
7 (68.7)	1.44	98.68	5.37
8 (78.5)	0.54	99.22	2.01
9 (88.3)	0.32	99.54	1.19
10 (98.1)	0.18	99.72	0.67
11 (107.9)	0.11	99.83	0.41
12 (117.7)	0.07	99.90	0.26
13 (127.5)	0.04	99.94	0.15
14 (137.3)	0.02	99.96	0.07
15 (147.2)	0.01	99.97	0.04
16 (157)	0.004	99.97	0.01

It is seen from Table 7.5 that the wheel loads vary over a large range but 94% of the wheel loads lie below 58.9 kN. A bridge will be subjected to the varied intensities of wheel loads in a random order over a period of 75 years (Commentary: CAN/CSA-S6-00). It is practically impossible to replicate the real-life loading on a bridge in a laboratory environment due to time constraints. The tests conducted in the laboratory are accelerated fatigue tests conducted over short durations. This is achieved by applying pulsating or rolling loads of significantly high magnitudes at fairly high frequencies to failure. The testing may be conducted under one or more peak load levels. It is necessary to translate the experimental results of fatigue tests into the probable fatigue life of a bridge structure under service loads. Logically, if a structure is subjected to cyclic loading of a high peak value, it will fail at a certain number of load cycles. If the same structure is subjected to cyclic loading of a significantly smaller magnitude, it will

be able to withstand a considerably larger number of load cycles. For example, a load cycle at a peak load of 400 kN may induce the same equivalent damage as 120 load cycles applied at 200 kN peak load while one load cycle applied at 650 kN peak load may induce damage equivalent to 50,000 load cycles applied at 200 kN peak load. The numbers of load cycles at the two different load levels are correlated. The relationship however, is not a straightforward one, and is dependent on several factors that have been discussed in Section 3 and Appendix-A. The Palmgren-Miner hypothesis is proposed to determine the total damage caused by the application of several different cyclic loads, and to calculate the equivalence between the damage caused by cyclic load of different magnitudes. One such model, developed by Mufti et al. (2002) was used to compare the fatigue performance of various configurations, is discussed in Section 7.3.7.

7.3.7 Model due to Mufti et al. (2002)

Mufti et al. (2002) proposed a mathematical expression based on the Palmgren-Miner hypothesis of cumulative damage, to establish such a relationship. Using this expression the number of load cycles, n_1, applied at a known peak load, P_1, causing a certain damage, can be converted to an equivalent number of load cycles, n_2, that would have to be applied to cause the same amount of damage, at another peak load, P_2,. The ratios of applied loads, P_1 and P_2, to the static failure load, P_s, are expressed as $R_1 = P_1/P_s$ and $R_2 = P_2/P_s$, respectively. The equivalent load cycles at load P_2 are calculated from equation (7.1) as shown.

$$n_2 = n_1 \cdot e^{30(R_1 - R_2)} \qquad (7\text{-}1)$$

Panel-A, Panel-D, and Panel-C were tested under several different peak loads, while Panel-B was tested under static load after applying 1,700 load cycles at 393kN peak load. The actual static failure load of Panel-B was used to revise the previously calculated failure loads for Panels A, C and D. The actual static strength of Panel-C was taken as 90% of its theoretically calculated strength because of the damage caused by the failure of Panel-D and Panel-B (Newhook 1997). Using the revised static failure loads, the number of load cycles applied at each load level was converted to equivalent

load cycles at three load levels of 196 kN, 393 kN, and 883 kN. The first load level corresponds to a factored design wheel load, while the second load level corresponds to the nominal peak load level adopted for all the panels in Phase-I and Panel-A in Phase-II. The third peak load level was common in Panels A, D, and C during Phase-II. The equivalent load cycles at 196, 393, and 883 kN load, for each panel are shown in the second column of Tables 7.7, 7.8, and 7.9, respectively. In each table, the third column shows the ratio of equivalent load cycles for a particular panel to the equivalent load cycles for Panel-A, the control panel.

Table 7-8 Equivalent Load Cycles at 196 kN (20-t) Peak Load for All Panels

Panel	Equivalent Load Cycles (ELC)	$(ELC)_{Panel}/(ELC)_{Panel\text{-}A}$
A	29,000 x10 ^{6}	1.0
B	69,000 x10 ^{6}	2.38
C	23,000 x10 ^{6}	0.79
D	14,000 x10 ^{6}	0.48

Table 7-9 Equivalent Load Cycles at 393 kN (40-t) Peak Load for All Panels

Panel	Equivalent Load Cycles (ELC)	$(ELC)_{Panel}/(ELC)_{Panel\text{-}A}$
A	240 x10 ^{6}	1.0
B	570 x10 ^{6}	2.38
C	240 x10 ^{6}	1.0
D	260 x10 ^{6}	1.08

Table 7-10 Equivalent Load Cycles at 883 kN (90-t) Peak Load for All Panels

Panel	Equivalent Load Cycles (ELC)	$(ELC)_{Panel}/(ELC)_{Panel\text{-}A}$
A	1,449	1.00
B	3,509	2.42
C	304	0.21
D	12,158	8.39

As evident from Tables 7.7, and 7.8, the number of load cycles that a panel will be able to withstand exceeds the commonly accepted minimum requirements by a substantially large margin for each configuration. In comparing relative performances, Panel-A was selected as the control. The ratios of the Equivalent Load Cycles shown in Tables 7.5, 7.6, and 7.7 at three different load levels, are consistent for Panel-B while the ratios for Panel-C are consistent at 196 and 393 kN load levels, and quite low at 883 kN load. The values for Panel-D vary over a wider range, with ratios of 0.48, 1.08, and 8.39 at 196, 393,and 883 kN, respectively. During testing, Panel-D was able to withstand 5,000 load cycles at 883 kN, while Panel-A had failed after 1243 load cycles at the same load level. The previous loading at 393, 637, and 786 kN, contributed only 206 load cycles to the total load cycles in Panel-A. The loading at 981, 1030 and 1079 kN contributed 7,158 load cycles to the total load cycles in the case of Panel-D. Judging from the actual load history of Panel-A and Panel-D, it can be asserted that the ratios at 883 kN appear to be more realistic as compared to the ratios calculated at 196 and 393 kN values. The equivalent load cycles for Panel-B were extrapolated from its static failure load, which theoretically, was equal to the failure load of Panel-A. Therefore, the values of equivalent load cycles for Panel-B should also be identical to those of Panel-A. A set of ratios is proposed as shown in Table 7.11 to modify the equivalent load cycles.

Table 7-11 Proposed Equivalent Load Cycle Ratios for All Load Levels

Panel	$(ELC)_{Panel}/(ELC)_{Panel\text{-}A}$
A	1
B	1
C	3*
D	8

* Panel-C failed after 309 load cycles at 883 kN peak load due dmage caused by failure of both adjacent panels. A conservative ratio of 3 is proposed by comparing its performance during Phase-I of testing.

Using the above ratios, the equivalent load cycles for Panels B, C, and D at 198 and 393 kN load levels are calculated from the equivalent load cycles for Panel-A. However, the following are two possible ways to calculate the equivalent load cycles: A) The equivalent load cycles for Panel-A, taken as base, are multiplied by the appropriate load

cycle ratio to arrive at the equivalent load cycles for a particular panel. B) The equivalent load cycles calculated for Panel-A are divided by highest load cycle ratio (8, for Panel-D), to derive the modified equivalent load cycles for Panel-A. Using the modified equivalent load cycles for Panel-A, the equivalent load cycles are calculated for other panels. Method-A provides a range of upper-bound values of equivalent load cycles while method-B provides a range of lower-bound values. The modified equivalent load cycles at 196 kN and 393 kN are shown in Table 7.12, and Table 7.13, respectively. The values derived by method-B are shown within brackets. These values will be used in conjunction with Fatigue Life Estimation models discussed in Section 3.11.

Table 7-12 Modified Equivalent Load Cycles at 196 kN Peak Load for All Panels

Panel	Equivalent Load Cycles (ELC)
A	29,000 x10 ^{6} (3,500 x10 ^{6})
B	29,000 x10 ^{6} (3,500 x10 ^{6})
C	87,000 x10 ^{6} (10,500 x10 ^{6})
D	232,000 x10 ^{6} (29,000 x10 ^{6})

Table 7-13 Modified Equivalent Load Cycles at 393 kN Peak Load for All Panels

Panel	Equivalent Load Cycles (ELC)
A	240 x10 ^{6} (30x10 ^{6})
B	240 x10 ^{6} (30 x10 ^{6})
C	720 x10 ^{6} (90 x10 ^{6})
D	1,920 x10 ^{6} (240 x10 ^{6})

7.3.8 Fatigue Life Estimation Models

Four different relationships as shown below, proposed by the following researchers were considered for estimating and comparing the fatigue life of various configurations of panels. The first two relationships are based on tests of reinforced concrete deck slabs and the third relationship is based on the tests conducted on reinforced concrete and

steel-free deck slabs. The fourth relationship is based on the tests conducted on steel-free deck slabs. The expressions for the reinforced concrete deck slabs are included to provide a basis for comparison between the two deck slab systems.

- Batchelor and Hewitt (1974)
- Youn and Chang (1998)
- Matsui et al. (2001)
- Mufti et al. (2002)

The four fatigue life estimation relationships are discussed in Sections 7.3.8.1 through 7.3.8.4.

7.3.8.1 Expression due to Batchelor and Hewitt (1974)

Batchelor and Hewitt (1974) conducted fatigue tests on five 1/8-scale models comprising panels with orthotropic and isotropic reinforcement and panels without reinforcement. They suggested the following expression for panels with orthotropic reinforcement.

$$(P_f / P'_S) = 1.0 - 0.102N + 0.006\,N^2 \qquad (7\text{-}2)$$

where,

P_f = applied load

P'_s = estimated static failure load

N = log of number of load cycles to failure

7.3.8.2 Expression Due to Yoon and Chang (1998)

Youn and Chang (1998) proposed the following expression for predicting the fatigue life of deck slabs based on tests conducted on one-third-scale models of reinforced concrete bridge decks.

$$\log(P/P_s) = -0.066 \times \log(N) + \log(1.4461) \qquad (7\text{-}3)$$

where,

P = applied peak load

P_s = static failure load

N = number of load cycles required to failure at the applied peak load

7.3.8.3 Expression Due to Matsui et al. (2001)

Based on full-scale models of both reinforced concrete and steel –free deck slabs tested in Japan, Matsui et al (2001) proposed the following equation for both types of deck slabs.

$$\log(P/P_s) = -0.07835 \times \log(N) + \log(1.52) \quad (7\text{-}4)$$

where,

P = applied peak load

P_s = static failure load

N = number of load cycles required to failure at the applied peak load

7.3.8.4 Expression Due to Mufti et al. (2002)

Based on testing of steel-free decks, Mufti et al. (2002) proposed a modification of Matsui's expression

$$P/P_s = 1.0 - \ln(N) / 30 \quad (7\text{-}5)$$

where,

P = applied peak load

P_s = static failure load

N = number of load cycles required to failure at the applied peak load

7.3.8.5 Applicability of Models

To compare the four expressions, a simple test is applied. For static failure N = 1 the ratio P/P_s = 1. If the value of N = 1 is substituted in each expression, the Batchelor and Hewitt (1974), and Mufti et al. (2002) expressions yield the value of P/P_s as 1. Youn and Chang (1998), and Matsui et al. (2001) expressions 1.446, and 1.52 respectively. The second and the third expressions do not to appear to be valid for the condition N = 1 and therefore may be inaccurate at higher values of P/P_s and a lower number of load cycles. Matsui et. al. (2001) have clarified that their expression is valid for N greater than 10,000. There is no express qualification, however, in the Youn and Chang (1998) model.

A graphical representation of the four expressions is shown in Figures 7.2. For brevity, the curves based on the expressions by Youn and Chang (1998), Matsui et al. (2001), and Mufti et al. (2002) are referred to as Batchelor's curve, Youn's curve, Matsui's curve, and Mufti's curve, respectively, in the following discussion.

At approximately 100 load cycles, Batchelor's and Mufti's curves coincide. The difference between the three expressions diminishes as the number of load cycles increases. At 100,000 load cycles, Batchelor's curve yields the value of 0.63, Matsui's and Mufti's curves yield identical values of 0.616, while Youn's curve provides a value of P/P_s = 0.675. At 1 million cycles, all four curves are close to each other with Batchelor's and Youn's curves providing the upper bound values of P/P_s at 0.6, and 0.59, respectively, and Matsui's and Mufti's curves providing the lower bound values of P/P_s at 0.51, and 0.54, respectively. Between 1 and 10 million cycles, the four curves are quite close, with Batchelor's curve providing the upper bound values, while Matsui's curve provides the lower bound values. Batchelor's curve levels off after 10 million cycles. If the curve is extended beyond 100 million load cycles it starts to increase again. At approximately 250 million cycles, Matsui's and Mufti's curves once again converge, while Youn's curve begins to move upwards. It should be noted, however, that these curve are based on experimental data covering a relatively smaller range of load cycles. For values of P/P_s below those corresponding to 2 million load cycles, the deck slabs are

assumed to have indefinite fatigue life and therefore the curves are not relevant beyond that threshold.

For engineers, the range of interest lies between 1 and 10 million load cycles. Two million load cycles has been widely accepted as the required minimum fatigue life of the deck slabs. The ratio P/P_s for 2 million cycles of fatigue life derived by each expression is: Batchelor's curve-0.596, Youn's curve-0.55, Matsui's curve-0.48, and Mufti's curve-0.52. The latter three curves are used in the discussion of fatigue life of the test panels. The first curve by Batchelor and Hewitt (1974) was not included in the discussion for the reasons mentioned in the preceding paragraph.

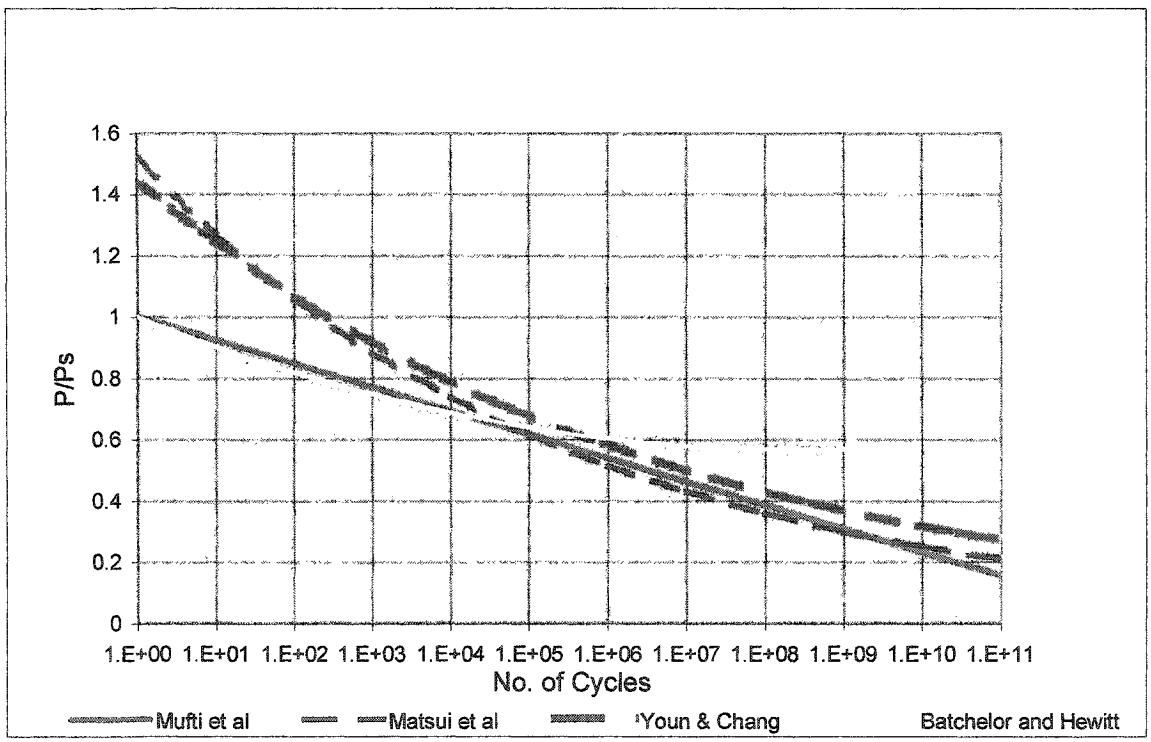

Figure 7-2 Fatigue-Life Estimation Models

7.3.8.6 Representation of Equivalent Load Cycles

The upper bound and the lower bound equivalent load cycles shown in Tables 7.9, 7.11 and 7.12 are plotted together with the three fatigue life estimation models by Youn and Chang (1998), Matsui et al. (2001), and Mufti et al. (2002).

The upper-bound equivalent load cycles for each panel at 196 kN peak load is shown in Table 7.11, together with the three fatigue life estimation curves are shown in Figures 7.3. The points representing Panels C, and D lie very close to Mufti's curve, while points representing Panels A. and B are positioned slightly farther. The values of P/Ps for Panels A, and B are the same, but differ for Panels C, and D, as they both have different theoretical static failure loads.

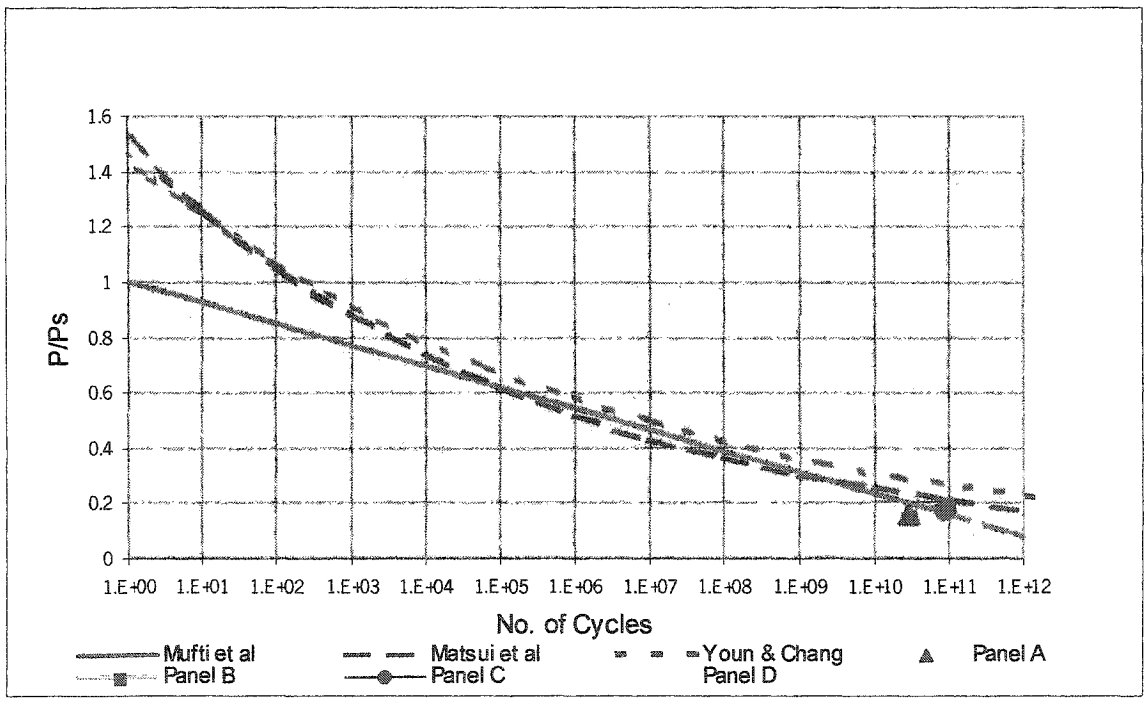

Figure 7-3 Fatigue Life Models and Equivalent Load Cycles (Upper-Bound) at 196 kN Peak Load

The data points for the upper-bound equivalent load cycles at 393 kN peak load are shown in Figure 7.4. The points representing Panels A, B, and D lie slightly under the curve while the point representing Panel-C is located slightly above.

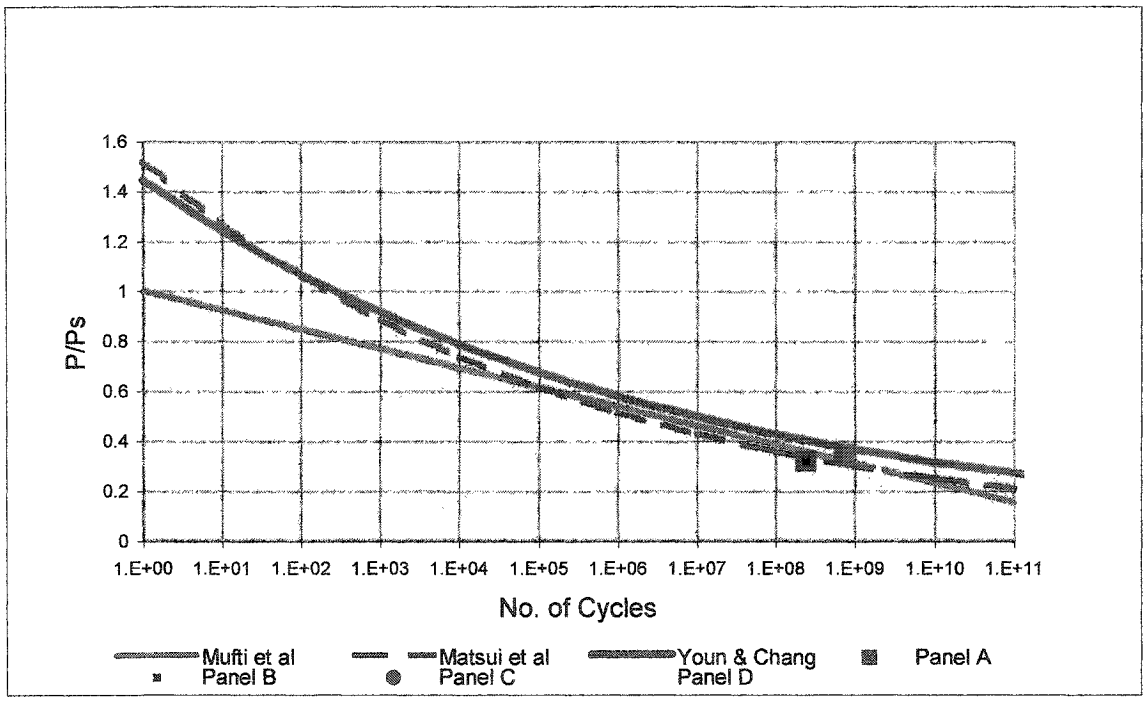

Figure 7-4 Fatigue Life models with Equivalent Load Cycles (Upper Bound) at 393 kN Peak Load

The data points for the equivalent load cycles at 883 kN peak load are shown in Figure 7.5. The points representing Panels A, B, and C lie just under Mufti's curve while the point representing Panel-D is located further below.

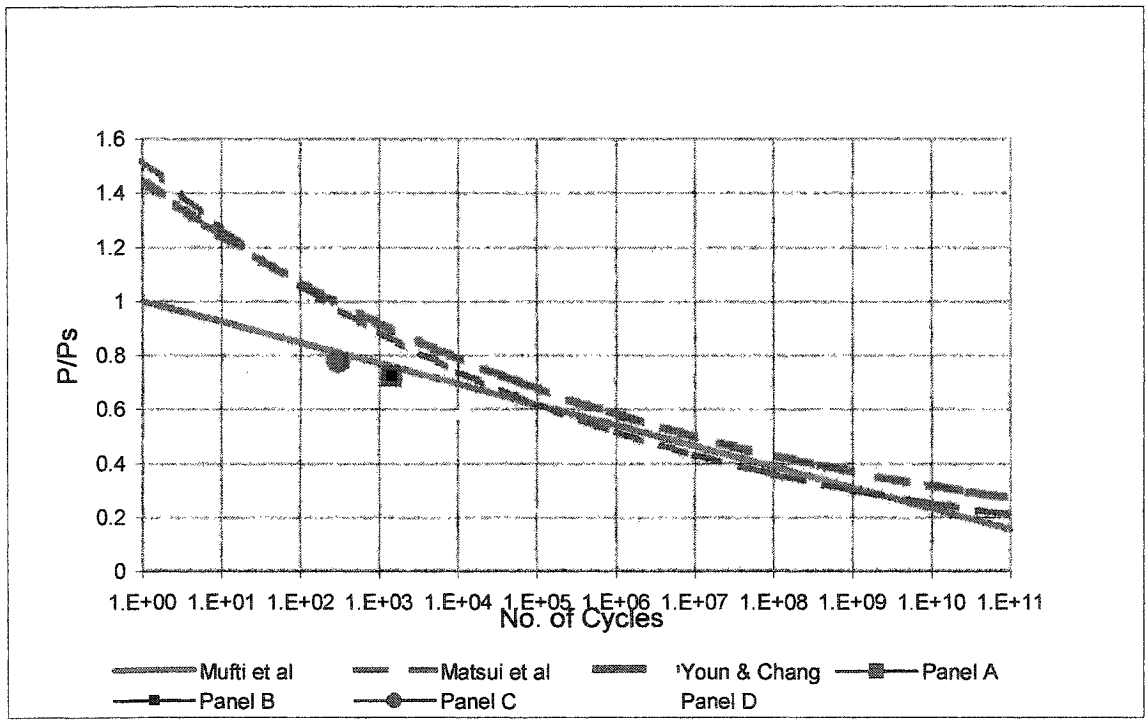

Figure 7-5 Fatigue Life Models with Equivalent Load Cycles (Lower-bound) at 883 kN Peak Load

The data points for the lower-bound equivalent load cycles at 196 kN peak load are shown in Figure 7.6. The points representing Panels A, B, C, and D all lie well below Mufti's curve.

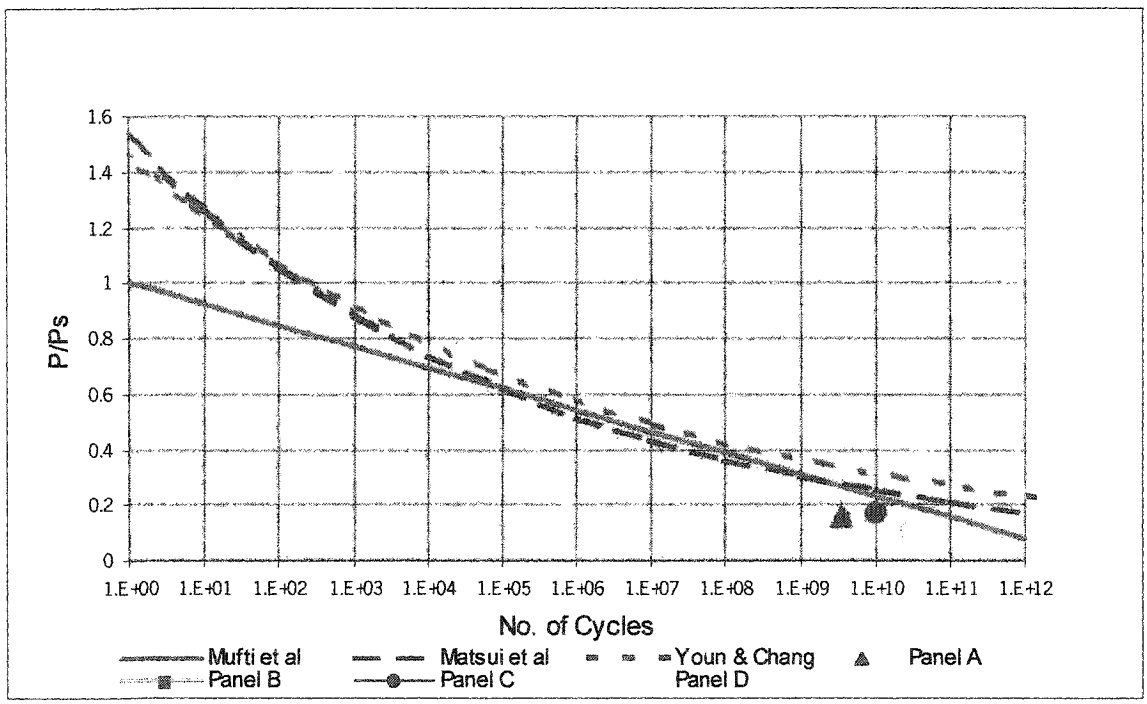

Figure 7-6 Fatigue Life models with Equivalent Load Cycles (Lower-bound) at 196 kN Peak Load

The data points for the lower-bound equivalent load cycles at 393 kN peak load are shown in Figure 7.7. The points representing Panels A, B, and D lie under the curve, while the point representing Panel-C is located slightly below.

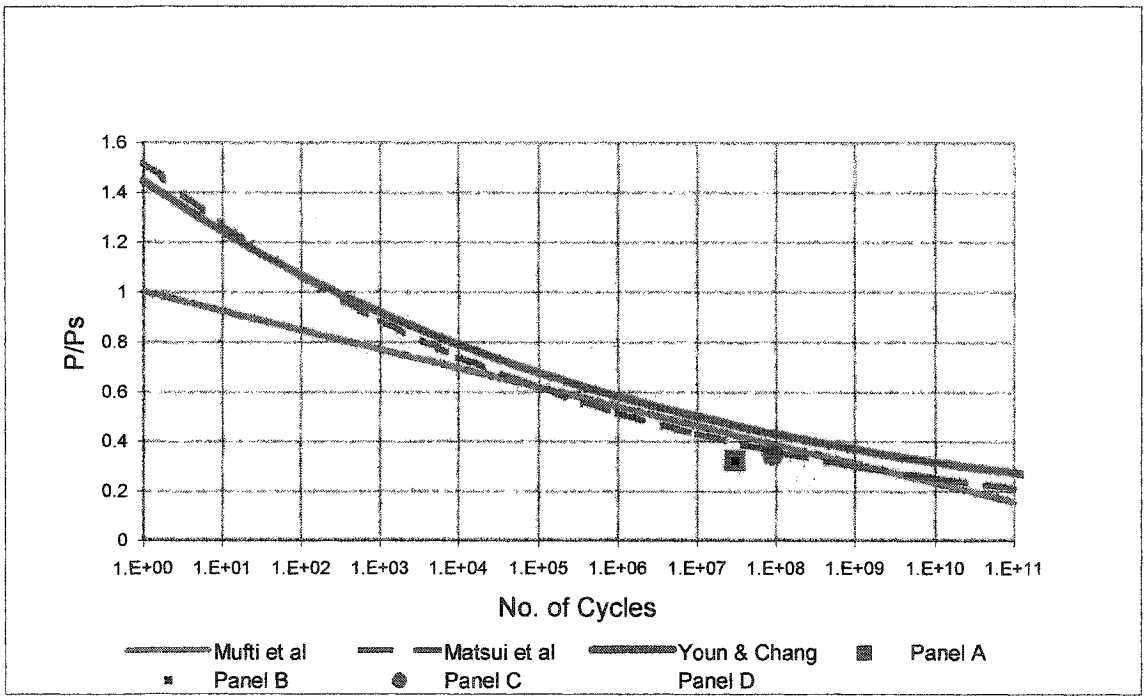

Figure 7-7 Fatigue Life Models with Equivalent Load Cycles (Lower-Bound) at 393 kN Peak Load

7.3.8.7 Recommended P-N Curves

As discussed in Section 7.3.7, upper and lower bound values of equivalent load cycles were calculated for each panel. As seen in Figures 7.3, 7.4,and 7.5, the upper bound data points representing all the four panels lie very close to Mufti's curve, while the lower-bound data points representing all the four panels, shown in Figures 7.6, and 7.6, lie either close to, or below Mufti's curve.

Using the upper bound values of equivalent load cycles at each load level, an envelope of curves was drawn as shown in Figure 7.8. The equations for the upper and the lower limits together with Mufti's curve are also shown therein. Mufti's curve lies between the two extremes, slightly closer to the upper limit curve.

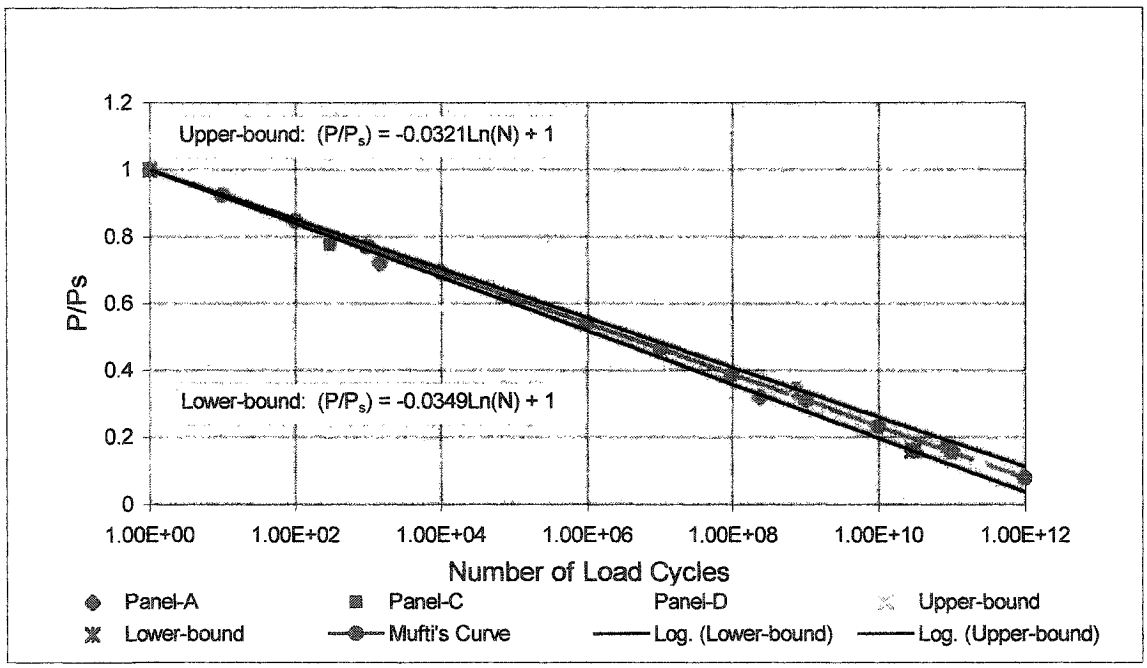

Figure 7-8 Envelop of Fatigue Life Curves (Upper-Bound)

A similar exercise was carried out using the lower-bound values of equivalent load cycles as shown in Figure 7.9. The lines representing the extremities of the envelope lie well below Mufti's curve. These curves would yield conservative estimates of the load cycles to failure.

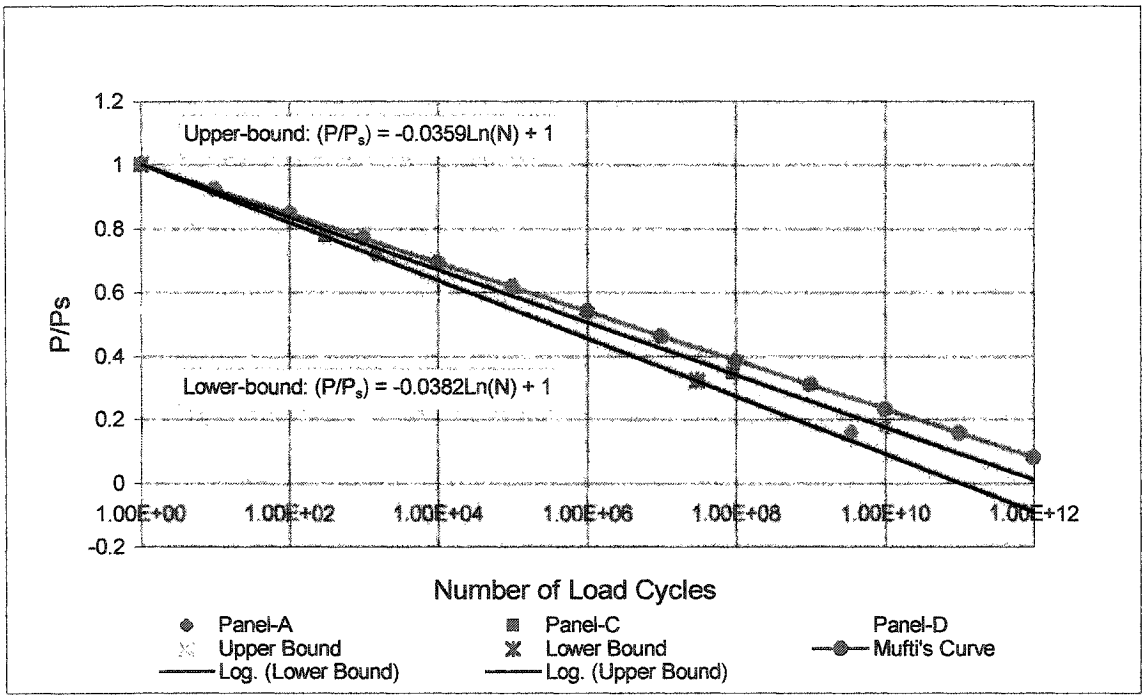

Figure 7-9 Envelope of Fatigue Life Curves (Lower-Bound)

To compare the values of fatigue life as calculated by the four equations shown in Figure 7.8, and Figure 7.9 and Mufti's equation, the number of load cycles to failure was calculated for P/Ps ratios ranging from 1 to 0.1 at each interval of 0.1. The values calculated by each equation are shown in Table 7.14.

Table 7-14 Comparison of Fatigue Life Estimates

Load Ratio	Number of Load cycles				
	Equation 7.5	Fig.7.8		Fig.7.9	
P/Ps	Mufti's	Upper Limit	Lower Limit	Upper Limit	Lower Limit
1	1	1	1	1	1
0.9	20	23	18	16	14
0.8	403	508	308	263	188
0.7	8,103	11,451	5,410	4,258	2,574
0.6	162,755	258,089	94,970	69,014	35,285
0.5	$3,27 \times 10^6$	5.82×10^6	1.67×10^6	1.12×10^6	4.84×10^5
0.4	6.57×10^7	1.31×10^8	2.93×10^7	1.81×10^7	6.63×10^6
0.3	1.32×10^9	2.96×10^9	5.14×10^8	2.94×10^8	9.08×10^7
0.2	2.65×10^{10}	6.66×10^{10}	9.02×10^9	4.76×10^9	1.25×10^9
0.1	5.32×10^{11}	1.50×10^{12}	1.58×10^{11}	7.72×10^{11}	1.71×10^{10}

Table 7.14 shows a wide variation in the number of load cycles calculated by different equations. The maximum permissible service wheel load, P, and the static punching strength, P_s, of a bridge are the most important factors in determining the fatigue load of a bridge deck slab. Their ratio, P/P_s, will influence the number of load cycles that the bridge deck will be able to withstand. In most cases the ratio, P/P_s, is very low, ranging from 0.1 to 0.25. The low ratios are achieved due to two reasons; a) the limits on the maximum permissible axle load, and b) higher punching shear strength of deck slabs obtained due to various design code requirements such as maximum span to depth ratios for the deck slabs, high compressive strength of concrete, adequate transverse confinement, either in the form of external confinement in the steel-free bridge decks, or in the form of bottom transverse reinforcement in case of a conventionally reinforced deck slab. The experimental results of tests on full-scale models reported by Newhook and Mufti (1998) are shown in Table 7.15. The test results of repaired panels are indicative of sufficient reserve strength inherent to the steel-free deck slabs. Khanna (1999) reported punching strengths ranging from 756 kN to 888 kN for deck slab panel reinforced with a single layer of isotropic reinforcement, two layers of isotropic reinforcement, and panels reinforced with only bottom transverse reinforcement.

Table 7-15 Experimental Results (Newhook and Mufti, 1998)

Test	f'_c (MPa)	Girder Spacing (mm)	Deck depth (mm)	P_{exp} (kN)
8	27	2,000	175	1,127
9	27	2,000	175	923
10	27	2,000	175	911
11	27	2,000	175	844
12	27	2,000	175	576
13	27	2,000	175	715
14	39	2,700	300	1,275
15	39	2,700	300	951
Repaired				
16	27	2,000	175	785
17	27	2,000	175	687
Reinforced Concrete				
18	-	2,133	190	631
19	-	2,000	150	622

Judging from the test results shown in Table 7.15, assuming a value of 800 kN for P_s can be considered to be quite conservative for deck slabs with a girder spacing of 2,000 mm and slab thickness of 175 mm. For a wheel load of P = 200 kN, the value of P/P_s is 0.25. For this ratio, Mufti's equation yields $N = 5.91 \times 10^9$ cycles, Matsui's equation yields, $N = 1 \times 10^{10}$ cycles, and Youn's equation yields, $N = 3.54 \times 10^{11}$ cycles while the equation based on lower bound values yields $N = 3.36 \times 10^8$ cycles. Even if the lowest value of $N = 3.36 \times 10^8$ cycles is accepted as the fatigue life of the deck slab, it is well above the required minimum number of load cycles. The total number of wheel passes at various load levels shown in Table 7.7 are equivalent to approximately 1.63 million load cycles at 200 kN wheel load.

As a conservative approach, the upper-bound trendline in shown in Figure 7.9 is proposed to estimate the fatigue life of steel-free deck slabs. The proposed relationship continues upto 100 million load cycles, yielding a a value of P/P_s = 0.34. Ratios of P/Ps below 0.34 are expected to yield theoretical fatigue life greater than the useful life of a bridge deck as shown in Figure 7.10. For 2 million cycles, the curve yields a value of P/P_s = 0.48. According to Youn and Chang, 0.555, according to Mufti et al., 0.516, and according to Matsui et al., 0.488. Although, from the past experience (Bakht and

Selvadurai 1997; Mufti et. al. 2000) it can be argued that the fatigue life of steel-free deck slabs exceeds the commonly accepted minimum fatigue life requirements by a fairly large margin, and that such calculations need to be performed as a matter of research interest.

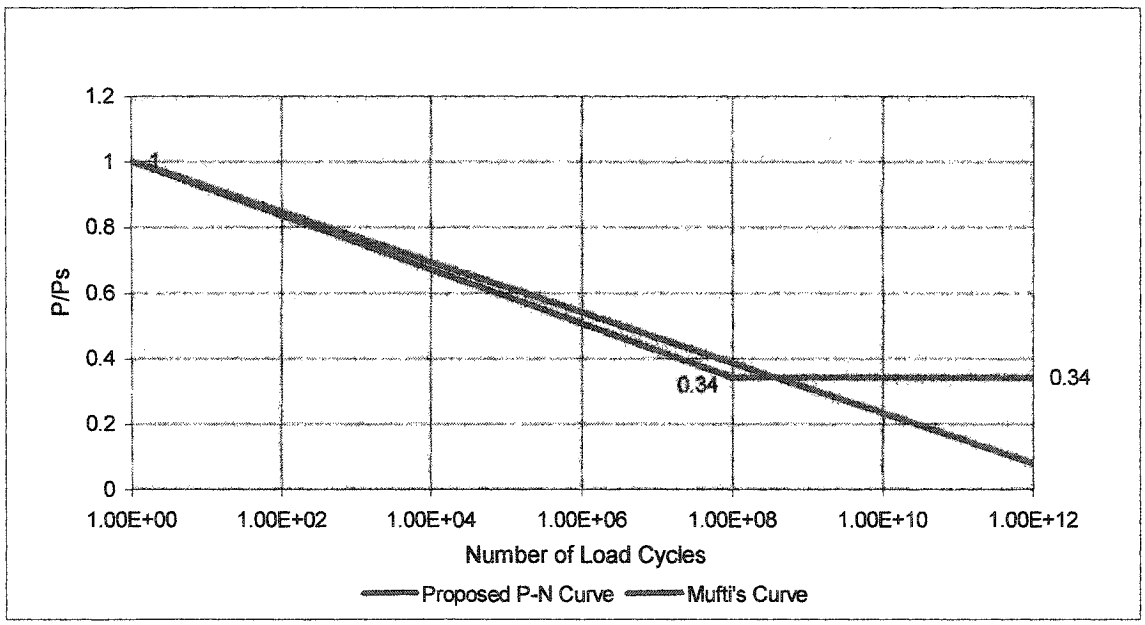

Figure 7-10 Proposed P-N curve for Steel-Free Deck Slabs

8.0 CONCLUSIONS AND RECOMMENDATIONS

8.1 Conclusions

The following conclusions are drawn from the results of the test program.

- One layer of the bottom crack control mesh reduces crack widths considerably and replaces a single, wide, longitudinal crack by several longitudinal and transverse cracks of significantly smaller widths, most of which are visible only on close inspection.
- The bottom crack control mesh enhances the stiffness of the confinement system and lowers internal strain levels in concrete while adding to the punching strength of the deck slab.
- Considering the crack widths, extent of cracking and the cross-sectional area of the meshes provided, the performance of Panel-C was was better than that of Panel-D with steel crack-control mesh.
- The static punch test on Panel-B has shown that the strength of a steel-free deck slab is not affected by a full-depth longitudinal crack.
- Fatigue life of all configurations of the steel-free deck slab is well above the commonly accepted minimum fatigue life requirements.
- Every increase in peak load is accompanied by increased damage, followed by a relatively stable behaviour.
- The fatigue performance of steel-free deck slabs is not affected by the longitudinal crack.
- The fatigue performance and failure pattern of steel-free deck slabs is not affected by full-depth transverse cracks.
- Failure under fixed position cyclic loading causes local degradation within the vicinity of the failure zone.
- Failure under static loading causes extensive damage and an overall degradation of the stiffness of the deck.
- Overall failure patterns of all the panels were similar despite having different internal configurations.

- Mufti's equation provides a reasonable estimate of the fatigue life of the deck slabs if the procedure for calculating equivalent load cycles is further refined.
- The results obtained from the acoustic attenuation technique match closely with the results provided by conventional instrumentation.
- The acoustic attenuation technique can be used to detect internal damage in concrete deck slabs.

8.2 Recommendations

- Steel-free deck slabs should be provided with a GFRP bottom mesh to control the width of their longitudinal cracks.
- A maximum spacing of 300 mm is recommended for the bars in the crack control mesh to be effective, as shown in Figure 7.1.
- Additional crack control mesh as shown in Figure 7.1 should be provided near the edge beams to control the initiation and propagation of Y-shaped cracks.
- It is recommended that the possibility of prestressing or post tensioning of straps and the deck slab, or providing some form of surface reinforcement should be explored for enhancing the arching action.
- Further experimental work on concrete cylinders is also recommended to improve the prediction of equivalent load cycles.
- Further testing should be conducted to determine the fatigue life of steel-free deck slabs under at least three different loads ratios of P/P_s in order to define the relationship between the load ratios and the total number of load cycles to failure, N.
- As a conservative approach, P-N curve shown in Figure 7.10 is proposed to estimate the fatigue life of steel-free deck slabs. For 2 million cycles, the curve yields a value of P/P_s = 0.48, as per Youn and Chang (1998) 0.555, as per Mufti et al. (2002) 0.516, and as per Matsui et al. (2001) 0.488. Although, from the past experience (Bakht and Selvadurai 1997, Mufti et al. 2001) it could be argued that the fatigue life of steel-free deck slabs exceeds the commonly accepted minimum fatigue life requirements by a fairly large margin, such calculations need to be performed as a matter of research interest.

- To reduce the occurrence of transverse cracks, the concreting sequence recommended by Ducret and Lebbet (1998) should be adopted on a trial basis for steel-free deck slabs.
- The acoustic attenuation technique should be further developed for identifying and detecting damage in bridge deck slabs.
- Multidirectional acoustic surveys should be used to determine the extent of damage in bridge deck slabs with greater accuracy.

9.0 REFERENCES

Bakht, B., (1996), Revisiting Arching Action in Deck Slabs, Canadian Journal of Civil Engineering, Vol. 3, No. 4, pp 973-981.

Bakht, B., Markovic, S., (1986), Accounting for Internal Arching in Deck Slab Design, The Journal of the Institution of Engineers (India), 67 (CI1), pp. 18-25.

Bakht, B., Mufti, A. A., (1998), Five Steel-Free Deck Slabs in Canada, Structural Engineering International, Vol. 8, No. 3, pp. 196-200.

Bakht, B., and Selvadurai,A. P.S., (1996), Performance of Steel-Free Deck slabs under Simulated Wheel Loads, Proceedings: 2nd Annual Conference on Advanced Composite Materials in Bridges and Structures, Montreal, pp. 767-776.

Banthia, V., Mufti, A. A., Bakht, B., and Svecova, D., (2002), Transverse confinement of Deck Slabs by Concrete Straps, Proceedings: 6th International Conference on Short and Medium Span Bridges (SMSB VI), Vancouver, BC, Canada.

Batchelor, B. de V., and Hewitt, B. E., (1974), Are Composite Bridge Slabs too Conservatively Designed?- Fatigue Studies, SP41-15, Abeles Symposium, Fatigue of Concrete, ACI Publication SP-41, American Concrete Institute, Detroit, pp. 331-346.

Beal, David, B., (1982) Load Capacity of Concrete Bridge Decks, Journal of Structural Division, Proceedings of the American Society of Civil Engineers, vol. 108, No. ST4, pp. 814-832.

Bennett, E. W., and Raju, N. K., (1971), Cumulative Fatigue Damage of Plain Concrete in Compression, Proceedings: International Conference on Structure, Solid Mechanics and Engineering Design, Southampton, April 1969, Part 2, pp.1089-1102, (Wiley Interscience, New York, 1971).

Breastrup, Mikael, W., and Morley, C. T., (1980), Dome Effect in RC Slabs: Elastic-Plastic Analysis, Journal of Structural Division, Proceedings of the American Society of Civil Engineers, vol. 106, No. ST6, pp. 1255-1262.

Braimah, A., Green, M. F., and Soudki, K. A., (1998), Polypropylene FRC Deck Slabs Transversely Prestressed with carbon Fiber Tendons, ASCE Journal of Composites in Construction, Vol. 2, Issue 4, pp. 149-157.

Butt, S. D., (2001), Experimental Measurement of Attenuation due to Fracture over 100 to 300 kHz Bandwidth, Pure and Applied Geophysics, V. 58, No. 9-10, 2001,pp.1783-1796.

Butt, S. D., Mukherjee, C., and Lebans G., (2000), Evaluation of Acoustic Attenuation as an indicator of Roof Stability in Advancing Headings, International Journal of Rock Mechanics and Mining Sciences, 37 (2000),pp.1123-1131.

Butt, S. D., Limaye, V., Mufti, A. A., and Bakht, B., (2004), Acoustic transmission Technique for Evaluating Fatigue Damage in Concrete Bridge Deck Slabs, ACI Structural Journal, Vol. 101, No. 1, pp.3-10.

Buyukozturk, O., (1998), Imaging of Concrete Structures, Nondestructive Testing and Evaluation International, Vol. 31, No. 4, pp. 223-243.

Canadian Highway Bridge Design Code, CAN/CSA-S6-00, Section 16, Fibre Reinforced Structures, Canadian Standards Association, Toronto, Canada.

Carpinteri, Alberto, (1982) Application of Fracture Mechanics to Concrete Structures, Journal of Structural Division, Proceedings of the American Society of Civil Engineers, Vol. 108, No. ST4, pp. 833-848.

Csagoly, P. F., and Dorton, R. A., (1978), Truck Weights and Design Loads in Canada, Structural Research Report, SRR-79-2, Ministry of Transportation and Communications, Downsview, Ontario, Canada.

Do, Minh-Tan, Challal, Omar, and Aitcin, Pierre-Claude, (1993) Fatigue Behavior of High-Performance Concrete, Journal of Materials in Civil Engineering, Vol 5, No. 1, pp. 96-111.

Ducret, Jean-Marc, and Lebet, Jean-Paul, (1999), Behavior of Composite Bridges during Construction, Structural Engineering International, 3/99, pp. 212-218.

Faming, Li, and Zongjin, Li, (2000), Acoustic Emission Monitoring of Fracture of Fiber-Reinforced Concrete in Tension, ACI Materials Journal, Vol. 97, No. 6, pp. 629-636.

Feldman, R. F., (1969), Volume Change and Creep of Concrete, CBD-119, Canadian Building Digest, Institute for Research in Construction, National Research Council, Canada, pp.1-6.

Fritsche, Josef, (1948), Massivebrucken, Franz Deuticke,Wien, Austria.

Grzybowski, Miroslaw, and Meyer, Christian,(1993), Damage Accumulation in Concrete with and without Fiber Reinforcement, ACI material Journal, V. 90, No.6, November-December 1993.

Guyon, Y., (1960), Prestressed Concrete Volume II, Translated by Amerongen, C. Van, John Wiley and Sons, Inc., New York, NY, USA.
Gyrogy, Balazs, L., (1991), Fatigue of Bond, ACI Materials Journal, Vol. 88, No. 6, pp. 620-629.

Hassan, Ammar, Kawakami, Makoto, Niitani, Kyoji, and Yoshika, Tamio, (2002), An Experimental Investigation of Steel-Free Deck Slabs, Canadian Journal of Civil Engineering, Vol-29, pp. 831-841.

Hewitt, Brian Edwin, (1972) An Investigation of the Punching Strength of Restrained Slabs with Particular Reference to the Deck Slabs of Composite I Beam Bridges, Ph.D. Thesis, Queen's University, Kingston ON, Canada, 1972.

Hewitt, Brian, E., and Batchelor, Barrington, deV., (1975), Punching Shear Strength of Restrained Slabs, Journal of Structural Division, Proceedings of the American Society of Civil Engineers, vol. 101, No. ST9, pp. 1837-1852.

Holman, Jan Ove, (1982), Fatigue of Concrete by Constant and Variable Loading, ACI Publication SP 75-4, American Concrete Institute, Detroit, US, pp 71-110.

Hordijk, D. A., and Reinhardt, H. W., (1993), Numerical and Experimental Investigation into the Fatigue Behavior of Plain Concrete, Proceedings: SEM VI International Congress on Experimental Mechanics, Las Vegas, USA.

Hsu, Thomas, T. C., (1981) Fatigue and Microcracking of Concrete, Materiaux et Constructions, Vol. 17. No. 97, pp. 51-54.

Hsu, Thomas, T. C., (1981) Fatigue of Plain Concrete, ACI Material Journal, Vol. 78. No. 5, pp. 292-305.

Ishida, Tsuyoshi, (2001), Acoustic Emission Monitoring of Hydraulic Fracturing in Laboratory and Field, Construction and Building Materials, 15 (2001), pp. 283-295.

Jiang, Da-Hua, and Shen, Jing-Hua, (1986), Strength of Concrete Slabs in Punching Shear, Journal of Structural Engineering, Vol. 112, No.12,pp. 2578-2591.

Jhamb, I. C., and MacGregor, J. G., (1974), Stress Concentrations Caused by Reinforcing Bar Deformations, Abels Symposium, Fatigue of Concrete, ACI Publication SP-41, pp. 169-182, American Concrete Institute, Detroit, USA.

Journel, A. G., and Huijbregts, 1978, Mining Geostatics, Academin Press, London, UK

Kinnunen, S, and Nylander, H, (1960), Punching of Concrete Slabs without Shear Reinforcement , Transactions: Royal Institute of Technology, Stockholm, Sweden, No. 158.

Kuang, J. S., and Morley, C. T., (1992) Punching Shear Behavior of Restrained Reinforced Concrete Slabs, ACI Structural Journal, Vol. 89, No. 1, pp. 13-19.

Lewis, Richard Gregory, (2002) Behaviour of High Volume Synthetic Fiber Reinforced Concrete under Flexural Fatigue Loading, M. A. Sc. Thesis, Dalhousie University, 2002.

MacGregor, James G, and Bartlett, Michael F., (2000), Reinforced Concrete-Mechanics and Design, 1st Canadian Edition, Prentice-Hall Canada Inc, Scarborough, Ontario, Canada.

Mahoney, Michael, A, (1997), Engineered Fiber Reinforced Cement Based Composites for Bridges, M. A. Sc. Thesis, Technical University of Nova Scotia, Halifax, NS, Canada,1997.

Mander, J. B., Priestley, M. J. N., and Park, R., (1988), Theoretical Stress-Strain Model for Confined Concrete, Journal of Structural Engineering, Vol.114, No. 8, August,1988, pp. 1804-1826.

Matsui, S, Tokai, D, Higashiyama, H, and Mizhokoshi, M, (2001), Fatigue Durability of Fiber Reinforced Concrete Decks under Running Wheel Load, Proceedings: 3rd International Conference on Concrete under Severe Conditions, Vancouver, B.C., Canada, pp 982-991.

Mehta, P.K., and Montrerio, (1993), Concrete Structure, Properties and Materials, Prentice-Hall Inc., New Jersey, NJ, USA.

Mellinger, Frank M., (1957), Prestressed Concrete Airfield Pavements, Proceedings: World Conference on Prestressed Concrete, July 1957,California, USA, pp. A-24-1-10.

Miner, Milton, A, (1945), Cumulative Damage in Fatigue, Journal of Applied Mechanics, pp. 159-164.

Mirza, Sher Ali, Hatzinikolas, Michael, and MacGregor, James G., (1979), Journal of Structural Division, Proceedings of the American Society of Civil Engineers, Vol. 105, No. ST6, pp. 1021-1037.

Mor, A., Gerwick, B. C., (1992), Fatigue of High-Strength Reinforced Concrete, ACI Materials Journal, Vol. 89, No. 2, pp. 197-207.

Mufti, A. A., Jaeger, L. G., and Wegner, L. D., (1993), Experimental Investigation of FRC Deck Slabs Without Internal Steel Reinforcement, Canadian Journal of Civil Engineering, Vol. 20, No.3, pp. 398-406.

Mufti, Aftab A, Jaeger, Leslie G., Wegner, Leon D, and Bakht, Baidar, (1991), Fibre Reinforced Concrete Deck Slabs Without Steel Reinforcement, Research Report No. 1-1991, Nova Scotia CAD/CAM Centre, Halifax NS, Canada.

Mufti, Aftab, A., Bakht, Baidar, Jaeger, Leslie, G., (1996), Bridge Superstructures New Design, National Book Foundation, Islamabad, Pakistan.

Mufti, Aftab A., Banthia, Nemkumar, Bakht, Baidar, (2001), Fatigue Testing of Precast Arch Panels, Proceedings: 3rd International Conference on Concrete under Severe Conditions, Vancouver, B.C., Canada, pp 1035-1041.

Mufti, A. A., and Newhook, John. P., (1998), Punching Shear Strength of Restrained Concrete Bridge deck Slabs, ACI Structural Journal, V. 95, No.4, pp. 375-381.

Mufti, A. A., Newhook, John. P., and Mahoney, Michael. A., (1999), Salmon River Bridge Field Assessment, Proceedings: CSCE Annual Conference 1999, Regina, Canada, pp. 51-61.

Mufti, A. A., Newhook, John. P., and Mahoney, Michael. A., (1999), Salmon River Bridge Field Assessment of Deck Cracking, Research Report No. 1-1999, ISIS Canada Project T3.3, No.3.

Mufti, A. A., Memon, Amjad H., Bakht Baidar, and Banthia, Nemkumar, (2002), Fatigue Investigation of Steel-Free Bridge Deck Slabs, ed. Balaguru, P., Naaman, A., and Weiss, W, ACI SP-206, American Concrete Institute, Farmington Hills, Mi., pp. 61-70.

Nelson, E. L., Carrasquillo, R. L., and Fowler, D. W., (1988), Behaviour and failure of High Strength Concrete Subjected to Biaxial-Cyclic compression Loading, ACI Materials Journal, Vol. 85, No. 4, pp. 248-253.

Neville, A. M., (1996), Properties of Concrete, Fourth and Final Edition, John Wiley and Sons, Inc., New York, NY, USA.

Newhook, J. P., and Mufti, A. A., (1996), Reinforcing Steel-Free Concrete Deck Slab for the Salmon River Bridge, Concrete International, Vol. 18,No. 6, pp. 30-34.

Newhook, J. P., Bakht, B., Tadros, G., and Mufti, A. A., (2000), Design and Construction of a Concrete Marine Structure using Innovative Technologies, Proceedings: The Third International Conference on Advanced Composite Materials in Bridges and Structures (ACMBS III), Ottawa, pp. 777-784.

Newhook, John Patrick, The Behavior of Steel-Free Concrete Bridge Deck Slabs under Static Loading Conditions, Ph.D. Thesis, Technical University of Nova Scotia, Halifax NS, Canada, 1997.

Oh, Byung Hwan, (1991), Cumulative Damage Theory of Concrete under Variable Amplitude Fatigue Loadings, ACI Materials Journal, V. 88,No. 1, January-February 1991, pp. 41-47.

Ohtsu, Masayasu, and Watanabe, Hiroshi, (2001), Quantitative Damage Estimation of Concrete by Acoustic Emission, Construction and Building Materials, 15, (2001), pp. 217-224.

Okleston, B. E., (1958), Arching Action in Reinforced Concrete Slabs, The Structural Engineer, vol. XXXVI. No. 6, pp. 197-201.

Ople, F. S. Junior, and Hulsbos, C. L., 1966, Proceedings: American Concrete Institute, Vol. 63, 1966, pp. 59-81.

Osman, M., Marzouk, H., and Helmy, S., (2000), Behavior of High-Strength Lightweight Concrete Slabs under Punching Loads, ACI Structural Journal, Vol. 97, No. 3, pp. 492-498.

Palmgren, Arvid, (1945), Ball and Roller Bearing Engineering, SKF Industries, Philadelphia, USA (Translators-Gunnar Palmgren, and Bryce Ruley).

Pla-Rucki, G. F., and Eberhand, M. O., (1995), Imaging of Reinforced Concrete; State-of-the-Art Review, Journal of Infrastructure Systems, V. 1, No. 2, pp. 134-141.

Perdikaris, Philip, C., and Beim, Sergio, (1988) RC Bridge Decks Under Pulsating and Moving Loads, Journal of Structural Engineering, Vol 114, No. 3, pp. 591-607.

Poorman, Alfred P, 1945, Strength of Materials, 4th Ed., McGraw-Hill Book Company, Inc, New York, USA.

Ramakrishnan, V., and Lokvik, Bjorn J., (1991), Fatigue Strength and Endurance Limit of Plain and Fiber Reinforced Concretes – A Critical Review, Proceedings: International Symposium on Fatigue and Fracture in Steel and Concrete Structures.

Rens, K. L., Transue, D. J., and Schuller, M. P., (2000), Acoustic Tomographic Imaging of Concrete Infrastructure, Journal of Infrastructure Systems, V. 6, No. 1, pp. 15-23.

Reynolds, Charles E., and Steedman, James, C., 1988, Reinforced Concrete Designer's Handbook, E. and F. N. Spon, London, UK.

Sansalone, Mary, Lin, Jiunn-Ming, and Streett, William B., (1988), Determining the Depth of Surface-Opening Cracks Using Impact-Generated Stress Waves and Time of Flight Techniques, ACI Materials Journal, Vol. 95, No. 2, pp. 168-177.

Selvadurai, A. P. S., and Bakht, Baidar, (1995), Simulation of Rolling Wheel Loads on an FRC Deck Slab, Proceedings; 2nd University-Industry Workshop on FRC, Toronto, Canada, pp. 273-287.

Shah, Surendra P., Schwartz, Stewart E., Ouyang, Chengsheng, (1995), Fracture Mechanics of Concrete, John Wiley and Sons, Inc., New York, NY, USA.

Sethna, James, http://www.lassp.cornell.edu/sethna/Cracks/FractureModes.html [July 18, 2003].

Shi, X. P., Fwa, T. F., and Tan, S. A., (1993) Flexural Fatigue Strength of Plain Concrete, ACI Materials Journal, Vol. 90, No. 5, pp. 435-440.

Su, Eric C. M., and Hsu, Thomas T. C., (1988), Biaxial Compression Fatigue and Discontinuity of Concrete, ACI Materials Journal, Vol. 85, No. 3, pp. 178-188.

Takhar, S. S., Jordaan, I. J., and Gamble, B. R., (1974) Fatigue of Concrete Under Lateral Confining Pressure, SP41-4, Abeles Symposium, Fatigue of Concrete, ACI Publication SP-41, American Concrete Institute, Detroit, pp. 59-69.

Tawfiq Kamal, Armaghani, Jamshid, and Ruiz, Rodolfo, (1999), Fatigue Cracking of Polypropylene Fiber Reinforced Concrete, ACI Materials Journal, Vol. 96, No. 2, pp. 226-233.

Thorburn, Lorna Jane, A study of Externally Reinforced Fibre-Reinforced Concrete Bridge Decks on Steel Girders, Ph.D. Thesis, DalTech-Dalhousie University, Halifax NS, Canada, 1998.

Toulemonde, Francois, and Ranc, Guillaume, Ranc, (2001), Fatigue Service Life of Transversely Cracked Reinforced Concrete Slabs Representative of Composite Bridge Decks, Proceedings: Third International Conference on Concrete under Severe Conditions, Ed. Banthia, N, Sakai, K, and Gjorv, O. E., University of British Columbia, Vancouver, Canada, pp. 1157-1164.

Trottier, Jean Francois, and Forgeron, Dean, (2001), Cumulative Effects of Flexural Fatigue Loading and Freezing and Thawing Cycles on the Flexural Toughness of Fiber Reinforced Concrete, Proceedings: Third International Conference on Concrete under Severe Conditions, Ed. Banthia, N, Sakai, K, and Gjorv, O. E., University of British Columbia, Vancouver, Canada, pp. 1165-1176.

Whithey, M. O., and Washa, G. W., (1954), Materials of Construction, John Wiley and Sons, Inc., New York, USA.

Wood, R. H., (1958), Composite Construction, The Structural Engineer, Jubilee Issue July 1858, pp. 197-201.

Youn, S. G., and Chang, S. P., (1998), Behavior of Composite Bridge Decks Subjected to Static and fatigue Loading, ACI Structural Journal, V. 95, No. 3, pp. 249-258.

Zhang, Binsheng, and Wu, Keru, (1997), Residual Fatigue Strength and Stiffness of Ordinary Concrete under Bending, Cement and Concrete research, Vol. 27, No. 1, pp.115-126.

APPENDIX-A

APPENDIX-A: THEORETICAL BACKGROUND ON FATIGUE

A.1 Fatigue in Metals

Some of the earliest studies on fatigue in metal were reported to have been carried out by Captains James and Gaston in about 1849, and the most exhaustive of the early test results on fatigue by Wöhler were published in 1858 (Withey and Washa 1954). Withey and Washa drew the following conclusions from Wöhler's study:

- Wrought Iron and steel will rupture at unit stresses below the ultimate and even below the elastic limit, if subjected to a sufficient number of cycles.
- Within certain limits, the range of unit stress, not the maximum stress, determines the number of cycles for failure.
- As the range is decreased, for a given maximum or minimum unit stress, the number of repetitions for rupture increases. For a given maximum or minimum unit stress there appears to be a limiting range within which the repetitions for rupture become infinite.
- As the maximum unit stress increases, the limiting range decreases.

Although the abovementioned tests were conducted in the mid-nineteenth century, these observations still remain valid.

A.2 Fatigue Resistance and Limits

To determine the fatigue life of a specimen, it must be tested to failure under cyclic loading. In order to be able to apply cyclic loading, the magnitude of the load effects due to the peak load must be smaller than the static strength of that specimen (Neville 1996). The number of load cycles, *N*, that can be applied before failure, is influenced by the magnitude of the applied peak load. Higher magnitudes cause rapid failure while lower magnitudes prolong fatigue life. If the magnitude of the applied load is below a certain level, the loading can be cycled indefinitely. In practice, however, it is impossible to test

a specimen over an infinite number of load cycles. Therefore, to be deemed as having the required fatigue resistance, a structure may be required to withstand a minimum number of repetitions of a load of a specified magnitude without failure. The specified number of cycles must exceed, by a substantially large margin, the total number of load cycles that the structure will most likely to be subjected to, during its entire service life. The endurance limit is defined, as the threshold load level below which the material will not fail in fatigue.

A.3 Phenomenon of Fatigue in Concrete

In metals, the appearance of the first crack is regarded as the first sign of impending fatigue failure. In metallic components subjected to high frequency cyclic loading, the time to total failure after the appearance of the first crack can vary considerably. However, a total failure of such components may have fatal consequences. For example, the failure of a rotating component may have disastrous effects, or a crack in the frame of an aircraft wing could lead to a crash. However, in concrete, the cracks are generally present in various forms, such as shrinkage cracks for example, and do not necessarily represent a failure. As well, even the best-compacted concrete contains air voids. Concrete, as a heterogeneous material, has a distinctly different behaviour compared to the metals. It exhibits totally different properties under tensile and compressive loads. While the conclusions in Section A-1 are generally applicable to concrete, the number of cycles required to fail a concrete component after the first crack is significantly larger than the corresponding number of cycles in a metallic component.

A.4 Effect of Cyclic Loading on Concrete

The effect of cyclic loading is to reduce the strength and the secant modulus of concrete. The strength reduction is the cumulative effect of several factors discussed in Section A.5.

Cyclic loading degrades the bond between the aggregates and the cementitious matrix

and between concrete and reinforcement, if present. The concrete contains a large number of randomly dispersed micro-cracks. In addition, it may also contain air voids of various sizes ranging from microscopic voids to large voids measuring several millimeters. While the micro cracks in the compressive stress regime tend to close under compressive loads, the cracks and the air voids cause stress concentrations in their immediate vicinity under both compressive and tensile loads. Cyclic loading causes the micro cracks to grow, extend and merge with the adjacent cracks thus extending the zone of damaged concrete. The tensile strength of concrete is very low in comparison to its compressive strength. Stress concentrations under tensile load will rapidly result in a critical condition, where the tensile stress in concrete in the vicinity of the crack will equal the tensile strength of concrete. As the loading continues, the cracks continue to extend and the stress at the critical concrete cross-section reaches the tensile strength of concrete over a much larger part of the cross-section and the member fails. Fatigue failure occurs mainly as a result of bond failure at the aggregate-cement matrix interface whereas static failure is characterized by aggregate rupture. The cracking of concrete is further discussed in Section A.4.1.

A.4.1 Cracking of Concrete

Microcracks are present in concrete due to various factors even before it is subjected to external loads. Such cracks often occur at the aggregate-paste interface due to shrinkage of cement paste. In addition, concrete contains air voids ranging from a few microns to several millimeters in diameter. Depending on its position with respect to the applied load, a crack can be loaded in three distinct modes (Shah et. al. 1995). Those are:

- Mode-I: Opening Mode
- Mode-II: Sliding Mode
- Mode-III: Tearing Mode

In Mode-I, the crack is stressed in the direction perpendicular to the plane of the crack (Figure.A.1). This mode results due to tensile stresses due to tension and bending.

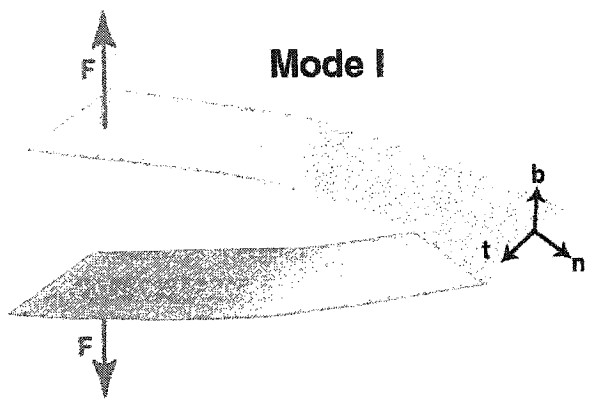

Figure A.1 Crack Loading Mode-I (Sethna 2003)

In Mode-II, the crack is stressed in the direction parallel to the plane of the crack along the depth of crack (in-plane sliding) (Figure A.2). This mode results from the application of shear forces.

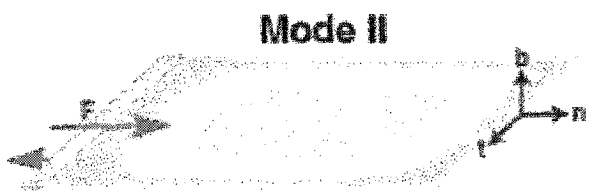

Figure A.2 Crack Loading Mode II (Sethna 2003)

In Mode-III, the crack is stressed in the direction parallel to the crack plane along the length of crack (out-of-plane sliding) (Fig.A.3). This mode also results from shear.

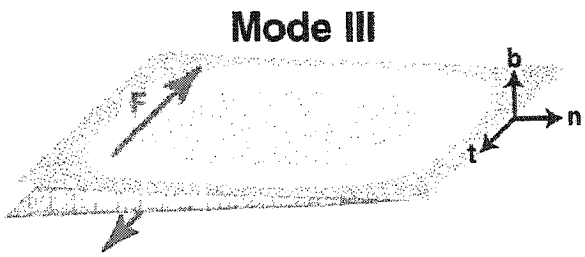

Figure A.3 Crack Loading Mode-III (Sethna 2003)

A.4.2 Significance of Crack Modes

The stressing of the crack generally occurs in a mixed mode exhibiting characteristics of more than one mode. The failure of concrete in fatigue is dependent on the mode in which its cracks are loaded. Mode-I is associated with direct tensile or bending stresses while modes II and III are caused by shear stresses. While studying the fatigue failure of steel-free deck slabs, the mode of crack stressing has added significance as the deck slab derives its strength solely by the development compressive membrane forces. The punching shear failure mechanism of steel-free deck slabs has been established (Newhook 1997). The deck slabs develop a longitudinal crack at the centre, which propagates to the top surface under repeated loads. Under load, this crack tends to close at the top and dilate at the bottom. The details of monitoring of the longitudinal crack in Panel-B are discussed in Section 4.

The circumferential cracks that develop around the load pad on the top surface tend to open under load and close upon removal of the load. The cracks on the top surface that radiate from the load pad tend to close when the panel is loaded and open when the load is removed, whereas the radial cracks on the soffit open under load and close upon removal of the load. The cracks that open under load propagate further as the loading continues. On the other hand, compressive stress perpendicular to the crack develops when the crack closes under load. It can be appreciated that the cracks that open under load will have less fatigue resistance than cracks that close under load. The failure, however, does not occur at the circumferential crack, but occurs due to the development

of shear stresses on a surface that can be idealized as the frustum of a cone. The failure crack therefore is loaded in Mode-II.

A.4.3 Cracking of Concrete and Crack Propagation in Concrete

The cracking of concrete is one of most widely studied topic on concrete behaviour. Researchers have conducted various tests to understand the phenomenon of cracking and to find means to reduce the extent and the width of cracks. The cracks in concrete appear due to several reasons such as plastic shrinkage, drying shrinkage, rapid release of the heat of hydration, temperature variation, differential movement of the structure, or application of loads.

The aggregates and the cement paste, both exhibit a linear elastic behaviour up to approximately 80% of their ultimate strength. However, the concrete, which comprises the aggregates and the cement paste, follows a non-linear path when loaded above 40 to 50% of its ultimate stress (Neville 1996). The concrete can be defined as a three-phase heterogeneous material comprising aggregates, cement paste and transition zone (TZ). The first two constituents need no further description. The transition zone (TZ) is the zone surrounding the aggregate, which is approximately 10 to 50 μm in thickness. This aggregate cement interface, i.e. the transition zone, is the weakest link in the structure of the concrete. Microcracks develop in the transition zone. The extent of microcracking in the transition zone depends on factors such as plastic shrinkage, drying shrinkage, rapid release of the heat of hydration, and curing.

The microcracks are influenced by the magnitude of the applied stress. Depending on the applied stress, the cracking of concrete can be divided into four stages as shown in Table A.1 (Mehta and Montrerio1993).

Table A.1 Loading Stages of Concrete (Mehta and Montrerio 1993)

Stage	Stress level as % of ultimate strength	Microcrack Behaviour	Stress-Strain Relationship
Stage - I	<30%	Stable	Linear
Stage - II	30 – 50%	Propagation of existing microcracks, development of new microcracks in TZ	Deviation from linear behaviour
Stage - III	50 – 75%	Cracks in cement paste at approximately 60% stress level, cracks in TZ become non-stable, cracks in cement paste propagate rapidly	Totally non-linear stress strain curve
Stage - VI	75 – 100%	Cracks in cement paste become continuous and will propagate rapidly. Cracks grow under sustained loads	Stress-strain curves peaks and begins to descend, denoting the start of failure

As the concrete is subjected to load, the microcracks develop progressively and coalesce into macrocracks. Cement paste includes air voids that act as stress raisers resulting in stress concentrations and initiation of cracks in the cement paste. With further increases in the applied load, the macrocracks propagate further and join the cracks developed in the cement paste.

A.5 Factors Influencing Fatigue in Concrete

The fatigue performance of concrete is influenced by several factors such as the rate of loading, age, the tensile and compressive strength of concrete, concrete mix design, the shape of the structural member, the type and the position of reinforcement and the

environment. The factors that are relevant to the current research are discussed in the following sections.

A.5.1 Nature of Loading

A structure can be subjected to three different modes of cyclic loading. In Mode I, the applied stress varies from zero to a predetermined maximum level, S_{max}. In Mode II, the stress varies between two stress levels of the same nature, S_{min} and S_{max}. In the Mode III, the stress varies between two stress levels that are opposite in nature, S_{+ve} and S_{-ve}. The stress range, SR, is defined as the difference between the maximum and the minimum values of applied stress, and is expressed in the following form:

$$SR = S_{max} - 0 \text{ ----------(Mode-I)} \quad (3.1)$$

$$SR = S_{max} - S_{min} \text{ ----------(Mode-II)} \quad (3.2)$$

$$SR = S_{+ve} \text{ and } S_{-ve} \text{ ---------- (Mode-III)} \quad (3.3)$$

The ratio of the stress range to the ultimate stress of the material, influences the endurance limit and the number of cycles required for the material to fail. Cyclic loading below the endurance limit is reported to improve the fatigue strength of concrete (Neville 1997).

Concrete is inherently weak in tension. The tensile strength of concrete is approximately 10% of its compressive strength. Therefore, a concrete structural member under tensile stress mode or a stress reversal mode will fail in fatigue at a significantly smaller number of load cycles, than the number of cycles required to fail in fatigue under compressive loads.

A.5.2 Concrete Ingredients

Aggregate, sand, cement and water are the basic ingredients of concrete. Cement, sand and water form the paste or the matrix, which binds the aggregates together to form the

hardened concrete. The concrete derives its strength from the bond between the aggregates and the matrix. Strong concrete will most likely fracture through the aggregates and the matrix under static load. However, under fatigue load, the bond between the aggregate and the matrix is subjected to successive cycles of compressive and tensile stresses. The fracture is most likely to begin at the aggregate-matrix interface. The aggregate-matrix bond is, therefore, an important factor influencing the fatigue life of concrete. The shape and the surface texture of the aggregates influence the bond strength. Use of crushed and well-graded aggregate results in a stronger bond with the matrix. The quantity of water affects the strength of the concrete. Water in excess of the amount that is required to complete the hydration process will gradually travel to the exposed surface leaving a series of continuously connected air voids. The presence of excessive air voids in the matrix is detrimental to the strength of the matrix.

Use of silica fumes, fly ash, and water-reducing admixtures, combined with optimal compaction of concrete, help enhance the strength of the aggregate matrix bond.

A.5.3 Role of Fibers in Concrete

It has been recognized that the addition of fibers to the concrete mix improves its mechanical properties. The fibers are effective in controlling the plastic shrinkage cracks and also impart post-crack strength to the concrete Trottier and Forgeron (2002). Tawfiq et al. (1999), and Mufti et al. (2001) reported that the fiber reinforced concrete has better ability to delay fatigue crack initiation and to prolong the crack propagation interval. They also reported that the fiber reinforced concrete had a lower rate of reduction of chord modulus and the addition of fibers delayed Stage-I by 67% and Stage-II by 16% when compared with the plain concrete as discussed in Section A.2.

A.5.4 Shrinkage of Concrete

The shrinkage of concrete induces cracks and therefore is an important factor in the study of fatigue in concrete. The cracks can be very small microscopic cracks, to large, continuous, and wide cracks, depending on the mixing, placing and curing of concrete. The phenomenon of shrinkage begins as soon as the concrete is placed and

compacted. The shrinkage occurs in two stages, which are:

a) Plastic shrinkage
b) Drying shrinkage

The significance of the two stages of shrinkage is discussed in the Sections A.5.4.1 and A.5.4.2.

A.5.4.1 Plastic Shrinkage

Plastic shrinkage begins as soon as the concrete is placed. It is caused by the evaporation of free water from the surface of wet concrete. This evaporation of water causes migration of more water from within the concrete to the exposed surface. The shrinkage cracks develop on the exposed surface of concrete. The width, depth and the extent of a crack can vary due to several factors. Low relative humidity, high ambient temperature, exposure to direct sunshine, and high wind speeds can cause rapid evaporation of the surface water and hence, more extensive cracking. A well-protected concrete surface will develop fewer cracks.

The evaporation of water from wet concrete can be reduced or prevented by taking suitable precautions such as provision of a vapour barrier and/or wet burlap on the exposed concrete surfaces. It has been shown that plastic shrinkage cracks can be reduced by addition of synthetic fibers (Trottier et al 2002). Plastic shrinkage stops when the concrete sets.

A.5.4.2 Drying Shrinkage

Drying shrinkage of concrete begins soon after the wet curing is discontinued and the concrete is exposed to the elements. At this stage, the concrete may still contain a fairly large amount of moisture within its pores. As the water evaporates from the exposed surface of concrete, there is a gradual movement of moisture from the saturated interior to the exposed surface. With the loss of water from its pores, the concrete begins to

shrink. If the concrete is restrained, it may develop large shrinkage strains. As is usually the case, most structural members have some form of restraint that would prevent the concrete from shrinking freely. The restraint can be in the form of reinforcing bars, shear connectors or some other structural arrangement that may form an integral part of the structure. The shrinkage strains are tensile in nature and may cause micro and macrocracking. While the cement paste surrounding the aggregate undergoes shrinkage, the aggregate remains passive due to its inert nature. Micro cracks develop at the aggregate matrix interface. Stress concentrations occur at the crack tips. Air voids, particularly those of larger sizes, cause discontinuity in the matrix and lead to stress concentration.

The magnitude of the shrinkage strain in a concrete member depends on several factors such as the shape of the member, cement content and type, mineral composition of aggregates, and the ambient relative humidity. Carbonation of concrete also leads to shrinkage (MacGregor and Bartlet, 2000). The maximum shrinkage due to carbonation occurs in 50% RH (relative humidity) environment (Feldman, 1969). If the concrete strain exceeds the strain level corresponding to the tensile strength of concrete, it leads to full-depth shrinkage cracks.

A.5.5 Effect of Reinforcing Steel

The presence of reinforcement also affects the behaviour of the structure during the intermediate stage. The deformations on the surface of the reinforcing bars induce stress concentration at the root of projecting lugs. Jhamb and Mac Gregor (1974) reported a stress concentration factor, K_T, ranging from 1.44 to as high as 2.664. While stress concentration at the root of the projecting lugs reduces the fatigue life of the reinforcing bars, their tips induce stress concentrations in the surrounding concrete at multiple locations along the length of the bar. Therefore, the stress range in the surrounding concrete would be significantly higher than the rest of the concrete. Under cyclic loading, the concrete in the vicinity of the lugs would fatigue faster and fail. Gradual failure of the surrounding concrete would result in the progressive debonding of

the reinforcement. As the reinforcement and the concrete lose their composite action a redistribution of forces across the section will occur causing higher stresses in concrete. A better bond between the concrete and the reinforcement extends the fatigue life of reinforced concrete (Mor and Gerwick 1992).

APPENDIX -B

APPENDIX-B: CONCRETE TEST RESULTS

1. Results of Tests on Fresh and Hardened Concrete

Table-B 1 Tests on Fresh Concrete

Truck No.	Quantity m^3	Temp. ^0C	Slump mm (as arrived)	Air Content %	Fibre v.f. %	Additive HRWA litre	Slump mm with HRWA
1	6.0	18	50-76	5.9	0.75	9.0	170
2	5.5	20	100	6.8	0.75	9.5	150

Table-B 2 OHBDC Index (Trial Mix)

Peak Post-Crack Strength MPa	Concrete Cracking Strength MPa	OHBDC Index
2.83	6.15	0.44

Table-B 3 Concrete Strength at 180 Days (Trial Mix) 4"X8" Cylinders

Cyl. ID	Failure load kg	Compressive strength Mpa	Concrete type
BI-6	36,400	44.1	Fiber Reinforced
BI-7	37,600	45.5	Fiber Reinforced
BI-9	35,000	42.4	Fiber Reinforced
BI-11	36,400	44.1	Fiber Reinforced
Average	Strength	43.9	

Table-B 4 Concrete strength at 7 Days (Truck no. 2) 6"x12" Cylinders

Cyl. ID	Failure load kg	Compressive Strength MPa	Concrete type
T2-F	52,000 kg	28.1	Fiber Reinforced
T2-P	46,000 kg	24.8	Plain

Table-B 5 Concrete Strength at 28 Days (Mix for Deck Concrete) 6"X12' Cylinders

Cyl. ID	failure load kg	Compressive strength MPa	Concrete type
T1-F	66,000	35.7	Fiber Reinforced (Tr-1)
T2-F	63,400	34.3	Fiber Reinforced (Tr-2)
T2-F	64,400	34.8	Fiber Reinforced (Tr-2)
T2-F	65,200	35.3	Fiber Reinforced (Tr-2)
Average	Strength	35.0	Fiber Reinforced(Tr-1,2)
T2-P	65,200	35.3	Plain (truck-2)

Table-B 6 OHBDC Index of the Concrete Mix used in Deck Slab

Peak Post-Crack Strength MPa	Concrete Cracking Strength MPa	OHBDC Index
2.53	5.64	0.45

Table-B 7 Compressive Strength at 167 Days (after Transverse Crack in Panel-A)

Cyl. ID	Failure load kg	Compressive strength MPa	Concrete type
T2-F	74 800	41.5	Fiber Reinforced (Tr-2)

Table-B 8 Tensile strength at 167 days (after transverse crack in Panel A)

Cyl. ID	Failure load kg	Tensile strength MPa	Concrete type
T1-F	11,300	3.5**	Fiber Reinforced (Tr-1)
T2-F	17,800/ 27,400	2.5*/3.8**	Fiber Reinforced (Tr-2)

* First Tensile Crack
** Total failure

Table-B 9 Compressive Strength at 240 Days (Commencement of Test on Panel-A)

Cyl ID	Failure load kg	Compressive strength MPa	Concrete type
T2-P	79,000 kg	42.7	Plain (Tr-2)
T2-F	91,000 kg	49.5	Fiber Reinforced (Tr-2)
T2-F	88,000 kg	47.6	Fiber Reinforced (Tr-2)
Average	Strength	48.6	Fiber Reinforced (Tr-2)

Table-B 10 Compressive strength at 927 days (After Completion of Test Program)

Cyl. ID	Failure load kg	Compressive strength MPa	Concrete type
T2-P	73,200 kg	39.6	Plain (Truck-2)
T2-F	89,000 kg	48.1	Fiber Reinforced (Truck-2)
T2-F	90,400 kg	48.9	Fiber Reinforced (Truck-2)
T2-F	89,200 kg	48.2	Fiber Reinforced (Truck-2)
Average	Strength	48.4	Fiber Reinforced (Truck-2)
T1-F*	38,400	46.7	Fiber Reinforced (Truck-1)

* 4" x 8" cylinder

Table-B 11 Tensile Strength at 927 Days (after Completion of Test Program)

Cyl. ID	Failure load kg	Strength MPa	Concrete type
T2-F	23,400/29,000	3.2*/4.0**	Fiber Reinforced (Truck-2)
T2-F	28,700/44,500	4.0*/6.2**	Fiber Reinforced (Truck-2)

* First Tensile Crack
** Total failure

APPENDIX-C

APPENDIX-C: SHRINKAGE STRAIN CALCUALTION

2. C-1 Likelihood of Transverse Cracks

Ducret and Lebet (1999) investigated the phenomenon of shrinkage cracking in bridge deck slabs. They proposed a factor β, the ratio of the cross-sectional area of the concrete deck slab to the cross-sectional area of the steel girders, in a slab on girder-bridge. They observed that a bridge deck with $\beta < 0.12$ was more likely to develop shrinkage cracks. The value of β computed for the experimental model was found to be 0.1095. This value of β is 8.75% below the threshold of 0.12.

$\beta = A_a / A_c$

Where

A_a = Cross-sectional Area of Girders = 2 x 330 x 30 + 1 x (640-60) x 10 = 30 820 mm^2
A_c = Cross-sectional Area Deck Slab = 3 000 x 175 + 2 x 50 x 380 = 563 000 mm^2
β = 30 820 /563 000 = 0.1095

3. C-2 Shrinkage Calculations by Euro Code (CEB)

Section 2.1.6.4.4 of the Euro code CEB-FIP Model Code 90 deals with the shrinkage strains developed in concrete. Equations (2.1-99) to (2.1-101) represent shrinkage of a concrete after prolonged curing (ts>14d) or pre-drying.

$h = 2A_c/u$ (2.1-69)

h = notional size of the member
A_c = Area of concrete = 563 000 mm^2
u = perimeter of the member in contact with the atmosphere = 6 020 mm
(u =1 x 3000 + 1 x 1530 mm + 2 x 175 mm + 2 x 430 + 4 x 70 = 6 020 mm)

h = 2 x 563 000 mm^2 / 6 020 mm = 187 mm

$$\beta_s(t-t_s)=\left[\frac{(t-t_s)/t_1}{350(h/h_a)^2+(t-t_s)/t_1}\right]^{0.5}$$

Calculation of t

First crack –Panel A (under Load Pad 2)

10 d (Feb) + 31 d (Mar) + 30 d (Apr) + 31d (May) +30 d (Jun) + 10 d (Jul)= 142 days

Second transverse Crack – panel C (under Load Pad 6)

10 d (Feb) + 31 d (Mar) + 30 d (Apr) + 31d (May) +30 d (Jun) + 27 d (Jul)= 159 days

t = age of concrete = 142 and 159 days

t_s = age of concrete at the beginning of shrinkage or swelling =7 days

β_s = given by (2-1-79)

$\varepsilon_{cs}(t, t_c) = \varepsilon_{csD}\beta_s(t-t_s)$ (2.1-74)

ε_{csd} - Notional shrinkage Coefficient eq. (2.1-75)

$\varepsilon_{csd}(t, t_c) = \varepsilon_s(f_{cm})\,\beta_{RH}$ (2.1-75)

$\varepsilon_s(f_m) = [160 + 10\beta_{sc}(9 - f_{cm}/f_{cmo})] \times 10^{-6}$ (2.1-76)

MacGregor and Bartlett recommend a multiplier of 1.2 as the Eurocode method underestimates the shrinkage strains of North American Concrete.

$\varepsilon_s(f_m) = 1.2\,[160 + 10\beta_{sc}(9 - f_{cm}/f_{cmo})] \times 10^{-6}$

β_{sc} = 5 for normal or rapid hardening cements N and R

f_{cmo} = 10 Mpa

f_{cm} = 35 Mpa

$\varepsilon_s(f_m) = [160 + 10 \times 5(9 - 35/10)] \times 10^{-6}$ (Eurocode)

$\varepsilon_s(f_m) = 1.2\,[160 + 10 \times 5(9 - 35/10)] \times 10^{-6}$ (MacGregor & Bartlett)

$\varepsilon_s(f_m) = [160 + 50(9 - 3.5)] \times 10^{-6} = 435 \times 10^{-6}$ (Eurocode)

$\varepsilon_s(f_m) = 1.2\,[160 + 50(9 - 3.5)] \times 10^{-6} = 522 \times 10^{-6}$ (MacGregor & Bartlett)

$\beta_{RH} = -1.55\,\beta_{sRH}$ for $40\% \le RH \le 90\%$ (2.1-77) (applicable case)

$\beta_{RH} = +0.25$ for $RH \ge 90\%$

$\beta_{sRH} = 1 - (RH/RH_o)^3$ (2.1-78)

RH – Ambient relative humidity of the atmosphere (%) (50%)

RH_o – 100%

$\beta_{sRH} = 1 - (50/100)^3 = 0.875$

$\beta_{RH} = -1.55 \times 0.875 = -1.356$

$$\beta_s(142-7) = \left[\frac{(142-7)/1}{350(187/100)^2 + (142-7)/1}\right]^{0.5}$$

$$\beta_s(142) = \left[\frac{(135)}{350 \times 3.497 + (135)}\right]^{0.5} = 0.315$$

$$\beta_s(159-7) = \left[\frac{(159-7)/1}{350(187/100)^2 + (159-7)/1}\right]^{0.5}$$

$$\beta_s(159) = \left[\frac{(152)}{350 \times 3.497 + (152)}\right]^{0.5} = 0.332$$

$\varepsilon_{cso} = 435 \times 10^{-6} \times (-1.356) = -590 \times 10^{-6}$ (Eurocode)

$\varepsilon_{cso} = 522 \times 10^{-6} \times (-1.356) = -708 \times 10^{-6}$ (MacGregor & Bartlett)

$\varepsilon_{cs}(142, 7) = -590 \times 10^{-6} \times 0.315 = 186 \times 10^{-6}$ (Eurocode)

$\varepsilon_{cs}(142, 7) = -708 \times 10^{-6} \times 0.315 = 223 \times 10^{-6}$ (MacGregor & Bartlett)

$\varepsilon_{cs}(159, 7) = -590 \times 10^{-6} \times 0.335 = 198 \times 10^{-6}$ (Eurocode)

$\varepsilon_{cs}(159, 7) = -708 \times 10^{-6} \times 0.335 = 235 \times 10^{-6}$ (MacGregor & Bartlett)

$\varepsilon s(f_m) = [160 + 50\ (9 - 3.5\ )] \times 10^{-6} = 435 \times 10^{-6}$ 435.0E-6

$\beta_{RH} = -1.55\beta_{sRH}$ for 40%≤RH≤ 90% (2.1-77) (applicable case)

β RH = +0.25 for RH≥ 90%

$\beta sRH = 1 - (RH/RH_o)3$ (2.1-78)

RH – Ambient relative humidity of the atmosphere (%) 50%

RH_o = 100%

$\beta_{sRH} = 1 - (50/100)^3 = 0.875$

$\beta_{RH} = -1.55x0.2063 = -0.3198$ -1.3563

$\varepsilon_{csD}(t, t_c) = 435 \times 10^{-6} \times ((-0.3198) = -139.11 \times 10^{-6}$ -590.0E-6

$\varepsilon cs(116, 2) = -139.11 \times 10^{-6} \times 0.985 = 137.22 \times 10^{-6}$

Shrinkage in 12.0 m length = $12{,}200 \times 137.22 \times 10^{-6} = 1.67$ mm

Shrinkage in 12.0 m length = $8{,}600 \times 137.22 \times 10^{-6} = 1.18$ mm

Strain $139.11 \times 10^{-6} = 0.00013911$

C-3 Shrinkage Strain Calculation by CPCI Method

According to Section 2.4 of CPCI Design Manual-Precast and Prestressed Concrete, the shrinkage strain in concrete ε_{sh} at time t is determined by the following expression.

$$\varepsilon_{sh} = \varepsilon_{shu}\left(\frac{t}{C_S + t}\right)P_{sh}$$

Where:

ε_{shu} = ultimate shrinkage strain

= 780×10^{-6} in the absence of specific shrinkage data for local conditions

Cs = Shrinkage coefficient

= 35 if concrete moist cured for 7 days

= 55 if steam cured for 1-3 days

P_{sh} = shrinkage modification factor for non-standard conditions

= $P_c P_h P_f P_r P_{sl} P_v$

From Figure 2.4.1 of Manual

$P_c = 1$, $P_h = 0.9$, $P_f = 1.0$, $P_r = 0.744$, $P_{sl} = 1.09$, and $P_v = 1.0$

P_{sh} = 1 x 0.9 x 1 x 0.744 x 1.09 x 1.0

$\underline{P_{sh} = 0.73}$

Shrinkage Strain at 142 and 159 days:

$$\varepsilon_{sh(142)} = 780x10^{-6}\left(\frac{142}{35+142}\right)x0.74 = 457x10^{-6}$$

$$\varepsilon_{sh(159)} = 780x10^{-6}\left(\frac{159}{35+159}\right)x0.74 = 467x10^{-6}$$

APPENDIX-D

APPENDIX-D: CALCULATION OF PUNCHING STRENGTH P_s, OF PANELS

Calculation of Axial Stiffness of Various Elements

Top Flange

$I_{flange} = 92 \times 10^6$ mm^4

Edge beam

Cross-sectional area of 2 Angles = 2 x 5,600 mm^2 = 11,200 mm^2

K' = EA / (Sl/2) = 200,000 x 800/(2,000/2) = 2,240,000 N / mm^2

Strap

Cross-sectional area = 16 mm x 50 mm = 800 mm^2

K = 200,000 x 800 / (2000/2) = 160,000 N / mm^2

Central Diaphragm

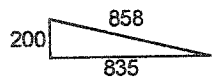

Cross-sectional area of angles = 2 x 816 mm^2

Effective area of angle = 1632 x (835/858) =1588 mm^2

K = 200,000 x 1588 / (2000/2) = 317,421 N / mm^2

Additional Stiffness due to Reinforcement in Panel-C

16 mm GFRP rods @ 500 mm centres = 2 x π x 8^2 = 402 mm^2 / m length of panel

E_{GFRP} = 40,000 MPa

K= 40,000 x 402 / (2000/2) = 16,080 N / mm^2

$K_{effective}$ = 16,080 x (140/225) = 10,005 N / mm^2

Additional Stiffness due to Reinforcement in Panel-D

10M bars @ 300 mm centres = 333 mm^2 / m length of panel

K= 200,000 x 333 / (2000/2) = 66,660 N / mm^2

$K_{effective}$ = 66,660 x (140/225) = 41,440 N / mm^2

Table D- 1 Axial Stiffness of Various Elements

Panel	Unit	K (N / mm^2)
A	Edge Beam	2,240,000
A	Straps 1, 2, and 3	160,000
B	Straps 4, 5,and 6	160,000
B/C	Diaphragm	317,421
C	Straps 7,8, and 9	170,000
D	Straps 10,11, and 12	226,600
D	Edge Beam	2,240,000

Table D- 2 Modified Axial Stiffness of Straps used in Calculating Punching Failure Loads

Panel	Unit	K (N / mm^2)
A	Straps 1, 2, and 3	300,000
B	Straps 4, 5,and 6	300,000
C	Straps 7,8, and 9	310,000
D	Straps 10,11, and 12	372,600

The modified stiffness of straps was calculated using SAP2000. The upper flange was modelled as a beam on springs. Properties shown in Table D-1 were used as spring constants. The moment of inertia of the top flange calculated on page 280 was used for the beam.

Table D- 3 Modified Punching Strength of Panels based on Failure Load of Panel-B

Panel	P_s (Unmodified) (kN)	P_s (Modified) (kN)
A		1,225
B		1,225
C		1,261
D		1,474

APPENDIX-E

APPENDIX-E: SENSOR RESPONSE AT 393 KN: PHASE-I

E 1 Panel-A

E 1.1 Active Load Pad-1

Table E- 1 Active Load Pad-1: Deflection and Strap Strains

Number of Load Cycles	Deflection Pad-1 (mm)	Strap-1 ($\mu\varepsilon$)	Strap-2 ($\mu\varepsilon$)	Strap-3 ($\mu\varepsilon$)	Average ST-2, ST-3 ($\mu\varepsilon$)
1	1.20	35.9	-106.1	0.0	-23.4
10	1.20	81.4	-55.3	0.0	8.7
100	2.07	183.4	241.7	0.0	141.7
300	2.18	204.5	286.4	87.8	192.9
500	1.98	209.6	290.3	86.0	195.3
700	2.16	218.3	303.0	100.0	207.1
900	2.28	225.5	304.9	115.7	215.4
1,100	2.23	224.4	302.0	116.1	214.2
1,300	2.31	225.2	302.6	113.4	213.7
1,500	2.35	228.6	307.1	117.1	217.6
1,700	2.41	231.4	308.8	119.4	219.9

Table E- 2 Active Load Pad-1: Concrete Strains

Number of Load Cycles	ST ($\mu\varepsilon$)	SM ($\mu\varepsilon$)	CT ($\mu\varepsilon$)	CM ($\mu\varepsilon$)	CB ($\mu\varepsilon$)	NT ($\mu\varepsilon$)	NM ($\mu\varepsilon$)
1	33.6	413.4	622.8	133.3	1,171.0	24.1	323.1
10	43.3	631.9	699.5	136.6	1,199.4	30.3	385.5
100	12.1	155.1	356.7	0.0	0.0	1.3	149.4
300	12.7	0.0	362.1	0.0	0.0	1.9	190.0
500	12.1	0.0	359.8	0.0	0.0	3.1	195.1
700	10.7	0.0	377.4	0.0	0.0	5.0	205.1
900	9.0	0.0	346.9	0.0	0.0	4.3	203.6
1,100	5.1	0.0	0.0	0.0	0.0	7.4	205.3
1,300	4.9	0.0	0.0	0.0	0.0	3.7	199.9
1,500	3.0	0.0	336.8	0.0	0.0	5.1	195.1
1,700	-0.1	0.0	0.0	0.0	0.0	3.5	196.3

E 1.2 Panel-A, Active Load Pad-2

Table E- 3 Active Load Pad-2: Deflection and Strap Strains

Number of Load Cycles	Deflection Pad-2 (mm)	ST-1 ($\mu\varepsilon$)	ST-2 ($\mu\varepsilon$)	ST-3 ($\mu\varepsilon$)	Average ST-2, & 3 ($\mu\varepsilon$)
101	3.33	95.7	303.8	0	310
110	2.84	98.9	318.3	0	331
200	3.22	99.35	335.4	284.6	353
400	3.04	106.6	351.2	311.0	359
600	3.00	112.8	370.9	334.4	367
800	3.25	119.3	372.5	345.8	371
1,000	3.35	121.7	379.5	354.9	381
1,200	3.35	119.9	382.5	360.5	389
1,400	3.33	121.2	387.0	374.9	310
1,600	3.43	121.7	393.9	383.5	331

Table E- 4 Active Load Pad-2: Concrete Internal Strains

Number of Load Cycles	ST ($\mu\varepsilon$)	SM ($\mu\varepsilon$)	CT ($\mu\varepsilon$)	CM ($\mu\varepsilon$)	CB ($\mu\varepsilon$)	NT ($\mu\varepsilon$)	NM ($\mu\varepsilon$)
101	-29.0	-302.8	490.3	0	0	-0.7	-34.5
110	-37.0	-378.2	426.3	0	0	-10.4	0.8
200	-33.9	0	350.3	0	0	-13.7	5.13
400	-32.0	0.0	295.8	0.0	0.0	-15.2	1.0
600	-24.7	0.0	299.2	0.0	0.0	-16.4	15.5
800	-28.5	0.0	260.0	0.0	0.0	-19.7	30.0
1,000	-30.0	0.0	0.0	0.0	0.0	-17.5	38.8
1,200	-31.3	0.0	0.0	0.0	0.0	-21.4	36.3
1,400	-29.4	0.0	0.0	0.0	0.0	-19.3	32.2
1,600	-30.5	0.0	0.0	0.0	0.0	-19.0	36.8

4. E 2 Panel-C

E 2.1 Panel-C, Active Load Pad-5

Table E- 5 Active Load Pad-5: Deflection and Strap Strain

Number of Load Cycles	Deflection Pad-5 (mm)	ST-6 ($\mu\varepsilon$)	ST-7 ($\mu\varepsilon$)	ST-8 ($\mu\varepsilon$)	ST-9 ($\mu\varepsilon$)	ST-10 ($\mu\varepsilon$)	Average ST-7, & 8 ($\mu\varepsilon$)
1	2.89	388.1	-226.0	-442.5	-223.3	-129.8	-23.4
10	3.13	418.9	-194.1	-415.0	-212.0	-123.1	8.7
100	2.50	288.4	72.1	-84.4	-7.4	2.2	141.7
300	2.60	289.2	134.7	76.0	83.1	43.1	192.9
500	2.63	292.0	135.9	82.9	89.2	42.7	195.3
700	2.66	294.1	145.1	104.6	98.6	43.8	207.1
900	2.70	297.3	154.3	125.9	108.8	47.8	215.4
1,100	2.71	297.2	159.1	140.6	115.5	50.3	214.2
1,300	2.72	297.7	159.5	142.0	115.9	50.6	213.7
1,500	2.68	300.2	160.9	157.2	121.3	51.6	217.6
1,700	2.69	301.7	161.8	158.0	121.4	51.8	219.9

Table E- 6 Active Load Pad-5: Bar Strain

Number of Load Cycles	SN-1 ($\mu\varepsilon$)	SN-2 ($\mu\varepsilon$)	SN-3 ($\mu\varepsilon$)	SN-4 ($\mu\varepsilon$)	SN-5 ($\mu\varepsilon$)
1	1.2	35.9	-106.1	0.0	-23.4
10	1.2	81.4	-55.3	0.0	8.7
100	2.07	183.4	241.7	0.0	141.7
300	2.18	204.5	286.4	87.8	192.9
500	1.98	209.6	290.3	86.0	195.3
700	2.16	218.3	303.0	100.0	207.1
900	2.28	225.5	304.9	115.7	215.4
1,100	2.23	224.4	302.0	116.1	214.2
1,300	2.31	225.2	302.6	113.4	213.7
1,500	2.35	228.6	307.1	117.1	217.6
1,700	2.41	231.4	308.8	119.4	219.9

Table E- 7 Active Load Pad-5: Concrete Internal Strains

Number of Load Cycles	SM ($\mu\varepsilon$)	SM ($\mu\varepsilon$)	SB ($\mu\varepsilon$)	CT ($\mu\varepsilon$)	CM ($\mu\varepsilon$)	CB ($\mu\varepsilon$)	NT ($\mu\varepsilon$)	NM ($\mu\varepsilon$)	NB ($\mu\varepsilon$)
1	1.1	5.0	21.5	480.9	2393.2	1203.8	17.9	6.2	15.9
10	2.1	6.0	25.5	585.3	2383.9	1199.1	21.6	7.8	18.2
100	-3.8	7.2	32.1	227.3	0.0	0.0	-0.1	7.7	26.9
300	100.6	19.3	34.5	350.7	0.0	0.0	12.8	37.9	45.0
500	75.3	36.1	45.0	364.6	0.0	0.0	19.0	42.8	44.4
700	51.9	35.7	42.4	369.4	0.0	0.0	20.2	44.6	45.2
900	41.1	31.9	41.6	371.7	0.0	0.0	23.9	46.3	45.0
1,100	33.7	27.9	40.8	392.0	0.0	0.0	25.7	45.1	44.3
1,300	31.2	27.5	41.6	391.0	0.0	0.0	22.8	46.0	45.1
1,500	23.6	25.5	41.4	398.7	0.0	0.0	26.1	47.2	46.5
1,700	22.6	24.5	39.4	0.0	0.0	0.0	25.3	47.3	47.2

E 2. 2 Panel-C, Active Load Pad-6

Table E- 8 Active Load Pad-6: Deflection and Strap Strains

Number of Load Cycles	Deflection Pad-6 (mm)	ST-6 ($\mu\varepsilon$)	ST-7 ($\mu\varepsilon$)	ST-8 ($\mu\varepsilon$)	ST-9 ($\mu\varepsilon$)	ST-10 ($\mu\varepsilon$)	Average ST-7, & 8 ($\mu\varepsilon$)
101	101	127.1	-43.8	-90.1	122.0	81.6	15.9
110	110	129.7	-41.4	-64.4	163.8	106.2	49.7
200	200	120.0	-18.0	41.3	234.2	131.8	137.8
400	400	122.2	-7.3	61.9	252.3	135.6	157.1
600	600	121.4	-1.9	86.4	268.5	140.6	177.5
800	800	122.2	2.9	96.8	275.2	142.2	186.0
1,000	1000	121.8	6.7	107.9	285.0	146.9	196.4
1,200	1200	122.8	7.0	106.1	285.4	147.4	195.8
1,400	1400	123.2	11.9	120.8	294.5	151.4	207.7
1,600	1600	122.4	12.7	126.2	295.5	149.2	210.9

Table E- 9 Active Load Pad-6: Bar Strains

Number of Load Cycles	SN-1 ($\mu\varepsilon$)	SN-2 ($\mu\varepsilon$)	SN-3 ($\mu\varepsilon$)	SN-4 ($\mu\varepsilon$)	SN-5 ($\mu\varepsilon$)
101	5.6	84.8	0.0	42.7	216.5
110	10.5	110.6	0.0	39.3	267.4
200	30.1	90.4	0.0	31.6	213.9
400	38.9	95.3	0.0	33.8	218.6
600	48.3	97.7	0.0	32.4	219.9
800	59.5	100.3	0.0	33.3	222.2
1000	65.9	103.9	0.0	33.9	222.1
1200	72.1	105.6	0.0	33.4	226.4
1400	75.5	105.4	0.0	34.2	224.2
1600	78.2	106.4	0.0	32.6	225.2

Table E- 10 Active Load Pad-6: Concrete Internal Strains

Number of Load Cycles	SM ($\mu\varepsilon$)	SM ($\mu\varepsilon$)	SB ($\mu\varepsilon$)	CT ($\mu\varepsilon$)	CM ($\mu\varepsilon$)	CB ($\mu\varepsilon$)	NT ($\mu\varepsilon$)	NM ($\mu\varepsilon$)	NB ($\mu\varepsilon$)
101	-37.2	70.7	57.2	267.2	0.0	0.0	-40.6	12.5	44.0
110	-3.9	113.5	51.6	243.3	0.0	0.0	-18.9	29.6	50.0
200	64.2	60.8	2.5	370.7	0.0	0.0	-24.2	21.9	41.3
400	23.7	73.4	3.0	374.2	0.0	0.0	-22.3	20.4	37.4
600	-9.2	59.1	-5.0	380.2	0.0	0.0	-17.9	20.9	34.3
800	-22.7	56.3	-9.9	384.1	0.0	0.0	-16.1	20.7	33.6
1,000	-34.0	54.6	-11.0	398.7	0.0	0.0	-13.9	19.0	31.4
1,200	-40.5	52.9	-12.8	400.9	0.0	0.0	-16.0	18.8	29.2
1,400	-45.3	54.4	-12.7	397.5	0.0	0.0	-14.3	18.4	28.9
1,600	-46.6	51.3	-16.6	0.0	0.0	0.0	-15.2	18.4	26.4

5. E 3 Panel-D

6. E 3.1 Panel-D, Active Load Pad-7

Table E- 11 Active Load Pad-7: Deflection and Strap Strains

Number of Load Cycles	Deflection Pad-7 (mm)	ST-9 ($\mu\varepsilon$)	ST-10 ($\mu\varepsilon$)	ST-11 ($\mu\varepsilon$)	ST-12 ($\mu\varepsilon$)	Average ST-10, & 11 ($\mu\varepsilon$)
1	2.34	123.6	315.6	344.3	116.4	330
10	2.62	142.4	362.5	395.3	140.3	379
100	2.25	148.3	347.9	316.0	117.9	332
300	2.34	151.5	358.1	323.1	121.1	341
500	2.35	152.7	361.9	325.0	121.3	343
700	2.37	152.7	363.1	326.1	122.8	345
900	2.35	152.0	362.6	326.9	123.6	345
1,100	2.34	154.3	365.7	329.0	122.1	347
1,300	2.31	153.2	365.9	329.9	123.4	348
1,500	2.25	152.7	366.0	328.3	124.0	347
1,700	2.34	123.6	315.6	344.3	116.4	330

Table E- 12 Active Load Pad-7: Bar Strains

Number of Load Cycles	SN-1 ($\mu\varepsilon$)	SN-2 ($\mu\varepsilon$)	SN-3 ($\mu\varepsilon$)	SN-4 ($\mu\varepsilon$)	SN-5 ($\mu\varepsilon$)
1	209.4	-154.6	897.4	111.3	-86.7
10	291.8	-168.6	981.0	178.9	-96.5
100	224.0	-141.0	789.6	116.1	-76.8
300	246.5	-140.8	807.5	125.0	-78.1
500	255.5	-142.2	812.8	130.1	-78.9
700	261.4	-138.7	814.0	130.4	-76.8
900	266.0	-137.9	815.6	132.8	-76.4
1,100	273.7	-139.3	832.8	134.1	-77.2
1,300	277.4	-138.4	832.2	135.8	-77.1
1,500	279.2	-137.0	831.0	135.9	-78.2
1,700	209.4	-154.6	897.4	111.3	-86.7

Table E- 13 Active Load Pad-7: Concrete Internal Strains

Number of Load Cycles	SM ($\mu\varepsilon$)	SM ($\mu\varepsilon$)	SB ($\mu\varepsilon$)	CT ($\mu\varepsilon$)	CM ($\mu\varepsilon$)	CB ($\mu\varepsilon$)	NT ($\mu\varepsilon$)	NM ($\mu\varepsilon$)	NB ($\mu\varepsilon$)
1	26.0	4.5	-20.2	45.0	75.9	28.8	-52.0	-12.6	23.1
10	21.8	-13.4	-17.7	95.2	62.0	15.7	-53.6	-18.8	21.9
100	-3.9	23.6	-24.8	9.4	33.3	24.9	-58.0	-10.9	30.2
300	-1.2	30.3	-22.0	11.7	33.2	24.8	-58.3	-13.0	29.0
500	1.0	32.0	-22.2	12.7	31.7	22.9	-60.1	-11.9	28.4
700	-1.7	29.4	-22.7	12.8	30.6	21.9	-59.2	-12.7	27.5
900	-0.8	32.7	-22.0	0.0	31.2	22.8	-59.6	-14.1	27.7
1,100	-1.1	34.9	-22.2	12.7	30.0	21.7	-60.8	-13.4	27.8
1,300	1.5	35.9	-21.1	15.0	30.6	21.1	-59.6	-14.7	26.0
1,500	0.8	36.3	-21.7	13.8	32.4	21.9	-59.4	-13.2	26.3
1,700	26.0	4.5	-20.2	45.0	75.9	28.8	-52.0	-12.6	23.1

E 3.2 Panel-D, Active Load Pad-8

Table E- 14 Active Load Pad-8: Deflection and Strap Strains

Number of Load Cycles	Deflection Pad-8 (mm)	ST-9 ($\mu\varepsilon$)	ST-10 ($\mu\varepsilon$)	ST-11 ($\mu\varepsilon$)	ST-12 ($\mu\varepsilon$)	Average ST-11, & 12 ($\mu\varepsilon$)
101	1.95	32.1	118.4	250.2	220.4	235.3
110	2.14	35.6	129.4	282.2	255.1	268.7
200	1.74	34.3	119.5	243.7	203.1	223.4
400	1.77	35.4	124.2	251.3	209.6	230.5
600	1.79	34.6	128.9	256.6	216.8	236.7
800	1.78	35.3	127.8	259.1	218.3	238.7
1,000	1.78	36.0	129.5	260.5	219.1	239.8
1,200	1.81	34.8	129.6	261.6	220.0	240.8
1,400	1.81	36.1	129.8	263.0	220.5	241.7
1,600	1.83	34.8	129.2	264.8	219.5	242.1

Table E- 15 Active Load Pad-8: Bar Strains

Number of Load Cycles	SN-1 ($\mu\varepsilon$)	SN-2 ($\mu\varepsilon$)	SN-3 ($\mu\varepsilon$)	SN-4 ($\mu\varepsilon$)	SN-5 ($\mu\varepsilon$)
101	90.2	1.7	264.9	60.0	9.8
110	101.3	7.6	272.3	70.1	15.9
200	86.0	1.5	256.2	61.8	11.0
400	91.3	1.6	262.5	65.7	13.3
600	97.2	1.9	267.7	68.8	11.5
800	98.4	0.8	269.0	67.6	13.1
1,000	101.0	1.6	269.2	67.8	13.9
1,200	101.5	3.1	269.8	66.2	14.2
1,400	103.8	3.2	272.0	68.8	12.4
1,600	105.2	2.8	272.9	68.9	13.0

Table E- 16 Active Load Pad-8: Concrete Internal Strains

Number of Load Cycles	SM ($\mu\varepsilon$)	SM ($\mu\varepsilon$)	SB ($\mu\varepsilon$)	CT ($\mu\varepsilon$)	CM ($\mu\varepsilon$)	CB ($\mu\varepsilon$)	NT ($\mu\varepsilon$)	NM ($\mu\varepsilon$)	NB ($\mu\varepsilon$)
101	-3.9	-7.7	1.9	37.7	20.0	16.6	-9.6	14.8	25.7
110	-4.2	-12.8	3.4	44.9	24.5	18.9	-9.2	20.1	30.7
200	-10.2	-11.0	1.5	34.6	17.7	14.6	-9.3	14.9	25.6
400	-12.9	-10.7	3.4	0.0	16.8	14.6	-8.0	16.7	25.4
600	-17.5	-11.2	4.1	39.9	16.5	14.3	-7.2	17.3	25.9
800	-18.7	-11.5	4.5	41.5	15.4	13.7	-7.4	15.7	25.7
1,000	-18.3	-9.8	5.2	40.9	14.9	12.9	-7.0	16.5	25.4
1,200	-20.4	-10.5	5.2	0.0	15.5	12.8	-8.0	15.9	25.1
1,400	-19.1	-8.8	5.5	44.6	14.1	12.0	-8.1	15.3	25.0
1,600	-20.6	-8.5	7.2	41.4	14.1	12.0	-7.3	16.4	24.5

7. E 4 Panel-B

E 4.1 Panel-B: Active Load Pad-3

Table E- 17 Active Load Pad-3: Deflection and Strap-Strains

Number of Load Cycles	Deflection Pad-3 (mm)	ST-3 ($\mu\varepsilon$)	ST-4 ($\mu\varepsilon$)	ST-5 ($\mu\varepsilon$)	ST-6 ($\mu\varepsilon$)	ST-7 ($\mu\varepsilon$)	Average ST-4, 5, & 6 ($\mu\varepsilon$)
1	1.93	116.3	262.5	477.8	345.9	-19.0	362.1
10	1.96	119.6	270.8	504.3	352.7	-19.0	376.0
100	1.82	120.4	265.6	461.4	329.0	-20.0	352.0
200	1.86	120.4	266.0	461.0	326.7	-16.4	351.2
300	1.83	116.9	268.4	470.1	332.8	-19.6	357.1
400	1.81	119.0	267.7	466.4	329.3	-20.4	354.5
500	1.84	117.0	270.8	468.4	330.6	-20.5	356.6
600	1.83	117.0	268.5	467.2	330.6	-21.5	355.4
700	1.81	115.5	266.0	460.0	324.5	-19.7	350.2
800	1.76	115.0	268.2	469.9	325.4	-20.3	354.5
900	1.79	114.5	266.3	464.4	328.1	-22.2	352.9
1,000	1.75	114.9	259.7	455.0	321.3	-20.8	345.3
1,100	1.78	116.4	268.3	471.3	331.5	-22.0	357.0
1,200	1.76	118.9	269.1	468.9	326.4	-18.3	354.8
1,300	1.78	115.7	265.9	467.2	326.7	-20.8	353.3
1,400	1.76	115.6	267.6	468.3	328.6	-22.2	354.8
1,500	1.76	115.2	268.4	469.6	327.7	-23.0	355.3
1,600	1.74	116.2	268.2	469.8	331.4	-24.5	356.5
1,700	1.74	115.6	268.0	469.5	328.6	-23.8	355.4

Table E- 18 Active Load Pad-3: Concrete Internal Strains

Number of Load Cycles	SM ($\mu\varepsilon$)	SM ($\mu\varepsilon$)	SB ($\mu\varepsilon$)	CT ($\mu\varepsilon$)	CM ($\mu\varepsilon$)	NT ($\mu\varepsilon$)	NM ($\mu\varepsilon$)	NB ($\mu\varepsilon$)
1	21.1	-4.6	-26.4	0.0	0.0	162.3	170.3	-41.6
10	14.4	-3.7	-26.5	0.0	0.0	137.9	318.3	-72.8
100	13.0	-4.1	-21.0	0.0	0.0	57.1	260.4	-114.3
200	11.7	-5.8	-21.6	0.0	0.0	56.9	267.7	-118.6
300	9.7	-5.0	-22.3	0.0	0.0	55.9	277.1	-133.9
400	11.3	-6.6	-22.1	0.0	0.0	55.5	279.7	-134.8
500	10.2	-4.9	-21.5	0.0	0.0	59.5	283.1	-134.3
600	9.6	-5.5	-20.5	0.0	0.0	58.7	282.4	-133.0
700	9.7	-6.3	-22.0	0.0	0.0	52.4	285.3	-137.0
800	10.4	-4.3	-19.4	0.0	0.0	53.0	294.1	-143.1
900	8.3	-7.1	-22.6	0.0	0.0	55.7	294.8	-144.2
1,000	8.0	-8.0	-21.6	0.0	0.0	51.8	291.5	-143.6
1,100	8.2	-7.3	-24.1	0.0	0.0	55.2	302.4	-153.0
1,200	8.2	-7.5	-23.1	0.0	0.0	54.0	298.5	-154.4
1,300	7.7	-6.9	-21.8	0.0	0.0	55.2	298.0	-152.9
1,400	7.4	-7.1	-21.9	0.0	0.0	54.0	297.9	-155.7
1,500	7.8	-7.8	-23.0	0.0	0.0	54.7	300.9	-153.8
1,600	7.8	-7.7	-22.4	0.0	0.0	54.8	298.8	-153.0
1,700	7.0	-7.8	-24.5	0.0	0.0	55.2	298.5	-155.4

APPENDIX-F

APPENDIX-F: SENSOR RESPONSE AT 393 kN-PHASE-II

8. Sensor Response Panel-A

The deflection and strap strains at 393 kN is shown in Table F-1. The changes in the peak load level have been highlighted.

Table F- 1 Panel-A: Deflection and Strap Strains at 393 kN

Peak Load (kN)	Load Cycles ('000.)	Deflection (mm)	ST-2 ($\mu\varepsilon$)	ST-3 ($\mu\varepsilon$)
393	1,700	3.29	391	376
	3,000	3.53	414	413
	4,000	3.48	416	421
	5,000	3.51	417	427
	6,000	3.53	418	427
	7,000	3.54	424	438
	8,000	3.52	418	436
	9,000	3.19	430	455
	10,000	3.59	424	448
	11,000	3.65	432	457
	12,000	3.57	429	453
	13,000	3.61	432	455
	14,000	3.09	425	449
	15,000	3.66	436	459
	16,000	3.66	437	457
	17,000	3.62	436	457
	18,000	3.65	441	461
	19,000	3.65	441	459
	20,000	3.64	439	459
	21,000	3.65	439	460
	22,000	3.59	438	459
	23,000	3.58	436	457
	24,000	3.66	439	461
	25,000	3.60	443	464
	26,000	3.50	443	463
	27,000	3.60	443	466
	28,000	3.55	443	466
	29,000	3.64	442	466
	30,000	3.58	442	467
	31,000	3.63	445	470

Table F-1 contd.				
Peak Load (kN)	Load Cycles ('000.)	Deflection (mm)	ST-2 ($\mu\varepsilon$)	ST-3 ($\mu\varepsilon$)
393	32,000	3.69	446	473
	33,000	3.62	446	472
	34,000	3.68	445	472
	35,000	3.67	447	472
	36,000	3.73	451	474
	37,000	3.71	450	475
	38,000	3.78	466	494
	39,000	3.83	463	494
	40,000	3.71	458	501
	41,000	3.75	461	498
	42,000	3.78	473	512
	43,000	3.82	475	516
	44,000	3.83	458	501
	45,000	3.85	476	519
	46,000	3.81	479	523
	47,000	3.87	477	522
	48,000	3.87	478	518
	49,000	3.85	479	521
393	**50,000**	**3.85**	**480**	**524**
635 (Peak Load Change)	**50,001**	**3.73**	**500**	**537**
	51,000	4.13	539	587
	52,000	4.06	580	626
	53,000	4.11	557	604
	54,000	4.11	592	636
	55,000	3.78	579	625
	56,000	4.10	585	635
	57,000	4.11	574	622
	58,000	4.03	580	630
	59,000	4.10	587	656
	60,000	**4.11**	**581**	**638**
785 (Peak Load Change)	**60,002**	**4.08**	**586**	**644**
	60,100	4.09	609	666
	61,000	3.92	598	649
	62,000	**4.01**	**604**	**657**
883 (Peak Load Change)	**62,001**	**3.51**	**531**	**585**
	63,000	3.27	585	634
	63,243	4.21	590	621

F.2 Sensor Response Panel-D

The deflection and strap Strains at 393 kN is shown in Table F-2. The changes in the peak load level have been highlighted.

Table F- 2 Panel-D: Deflection and Strap Strains at 393 kN

Peak Load (kN)	Load Cycles ('000.)	Deflection (mm)	ST-9 ($\mu\varepsilon$)	ST-10 ($\mu\varepsilon$)	ST-11 ($\mu\varepsilon$)	ST-12 ($\mu\varepsilon$)
393	1,700	2.30	155	365	330	122
883	1,701	2.49	135	363	329	121
	1,800	2.60	248	492	447	146
	2,700	2.68	263	518	473	152
	3,700	2.64	261	519	477	152
	4,700	2.67	259	518	475	151
	5,700	2.67	261	514	470	149
	6,700	2.68	265	521	478	153
981	6,721	2.65	261	504	465	150
	6,741	2.64	265	507	469	152
1,031	6,796	2.59	268	507	469	153
1,079	6,897	8.33	298	491	472	184

APPENDIX-G

APPENDIX-G: ACOUSTIC PROCEDURES

G-1 Acoustic Waveforms during Phase-I and II

The acoustic sensors were mounted in strategic locations so that the waveforms generated by an artificial acoustic source (pendulum) would pass through the regions of the panel that were expected to develop cracks during testing. The two sensors, S1 and S2, were located so that they bounded the zone of expected damage. Sensor S1 served as a reference sensor for the waveform recorded at the active sensor, S2, which would have propagated through the damaged zone. In between loading cycles, twenty pulses were applied in rapid succession at each stage of the test. Also, both sensors listened passively and recorded the waveforms generated by crack development during loading cycles. Layout of acoustic sensors adopted for Panel-A during Phase-I is shown in Figure G-1.

Figure G-2 highlights the influence of the cracks on the propagation of the acoustic waves. Prior to the commencement of the loading, the artificial waveform arrives later on the active sensor, S2, with slightly reduced amplitude as compared to the reference sensor, S1. After the development of cracks in between two sensors, the waveform recorded by S2 decreased significantly in amplitude and its differential arrival time increased from 140 to 150 μs. As the damage increases the strength of the signal arriving at the active sensor declines further and the differential arrival time also increases.

After the test of Panel-A in Phase-I, it was observed that most of the damage occurred in the zone between the two load pads. Therefore, for all the other tests the sensors were positioned close to the damage zone as shown in Figure G-3.

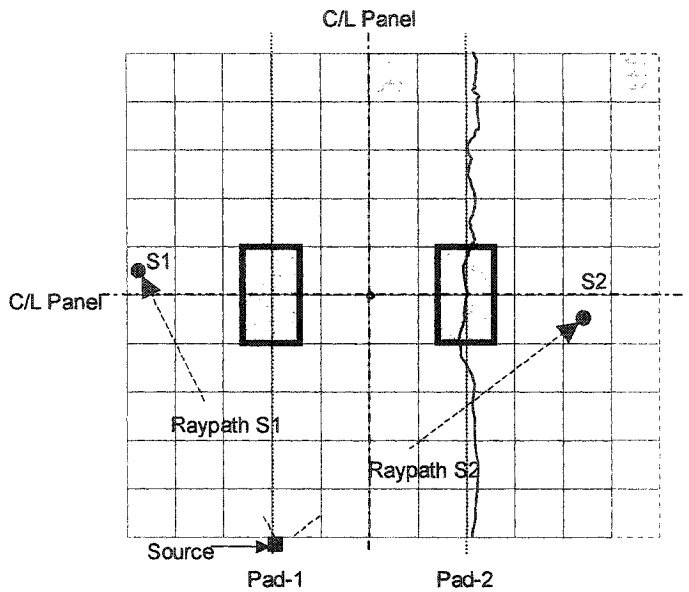

Figure G- 1 Layout of Acoustic Sensors in Panel-A during Phase-I

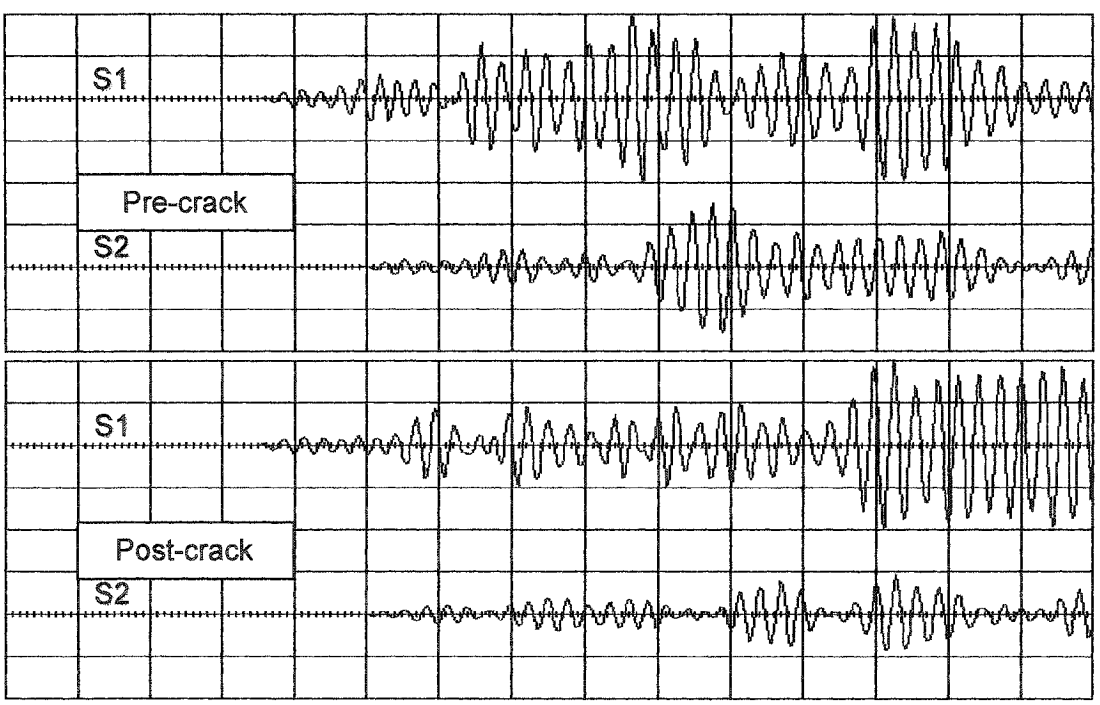

Figure G- 2 Acoustic Waveforms before and after Development of Crack

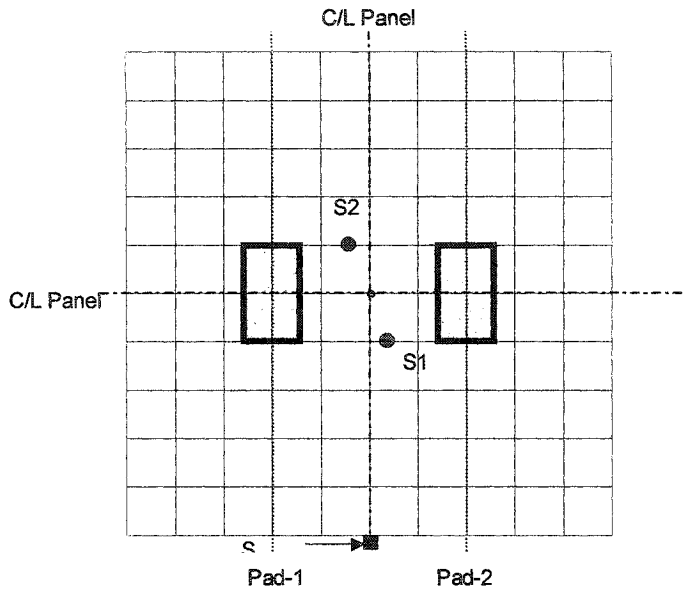

Figure G- 3 Positions of Acoustic Sensors on Panels B, C, and D during Phase-I, and All Panels during Phase-II

G-1.1 Criteria for Comparison of Waveforms

There are three main characteristics of the acoustic signal that change due to the internal damage occurring in the concrete. Those are: 1) the integrated amplitude, 2) the integrated amplitude ratio, and 3) the differential arrival time.

If two identical acoustic signals passing through the concrete slab are recorded by the active sensor and the reference sensor, with one signal passing through when the slab is in an uncracked state, and the other signal passing through after the damage has occurred, then the amplitude of the signal recorded by the reference sensor will remain virtually unchanged while the amplitude of the signal recorded by the active sensor will diminish due the partial discontinuity in the concrete medium caused by the damage.

The integrated amplitude, the total area under the waveform, would also be reduced due to reduced amplitudes of the wave.

The velocity of the sound wave decreases when it travels through a fractured media. The time required for the signal to arrive at the active sensor would therefore increase due to the presence of cracks; however, the time required for the signal to arrive at the reference sensor would remain unchanged.

The damage can be detected by a change in the integrated amplitude of the waveform. A reduced integrated amplitude would denote damage.

The damage can also be detected by comparing the ratios of the integrated amplitude of the reference sensor and the integrated amplitude of the active sensor. A higher ratio would indicate greater damage.

The differential arrival time as well can provide a basis for comparing the signals before and after the occurrence of damage. A higher differential arrival time would indicate greater damage.

The artificial pulses made by the striking pendulum can vary in strength considerably. This can affect the characteristics of the generated signal. A test was conducted to assess the effectiveness of each method of comparison (Butt et al. 2004). Twenty acoustic pulses were generated in rapid succession. The ratios of the peak amplitude, the ratios of the integrated amplitudes and the differential arrival time were calculated. It was found that the calculation of the integrated amplitude and the integrated amplitude ratio can be calculated by the computer system automatically; the differential arrival time for each individual waveform has to be determined manually.

The study of integrated amplitudes and the integrated amplitude ratios showed that there was a large scatter in the values of integrated amplitudes for twenty consecutive pulses artificially generated by the pendulum, whereas the integrated amplitude ratios were confined within a relatively small range (Figures G-4 a and b).

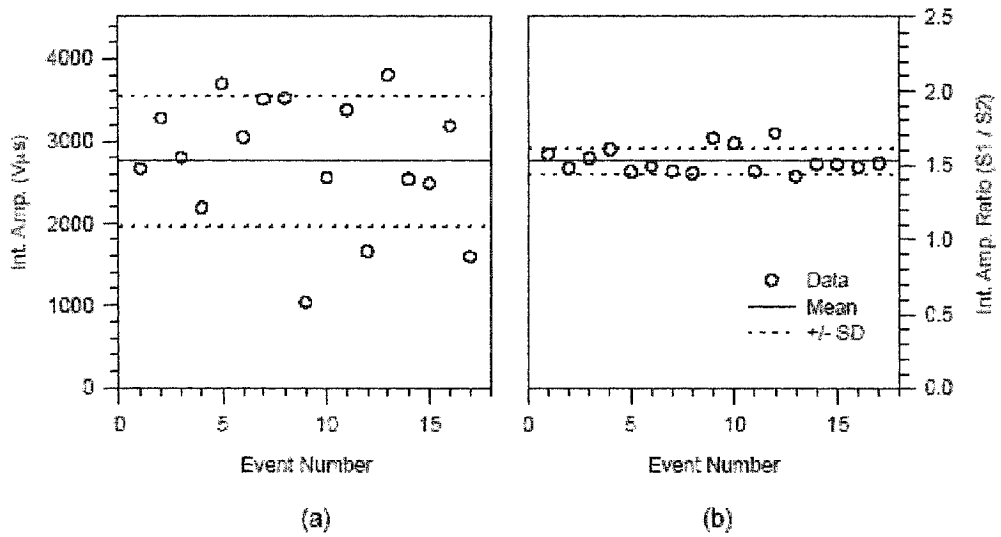

Figure G- 4 Variability of Integrate Amplitude and Integrated Amplitude Ratio

The low variability of the integrated amplitude ratios was further complimented by taking the average value of integrated amplitude ratios for 20 pulses, generated in rapid succession, as one reading. This also helped narrow down the scatter in the results.

The studies (Butt 2001) on acoustic transmission in rocks indicate that the relative change in velocity due to occurrence of fracture is low. Therefore the differential arrival time would be less sensitive to the degree of damage as compared to the integrated amplitude ratios. The comparison of the three aforementioned methods discussed is given in Table G-1.

Table G- 1 Comparison of Damage Detection Criteria

Method	Range	Mean	Standard deviation as % of mean	Remark
Integrated amplitude (V μs)	1000-4000	2750	28%	Unacceptable
Integrated amplitude ratio	1.4-1.7	1.52	7%	Acceptable
Differential arrival time (μs)	130-150	132.35	4.8%	Prolonged manual processing

G-2 Acoustic Survey after Failure

G-2.1 General

Relative attenuation imaging has been used as a tool to detect defects in concrete structures (Pla-Rucki and Eberhand1995; Buyukozturk 1998; Rens et al. 2000). To assess the effectiveness of the acoustic attenuation technique in detecting cracks an acoustic survey of the entire deck slab was carried out. As discussed earlier, the top surface of the deck slab was whitewashed for easy identification of the cracks. The entire surface was divided into small squares with each square measuring 305 x 305 mm, starting from the center of the model. The grid system helped map the cracks accurately. The same grid pattern was used to position the acoustic sensors.

G-2.2 Acoustic System

The system for the survey comprised a mechanical sound source, two acoustic sensors, a PC based acoustic signal digitizing and recording system and custom data processing software. Steel strike plates, measuring 75 x 75 mm, were bonded to the sides of the deck slab at mid-depth using quick setting epoxy. A ball-peen hammer was used to strike the steel plates to generate the acoustic signal. The location of the sensor was at the junction of two orthogonal gridlines. The top surface of the slab was scraped and the sensors were mounted using vacuum grease as an acoustic couplant.

G-2.3 Survey Procedure

The acoustic survey was conducted along each transverse gridline with the readings taken at the junction of each longitudinal line. The first survey line was located at 305 mm from the transverse edge of Panel-D. The survey procedure is given below.

1) One acoustic sensor (the reference sensor) was positioned at 305 mm from the edge of the panel
2) The second sensor (the active sensor) was initially positioned by the side of the sensor
3) The hammer source was struck on the steel plate, and the system recorded the same waveform as it propagated past the reference and the active sensor. Multiple hammer strikes were made and the acquired signals averaged during data processing.
4) The active sensor was moved to a new position 305 mm away and Step 3) was repeated.
5) Step 4) was repeated until the active sensor was positioned in its final location at the longitudinal centerline of the deck slab.

Steps 1) through 5) were then repeated for the next transverse gridline. After the survey was completed along one side of the deck slab the procedure was repeated on the other side of the deck with the final position of the active sensor ending at the longitudinal centerline of the deck. A schematic view of the sensor positioning is shown in Figure G-5.

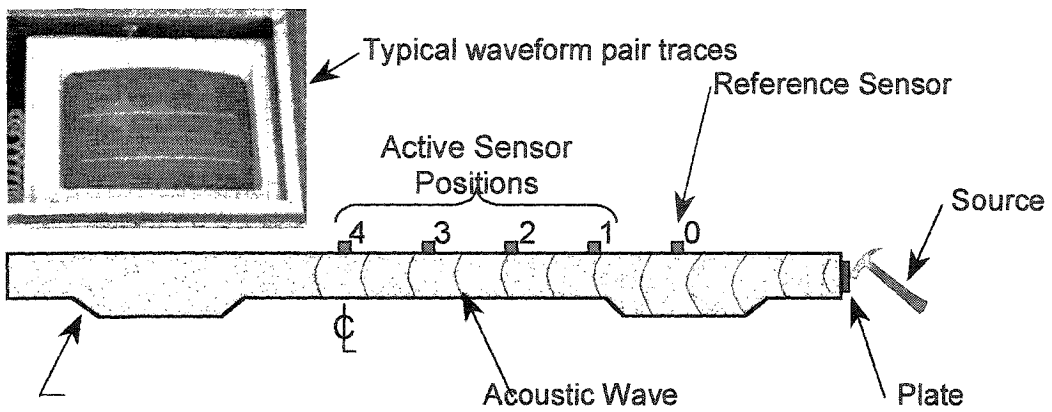

Figure G- 5 Schematic View Of Acoustic Survey Setup

G 2.4 Acoustic Data Processing

The acoustic waveform magnitude measured by each sensor for the hammer strike was computed by summing the positive area under the recorded waveform to get the integrated amplitude *IAmp*. The normalized magnitude M of each waveform was determined by,

$$M = IAmp_a/IAmp_r \quad \text{(G-1)}$$

Where

$IAmp_a$ is the integrated amplitude of the active sensor

Amp_r is the integrated amplitude of the reference sensor

Analysis of the dataset of M values was then conducted to evaluate the standard fall-off of the acoustic signal magnitude Fs during the propagation from one sensor position to the next in the undamaged regions of the deck,

$$Fs = M_{n+1}/M_n \quad \text{(G-2)}$$

Where the M_n and M_{n+1} are the normalized waveform magnitudes at two sensor positions spaced 305 mm apart along the same transverse survey line with little or no

damage between them. The standard fall-off values resulting from this analysis are shown in Figure G-6.

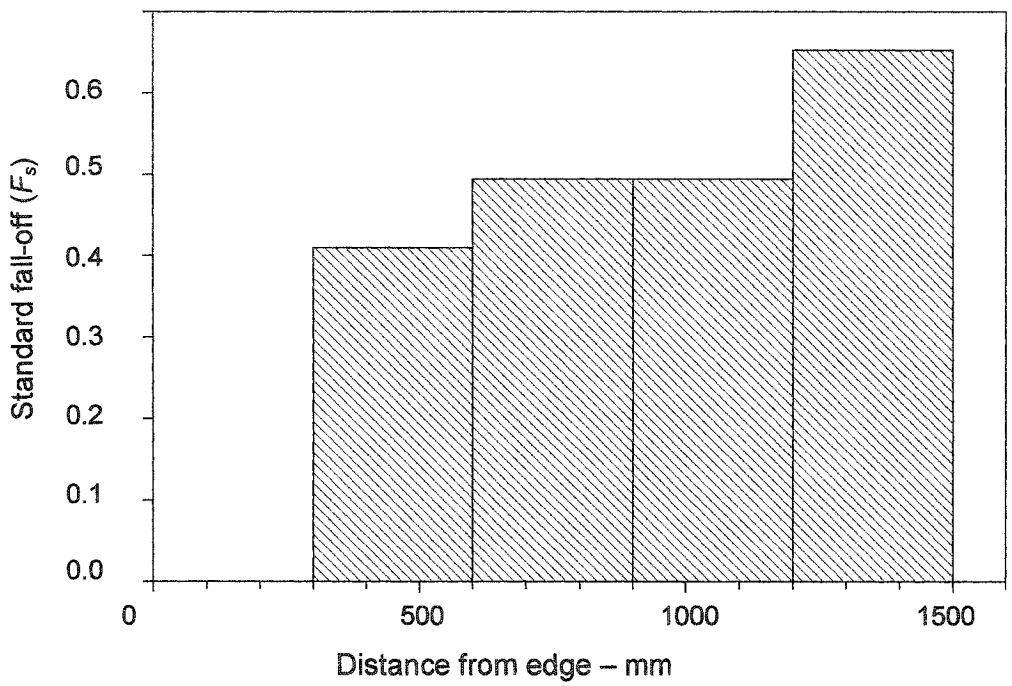

Figure G- 6 Values Of Standard Fall-Off Used to Determine Relative Attenuation

Note the anomalous fall-off values from 600 mm to 1,200 mm which are attributed to the focusing of the acoustic waveform when propagating from the thickened haunches to the thinner deck slab.

The relative attenuation, $Atten_{rel}$, of the waveform was calculated as,

$$Atten_{rel} = [F_s - (M_{n+1}/M_n)]/F_s. \quad \text{(G-3)}$$

Where the M_n and M_{n+1} are the normalized waveform magnitudes at two sensor positions spaced 305 mm apart and F_s is the standard fall-off for the same two sensor positions. Thus the relative attenuation represents the decimal percentage that the

actual signal fall-off is less than the standard fall-off i.e. when there is no damage along the wave travel path.

G-2.5 Image Generation

Image generation was based on the presentation of the relative attenuation values computed during data processing as a 2-D plan image of the deck. The relative attenuation values were assigned 2-D coordinates which were 150 mm from the active sensor position along the transverse survey line in the direction of the reference sensor. Global variogram analysis was conducted to generate a suitable semi-variogram model for the relative attenuation data, and standard point estimation methods using ordinary kriging (Journel and Huijbrets 1978) were used to estimate the relative attenuation values on a 150 x 150 mm grid covering the full plan of the deck model. Industry-standard geostatical modeling software was then used to generate the contoured relative attenuation image.

Due to space restrictions, it was not possible to photograph the entire deck surface at the end of the testing program. A composite image of the top surface was created by merging more than 100 side-by-side digital images of the model. The plan view of the model showing the cracks mapped on the upper surface of the slab and the upper perimeter of the punch through for each panel is shown in Figure G-7. The relative attenuation image of the model is shown in Figure G-8. The correlation between the damaged and cracked regions of the deck and the regions of highest attenuation is quite evident, with the regions of attenuation matching the mapped cracks on the deck slab and the location of the punched-through failures.

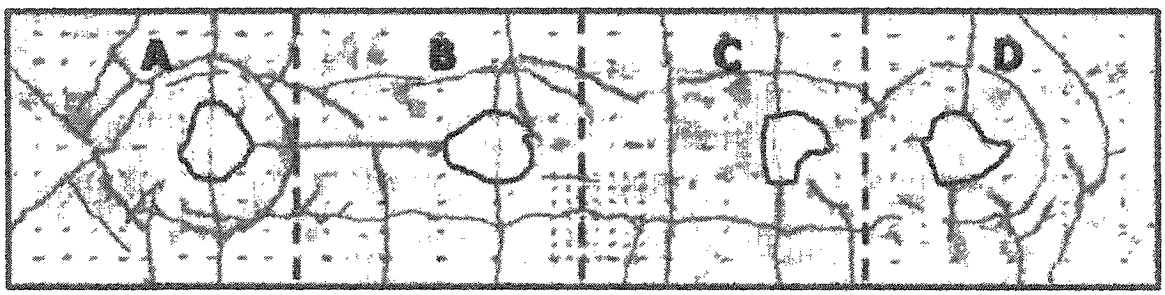

Figure G- 7 Top View Of Deck Slab after Failure

Figure G-7 shows the entire slab surface divided into five distinct colour shades with each shade representing a range of attenuation. The zone with the hatched lines represents that area of slab where the active sensor did receive any signal. The zone represented by the black colour had from 32% to 40% relative attenuation. The zone coloured red represent the area with relative attenuation ranging form 24% to 32%. The grey shaded area represents the relative attenuation ranging from 16% to 24%. The blue shaded area indicates a relative attenuation of less than 16%.

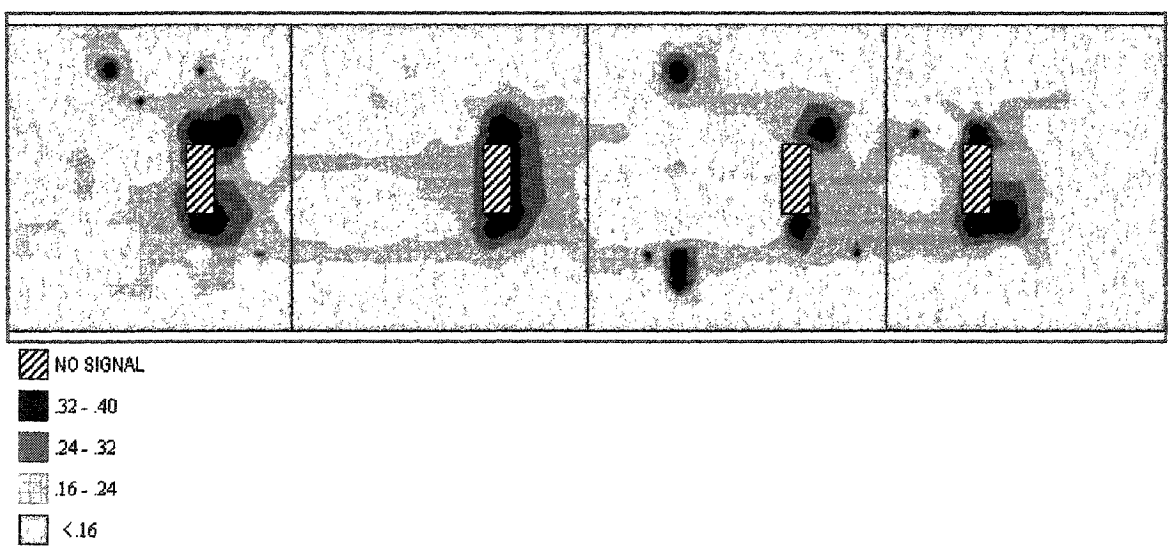

Figure G- 8 Relative Attenuation Image of Deck Slab after Failure

G 2.6 Discussion

Comparing Figure G-7 and Figure G-8 it is obvious that there is a correlation between the regions of highest acoustic attenuation shown in figure G-8, and many of the damaged regions visible on the top deck surface shown in Figure G-7.

1. Each of the four punch-out cones is surrounded by a zone of greater than 16% relative attenuation, which increases to up to 40% relative attenuation immediately adjacent to detached concrete slab segments.
2. Several longitudinal cracks are imaged as zones of greater than 16% relative attenuation. The full-depth crack over the crack trainer in Panel-B, as well, the longitudinal cracks along the girder are clearly visible.
3. Several other cracks are partially imaged as zones of greater than 16% attenuation such as the full-depth transverse crack in Panel-C and several radial and circumferential cracks in Panel-A.

The cracks that are not imaged well include the discontinuous longitudinal crack running from Panel-A to Panel-D near the north girder and most of the transverse cracks. The discontinuous longitudinal crack did not have a consistently wide aperture (as compared to the longitudinal cracks that were well imaged) suggesting that it was more shallow and thus would be expected to have a lower level of relative attenuation. The transverse cracks are in a direction parallel to the survey direction and thus are not crossed by the acoustic wave raypath between the sensors.

An important aspect of these imaging results is that there are no regions with high levels of relative attenuation that do not have corresponding damage. In other words, the acoustic imaging technique does not generate false positives indicating damage where there is none. This aspect of the acoustic imaging technique makes it a suitable to correctly identify the locations where damage is present.

It is seen that the cracks that ran perpendicular to the direction of the survey were detected correctly while the cracks that ran parallel to the survey direction were not

imaged. This leads to the conclusion that a multidirectional survey will help in obtaining a better acoustic image of the damage in concrete.

APPENDIX-H

APPENDIX-F: CALCULATION OF EQUIVALENT LOAD CYCLES (Mufti et al. 2002)

Table H- 1 Panel-A: Summary of Equivalent Load Cycles at 196, 393, and 883 kN Peak Load

Applied peak load (kN)	Applied load Cycles (No.)	Equivalent load cycles at 196 kN	Equivalent load cycles at 393 kN	Equivalent load cycles at 883 kN
393	50,000	6.1E+06	5.0E+04	0.3
638	10,000	5.0E+08	4.1E+06	25
785	2,000	3.6E+09	3.0E+07	181
883	1,243	2.5E+10	2.0E+08	1,243
Total		2.9E+10	2.4E+08	1,449

Table H- 2 Panel D: Summary of Equivalent Load Cycles at 196, 393,and 883kN Peak Load

Applied peak load (kN)	Applied load Cycles	Equivalent load cycles at 196 kN	Equivalent load cycles at 393 kN	Equivalent load cycles at 883 kN
393	1,700	9.2E+04	1.7E+03	0.1
883	5,000	5.9E+09	1.1E+08	5000.0
981	41	3.5E+08	6.5E+06	302
1,030	50	1.2E+09	2.2E+07	999
1,079	108	6.9E+09	1.3E+08	5857
Total		1.4E+10	2.6E+08	12158

Table H- 3 Panel C: Summary of Equivalent Load cycles at 196, 393,and 883 kN Peak Load

Applied peak load (kN)	Applied load Cycles	Equivalent load cycles at 196 kN	Equivalent load cycles at 393 kN	Equivalent load cycles at 883 kN
393	1,700	3.0E+05	1.7E+03	0
883	304	2.3E+10	1.3E+08	304
Total		2.3E+10	1.3E+08	304

Table H- 4 Panel A: Calculation of Equivalent Load Cycles at 196 kN

P_s	P_1	P_2	R_1	R_2	S	n_1	n_2
1,218	393	196	0.32	0.16	4.80	50,000	6.1E+06
	638	196	0.52	0.16	10.81	10,000	5.0E+08
	785	196	0.64	0.16	14.41	2,000	3.6E+09
	883	196	0.72	0.16	16.82	1,243	2.5E+10
						Σn_2	2.9E+10

Table H- 5 Panel-D: Calculation of Equivalent Load cycles at 196 kN

P_s	P_1	P_2	R_1	R_2	S	n_1	n_2
1,472	393	196	0.27	0.13	3.99	1,700	9.2E+04
	883	196	0.60	0.13	13.98	5,000	5.9E+09
	981	196	0.67	0.13	15.97	41	3.5E+08
	1,030	196	0.70	0.13	16.97	50	1.2E+09
	1,079	196	0.73	0.13	17.97	108	6.9E+09
					Total	Σn_2	1.4E+10

Table H-6 Panel-C: Calculation of Equivalent Load Cycles at 196 kN

P_s	P_1	P_2	R_1	R_2	S	n_1	n_2
1,138	393	196	0.35	0.17	5.19	1,700	3.0E+05
	883	196	0.78	0.17	18.15	304	2.3E+10
					Total	Σn_2	2.3E+10

Table H-7 Panel-A: Calculation of Equivalent Load Cycles at 393 kN

P_s	P_1	P_2	R_1	R_2	S	n_1	n_2
1,218	393	393	0.32	0.32	0.00	50,000	5.0E+04
	638	393	0.52	0.32	6.01	10,000	4.1E+06
	785	393	0.64	0.32	9.61	2,000	3.0E+07
	883	393	0.72	0.32	12.01	1,243	2.0E+08
						Σn_2	2.4E+08

Table H- 8 Panel-D: Calculation of Equivalent Load Cycles at 393 kN

P_s	P_1	P_2	R_1	R_2	S	n_1	n_2
1,473	393	393	0.27	0.27	0.00	1,700	1.7E+03
	883	393	0.60	0.27	9.98	5,000	1.1E+08
	981	393	0.67	0.27	11.98	41	6.5E+06
	1,030	393	0.70	0.27	12.98	50	2.2E+07
	1,079	393	0.73	0.27	13.98	108	1.3E+08
					Total	Σn_2	2.6E+08

Table H- 9 Panel-C: Calculation of Equivalent Load Cycles at 393 kN

P_s	P_1	P_2	R_1	R_2	S	n_1	n_2
1,138	393	393	0.35	0.35	0.00	1,700	1.7E+03
	883	393	0.78	0.35	12.96	304	1.3E+08
					Total	Σn_2	1.3E+08

Table H- 10 Panel-A: Calculation of Equivalent Load Cycles at 883 kN

P_s	P_1	P_2	R_1	R_2	S	n_1	n_2
1,218	393	883	0.32	0.72	-12.01	50,000	0.3
	638	883	0.52	0.72	-6.01	10,000	24.6
	785	883	0.64	0.72	-2.40	2,000	181.0
	883	883	0.72	0.72	0.00	1,243	1,243.0
					Total	Σn_2	1,448.9

Table H- 11 Panel-D: Calculation of Equivalent Load Cycles at 883 kN

$P_{s\text{-}t}$	P_1	P_2	R_1	R_2	S	n_1	n_2
1,473	393	883	0.27	0.60	-9.98	1,700	0.1
	883	883	0.60	0.60	0.00	5,000	5,000.0
	981	883	0.67	0.60	2.00	41	301.9
	1,030	883	0.70	0.60	2.99	50	999.2
	1,079	883	0.73	0.60	3.99	108	5856.7
					Total	Σn_2	12,157.9

Table H- 12 Panel-C: Equivalent Load Cycles at 883 kN

P_s	P_1	P_2	R_1	R_2	S	n_1	n_2
1,138	383	883	0.35	0.78	-12.96	1,700	0.0
	883	883	0.78	0.78	0.00	304	304.0
					Total	Σn_2	304.0

APPENDIX-I

Sensor Response Curves for the Test Program are Given
on CD
Thesis-Vidyadhar Limaye/Appendix-I and J/Appendix-I

APPENDIX-J

Crack Patterns for the test program are on CD
Thesis-Vidyadhar Limaye/Appendix-I and J/Appendix-J